

Final Report for Contract  
ENC #C154213

State of Colorado  
Dept. of Natural Resources

Project entitled:

**Development of New Methodologies  
for Determining Extreme Rainfall**

Prepared by

William R. Cotton, P.I.  
with Co-Investigators  
Ray L. McAnelly and Travis Ashby  
Colorado State University  
Dept. of Atmospheric Science  
Fort Collins, CO 80523-1371

February 3, 2003

**Table of Contents**

<b>Executive Summary .....</b>	<b>3</b>
<b>1. Introduction .....</b>	<b>5</b>
<b>2. Background .....</b>	<b>6</b>
<b>3. Modeling Methodology .....</b>	<b>12</b>
<b>3.1 The numerical model .....</b>	<b>12</b>
<b>3.2 Ensemble modeling methodology .....</b>	<b>13</b>
<b>3.3 General problems encountered .....</b>	<b>14</b>
<b>4. Summary of Cases and Simulation Results .....</b>	<b>14</b>
<b>4.1 Introduction .....</b>	<b>14</b>
<b>4.2 Big Thompson storm of 31 July 1976 .....</b>	<b>15</b>
<b>4.3 Fort Collins storm of 28 July 1997 .....</b>	<b>32</b>
<b>4.4 Saguache Creek flood of 25 July 1999 .....</b>	<b>51</b>
<b>4.5 Dallas Creek flood of 31 July 1999 .....</b>	<b>55</b>
<b>4.6 Park Range heavy rain event of 18-21 September 1997 .....</b>	<b>65</b>
<b>4.7 Southwest Colorado/Dove Creek event of 2-6 September 1970 ...</b>	<b>71</b>
<b>5. Implications to Altitude Dependence on Extreme Precipitation in Colorado</b>	<b>81</b>
<b>5.1 Simulation maxima of total precipitation, rain and hail .....</b>	<b>82</b>
<b>5.2 Common grid .....</b>	<b>88</b>
<b>5.3 Identification of depth-area-duration events .....</b>	<b>93</b>
<b>6. Mapping Technique .....</b>	<b>99</b>
<b>7. A New Method of PMP Estimation .....</b>	<b>109</b>
<b>8. Summary and Conclusions .....</b>	<b>127</b>
<b>9. Suggestions for Future Research .....</b>	<b>128</b>
<b>References .....</b>	<b>129</b>
<b>APPENDIX 1 .....</b>	<b>134</b>

## Executive Summary

A new approach to extreme precipitation estimation has been developed using a convective-storm-resolving mesoscale model, the Regional Atmospheric Modeling System (RAMS). RAMS was run for six historical heavy precipitating cases over Colorado. The storms simulated were the Aug. 31, 1976 Big Thompson Storm, the July 28, 1997 Fort Collins Storm, the July 31, 1999 Dallas Divide Storm, the Sept. 18-22, 1997 Park Range Storm, the Sept. 4-6, 1970 Southern San Juans Storm, and the July 26, 1999 Saguache Creek Storm. A total of 27 simulations have been performed for these case studies in which land surface parameters such as soil moisture are varied, model parameters are varied, different large-scale analyses are used, and the synoptic pattern is moved relative to the underlying terrain.

The precipitation fields from each simulation were re-mapped on a common grid to produce composite results for PMP estimation. Maximum precipitation for a given duration, and maximum depth-area-duration (DAD) events produced by all simulations were mapped on the common grid. The re-mapped data were then used to compute Hershfield parameters. The sampled Hershfield parameters were then kriged and co-kriged back onto an estimation grid and these data were used to make PMP estimates.

The following conclusions have been drawn from the analyses of these cases.

- In each of the observed extreme precipitation cases, RAMS is able to produce one or more heavy rain events. However, the position and timing of those events does not always coincide with the observations. Typical spatial and timing errors are 10 to 50km and one to several hours, respectively.
- The most accurate control simulations occur with the least convective, large-scale forced storms like the San Juan and Park Range storms. The least successful simulations occur with the older convective events like the Big Thompson storm. This is likely due to the coarse resolution of the initial NCEP reanalysis data used for the older events and unavailability of good, high-resolution soil moisture data. More recent cases in which ETA upper air and surface analysis data plus ETA soil moisture data provide the best agreement with observations.
- Even in cases where the maximum simulated precipitation amounts are in close agreement with observations, the actual scenario of convective evolution is often different from that observed. In other words, owing to the inability of upper air, and surface data, as well as land-surface parameters (especially soil moisture) to represent completely the real world, the model climatology differs from actual climatology. These data are more poorly observed in the older convective cases so that the model climatology of those events varies more from the observed storm behavior, than in the more recent storms.
- Sensitivity tests reveal that simulations of heavy convective events are highly sensitive to the specification of initial soil moisture fields.

- Precipitation maxima occurring at higher elevations have significant contributions from hail, which reduces surface runoff rates due to prolonged melting.

The PMP estimates that we have made should be viewed as a demonstration of concept only. The data used for our estimates are too limited to provide useful quantitative PMP estimates. We had to limit our analysis to recent storms because we found that the NCEP reanalysis data were inadequate for the purpose of extreme precipitation simulations. Higher resolution ETA-based reanalysis data may overcome this deficiency and permit more reliable PMP estimates in the future.

## 1. Introduction

Extreme precipitation events in mountainous terrain can lead to devastating flash floods in mountain drainages and canyons. A thorough knowledge of the frequency and magnitudes of such events is necessary in order to develop reliable estimates of probable maximum precipitation (PMP) and probabilities of events of various magnitudes (e.g., 100 or 500-year storms). Such probabilistic measures of extreme precipitation occurrence are important in developing design standards for structures such as dams in mountainous terrain.

Unfortunately, the knowledge base of extreme precipitation events in the Rocky Mountains of Colorado is limited, primarily because of a historical sparse population and general lack of observations over much of the region (particularly in higher elevations), combined with a relatively short period of record (<~100 years) for the precipitation observations that do exist. To overcome these observational deficiencies, various assumptions have to be made about extreme storm characteristics to estimate high elevation PMP, and these assumptions rely heavily on a more robust observational record of extreme precipitation events at lower elevations in and adjacent to the Rocky Mountains (Hansen et al. 1988).

However, Jarrett (1983) and Jarrett and Costa (1983) concluded that there is little paleohydrologic evidence of extreme rainfall and flash-flooding above 7500 ft elevation in Colorado. Their findings suggest that current estimates of PMP and extreme rainfall potential may be significantly over-estimated at higher elevations. Thus, there is a need for developing alternate methods to assess extreme rainfall potential at high elevations in order to improve PMP estimates.

In an effort to better understand extreme precipitation potential and its variability in Colorado's mountainous terrain, the Colorado Department of Natural Resources (DNR) is supporting an extensive, multi-phased program that may eventually lead to improved estimates of PMP. The first phase of this program was conducted by McKee and Doesken (1997), who compiled an extensive database of precipitation and streamflow observations and identified over 300 extreme precipitation events in and near the region of interest dating back to the late 1800s.

In this report, we present the final results of the second phase of this Colorado DNR program, in which the development of new methodologies for estimating extreme precipitation at higher elevations in Colorado was explored. The methodology involves the use of a cloud resolving mesoscale model to simulate observed cases of extreme precipitation in Colorado and an examination of regional and elevational dependencies on the significant simulated precipitation events.

In the next section, the climatological background for this study is summarized. Section 3 describes the cases selected for simulation, and Section 4 summarizes the simulation results. The regional and elevational dependencies of the simulated extreme

precipitation are discussed in Section 5. Sections 6 and 7 describe a technique whereby the simulated heavy precipitation occurrences are spatially interpolated, with elevational dependencies, onto the entire Colorado Rocky Mountain region, to provide an estimate of extreme precipitation. In Section 8 we summarize the results of this study and provide recommendations for future research.

## 2. Background

McKee and Doesken's (1997) report (hereafter MD97), the "Colorado Extreme Storm Precipitation Data Study," provided the starting point for our investigation. Their Table 5 is the "recommended final list of storms for consideration in investigating extreme rainfall potential in the Rocky Mountain region of Colorado." It consists of 36 events out of the 328 entries in their "complete storm list" (their Appendix A). These events are representative of the heaviest rain events documented over the various hydroclimatic regions of Colorado (Fig. 1), with a bias toward more recent events, due to more extensive meteorological data being available for numerical modeling applications. We were restricted to events that occurred in the era of synoptic balloon-borne upper air observations beginning in the 1950s. For consistency of data assimilation techniques applied to these observations, we utilized the National Center for Environmental Prediction (NCEP) reanalysis products (Kalnay et al. 1996), which extend back to 1957.

Table 1 lists 21 storm events beginning in 1957 from MD97's recommended final list and represents the candidate cases for our simulations. (Their storm event 195, Gibson Dam, MT, on 6-8 June 1964, was excluded from consideration due to its extreme distance from Colorado). Five events that occurred since the MD97 study, and which deserve inclusion in an updated final recommended list (Doesken, personal communication; Jarrett, personal communication), have been added to Table 1. These include two events in the Front Range and Eastern Foothills hydroclimatic region (the Fort Collins flood event on July 28, 1997, and the Colorado Springs and Front Range flooding on April 28-30, 1999); an event in the Northwest Mountain region (along the Park Range near Clark on September 18-21, 1997); and two events in the Southwest Mountain region (Saguache Creek flood on July 26, 1999, and Dallas Creek flood on July 31, 1999). The locations of the 26 events in Table 1 are indicated in Fig. 2. Note that several events beyond Colorado are included, in order to increase the sample size for very extreme events (Rapid City, South Dakota flood of June 9, 1972) and for regions having relatively few in-state events (Colorado Plateau and Northern Basin regions); the rationale here is that simulation of these events can be applied to Colorado by transposing the meteorological fields.

Included in Fig. 2 are the storm types as classified by MD97 and the month of their occurrence. Since many of the events considered by MD97 occurred prior to the sounding era, their classification scheme is based primarily on scales of the reported precipitation and associated forcing, and not on specific synoptic patterns. Local Convective (LC) storms account for 17 of the 26 cases, and they most frequently occurred in July and August. General (G) storms account for six events and occurred in

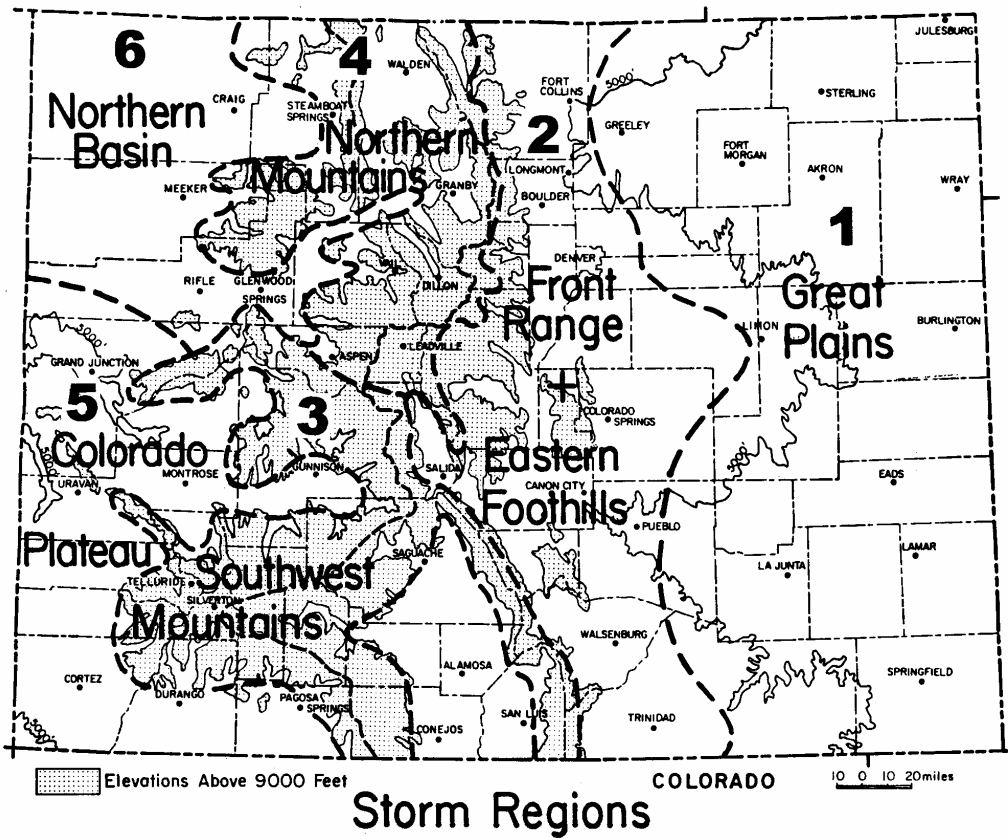


**Figure 1:** Approximate hydroclimatic regions of Colorado used to describe and characterize extreme precipitation events. From McKee and Doesken (1997, their Fig. 2).

**Table 1.** Candidate storm events for this study. Event numbers 173-315 are from McKee and Doesken's (1997) Table 5 (Recommended final list of storms for consideration in investigating extreme rainfall potential in the Rocky Mountain region of Colorado). Events R01-R05 are more recent heavy precipitation events.

No	Storm Name	Date	Maximum Precipitation	Climatic Region	Storm Type	Synoptic Type
173	San Luis	12 Aug 1957	2.9"/h, 8,000ft	3,5	LC	IV
174	Gateway	21 Aug 1957	3"/1.5h	5	LC	IV
175	Morgan, UT	16 Aug 1958	6-8"	6	LC	I
181	Pyramid	20-24 Sep 1961	3-5"	4,6	G	III
200	Plum Cr/Holly	16-17 Jun 1965	14-16"	1,2	GLC	III
215	Blanding, UT	1 Aug 1968	4-6"	5	LC	IV
217	Paonia	8 Aug 1968	4-5"	5	LC	IV
220	Big Elk Meadows	4-8 May 1969	6-14"	2,4	G	III
*231	SW CO/Dove Cr	4-6 Sep 1970	6"	3,5	G	III
234	Rapid City, SD	9 Jun 1972	15"	2	LC	I
237	SW CO/Durango	19-20 Oct 1972	5"	3,5	G	III
242	Sweetwater	12 Jul 1976	6"	4,6	LC	IV
*243	Big Thompson	31 Jul 1976	12"	2	LC	I
256	Frijole Creek	2-3 Jul 1981	8-16"	1,2	LC	I
270	Jim Creek	20 Jul 1983	2"/<1h, high el.	4	LC	I
277	Redstone	5-8 Jun 1984	3"	3,4	G	III
304	Deadman Hill	1 Aug 1989	2.8", high el.	4	LC	I
306	Opal, WY	16 Aug 1990	7"/2h	6	LC	I
312	Rifle/Gov't Cr	15 May 1993	4"/2h	6	LC	II
313	Delta/Roubideau	10 Aug 1993	4"/2h	5	LC	I
315	SW CO/Wolf Cr	27-30 Aug 1993	3-6"	3,5	GLC	II
*R01	Fort Collins	28 Jul 1997	10"/5.5h	2	LC	I
*R02	Park Range	18-21 Sep 1997	8", 10,500ft	4	GLC	III
R03	Front Rng/CoSpr	29Apr-1May1999	4-8"	2	G	III
*R04	Saguache Creek	25 Jul 1999	7.5"/1.5h	3	LC	IV
*R05	Dallas Creek	31 Jul 1999	4-5"	3	LC	IV

\* denotes cases simulated in this study

the spring and fall in association with stronger, more baroclinic synoptic systems. Three events were of the hybrid GLC classification, or Local Convective storms embedded in a General storm system (GLC); these occurred from June to September.

Since our case selection is confined to the sounding era, we can apply a classification scheme based on synoptic pattern, which is useful in examining case representativeness and variability within a grouping of similarly classified systems. Maddox et al. (1980) developed a synoptic classification scheme for flash flood events in the western United States, based on a survey of events from 1973-1978 (plus one event from 1972) documented in Storm Data. Because of varying geographic foci, objectives and approaches taken in their classification schemes, there is little correspondence between the 61 events surveyed by Maddox et al. (1980) and the 15 considered by MD97 (their App. A) during the same period. For instance, only seven of the Maddox et al. events occurred in Colorado, and they all occurred in the Front Range and Eastern Foothills region. Only three of those Colorado events were included in McKee and Doesken's full sample, with two remaining in their recommended final list. The Rapid City, South Dakota flood event was the fourth case common to both studies.

Despite these differences, the generalized Type I-IV synoptic patterns described by Maddox et al. (1980) are suitable for typing the extreme precipitation events in Colorado. Type I events involved a short-wave trough moving northward along the west side of a large-scale ridge, as in the Big Thompson case, while Type II events occurred in advance of a short-wave trough moving southward along the east side of a long-wave ridge (Figure 3). Type III events were associated with strong synoptic systems, with heavy orographic precipitation affecting large areas over several days. While most of the Type III events in Maddox et al. occurred along the west coast in association with eastward propagating large-scale troughs, this type is also an appropriate characterization of strong baroclinic waves (often developing into deep cut-off lows) moving into the intermountain west and Colorado; Maddox et al. included one such Type III event along the Front Range and Eastern Foothills region. The final Type IV is associated with very weak short-wave troughs, moving either westward or eastward in zonal flow to the south or north, respectively, of an east-west oriented large-scale ridge.

This synoptic classification scheme was applied to the 26 cases as shown in Table 1, and is indicated by the digit inside each circle or square in Fig. 2. There are nine Type I events; six of these occurred in the Front Range and Eastern Foothills region, and the other three occurred well west of the Continental Divide. These are all LC events as characterized by MD97, occurring mostly in July and August (one in June). Type II events were relatively infrequent, consisting of one LC event in May and one GLC event in August. This is consistent with the sample in Maddox et al. (1980), where only two of their 12 Type II events occurred in Colorado. In Fig. 2 Type III events account for eight of the 26 cases in Table 1, occurring both east and west of the Continental Divide. These strong synoptic events were classified by MD97 as G and GLC events and occurred in spring and fall. The remaining five cases in Table 1 are Type IV, most in the mountain and plateau regions of western Colorado. These occurred in July and August,

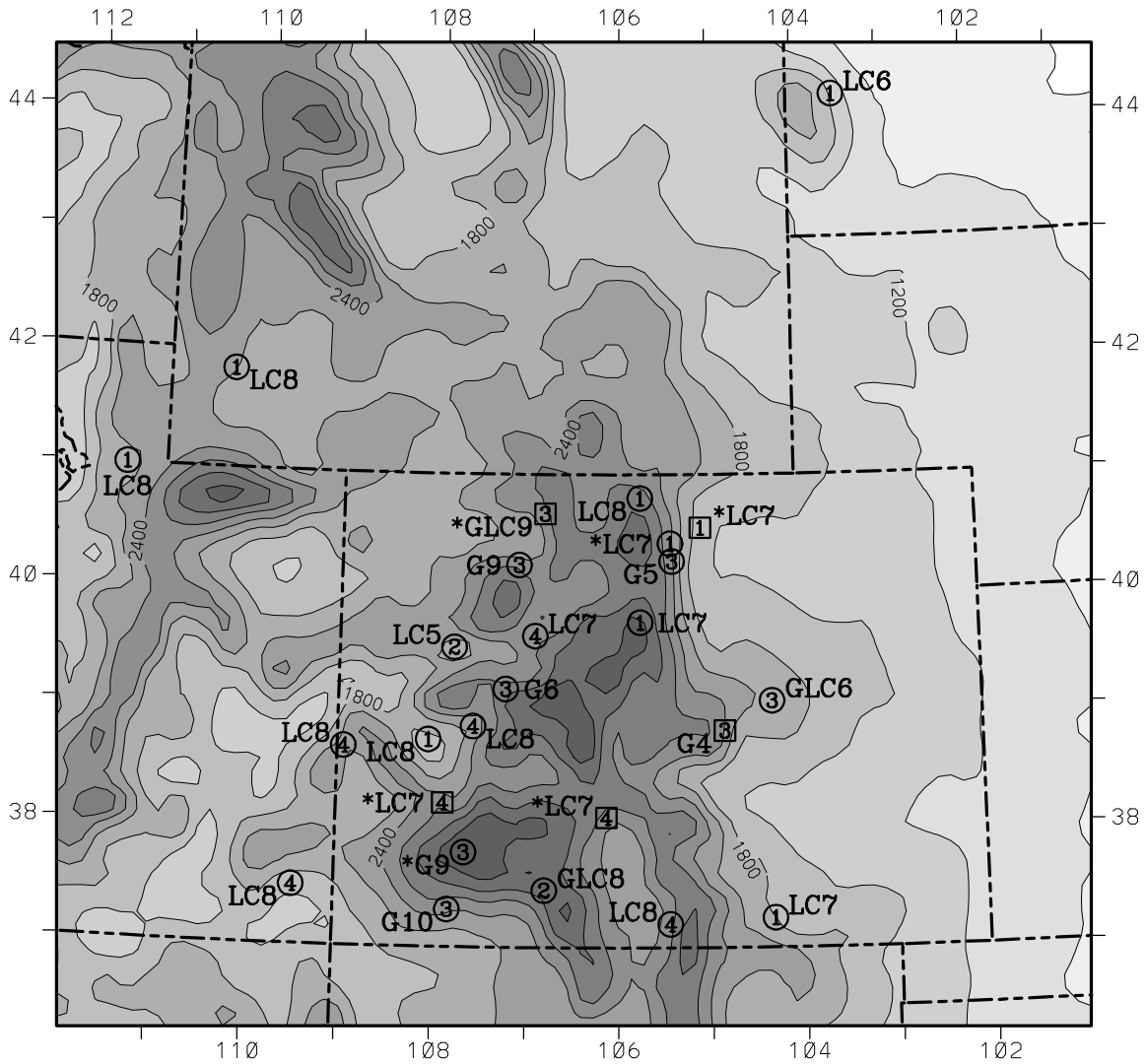


**Figure 2:** Locations of extreme precipitation events since 1957 from "final recommended list" of McKee and Doesken (1997, their Table 5; denoted by circles). Five more recent events are included (squares). Events are classified as General (G) storms, Local convective (LC) storms, or Local Convective storms embedded in General storm systems (GLC), and are appended with the month of occurrence. Single digits 1-4 inside a circle or square designates synoptic pattern I-IV as described by Maddox et al. (1980).

and along with the Type I events, are associated with the southwest monsoon and its extension into Colorado.

This set of candidate cases encompasses the range of synoptic situations that are most likely to produce extreme precipitation over Colorado. An exception may be cases of weakening tropical storms moving northwestward from the Gulf of Mexico. Such storms considered by Hansen et al. (1988) occurred mostly in Texas but almost as far northwest to the Eastern Foothills climatic zone in southern Colorado, and thus could

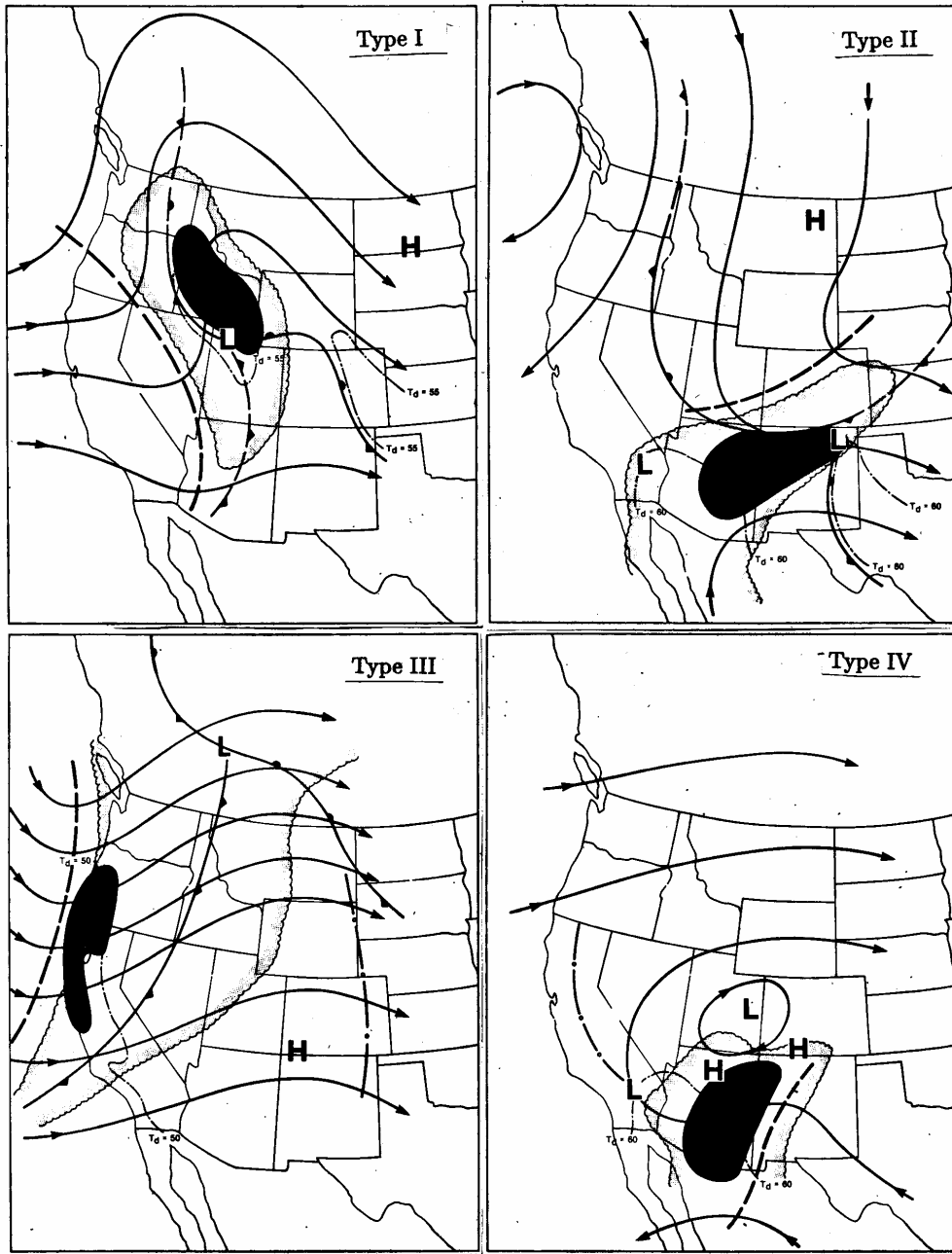


**Figure 3:** Generalized 500 mb and surface patterns for Types I-IV western flash floods (reproduced from Maddox et al., 1980). Features at 500 mb include flow (solid streamlines), troughs (heavy dashed), and region with dewpoint depression  $\leq 6$  deg C (scalloped/shaded boundary). Surface features include fronts, pressure centers, and isolines of high dewpoints. Area of greatest flood potential is shaded. For Types I, II, and IV, time is 0-3h prior to onset of storm activity. For Type III, time is near end of precipitation event.

impact the study area. However, proper perturbations included in ensemble runs for cases in Table 1, most appropriately Type I or IV events, could reasonably account for these scenarios as well.

### **3. Modeling Methodology**

#### ***3.1. The numerical model***

Our methodology for estimating extreme precipitation in Colorado's complex terrain is based on three-dimensional numerical simulation of the events in Table 1. The model used is the Regional Atmospheric Modeling System (RAMS; Pielke et al., 1992; Cotton et al., 2002), developed at Colorado State University under the direction of the Principal Investigator. While RAMS version 3b was used extensively in the preliminary stages of this work, all simulations included in this report utilized RAMS version 4.29. This version features a number of improved physical modules including those for microphysics and precipitation (Walko et al. 1995; Meyers et al. 1997), radiation (Olsson et al. 1998; Harrington 1997; Harrington et al. 1999), and land surface/ atmospheric exchanges of heat and moisture (Walko et al., 2000).

Interactive grid nesting is utilized, where the largest grid covers the western U.S. with a grid spacing of about 80km. Successively smaller and finer nested grids focus down to the region impacted by the observed event, with the finest grid covering an area on the order of  $(200 \text{ km})^2$  with a grid spacing of about 2 km. Mesoscale features that are simulated reasonably on coarser grids (e.g., a short wave and the accompanying vertical motion field) can advect or propagate onto finer grids, where smaller scale features can be simulated. The finest grid is termed a cloud-resolving grid because it can reasonably simulate the evolution of individual deep convective clouds. The highly resolved topography on the fine grid is very important in simulating precipitation in Colorado's complex terrain. With the two-way interactive nesting, effects resulting from resolved processes on finer grids (e.g., compensating subsidence in the near environment of deep convection) are fed back realistically to coarser grids. This configuration allows for the realistic simulation of synoptic to cloud-resolving scales over the western U.S. to the meso-beta-scale area of the extreme precipitation event, respectively.

For a given case, the model is initialized using large-scale analyses such as NCEP reanalysis data, or for more recent cases, higher resolution analyses such as NCEP's Rapid Update Cycle (RUC) or Eta model analysis. Analyses at subsequent times (6h intervals for the NCEP data) are used to provide time-dependent lateral and top boundary conditions. For LC cases, simulations are initialized at 1200 UTC (0500 MST) and are 24 h in duration (sometimes shorter if all significant precipitation has ceased), which encompasses the afternoon and evening convection of the event. The finest grid in LC cases has a grid spacing of 1.67 km in order to better resolve the dominant deep convective storms. For more extended GLC and G events, where convection is less dominant and the fine grid may need to be larger to include a larger impact area, the finest grid spacing is increased to 2.0 and 3.0 km, respectively.

### *3.2. Ensemble modeling methodology*

Our plan was to perform numerous ensemble simulations for as many cases in Table 1 as possible. Each case would consist of a control run initialized with an objective analysis of the observed conditions as described above, and alternate runs where one or more aspects of the control run are altered. These alterations can include using a different gridded dataset for initialization (e.g., Eta analysis vs. NCEP reanalysis); incorporating surface and sounding observations to add mesoscale detail to the coarse NCEP reanalysis; various soil moisture and temperature perturbations such as elevational dependent moistening or drying (which strongly affects topographic solenoidal circulations); atmospheric perturbations (e.g., increasing precipitable water up to maximum expected levels); and a number of specific model settings involving grid configuration, boundary conditions, cumulus and diffusion parameterizations, etc. Although we used a 1-moment bulk microphysics scheme with unchanged settings in all simulations, ensemble runs based on alternate microphysical settings or using a 2-moment scheme could also be done.

The ensemble members for a given case are intended to encompass the range of uncertainty in initial conditions, provide scenarios with even more extreme conditions than in the observed case (e.g., increased precipitable water), and provide alternate outcomes as a function of model settings only. From the collective ensemble results for a given case, the maximum precipitation that might be expected to occur with slight variations of the observed event can be estimated. The ensemble's spatial distribution of heavy events provides guidance as to which topographic regions and elevations are more susceptible to extreme precipitation. The partitioning of modeled precipitation between rain and frozen contributions shows a greater proportion due to hail at higher elevation; with its delayed runoff due to melting, this may limit the potential for flash-flood producing rains at higher elevations.

An alternate ensemble simulation approach was utilized wherein the initial meteorological fields are shifted relative to the topography, allowing the specific region of forcing in a given case to be shifted to other regions in Colorado. Besides providing a means to test the storm transposition assumption used in traditional PMP estimation, this technique potentially offers a way to increase the limited sample size of observed cases to a much larger number of artificial cases studies. Provided that the ensemble simulations for the observed cases generally bracket the observed outcomes, with one or more members simulating the observed extreme precipitation reasonably well, then transpositioned simulations allow a way to evaluate the range of extreme precipitation outcomes that could result with the same synoptic scenarios interacting with different topography. Potentially, this technique could lead to a model-based methodology for estimating PMP over specific high elevation locations as an alternative to current methodology.

### ***3.3. General problems encountered***

A number of problems prevented us from simulating as many cases as intended in Table 1, or from making the desired number of ensemble runs for some of the cases we did simulate. Each case generally required several preliminary runs before a reasonable control run could be realized, or required re-running the control simulation and some preliminary ensemble runs when serious modeling problems were discovered with a later ensemble run. The coarse resolution of the NCEP reanalysis data caused some of these problems, when the large scale was found to evolve improperly in several preliminary runs. The solution was an interactive process of finding the proper grid configuration and/or adding observations so that the large scale evolution became acceptable. Improper model settings caused some of the problems, such as too long of a time step or inappropriate diffusion settings that resulted in numerical noise well into a simulation. Another problem was that the perturbation runs often produced unexpected results. For instance, moistening the low-mid troposphere in the environmental inflow region might be expected to supply more moisture to a storm and produce more precipitation. However, many such moistening simulations resulted in increased cloud cover, reduced insolation and surface heating, and decreased storm development. Thus a series of perturbation runs with successively less moistening had to be performed before a reasonable extreme-precipitation outcome was realized. The transposition runs also often produced no extreme precipitation. In addition, the location of where intense precipitation events occurred in a transposed run was virtually unpredictable by us. Thus many of the transposed runs became a hit and miss procedure. Finally, a number of simulations were significantly delayed by hardware and software problems as well.

As a result of such delays and time consuming experimentation, we were able to perform one or more simulations for only six of the 26 cases in Table 1. Moreover, we concentrated on more recent cases where ETA analysis data were available once we realized the NCEP reanalysis data were generally inferior for this study. The preliminary or experimental runs that did not produce extreme precipitation are not included in our results.

## **4. Summary of cases and simulation results**

### ***4.1 Introduction***

We simulated the six cases marked with an asterisk in Table 1. In this section we briefly describe the synoptic setting and observed precipitation for each event, and present the simulated precipitation for each ensemble member.

The cases are presented in their reordered sequence in Table 2. The first two cases, the Big Thompson and Fort Collins storms, are both LC, Type I events in the northern portion of hydroclimatic region 1 in Fig. 1 (Front Range and Eastern Foothills). The third and fourth cases, the Saguache Creek and Dallas Creek events, are both LC, Type IV events in hydroclimatic region 3 (Southwest Mountains). The fifth case is a GLC, Type III event that occurred in the Park Range in region 4 (Northern Mountains).

The final case, a G, Type III event, produced widespread heavy precipitation in the San Juan Mountains in region 3 (Southwest Mountains), along with more localized heavy rain near the town of Dove Creek in region 5 (Colorado Plateau). These cases represent widespread geographical coverage over the three high-elevation hydroclimatic regions in Fig. 1, all three of MD97's storm classifications, and all of the synoptic classifications in Fig. 3 except for the relatively infrequently occurring (in Colorado) Type II. We were biased toward more recent cases in trying to achieve this representativeness because of the availability of the higher resolution Eta analyses, digital radar data, and other modern datasets.

The general model setup for each case is given in Table 2. Table 3 gives more detailed information on all ensemble members for the six cases, including atmospheric and soil initialization methods, and any applicable perturbations, transpositioning, alternate grid configurations, and/or alternate settings from the default model parameters shown in Table 4. Appendix A is a complete listing of the input name list (called RAMSIN; Walko and Tremback, 2000) for Simulation 401, the Dallas Creek control run. It provides many model settings used in all the simulations, and it uses the default settings in Table 4. Appendix A, combined with information from Tables 2, 3 and 4 and the nested grid configurations illustrated in subsequent figures, provides a nearly complete description for duplicating all simulations using standard RAMS version 4.29. The only exceptions are several instances of customized code development that were necessary to create some of the initialization and nudging options shown in Table 3.

#### ***4.2 Big Thompson storm of 31 July 1976***

The storms that produced the Big Thompson flood occurred in the late afternoon and evening of 31 July 1976. Detailed analyses of the event are found in Maddox et al. (1977) and Caracena et al. (1979). The large scale conditions at 500mb that morning are shown in Fig. 4 by the initial conditions on the RAMS coarsest grid (Grid 1), based on NCEP reanalysis. A negatively tilted ridge that is characteristic of Type I events (Fig. 3) is evident from eastern Oklahoma, across northeastern Colorado, Wyoming, and into Idaho. Weak southerly flow occurs over Colorado, just to the west of the ridge axis. Although a northward propagating shortwave over Arizona and New Mexico that was analyzed by Maddox et al. (1977) is not evident in the coarse NCEP reanalysis, the relative humidity (RH) field in Fig. 4 shows the associated moisture advecting northward into Colorado. Also indicated in Fig. 4 are the nested Grids 2-4; this grid configuration was identical for all ensemble runs for this event.

The initial large scale conditions at the first model level above ground on Grid 2 are shown in Fig. 5. This model level is a terrain-following surface about 42 to 49m (depending on elevation) above the model topography, so these fields are referred to as surface conditions. The potentially warmer air over higher topography reflects the stably stratified atmosphere. The most prominent feature is potentially cool, easterly flow in the northern plains, advecting moist air into northeastern Colorado, where the finer Grids 3-4 are nested. This flow is associated with a cool anticyclone centered in southern Saskatchewan and Manitoba, with a stationary front (not marked) across Kansas,

eastern Colorado, and turning northward against the mountains separating the cool air from warmer, southwesterly flow to the south. Such a surface front is typical of Type I events (Fig. 3).

A rainfall analysis by Maddox et al. (1980), reproduced in Fig. 6, shows a north-south axis of cumulative rain at an elevation of 8000-6000 ft along the eastern slope of the Front Range. Two maxima exceeding 10" appear over the Big Thompson River basin between Estes Park and Drake at about 8000' (2400m), with another 10" maximum at about 6500' (2000m) west of Fort Collins. Hansen et al. (1988) cite a maximum of 12.5" (317mm) in 4h for the Big Thompson storm. It caused a flash flood in the Big Thompson canyon that resulted in 139 people killed and over \$35 million in property damage (Maddox et al. 1977).

**Table 2.** Cases simulated and ensemble run parameters.

<b>Storm No. Name</b>	<b>Max Precip. Elev (ft)</b>	<b>Region, Types</b>	<b>Initial Time (UTC)</b>	<b>Max Sim Length (h)</b>	<b>Del-x,y (km) Del-t(s)</b>	<b>Fine Grid Area (km<sup>2</sup>)</b>	<b># Ensemble Members</b>
243 Big Thompson	12.5"/4h 8000	2 LC, I	1200 31 Jul 1976	24	<b>Grid1 Grid2 Grid 3 Grid4</b> 80km 20 5.0 1.67 60s 20 6.67 3.33	30,019	8
R01 Fort Collins	10"/5.5h 5200	2 LC, I	1200 28 Jul 1997	24	80km 20 5.0 1.67 90s 30 10.0 5.0	27,194	11
R04 Saguache Creek	7.5"/1.5h 8500	3 LC, IV	1200 25 Jul 1999	24	80km 20 5.0 1.67 60s 20 6.67 3.33	28,336	1
R05 Dallas Creek	4-5" 9000	3 LC, IV	1200 31 Jul 1999	24	80km 20 5.0 1.67 60s 20 6.67 3.33	30,019	4
R02 Park Range	8"/4d 10500	4 GLC, III	0000 18 Sep 1997	144	72km 24 6.0 2.0 60s 30 10.0 2.0	29,548	2
231 SW CO/Dove Cr.	6"/3d 10800/6500	3,5 G, III	0000 04 Sep 1970	72	81km 27 9.0 3.0 40s 20 10.0 5.0	62,001	1

**Table 3.** Simulations included in extreme precipitation results.

Storm Event	Simulation Name	Sim #	Atmospheric Init., Nudging	Atmospheric/Grid Modification	Soil Moisture Initialization <sup>k</sup>	Alternate Settings (Table 4)
Big Thompson	BigT-Control2	101	NCEP, 6h <sup>a</sup>		50% homogeneous	2a 5b
	BigT-Control4	102	NCEP, 6h		35,50% (5578 ft)	2a
	BigT-50p70m	103	NCEP, 6h		50,70% (6000 ft)	2a
	BigT-WObs1	104	NCEP+obs, 6h <sup>b</sup>		37,50% (5578 ft)	2a
	BigT-243-1	105	NCEP, 6h		35% homogeneous	2b 3a 4a 5a 6a 7a 8a
	BigT-243-2	106	NCEP, 6h		35% homogeneous	1a 2a 3a 4a 5a 6a 7a 8a
	BigT-243-3	107	NCEP, 6h		35, 65% (6000 ft)	1a 2a 3a 4a 5a 6a 7a 8a
	BigT-243-4	108	NCEP, 6h		50, 70% (6000 ft)	1a 2a 3a 4a 5a 6a 7a 8a
Fort Collins	FCL-Control	201	NCEP, 12h <sup>c</sup>		50% homogeneous	3b 5b
	FCL-30p50m	202	NCEP, 12h		30,50% (6000 ft)	3b 5b
	FCL-50p30m	203	NCEP, 12h		50, 30% (6000 ft)	3b 5b
	FCL-50p70m	204	NCEP, 12h		50, 70% (6000 ft)	3b 5b
	FCL-70p50m	205	NCEP, 12h		70, 50% (6000 ft)	3b 5b
	FCL-LLMoist	206	NCEP, 12h	Moisture pert. M1 <sup>f</sup>	50% homogeneous	3b 5b
	FCL-EtaMoist	207	Eta, 3h <sup>d</sup>	Moisture pert. M2 <sup>g</sup>	Eta	3b 5b
Saguache Creek	FCL-Eta-2	208	Eta, 3h		Eta	3b 5b
	FCL-Prelim	209	NCEP+obs, 12h <sup>e</sup>		Eta	1c 3c 4b 5b 6b 7c 9a
	FCL-Pre-Shift	210	NCEP+obs, 12h	Transposition T1 <sup>h</sup>	Eta	1c 3c 4b 5b 6b 7c 9a
	FCL-Pre-SoilT	211	NCEP+obs, 12h		Eta	1c 3c 4b 5b 6b 7d 9a
	Sag-Control	301	Eta, 3h		Eta	
Dallas Creek	Dal-Control	401	Eta, 3h		40, 70% (6000 ft)	
	Dal-EtaSoil	402	Eta, 3h		Eta	
	Dal-Mpert1	403	Eta, 3h	Moisture pert. M3 <sup>i</sup>	40, 70% (6000 ft)	
	Dal-COS	404	Eta, 3h	Relocated G3, 4 <sup>j</sup>	Eta	
Park Range	PRange-Control	501	Eta, 3h		Eta	
	PRange-LLMoist	502	Eta, 3h	Moisture pert. M2	Eta	
SWCO/Dove Cr	SWColo-Control	601	NCEP, 6h		35% homogeneous	1b 2b 3a 4a 5a 6a 7b

<sup>a</sup> NCEP reanalysis (2.5deg lat/lon, 17 pressure levels), 6h intervals.
<sup>b</sup> NCEP reanalysis + surface obs and soundings for initialization; NCEP at 6h intervals for nudging.
<sup>c</sup> NCEP reanalysis, 12h intervals.
<sup>d</sup> Eta analysis (40km spacing, 26 pressure levels), 3h intervals.
<sup>e</sup> NCEP reanalysis + surface obs and soundings for initialization and nudging, 12h intervals.
<sup>f</sup> Moisture perturbation M1: relative humidity RH increased regionally to 98% at and below 850mb (if not already that high), and weighted toward 90% at 700mb.
<sup>g</sup> Moisture perturbation M2: relative humidity RH increased west of 106W to 90% at and below 500mb (if not already that high), with lesser moistening at 450 and 400mb.
<sup>h</sup> Transposition T1: Synoptic fields shifted southward 234 km.
<sup>i</sup> Moisture perturbation M3: relative humidity RH increased regionally to 85% at and below 500mb (if not already that high), with lesser moistening at 450 and 400mb.
<sup>j</sup> Grids 3 and 4 relocated from southwestern Colorado to Front Range over Colorado Springs.
<sup>k</sup> Values are per cent saturation and apply to all layers; 100% saturation is 0.42 m <sup>3</sup> /m <sup>3</sup> volumetric fraction for soil type used; when two values are listed, the first (second) value specifies soil moisture below (above) the separating elevation. 'Eta' indicates a 3-dimensional soil moisture (soil temperature too unless otherwise noted as an altered setting for category 7 in Table 4) initialization based on the two-(four-)level Eta soil model analysis at the initial time for the 1997(1999) cases.

**Table 4.** RAMS 4.29 default model settings used in simulations, except for alternates noted in Table 3. Other settings that are identical for all simulations are in Appendix A.

Model Category	Default Settings	Alternate Settings
1. Vertical grid structure	44 sigma-z levels; del-z = 100m at surface, stretches by 1.12/level to max del-z of 800m aloft; model top at 25.1 km	1a: 40 sigma-z levels to 21.9 km 1b: 39 sigma-z levels to 21.1 km 1c: 37 sigma-z levels to 19.5 km
2. Cumulus parameterization	Modified Kuo scheme, Grid 1 only	2a: Parameterization not used 2b: Mod-Kuo scheme, Grids 1 and 2
3. 4DDA (nudging) e-folding timescales	Lateral boundaries: 200s; Top boundary: 300s	3a: 900s, 7200s 3b: 1800s, 900 s 3c: 900s, 43200s
4. Vertical diffusion	Mellor-Yamada (M-Y) scheme on Grids 1, 2, and 3; Smagorinsky (Smag.) scheme on Grid 4	4a: M-Y on Grids 1-4 4b: Smag. On Grids 1-3, M-Y on Grid 4
5. Coefficients for constraining minimum horizontal diffusion	0.6, 0.75, 1.0 and 1.8 for Grids 1-4, respectively	5a: stronger diffusion; 0.85, 1.0, 1.2, 2.5 5b: weaker diffusion; 0.6, 0.6, 0.6, 0.6
6. Soil layers	7 layers, lower boundaries at - 2.00, -1.30, -0.82, -0.50, -0.29, - 0.15, -0.06 m	6a: 8 layers, -1.20, -0.80-0.60, - 0.40, -0.30, -0.20, -0.10, -0.05 m 6b: 8 layers, -0.40, -0.30, -0.25, - 0.20, -0.16, -0.12, -0.09, -0.06 m
7. Soil temperature	Based on Eta soil model analysis when soil moisture is also based on Eta analysis; otherwise set to surface air temperature ( $T_{sfc}$ )	7a: deep (shallow) layers 5C warmer (1C warmer) than $T_{sfc}$ 7b: deep (shallow) layers 5C warmer (2C cooler) than $T_{sfc}$ 7c: all layers several C cooler than $T_{sfc}$ 7d: deep (shallow) layers 1C warmer (1.5C cooler) than $T_{sfc}$
8. Timesteps	Case defaults in Table 2	8a: For simulations 105-108 Grid 1-4 used 80, 26.7, 8.89, and 4.44s, respectively
9. Microphysics and nested grid activation	Grids 1-4 all active at initialization with full microphysics	9a: Grids 1-3 active at 0h with condensation only, full micro activated at 3h; Grid 4 with full micro spawned at 6h

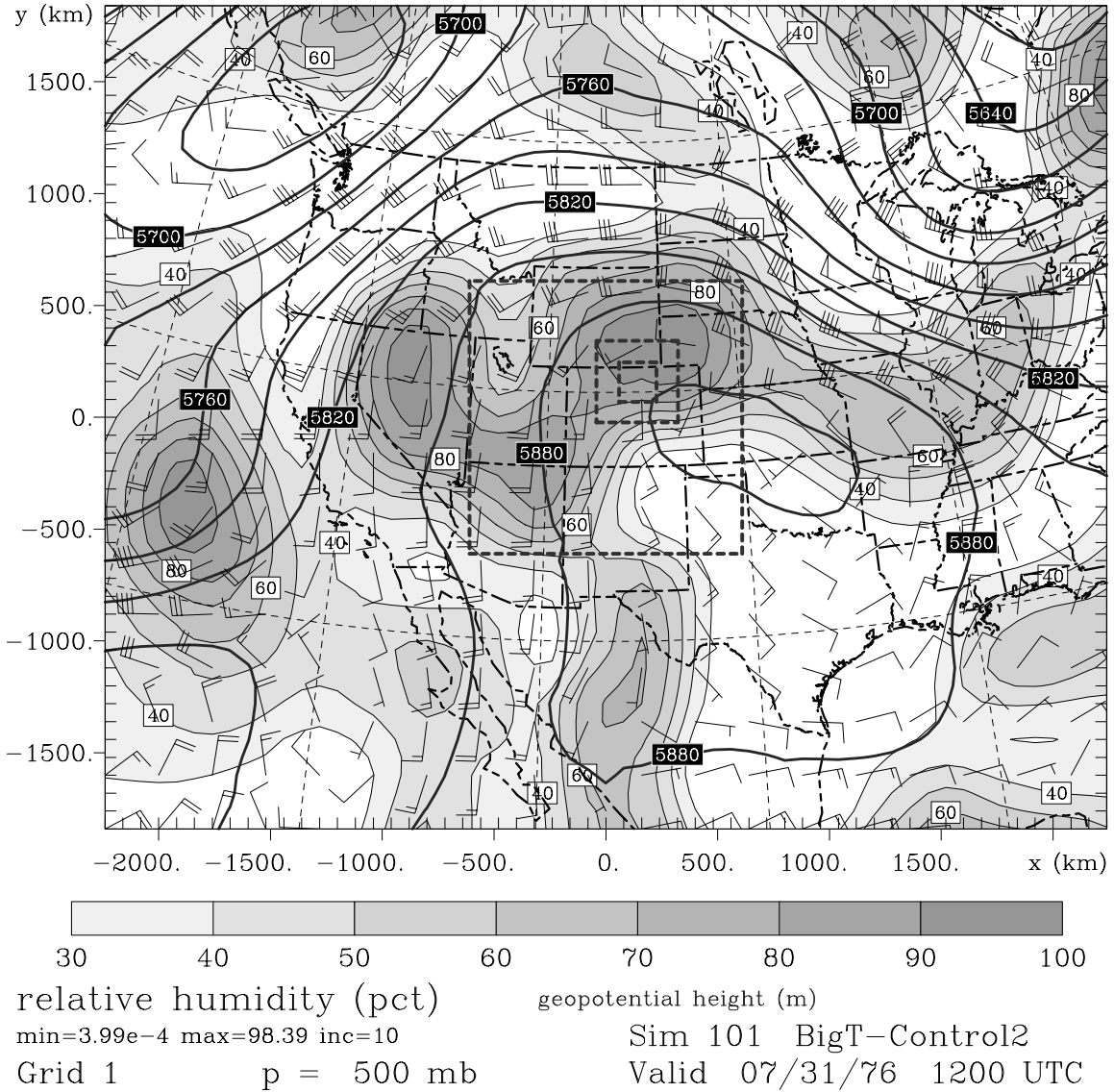


**Figure 4:** RAMS initialization, at 1200 UTC 31 July 1976, at 500mb on Grid 1 for Simulation 101 (Big Thompson control run). Fields include geopotential height (heavy contours), relative humidity (shaded), and wind barbs (full barb = 5m/s). Locations of nested Grids 2-4 are shown by dashed boxes.

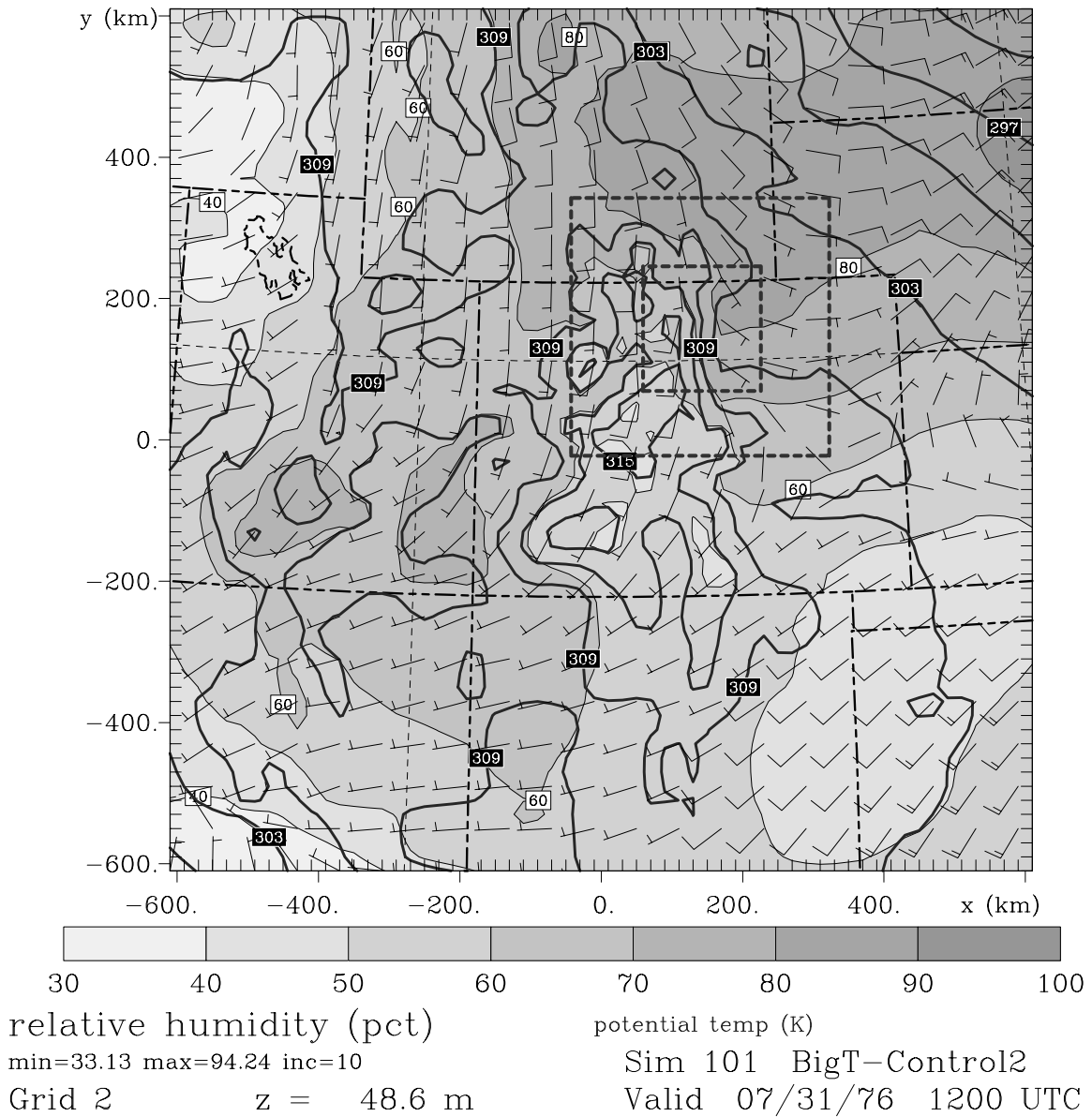


**Figure 5:** RAMS initialization, at 1200 UTC 31 July 1976, at surface on Grid 2 for Simulation 101 (Big Thompson control run). Fields include potential temperature (heavy contours), relative humidity (shaded), and wind barsbs (full barb = 5m/s). Locations of nested Grids 3-4 are shown by dashed boxes.

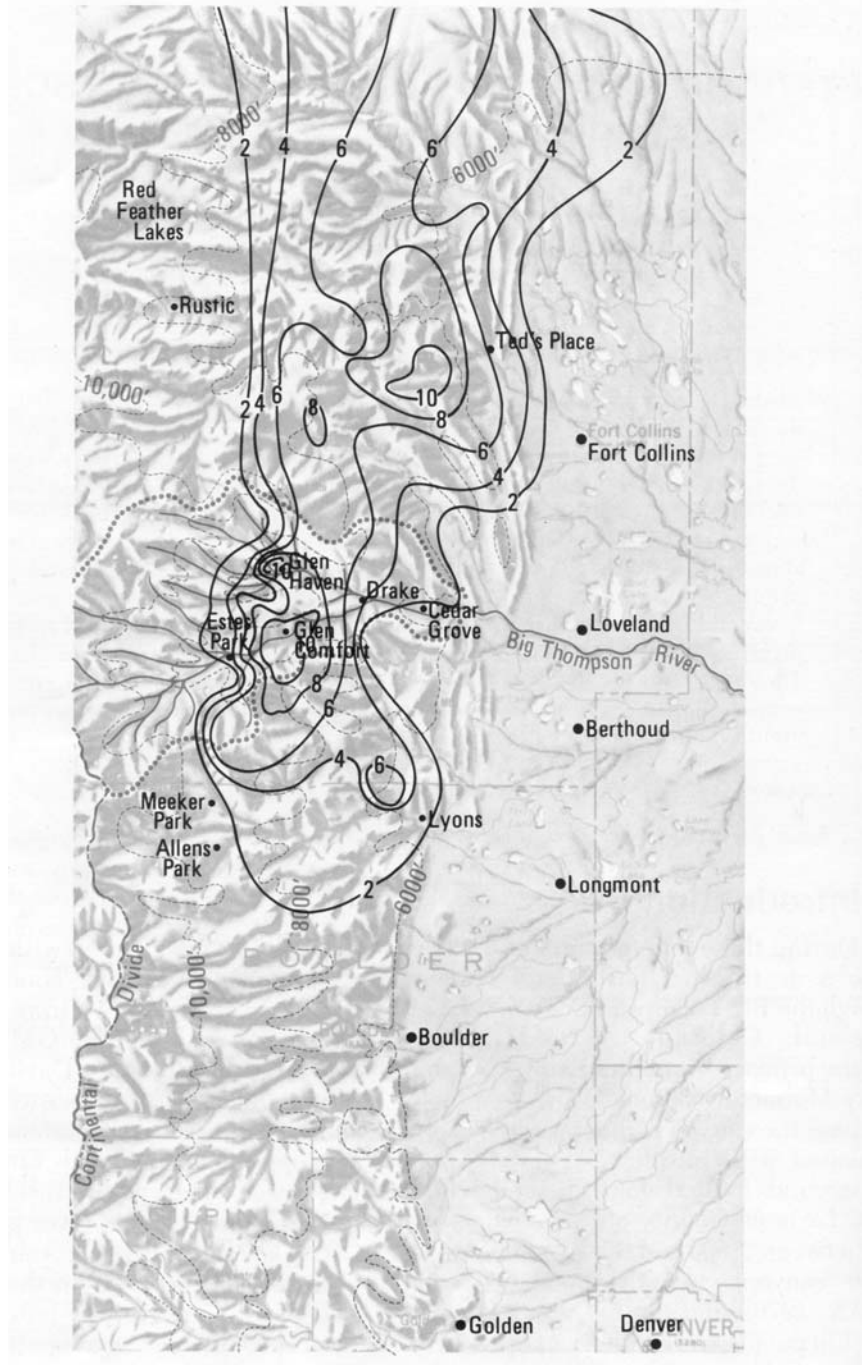


**Figure 6:** Big Thompson and North Fork of the Big Thompson drainages. Towns within and near the flash flood area are identified. Cumulative rainfall isohyets (solid lines) for the period 31 July-2 August 1976 are shown. Terrain contours (dashed lines) are in feet above mean sea level. The precipitation summary and isohyetal map were prepared by the National Weather Service Central Region Headquarters in Cooperative with other Federal Agencies. Extent of map is 67km east-west by 134km north-south. [From Maddox et al., 1977.]

Eight ensemble simulations are included for the Big Thompson case, identified in Table 3 as simulations 101-108. Simulation 101 utilized NCEP reanalyses for initialization and 6h nudging data, and soil moisture was set to a uniform 50% of saturation. For the soil type specified in Appendix A, the volumetric fraction at saturation is  $0.42 \text{ m}^3 \text{ water/m}^3 \text{ soil}$ . No cumulus parameterization was used on any grid, and horizontal diffusion constants were set relatively low. Total precipitation in Simulation 101 is shown in Fig. 7 (solid contours). The pattern resulted from early afternoon convection in the mountainous western half of the domain, and the later development of convection in the lower foothills and plains that progressed from south to north. Maximum precipitation is 293mm in a relatively small, intense core south of Boulder (BOU), at an elevation of 1863m. Although this simulated maximum approaches the observed value, the simulated convective evolution was quite ordinary and did not exhibit the unusually stationary, quasi-steady characteristics described by Maddox et al. (1977).

The next experiment run was identical, except soil moisture was initialized at 35% saturation below 5600 ft and 50% above 5600 ft. This was done in an attempt to improve the simulated low-level surface temperature and dewpoint over Simulation 101. In this run, the drier soil heated faster, and with the same weak horizontal diffusion used in Simulation 101, numerical instability developed. Thus, the diffusion parameters were strengthened, and the experiment was successfully rerun as Simulation 102. Although convective evolution was similar to Simulation 101, the maximum of 177mm in the total precipitation field (Fig. 8) occurs at a much higher elevation, near the crest of the Front Range in the southwestern portion of Grid 4. Several maxima exceeding 150mm are evident near Estes Park (EPK), Drake (DRK) and to the north in the Cache le Poudre River basin, all at intermediate elevations as was observed. A comparison of Figs. 7 and 8 (and subsequent precipitation fields) reveals that the stronger diffusion results in a qualitatively smoother precipitation pattern with slightly larger, more coherent storm cores. Analysis of precipitation rate patterns shows that this is due to storms in the higher diffusion runs similarly having a smoother, more coherent structure.

Simulation 103 was identical to 102, except soil moisture was initialized to 50% and 70% below and above 6000' elevation. The moister soil resulted in less surface sensible heating and a cooler boundary layer than in Simulation 102. As a result, downdraft outflow was weaker and storms became more organized and propagated more slowly. The resulting precipitation field (Fig. 9) is more tightly focused, with a maximum of 201mm at an intermediate elevation of 2111m in the Poudre basin.

In an attempt to add initial mesoscale detail that is lacking in the  $2.5 \times 2.5$ -deg lat/lon NCEP reanalysis data, Simulation 104 was similar to 102 and 103, except surface observations and soundings were incorporated, and soil moisture was set to 37% and 50% below and above 5600', respectively. The precipitation field for this run (Fig. 10) had

Sim 101: BigT-Control2

Tot precip, hail (mm)

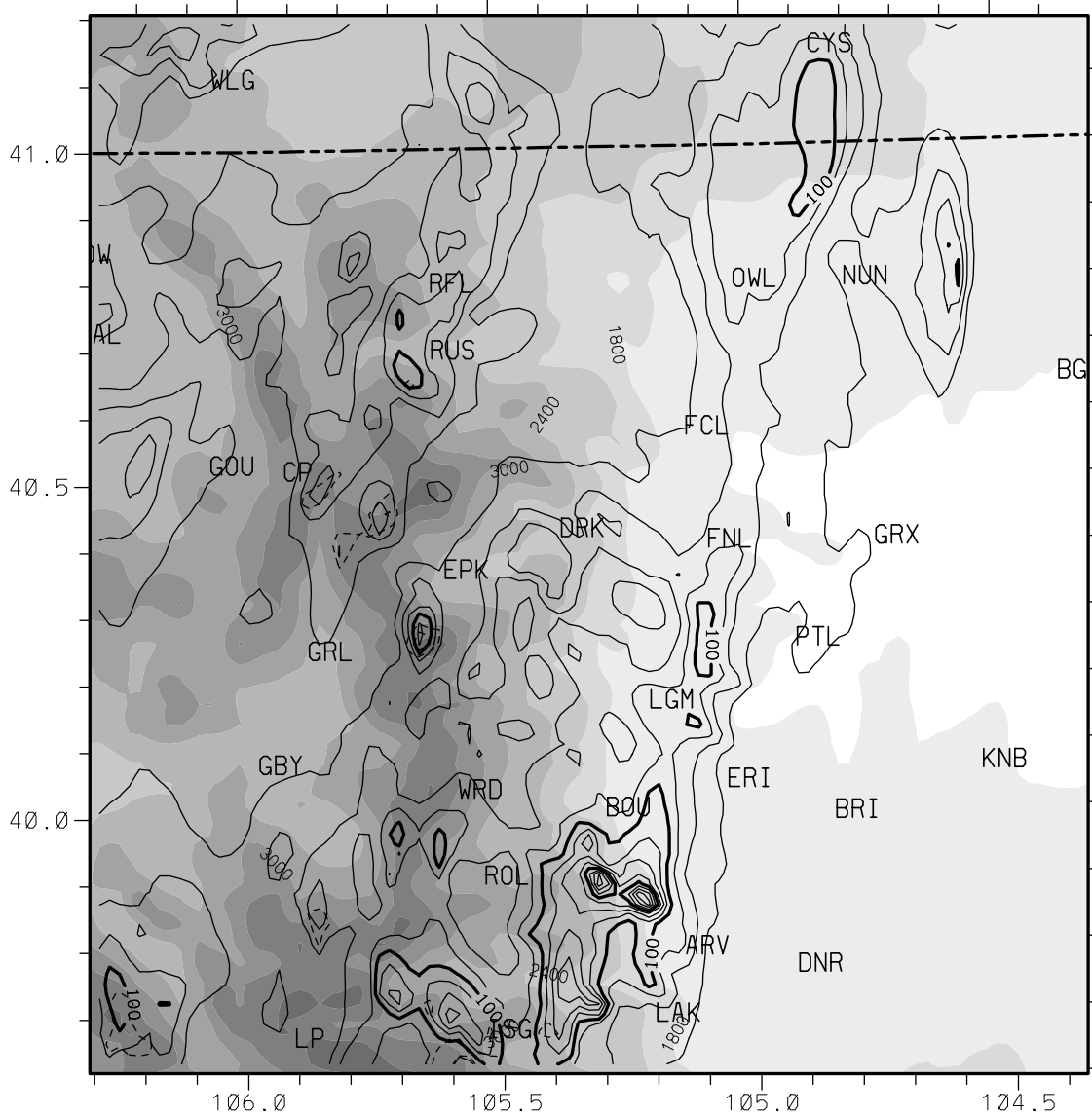


**Figure 7:** Simulated total precipitation (solid contours) and precipitation due to hail (dashed contours) on Grid 4 for Simulation 101. For both fields, isohyets begin at 25mm and are at 25mm increments (~1 inch); heavy contours are multiples of 100mm (~4 inches). Topography is progressively shaded at 300m intervals.

Sim 102: BigT-Control4

Tot precip, hail (mm)

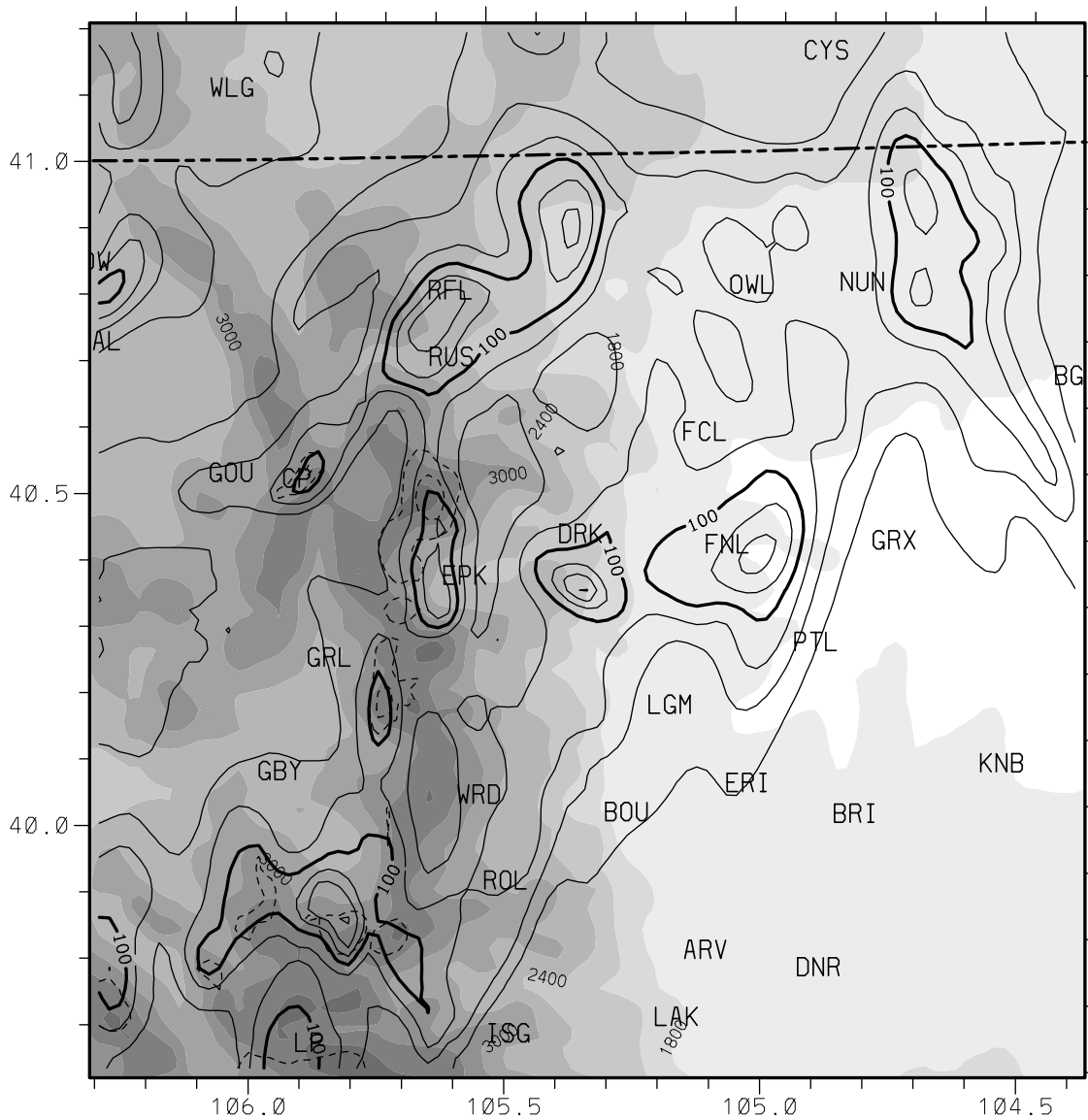


**Figure 8:** Simulated total precipitation and precipitation due to hail on Grid 4 for Simulation 102. Details are as in Fig. 7.

Sim 103: BigT-50p70m

Tot precip, hail (mm)

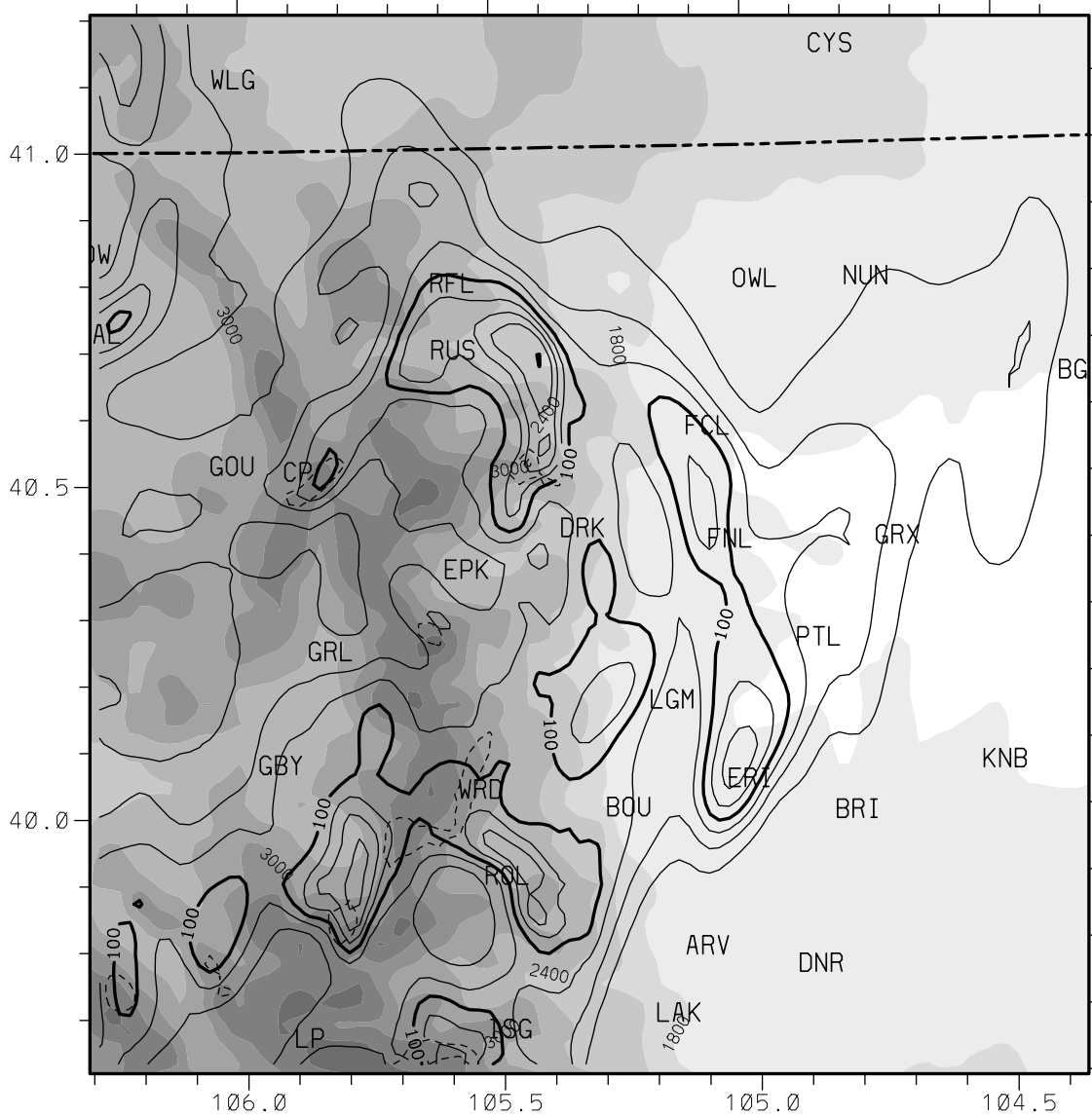


**Figure 9:** Simulated total precipitation and precipitation due to hail on Grid 4 for Simulation 103. Details are as in Fig. 7.

Sim 104: BigT-WObs1

Tot precip, hail (mm)

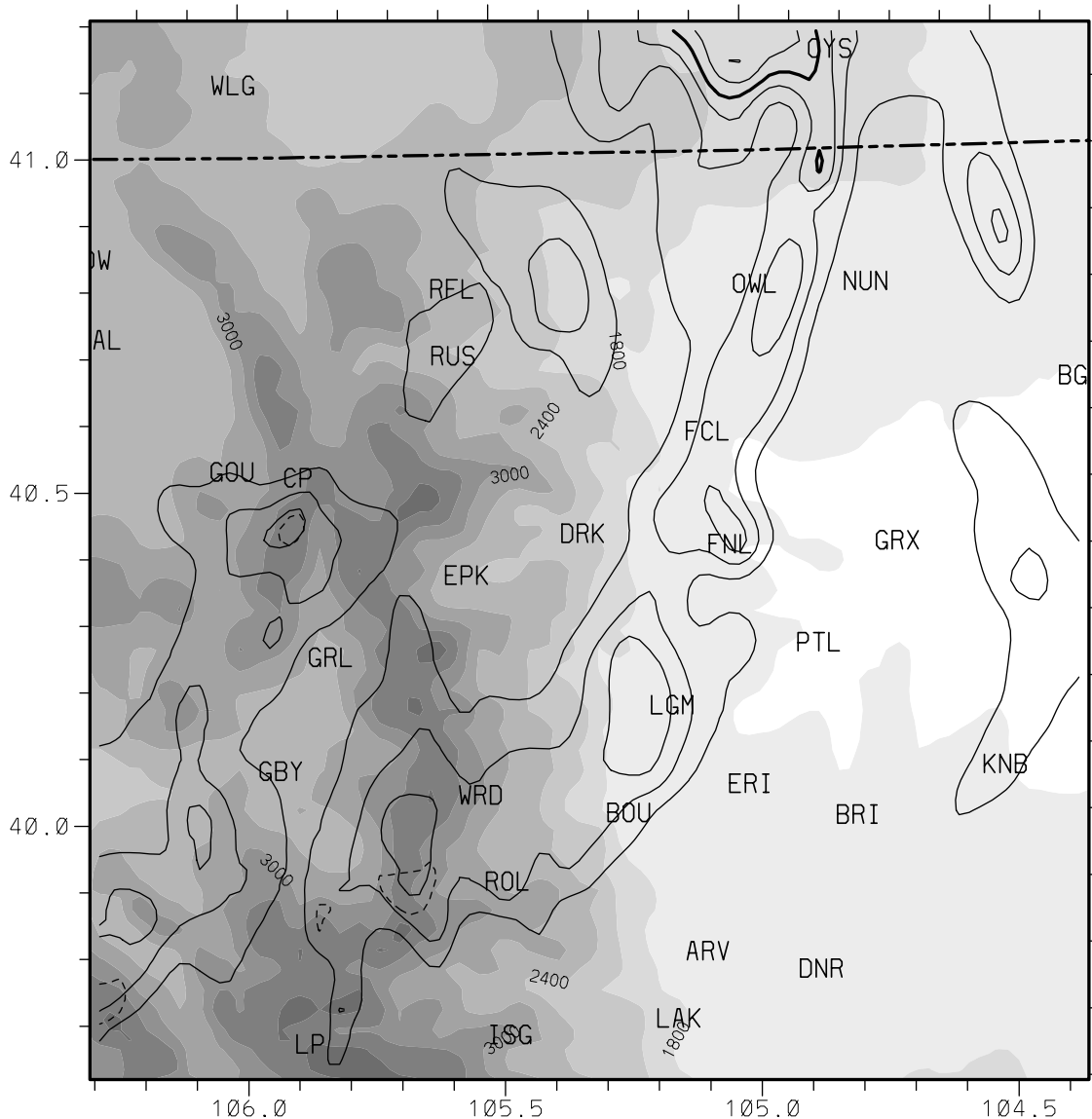


**Figure 10:** Simulated total precipitation and precipitation due to hail on Grid 4 for Simulation 104. Details are as in Fig. 7.

the smallest maximum of any of the Big Thompson runs (151mm near the northern edge) and a complete lack of significant precipitation in the Big Thompson basin. Thus adding the observations to the NCEP reanalysis did not improve the location nor enhance the magnitude of significant precipitation.

Another set of Big Thompson runs utilized the NCEP-based initialization (without observations), but a number of different settings as specified in Tables 3 and 4, including even slightly stronger diffusion than used in Simulations 102-104. Simulation 105 used 35% homogeneous soil moisture and a cumulus parameterization on Grids 1 and 2. Its total precipitation field (Fig. 11) shows a pattern along the eastern slope of the Front Range similar to the observed pattern in Fig. 6, but with a maximum axis along the crest

Sim 105: BigT-243-1

Tot precip, hail (mm)

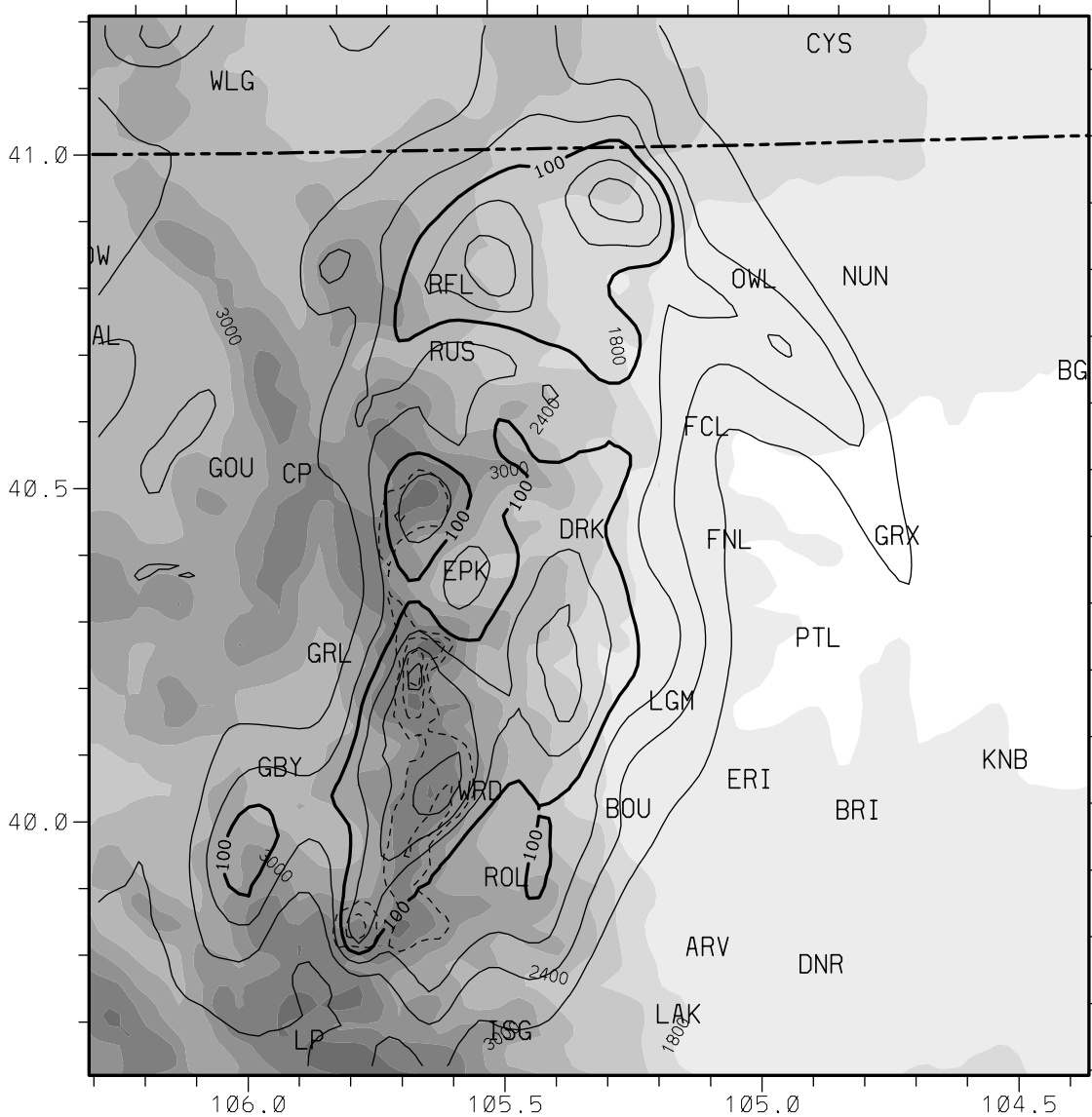


**Figure 11:** Simulated total precipitation and precipitation due to hail on Grid 4 for Simulation 105. Details are as in Fig. 7.

in the central to southern portions of the range, where the maximum of 187mm is at 3559m above Ward (WRD). Intermediate elevation maxima exceeding 150mm are seen south of the Big Thompson basin and in the northern Poudre basin.

A convective parameterization such as utilized in Simulation 105 is generally used on coarse grids in order to account for the effects of latent heating and moisture redistribution due to unresolved convection. Inclusion of these parameterized effects presumably leads to improved simulations of the mesoscale and even large-scale environment in which convection occurs. However, all such schemes are only crude approximations of convective effects, and there are numerous problems concerning

the triggering, timing, location and effects of parameterized convection. Complicating the matter is that there has been great difficulty in designing a scheme that is suitable for intermediate grid spacings on the order of 20km (as with our Grid 2). Published research (e.g., Warner and Hsu, 2000), as well as our own experience with case studies and the realtime RAMS forecast model, have shown that a convective parameterization on coarse grids can have detrimental effects on the explicit simulation of convection on finer grids. Because the parameterized precipitation on Simulation 105's Grid 2 (not shown) was generally quite small in regions exterior to the nested Grids 3 and 4, it is reasonable to expect that the parameterized effects in Simulation 105 may be relatively weak and unimportant to the overall simulation, and that by excluding the parameterization, any detrimental effects feeding back into the finer grids might be eliminated. Thus Simulation 106 was run almost exactly as 105, except with no convective parameterization. Indeed, the large-scale evolution and precipitation pattern over most of the model domain in Simulation 106 was very similar to that in 105. The total precipitation pattern on Grid 4 in Simulation 106 (Fig. 12) is quite similar to Simulation 105's (compare with Fig. 11), including both high and intermediate elevation axes of heavier precipitation. However, Simulation 106 has larger maxima: the absolute maximum of 246mm over the Continental Divide south of Estes Park is 59mm larger than the corresponding maximum in Simulation 105, and the other maxima are about 25mm larger. In addition, significant precipitation extends further east from the mountains in Simulation 106. Thus, lack of a convective parameterization on the coarser grids resulted in more precipitation on the cloud-resolving grid.

In general, the high elevation maxima in the preceding Big Thompson runs were a result of early afternoon convective development within 20 km of the ridgeline, apparently forced by converging upslope flow from both east and west slopes, combined with their slow movement due to the weak mid-level flow. Eventually, however, cold pools developed beneath slow-moving, high elevation storms, which led to propagating density currents that altered the storm characteristics. In some of the previous simulations, the outflows merged into a unified mesoscale outflow. The outflows propagated down the slope faster than the slow-moving storms and repeatedly forced new convection near the gust front ahead of the earlier storms. This resulted in a weakening of the storms that dominated the first few hours, and the development of sometimes broader and more complex multi-cell storm structures with generally weaker updrafts than seen earlier. This eastward propagation also resulted in more precipitation extending onto the plains than was observed.

In contrast to this general simulated evolution, the analyses of Maddox et al. (1977) and Caracena et al. (1979) show that the actual storms formed at intermediate elevations on the Front Range and were quasi-stationary. Individual cells were observed to move northward to northwestward with the prevailing easterly low-level to southerly mid-level flow, with repetitive new cell formation on the southeastern flank of the storm leading to its quasi-stationarity. The discrepancies in the simulations are apparently related to a simulated boundary layer that is too warm, dry and deep, leading to the high cloud bases and allowing significant sub-cloud evaporative cooling and gust

front propagation. The observed cloud base was about 1000m lower, which prevented

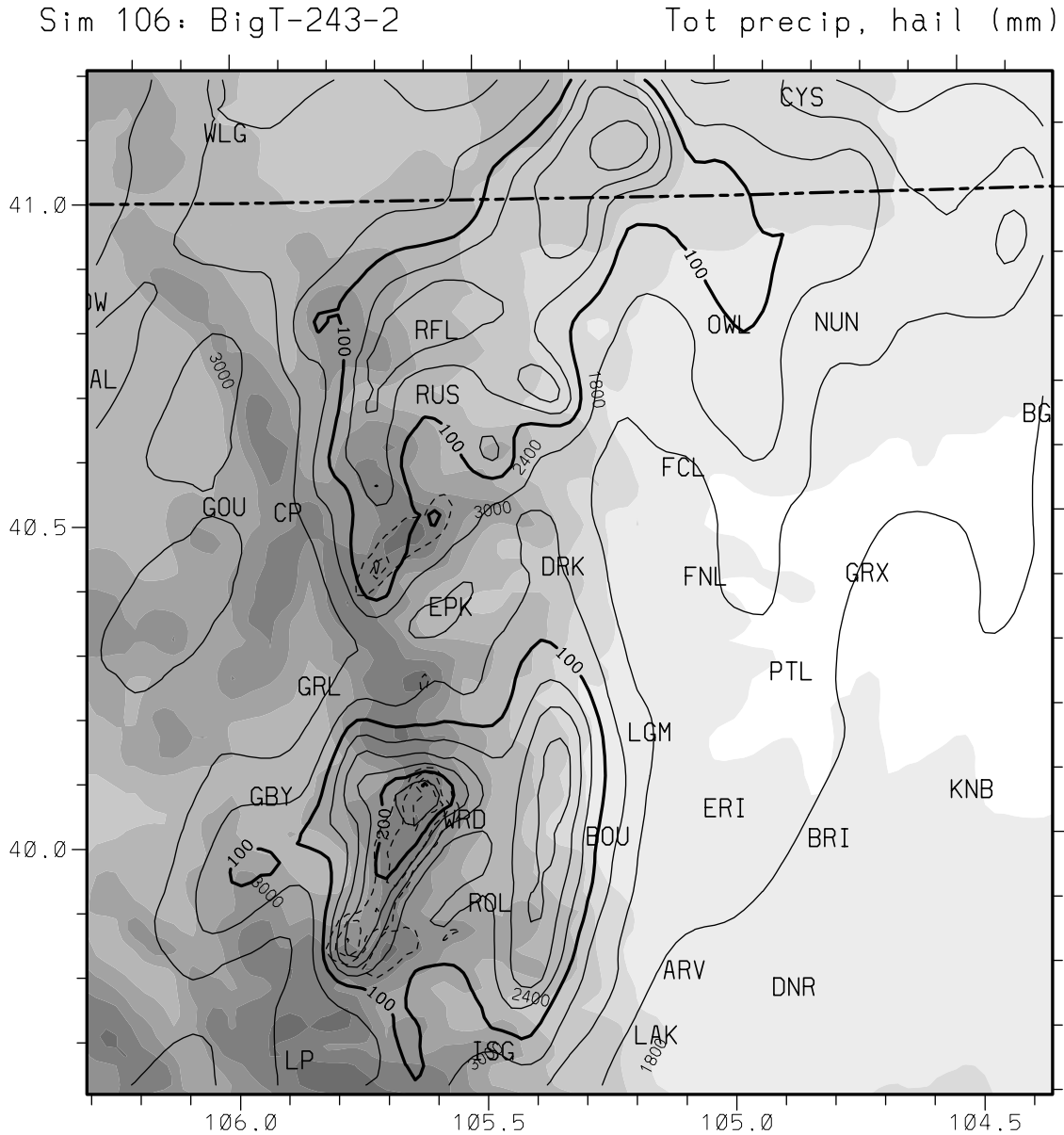


**Figure 12:** Simulated total precipitation and precipitation due to hail on Grid 4 for Simulation 106. Details are as in Fig. 7.

In an attempt to lower the elevation of simulated storm formation, Simulation 107 had increased initial soil moisture (65%) above 6000', with the same 35% below 6000' as in Simulation 106. With more moistened higher elevations, it was thought that reduced surface heating along the slopes would result in weaker upslope flow, perhaps resulting in less ridge-top convergence and allowing convection to develop instead at lower elevations. However, convective evolution in Simulation 107 was still similar to the earlier simulations, including high-elevation storm formation, eastward propagation, and

overall precipitation patterns. The precipitation field for Simulation 107 (Fig. 13) reflects these similarities.

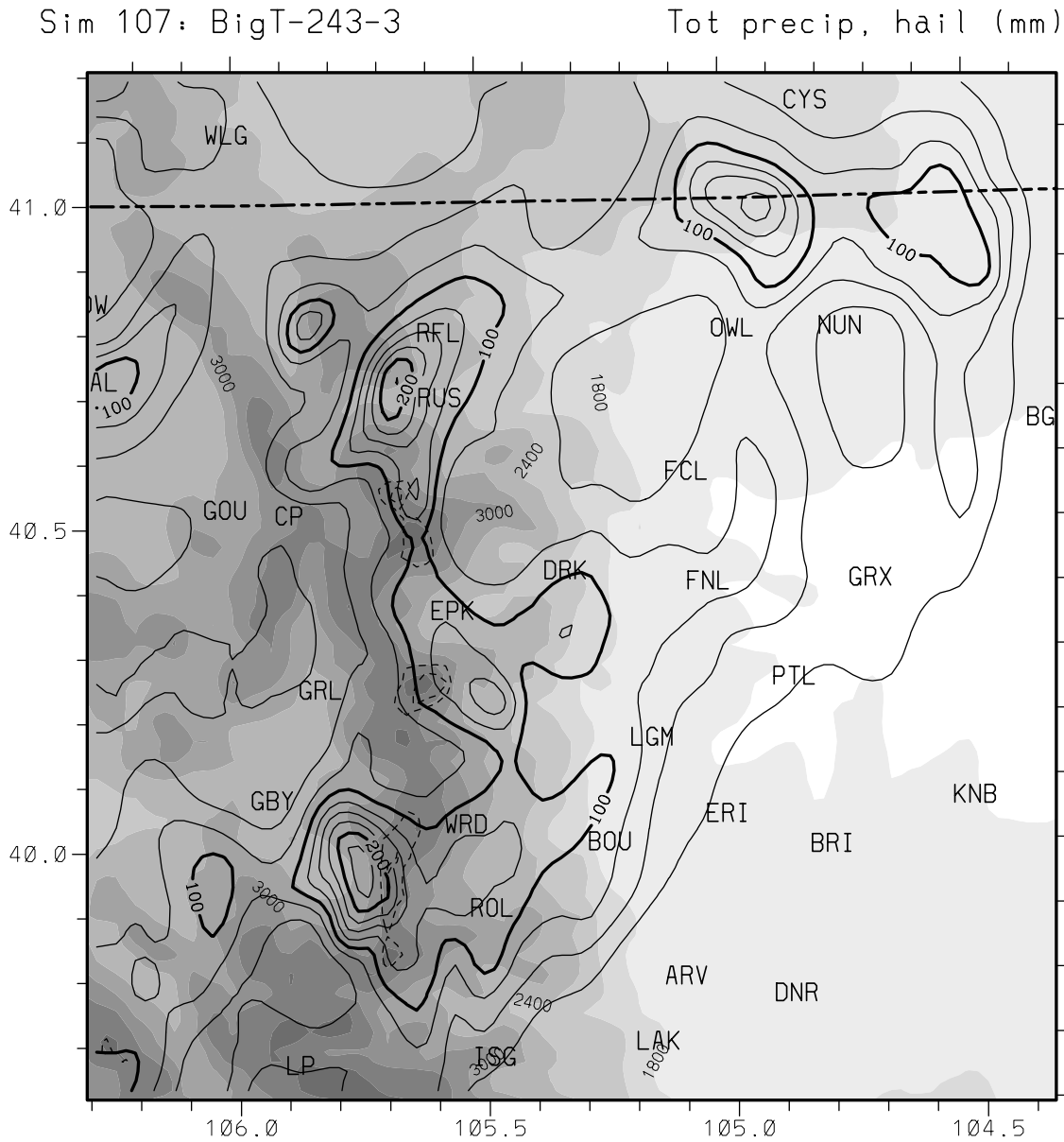


**Figure 13:** Simulated total precipitation and precipitation due to hail on Grid 4 for Simulation 107. Details are as in Fig. 7.

An additional soil moisture alteration experiment was conducted, in which moisture below and above 6000' was increased to 50% and 70% of saturation, respectively. Although we have no soil moisture observations for this case, recent rains preceding the Big Thompson storm in Colorado and the central plains provide a rationale for trying this sensitivity test. The moist soil in this run, Simulation 108, resulted in a cooler, moister and shallower boundary layer over the plains that more closely

resembled observations. In turn, storm bases in Simulation 108 were at 2500m MSL, the same as depicted by Maddox et al. (1977, their Fig. 45). The sensible heating suppression due to the moistened soil also resulted in a weaker mountain/plains solenoid and weaker upslope flow that also matched observations better.

Total precipitation for Simulation 108 is shown in Fig. 14. Despite the major changes due to soil moistening, initial storm development still occurred at high elevations. However, the lower storm bases and cooler boundary layer in Simulation 108 resulted in much weaker cold pool development and slower gust front propagation; storms were even slower to move off the high terrain, with greater high-elevation precipitation accumulations through the first few hours of storm activity. By about 00z the storms had moved to intermediate elevations, and the weaker cold pool forcing allowed storms to remain at these elevations, with general northward movement as was observed (Caracena et al. 1979). This resulted in more precipitation at intermediate elevations than in the previous simulations, in better agreement with the observed case; the maximum of 282mm occurs at 2671m a little south of the of the Big Thompson basin.

Also indicated in the precipitation fields in Figs. 7-14 are precipitation due to hail (dashed contours). Maxima in Simulations 101-108 range from 44 to 122mm equivalent water depth, all at elevations above 3300m near the ridgeline. In general, the model settings used in Simulations 105-108 resulted in greater hail maxima and larger patterns along the ridgeline.

Sim 108: BigT-243-4

Tot precip, hail (mm)

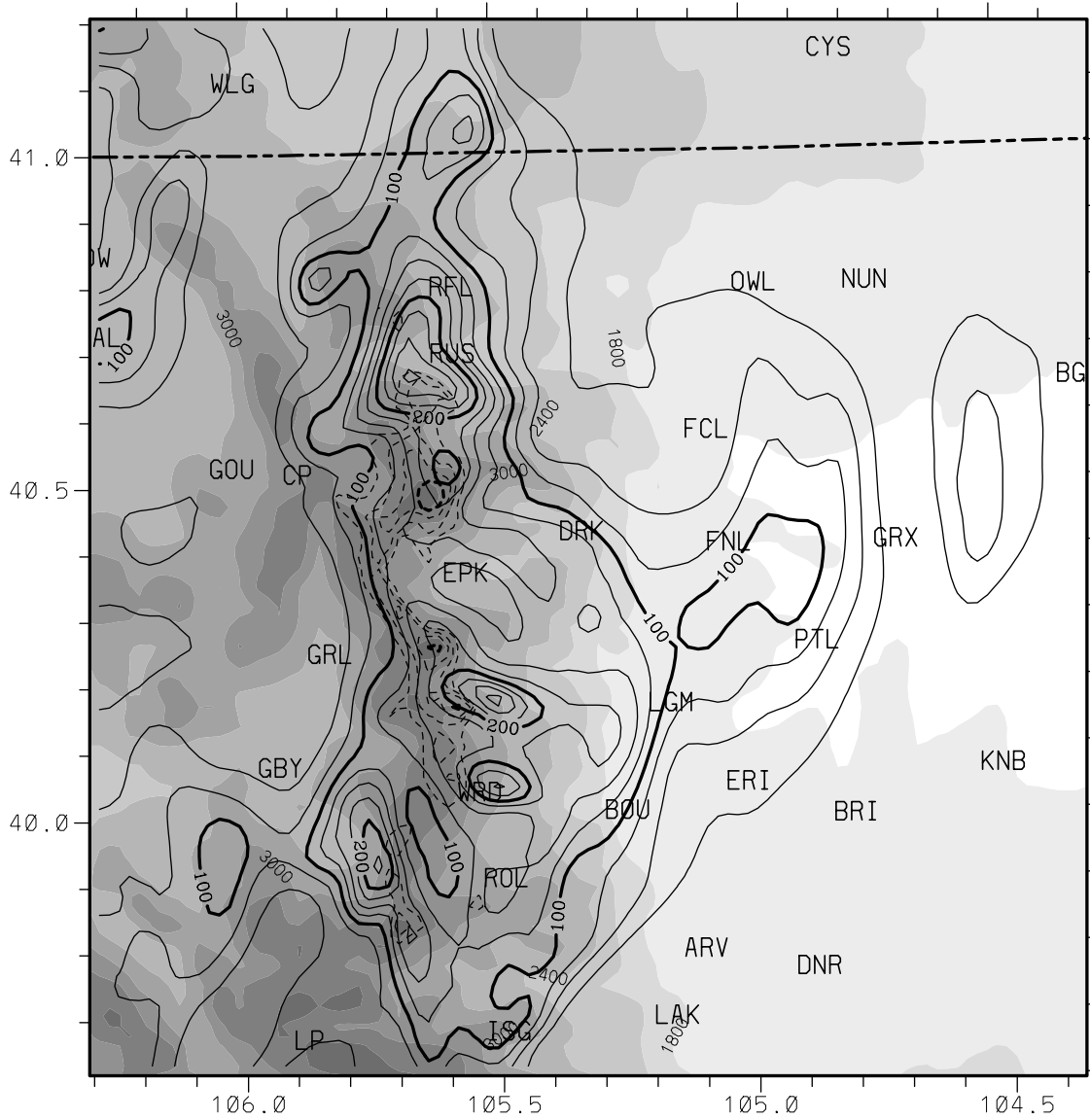


**Figure 14:** Simulated total precipitation and precipitation due to hail on Grid 4 for Simulation 108. Details are as in Fig. 7.

### ***4.3 Fort Collins storm of 28 July 1997***

On the evening of 28 July 1997, an extreme rainstorm occurred in Fort Collins, Colorado. A multiscale analysis of this relatively recent event, including dual-Doppler and polarimetric radar analyses of the storm, appears in Peterson et al. (1999). The RAMS initialization on Grid 1, based on NCEP reanalysis, shows the large scale conditions that morning (Fig. 15). As in the Big Thompson case, this Type I environment features a negatively tilted ridge extending northwestward from Oklahoma, across northeastern Colorado, and into the northwestern U.S. Colorado was in moist, light to moderate, southerly to southwesterly flow. An east-west oriented shortwave embedded in the southerly flow across Utah is barely discernable in the coarse NCEP reanalysis. The surface conditions at this time, shown on Grid 2 in Fig. 16, shows features typically associated with Type I events in the Front Range and Eastern Foothills region: cool, moist, postfrontal easterly upslope winds. In this case, the surface front, located (but not indicated) near the southeastern border of Grid 2 in Fig. 16, was further south of the extreme precipitation event than in the Type I schematic in Fig. 3 and in Type I cases such as the Big Thompson and Rapid City floods (Peterson et al. 1999).

Antecedent rainfall was an important factor in this event (Doesken and McKee 1998; Peterson et al. 1999). From the afternoon of 27 July through the morning of 28 July, considerable rain fell along the foothills just to the west of Fort Collins. A maximum of 9" occurred about 10km northwest of Fort Collins (which caused local flooding there), with amounts decreasing southward and eastward to 4-5" at the western city/foothills interface and to <1" in eastern Fort Collins. Thus in the western portions of the city the soil was at or near saturation and very susceptible to flooding on the afternoon of 28 July. In addition, the moistened soil could have played an important role in how and where the subsequent flood-producing storm evolved.

In this very moist environment, convection was widespread on the afternoon of 28 July, developing throughout the Front Range and Eastern Foothills region. While rains remained close to the foothills near Fort Collins, storms further south displayed the more usual eastward propagation onto the plains. Showers began in Fort Collins after 2300 UTC, with two episodes of heavy rain from cells moving north-northeastward from the southwestern portion of the city over the next 2h. A quasi-stationary storm developed over southwestern Fort Collins from 0230 to 0400 UTC, producing over 5" in 90 min. Increased easterly inflow to this storm may have been dynamically related to a bow-echo convective system that had propagated northeastward from the Denver area. The storm finally moved out of Fort Collins by 0500 UTC. Doesken and McKee's (1998) rainfall analysis from 2330 to 0500 UTC (Fig. 17) shows a maximum exceeding 10" in southwestern Fort Collins, an axis aligned north-south near the base of the foothills, and amounts decreasing rapidly to the east and west. The flood caused five fatalities and over \$200 million in property damage.

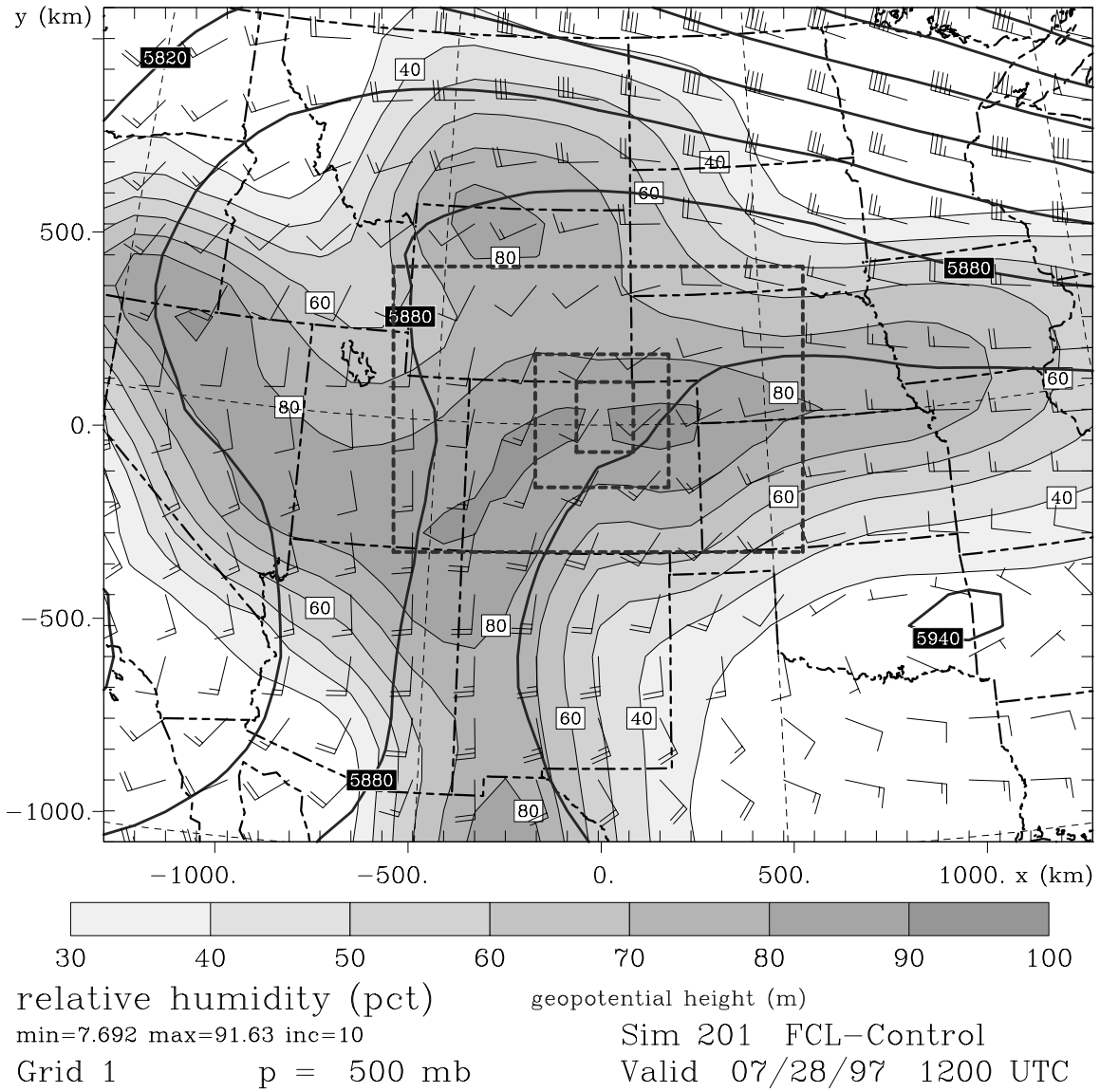


**Figure 15:** RAMS initialization, at 1200 UTC 28 July 1997, at 500mb on Grid 1 for Simulation 201 (Fort Collins control run). Details are as in Fig. 4.

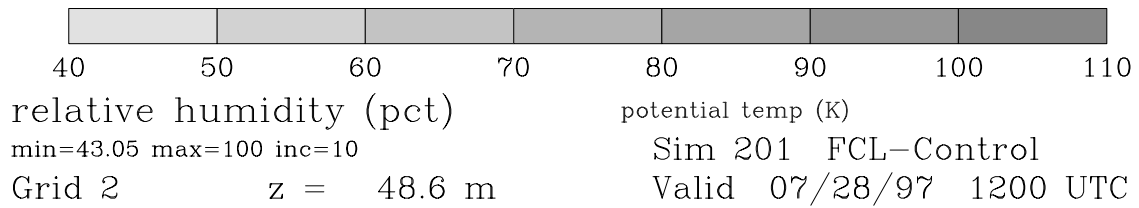
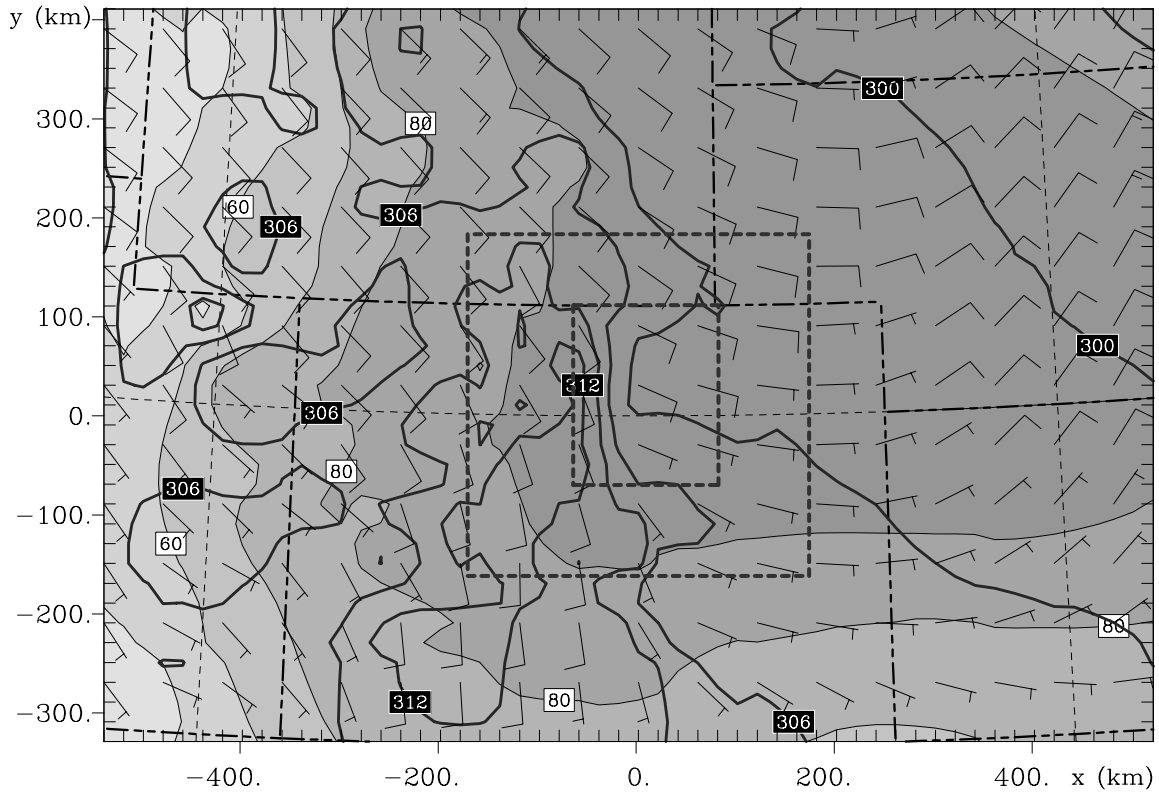


**Figure 16:** RAMS initialization, at 1200 UTC 28 July 1997, at surface on Grid 2 for Simulation 101 (Fort Collins control run). Details are as in Fig. 5.

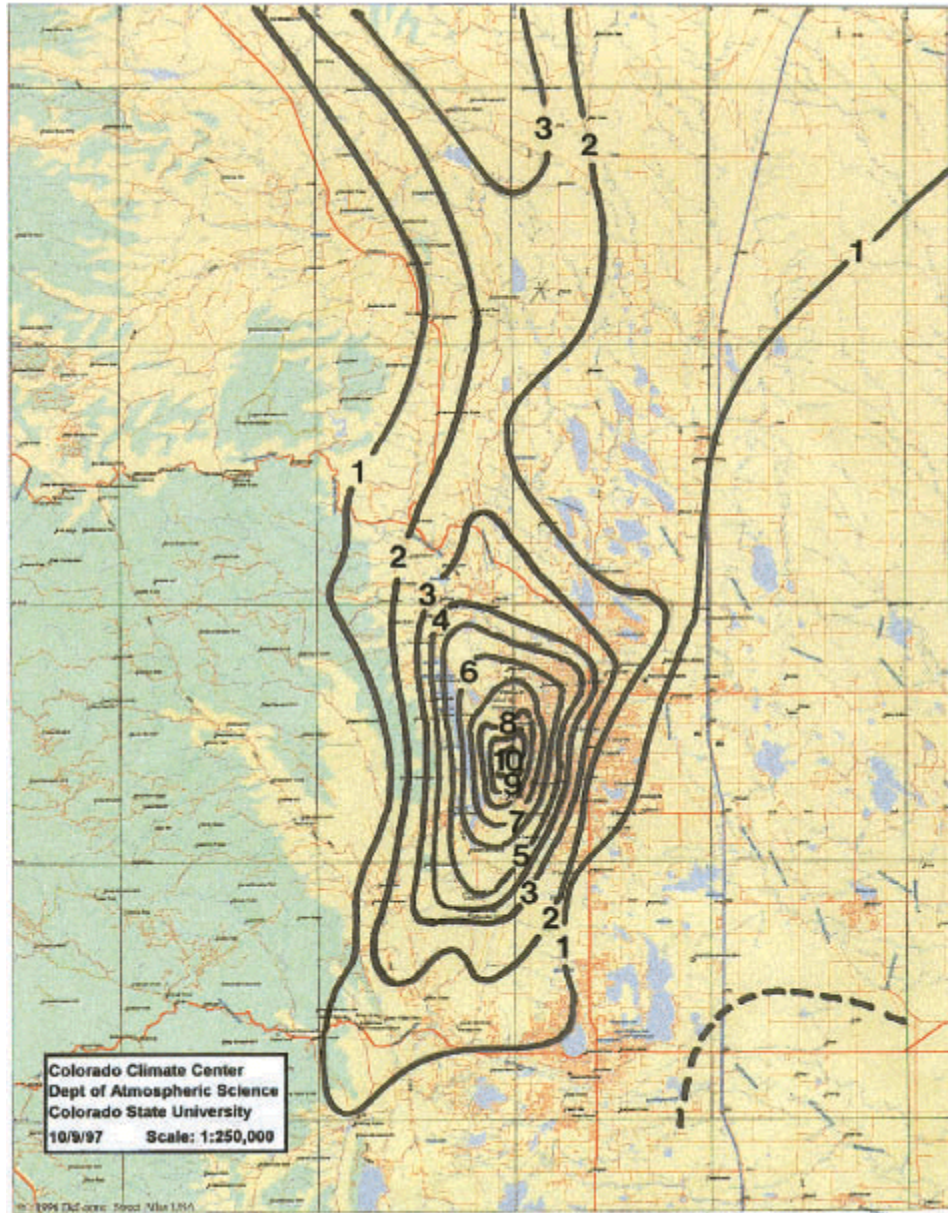


**Figure 17:** Rainfall (inches) for eastern Larimer County, Colorado for 5:30-11:00 p.m. MDT for July 28, 1977. Extent of map is 50km east-west by 64km north-south. [From Doesken and McKee, 1998.]

The areal extents of Grids 1 and 2 in Fig. 15-16, used for all 11 simulations based on the Fort Collins event, are considerably smaller than those used for the Big Thompson simulations and for the other cases. This aspect derives from memory and single-processor limitations on computers we used prior to acquiring the DNR-funded PC cluster that was used for this project. This smaller grid configuration was used successfully by Nachamkin and Cotton (2000) to simulate a mesoscale convective system in eastern Colorado, and it was used by Ashby (2001) to investigate soil moisture sensitivities in the Fort Collins event using RAMS version 3b. We retained the smaller configuration for this event when we began the RAMS version 4.29 simulations, even though the DNR-funded PC cluster allowed larger grids.

The first five simulations of the Fort Collins event are all identical except for their soil moisture initialization. NCEP reanalyses provide the atmospheric initialization and, in this case, 12h nudging files. Horizontal diffusion was weak, which, as seen for the Big Thompson Simulation 101, results in finer scale precipitation structure. Soil moisture was set to a homogeneous 50% saturation in Simulation 201, while Simulations 202-205 had different values below and above 6000' elevation (for plains and mountain regions): 202 used 30% (50%) for plains (mountains); 203 used 50% (30%); 204 used 50% (70%); and 205 used 70% (50%). Figures 18-22 show total precipitation for Simulations 201-205, respectively. Although different patterns result from the various soil moisture initializations, overall convective evolution was very similar. In all these runs, relatively weak morning convection developed along the foothills, as was observed, and moved east through the morning. Convective development began around mid-day or early afternoon at high elevations in the southwestern portion of Grid 4, with separate mid-afternoon convection developing on the plains in the south-central portion of Grid 4 along a north-south oriented convergence zone. Storm movement was generally to the east or northeast, and in some runs the mountain storms overtook the plains storms and merged to form more complex multi-cell clusters or small bow-echo squall lines. Another common area of storm development was on the plains in the northeastern portion of Grid 4; these storms generally moved slower and sometimes even westward. Although all runs have local maxima exceeding 100mm near Fort Collins (FCL), there was no anchoring of storms against the foothills as was observed. Larger maxima were produced by mountain storms to the southwest, by the multi-cell systems to the southeast, and the slower moving convection in the northeast. Maximum precipitation ranges from 425mm in Simulation 201 to 322mm in Simulation 202; these all occur at lower elevations except in the simulation with the driest plains soil (202). Local maxima in the mountains are about 250-325mm, with hail accounting for as much as 85-95mm at highest elevations.

One more simulation was run with this general setup (with 50% homogeneous soil moisture again), except the layer below 700mb was moistened to 98% RH in the lower tropospheric inflow sectors to the east and south. Maximum precipitation in Simulation 206 (Fig. 23) was 291mm, less than any of Simulations 201-205. Although overall convective evolution was similar to that described above for Simulations 201-205, the lower tropospheric moistening in Simulation 206 resulted in less average precipitation over Grid 4 than in any of the above simulations except 202, which had the driest plains soil.

Sim 201: FCL-Control Tot precip, hail (mm)

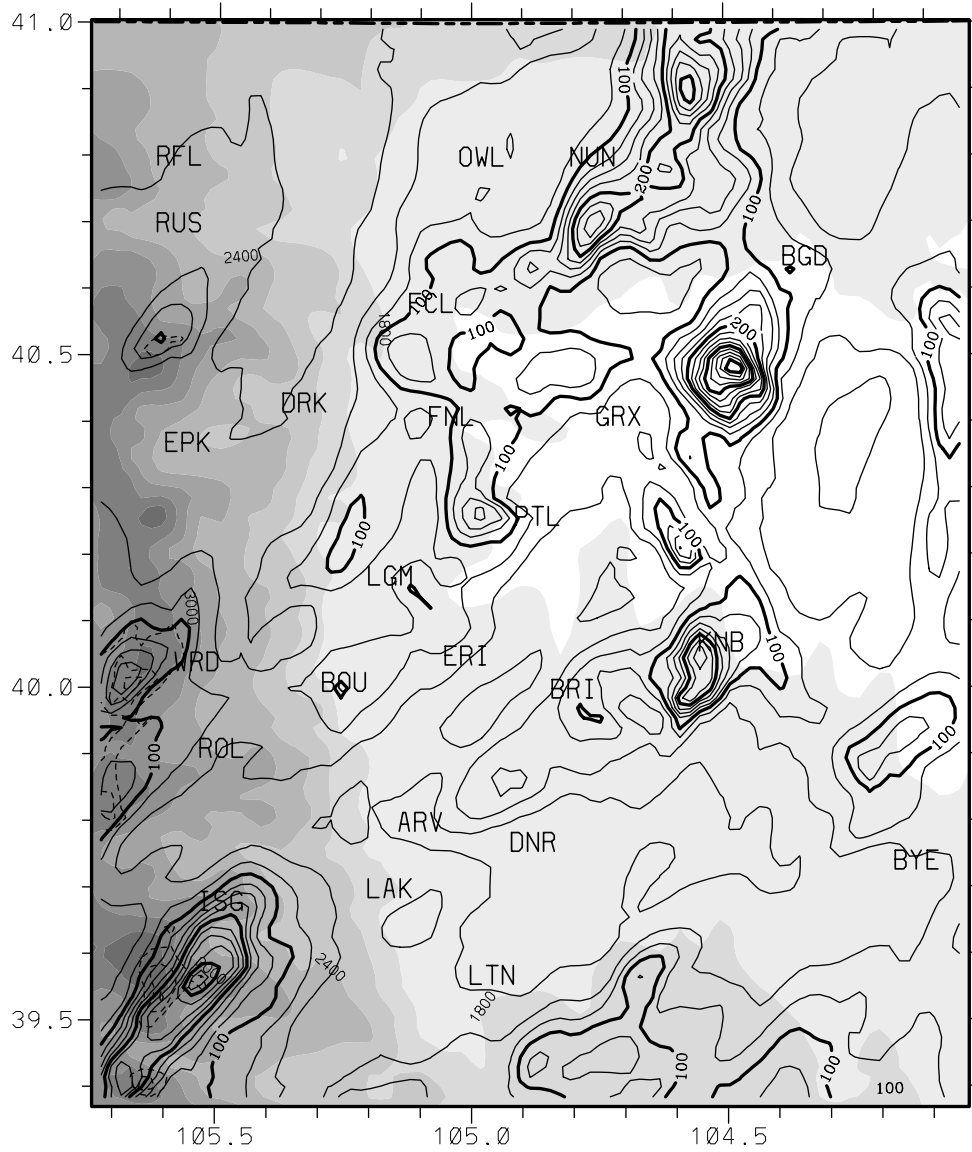


**Figure 18:** Simulated total precipitation and precipitation due to hail on Grid 4 for Simulation 201. Details are as in Fig. 7.

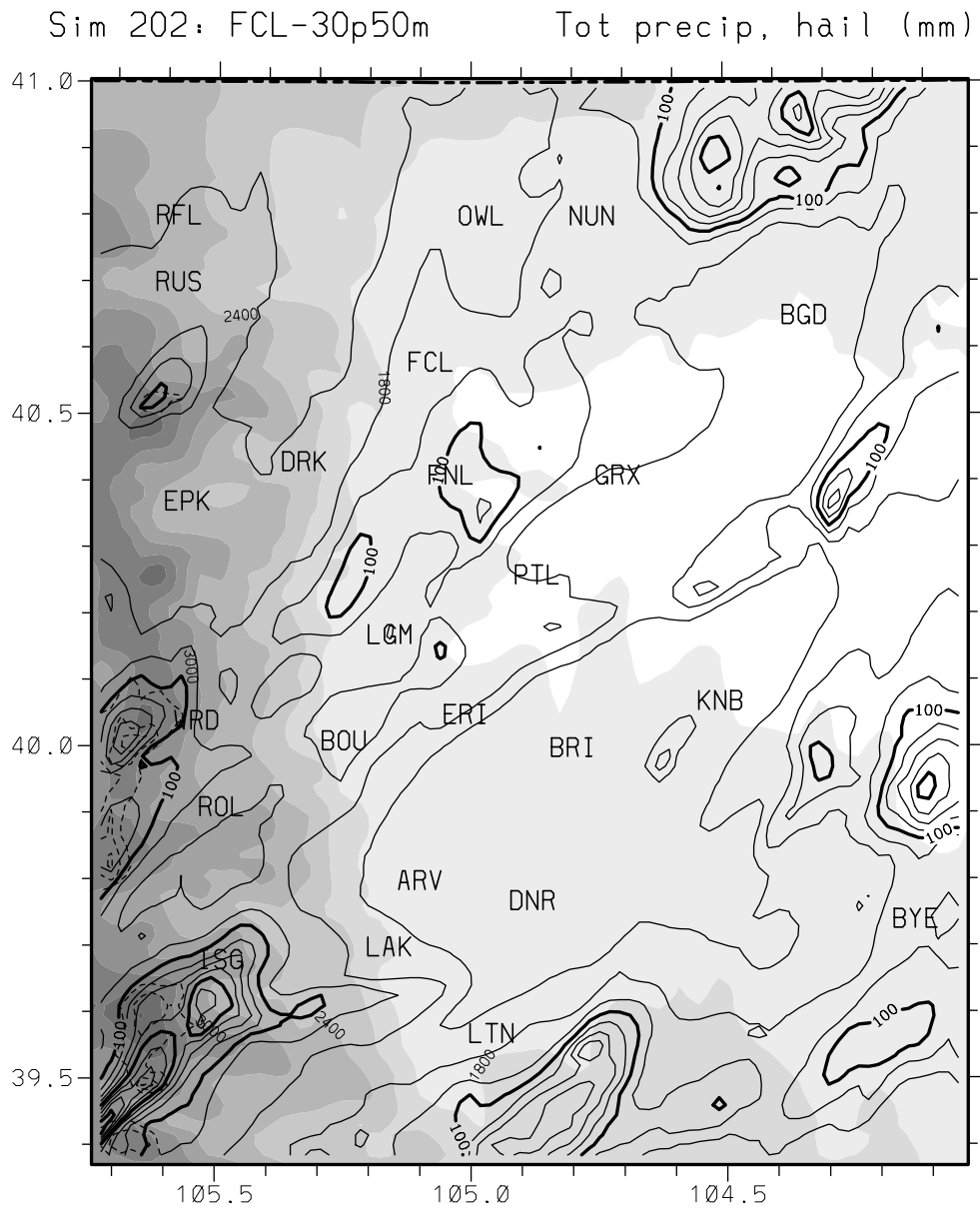


**Figure 19:** Simulated total precipitation and precipitation due to hail on Grid 4 for Simulation 202. Details are as in Fig. 7.

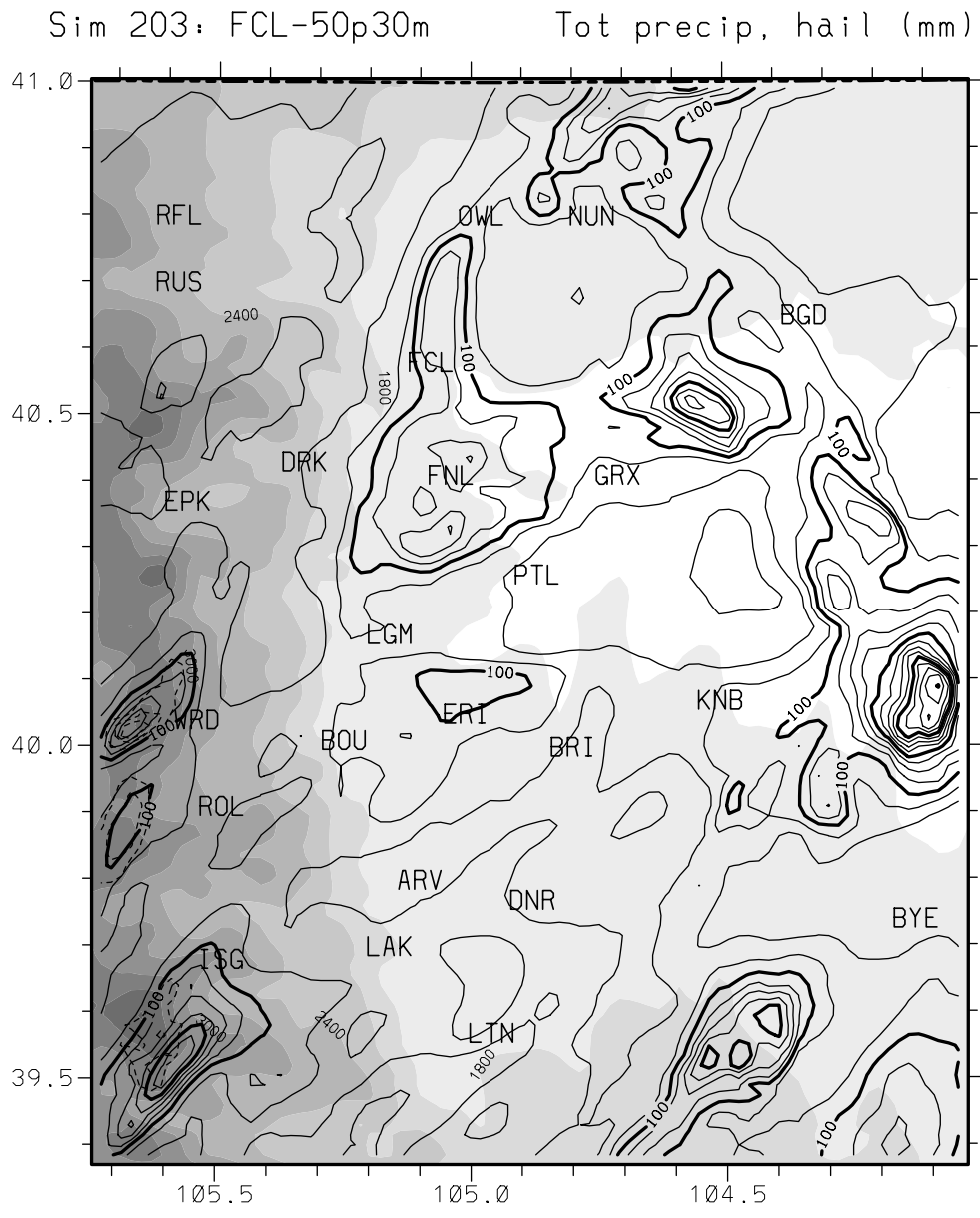


**Figure 20:** Simulated total precipitation and precipitation due to hail on Grid 4 for Simulation 203. Details are as in Fig. 7.

Sim 204: FCL-50p70m Tot precip, hail (mm)

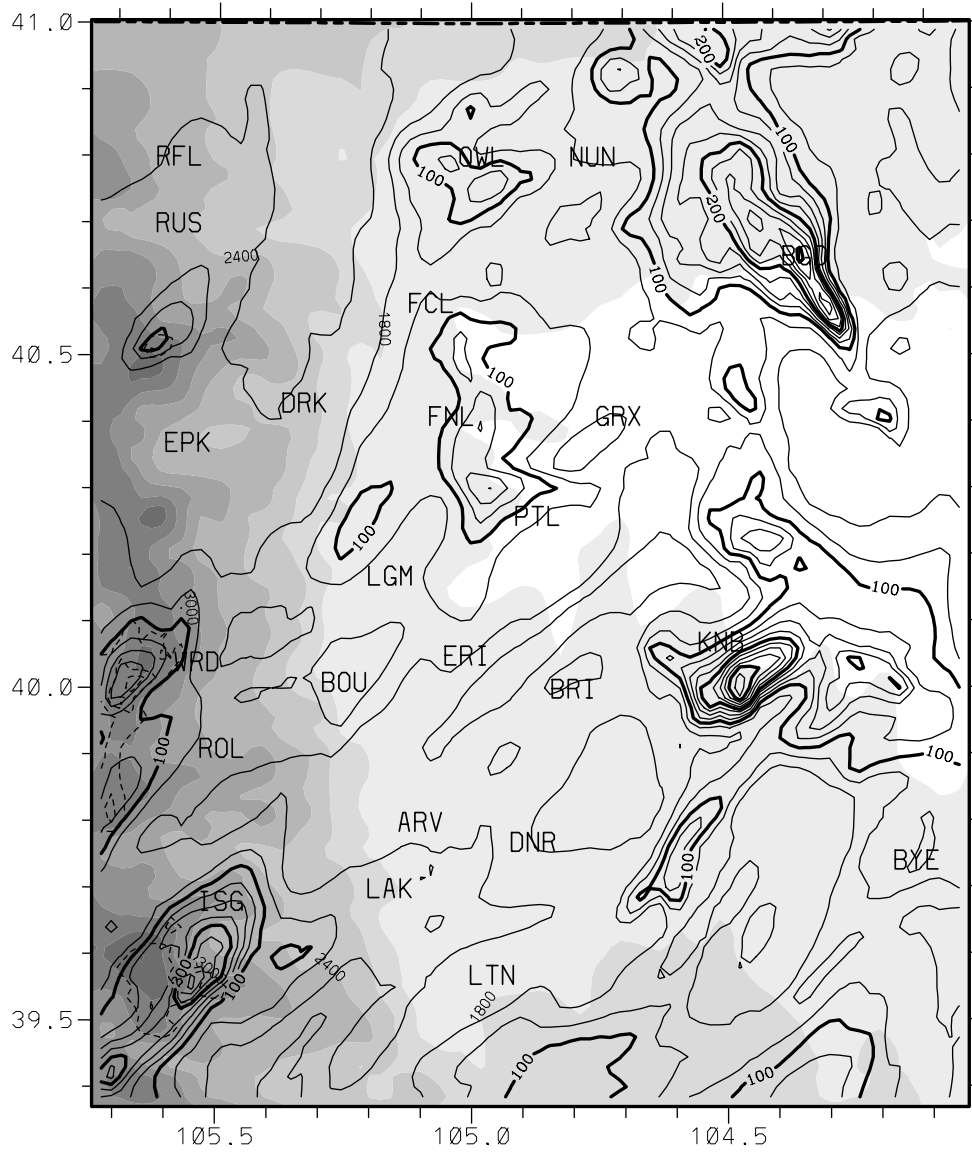


**Figure 21:** Simulated total precipitation and precipitation due to hail on Grid 4 for Simulation 204. Details are as in Fig. 7.

Sim 205: FCL-70p50m Tot precip, hail (mm)

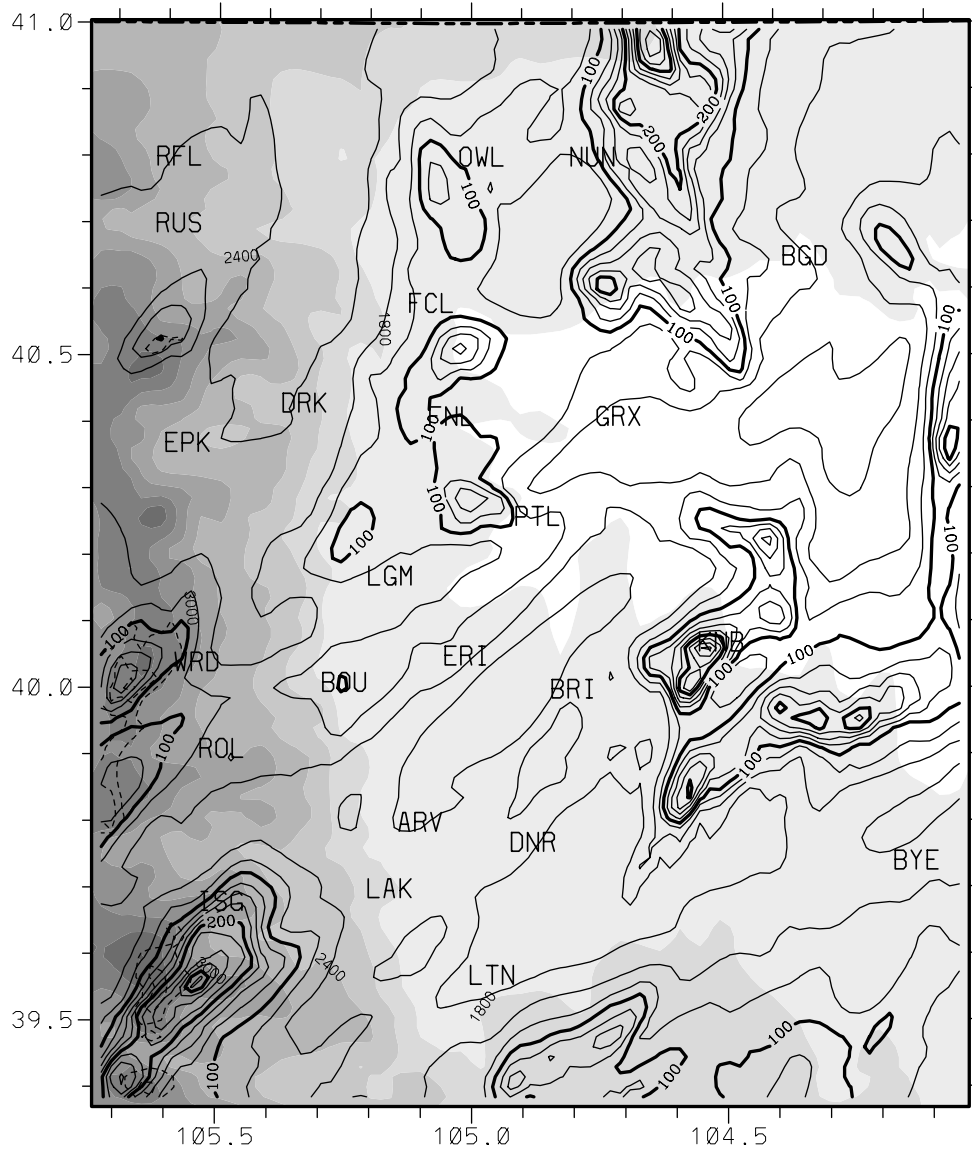


**Figure 22:** Simulated total precipitation and precipitation due to hail on Grid 4 for Simulation 205. Details are as in Fig. 7.

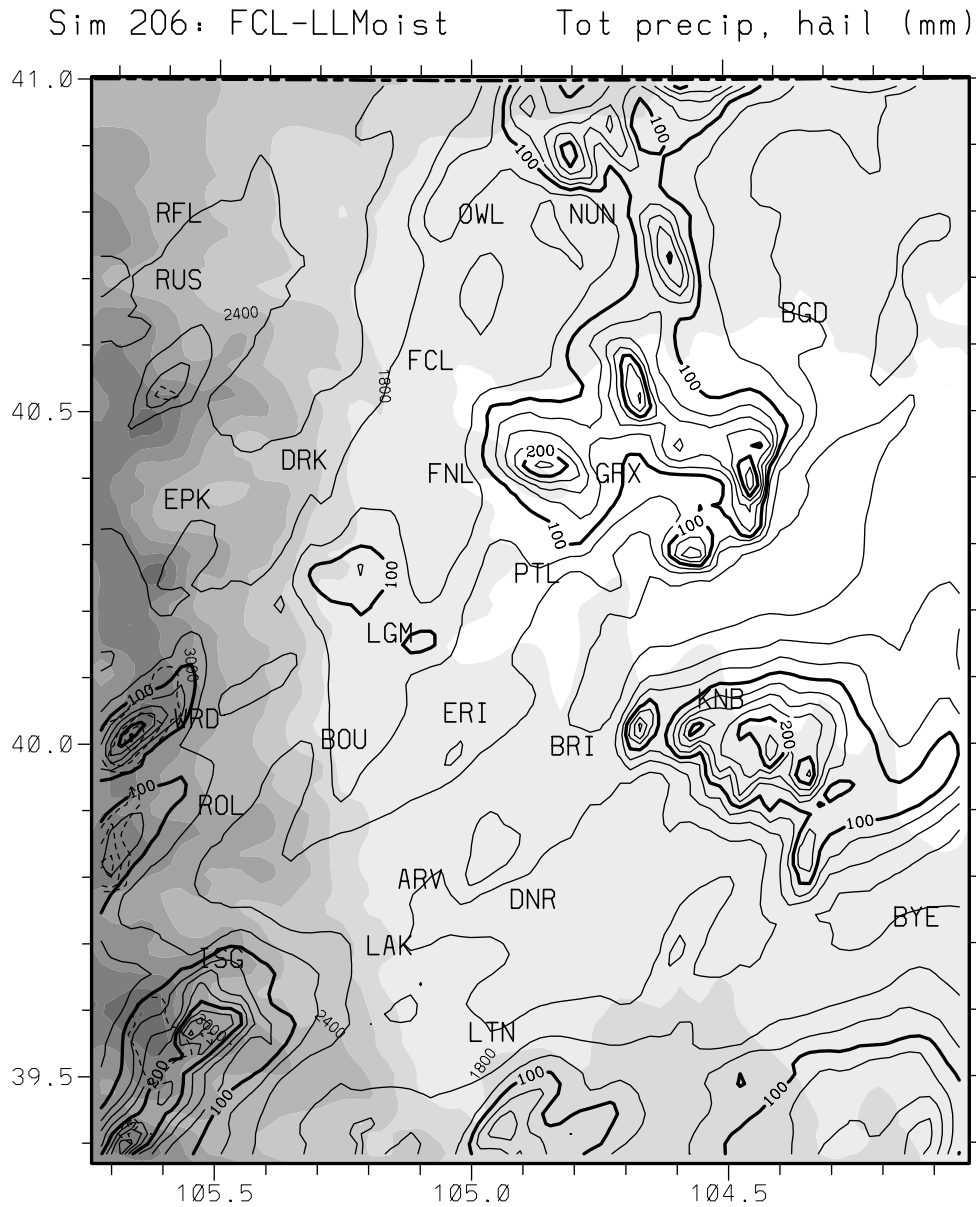


**Figure 23:** Simulated total precipitation and precipitation due to hail on Grid 4 for Simulation 206. Details are as in Fig. 7.

We then tried some Fort Collins simulations using NCEP's operational Eta model analysis for both atmospheric and surface (moisture and temperature) initialization and 3h boundary nudging information, to see if its higher horizontal, vertical and temporal resolution would result in more accurate simulations. The first of these, Simulation 207, used 50% homogeneous soil moisture and had a moisture perturbation to the west of 106°W, where RH was increased to 90% up through 500mb. This is the same moisture perturbation used for the subsequent Park Range event. The total precipitation for Simulation 207 (Fig. 24) shows a very different pattern than the previous Fort Collins simulations. In this run, morning rainfall was widespread but concentrated at intermediate elevations along the northern Front Range, and it was more

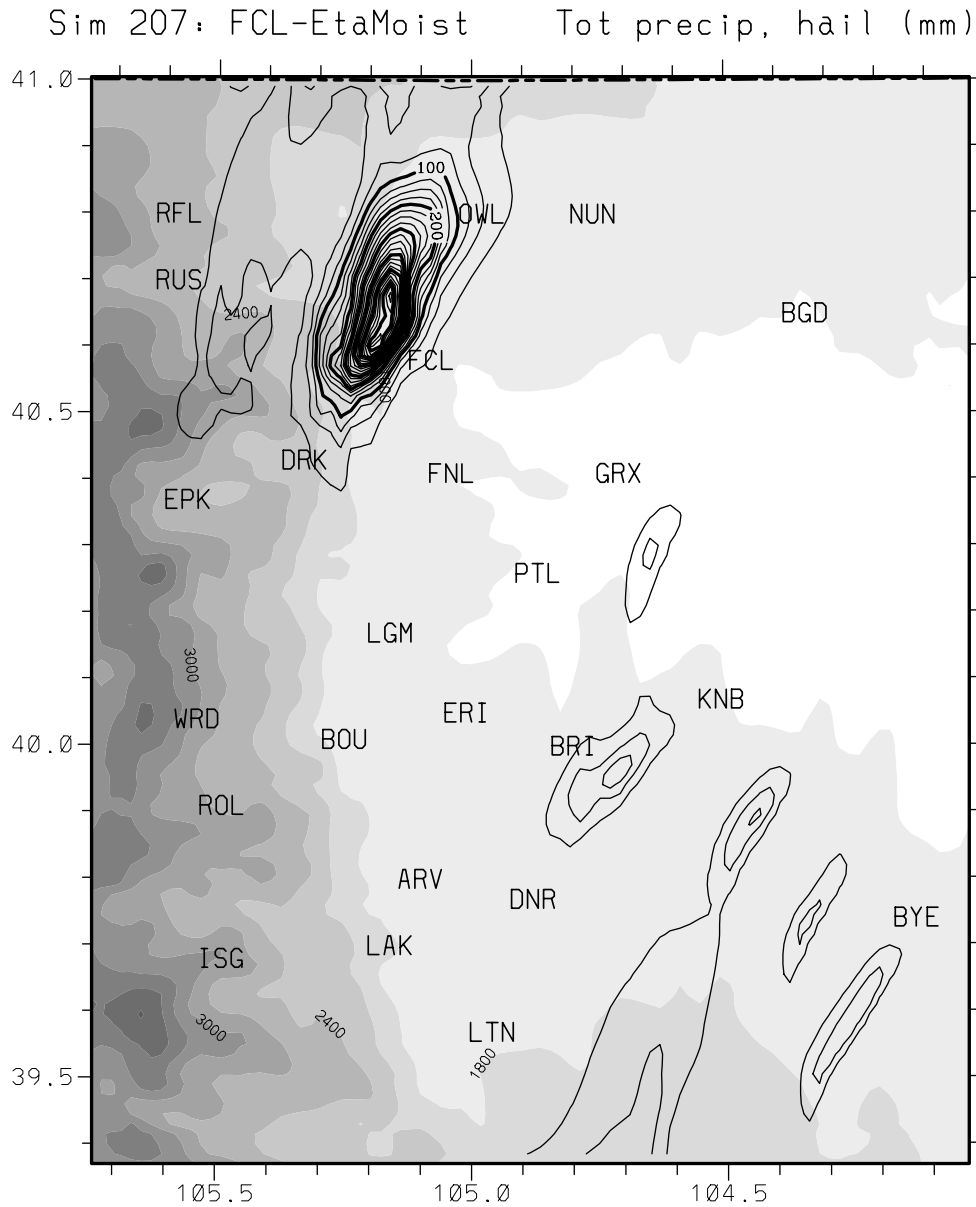


**Figure 24:** Simulated total precipitation and precipitation due to hail on Grid 4 for Simulation 207. Details are as in Fig. 7.

stationary than in Simulations 201-206. Although high elevation convection developed at mid-day as in 201-206, it was much weaker and did not propagate eastward off the mountains. The first strong convection developed near Denver (DNR) in mid-afternoon; several strong cells maintained their individual identities and together propagated northeastward, similar in time and movement as the observed bow echo (Peterson et al. 1999), but not well organized into a bow-echo squall line. A north-south line of convection redeveloped in the lower foothills of the northern Front Range after 0000 UTC and rapidly intensified to the southwest of Fort Collins (FCL) after 0130 UTC. These cells moved slowly northward, and by about 0300 UTC the storm became quasi-stationary, centered to the northwest of FCL. Cells repeatedly formed in the lower

foothills southwest of FCL and trained northward into the quasi-stationary system, with simulated precipitation rates exceeding 200mm/h from 0300 to 0530 UTC. By 0700 UTC the storm had weakened and moved northeastward away from the foothills.

The evolution of this extreme quasi-stationary storm in Simulation 207 is quite similar to that described by Peterson et al. (1999), with the timing of the simulated evolution lagged by 1-2h. The maximum precipitation in Simulation 207 was 664mm, about 50% more than the largest maxima in any of the other simulations. Although the size and magnitude of the simulated precipitation pattern in Fig. 24 are considerably larger than for the observed pattern in Fig. 17, the similarity of the patterns is striking. It is interesting that hail was negligible in Simulation 207, and mean precipitation on Grid 4 was only about 25% of the mean depths in 201-206. The dramatic differences between Simulation 207 and the others for this event are due to the moisture perturbation to the west. This moist air advects over the mountains, and as it entrains into the storm it descends essentially moist adiabatically, so that downdraft outflow is not substantially cooler than the low-level environment (soundings show a near moist-adiabatic environment). This greatly reduced the eastward propagation speeds of mountain storms, an unrealistic feature of all the other simulations of this case.

Simulation 208 used the same Eta initialization, but without any moisture perturbation, so that it is an Eta-based control run. Its total precipitation field is shown in Fig. 25. In this run, weak morning convection was similar to that in the other runs. Like simulation 207, strong convection first developed at lower elevations in mid-afternoon, with one slow-moving cell producing 270mm of rain near Byers (BYE) from 2200 to 0100 UTC, and another set of cells developing in the foothills southwest of Denver (DNR). Discrete propagation of this weak disorganized cluster toward the northeast led to a stronger storm developing south of Greeley (GRX) by 0130 UTC, while during the same period high elevation convection moved off the northern Front Range eastward over Fort Collins (FCL). These two storms merged into a slow-moving multi-cell cluster by 0300 UTC and rained for three more hours in the Greeley area. A final convective cluster originated in the foothills west of Boulder about 0400 UTC and moved east-northeastward over the Greeley area during the next few hours. The resulting rain total near Greeley exceeded 200mm over a large area, with a maximum of 315mm. Like Simulation 207, this Eta-based run produced no significant hail.

Three additional simulations based on the Fort Collins event were carried out. These were some of our initial RAMS 4.29 parallel runs on the DNR cluster, where we adopted the grid configuration and many model options used by Ashby (2001) in his RAMS version 3b simulations of the Fort Collins event. One of these options that differs from all other simulations in this report is the delayed activation of full microphysics by 3h and the delayed activation of Grid 4 by 6h after initialization. Like the smaller Grids 1 and 2, these options are unnecessary carryovers from the pre-DNR cluster era, originally chosen to speed up simulations that took weeks. Instead of using the RUC-based initialization as did Ashby, however, this was our first utilization of NCEP reanalysis data for creating initialization and nudging files. Despite its coarser resolution than the RUC or Eta data that were available for this and other recent cases, we

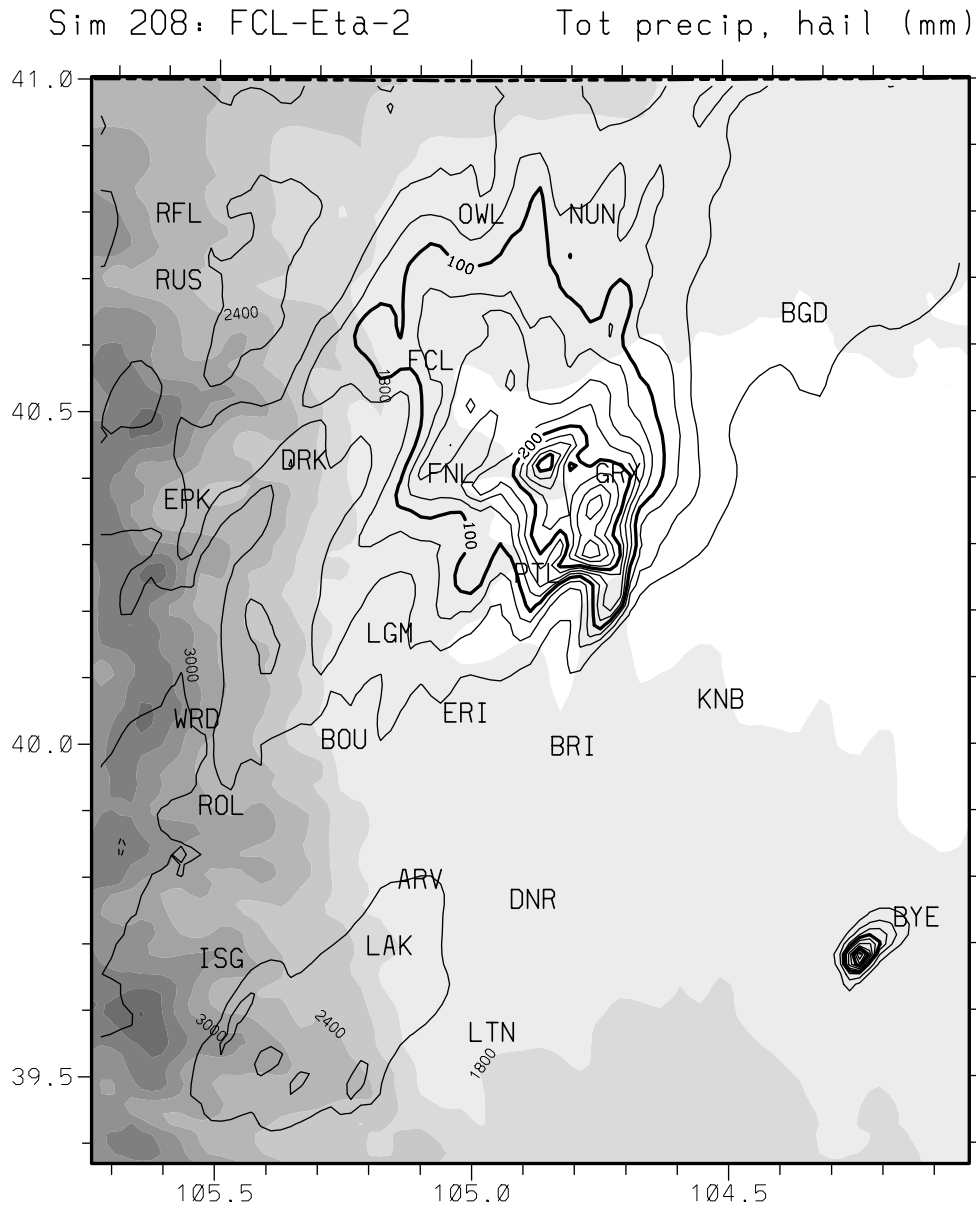


**Figure 25:** Simulated total precipitation and precipitation due to hail on Grid 4 for Simulation 208. Details are as in Fig. 7.

felt a need to use the NCEP reanalysis since it would be required for older cases. In these runs, surface observations and soundings were also incorporated into the initialization and 12h nudging files. As Ashby (2001) did with one of his version 3a runs, soil moisture was initialized with the Eta soil model analysis.

The initial run in this setup, Simulation 209, produced the smallest mean precipitation on Grid 4 and smallest maximum value of all runs 201-211 (Fig. 26). Deep convection first developed in mid-afternoon at high elevation in the central Front Range and organized into a convective line that moved eastward. Additional convection developed 2-3h later between Denver and the foothills and propagated northeastward.

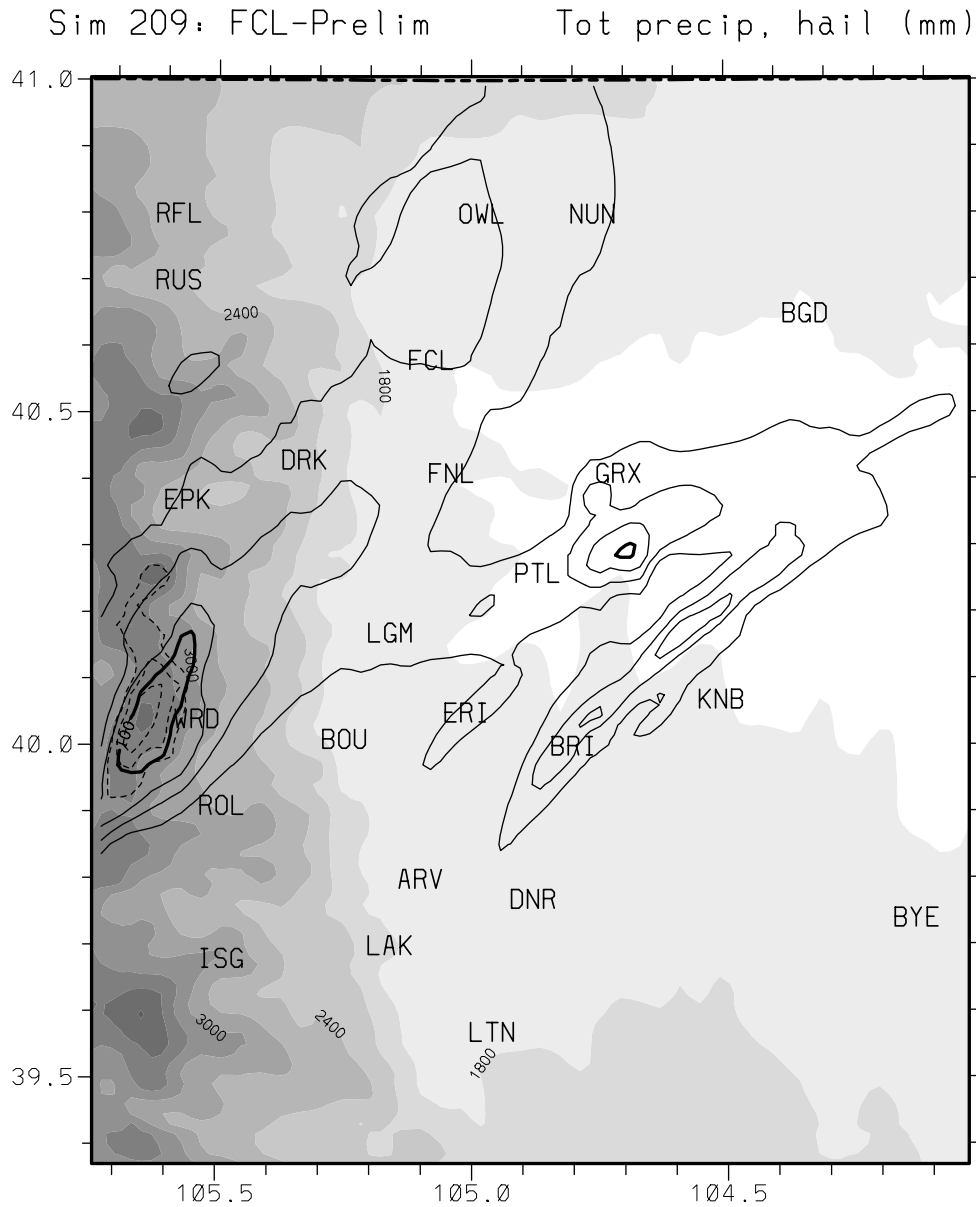


**Figure 26:** Simulated total precipitation and precipitation due to hail on Grid 4 for Simulation 209. Details are as in Fig. 7.

These two groups of convection merged in the center portion of Grid 4 about 0130 UTC and developed into a modest multi-cell cluster that continued to move on eastward. This evolution was quite different than in the other Fort Collins simulations. Maximum precipitation of 115mm (consisting mostly of hail) occurred on the Front Range ridgeline, with a lower elevation maximum of 104mm near Greeley (GRX).

It was discovered after this run that in implementing the Eta soil moisture into the initialization, the soil temperature was inadvertently lowered a few degrees Celsius, due to differences between RAMS versions 3b and 4.29. This resulted in a 2-3h lag in daytime heating of the topmost soil layer and thus the boundary layer, and directly led to

the relatively low precipitation in Simulation 209. The same error exists in the transposition Simulation 210, discussed below. After discovering this error, we re-ran this setup with the soil temperature correctly specified by the input name list. In this corrected run, Simulation 211, the convective evolution was somewhat similar but much more robust than in 209. Maximum precipitation, still occurring at high elevation, almost doubled, as did mean precipitation on Grid 4, and numerous maxima exceeding 100mm occurred on the plains (Fig. 27).

The final run based on the Fort Collins event, Simulation 210, was a transposition experiment. The objective here was to model hypothetical scenarios based on an observed case, wherein the meteorological pattern is artificially shifted relative to the topography. We made several version 4.2 experiments wherein the meteorological fields (using the NCEP reanalyses) of the Fort Collins event were shifted. These results indeed show that very plausible storm events can be simulated using this methodology.

In preliminary experimentation leading to Simulation 210, the fields were shifted about 310km to the south-southwest, to see if the storm would shift accordingly from the Fort Collins area to the extreme northwest portion of the San Luis Valley. This represents an attempt to force an event that occurred in region 2 in Fig. 1 (Front Range and Eastern Foothills) to region 3 (Southwest Mountains). In doing so, the upslope conditions conducive to heavy rains are shifted from the Front Range of northeastern Colorado to the Sangre de Cristos and San Juans to the south and southwest, and the storm would have to "jump" the easternmost barrier (Sangre de Cristos) to occur in the intermountain region. In a three-grid run (finest grid spacing is 5km), the grids were also shifted identically, though that is not necessary. While grid 3 cannot resolve convection well, it nevertheless provides a good indication of strong convection which would be well resolved with a nested grid 4. Grid 3 precipitation showed several storms in northern New Mexico and southern Colorado, with the heaviest concentration along the Sagre de Cristos on the upper reaches of Raton Mesa, on the Colorado/New Mexico border. Compared to the 310km south-southwest shift of the meteorological fields, the simulated storm maximum occurred about 400km due south of the observed event. Thus in this shifted experiment, the strongest convection did not "jump" the eastern barrier into the intermountain region, but instead remained concentrated along the eastern barrier.

Seeing that this synoptic situation favored eastern slope storms, another experiment was run with the original fields and grids shifted 234km almost due south. This was attempt to shift the observed storm accordingly to the foothills somewhere west of Pueblo, where the upslope forcing would likely be similar to that along the Front Range in the real event. However, convection still was favored further south on the east slope of the Sangre de Cristos, this time to the north of Raton Mesa. Thus both of these shifted experiments produced the rainfall maxima further removed from the observed event than the shift, and in the same general area.

In an effort to better resolve the convection in this shifted scenario, Simulation 210 was conducted that included a Grid 4 with 1.67km spacing. In this experiment, the shifted meteorological fields were as in the previous run (234km south), and the grids

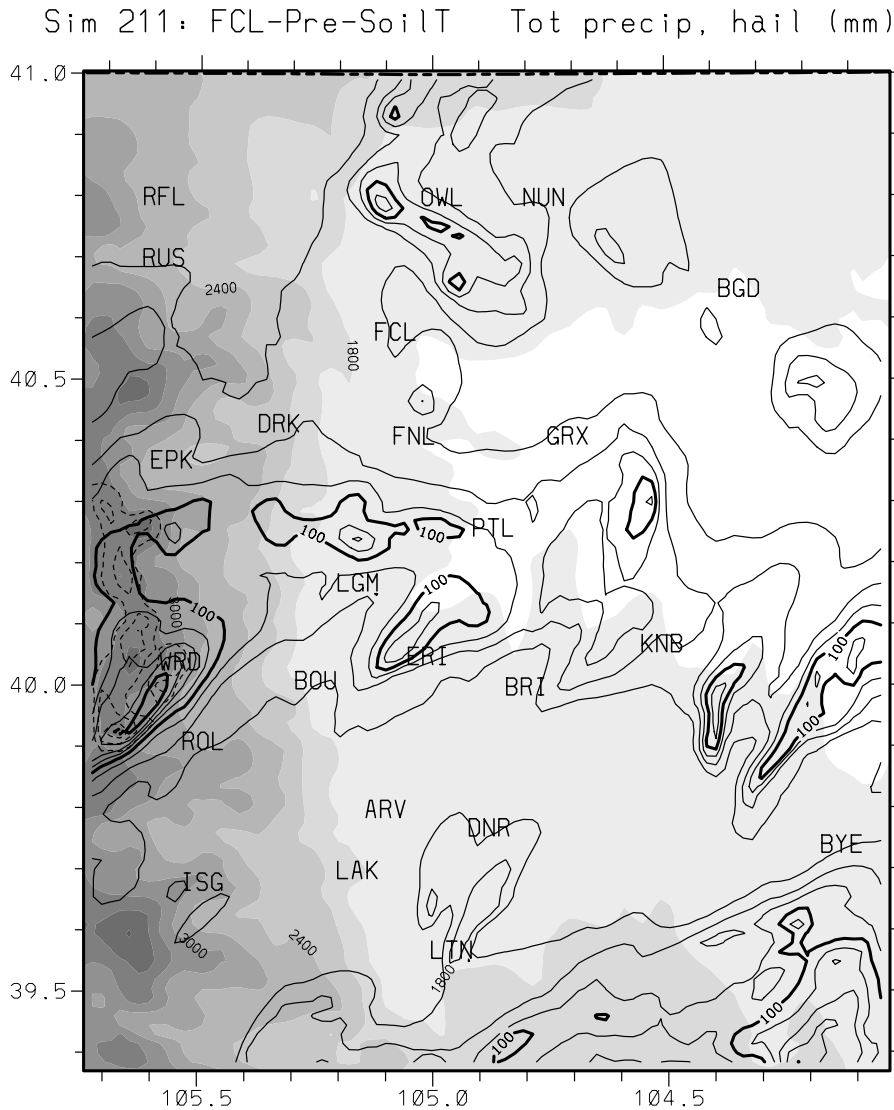


**Figure 27:** Simulated total precipitation and precipitation due to hail on Grid 4 for Simulation 211. Details are as in Fig. 7.

were shifted further south to be better centered on the Raton Mesa area. Figure 28 shows the 500mb field on Grid 1 at 6h into the simulation, when Grid 4 was spawned. Comparison with Fig. 15 clearly shows the southward shift of the fields, and the nested grid locations indicate their final location as determined from the experimental runs. Total precipitation on Grid 4 in this transposed Simulation 210 (Fig. 29) reflects three areas of heavy rainfall. The northernmost area is the heaviest, with a maximum of 288mm. Half of that amount occurred in a 2h period, indicative of a flash-flood producing storm. This occurred about 50km to the north of Raton Mesa and Trinidad, in a location quite unlike the observed event. This storm involved multi-celled storms propagating northeastward from the Sangre De Cristo ridge in New Mexico and Colorado, which merged with storms propagating northward from their origins along Raton Mesa.

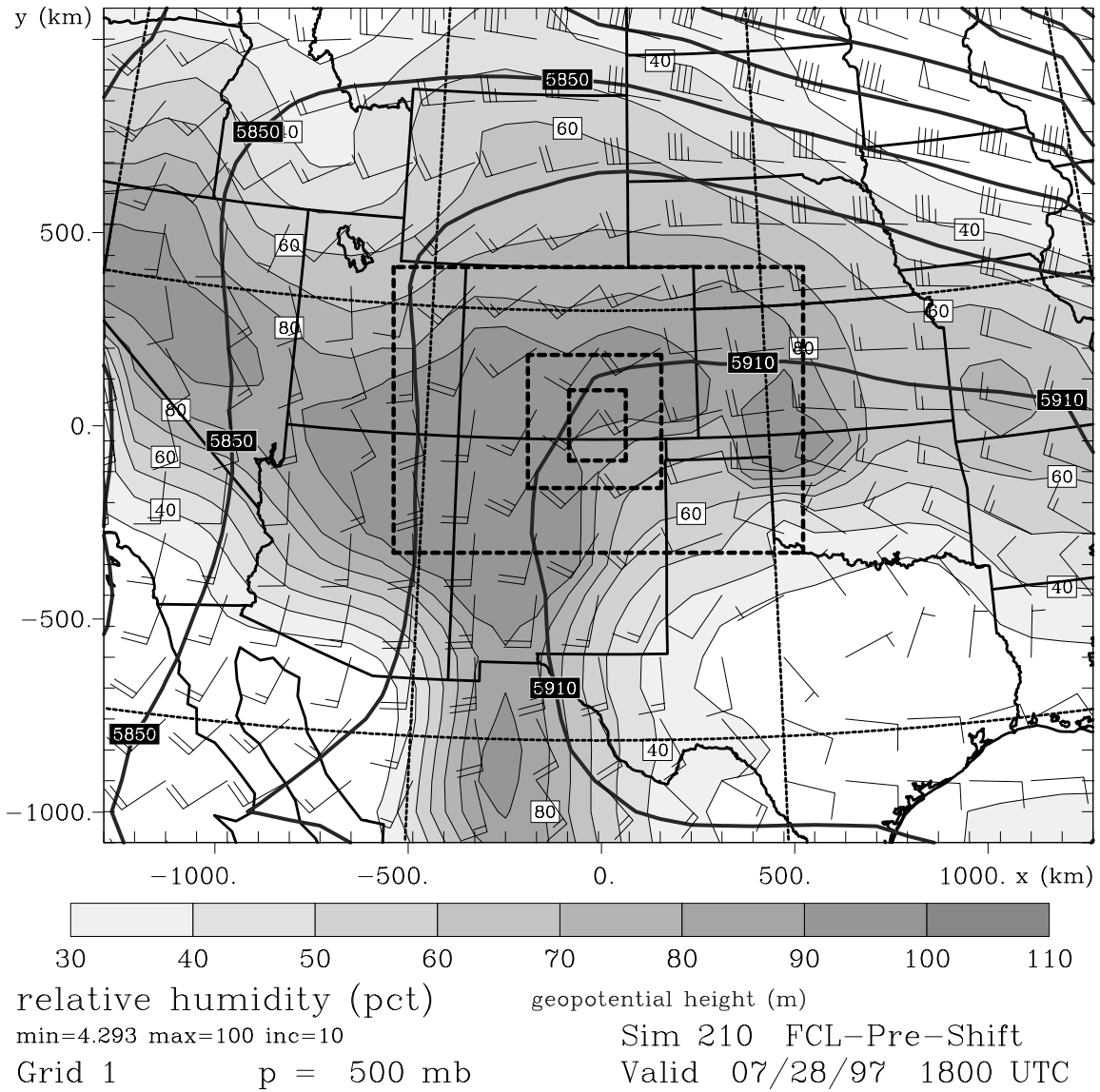


**Figure 28:** Simulated conditions at 500mb on Grid 1 in RAMS Simulation 210 (Fort Collins transposition run), valid 6h into the run at 1800 UTC 28 July 1997. Details are as in Fig. 4.

Sim 210: FCL-Pre-Shift Tot precip, hail (mm)

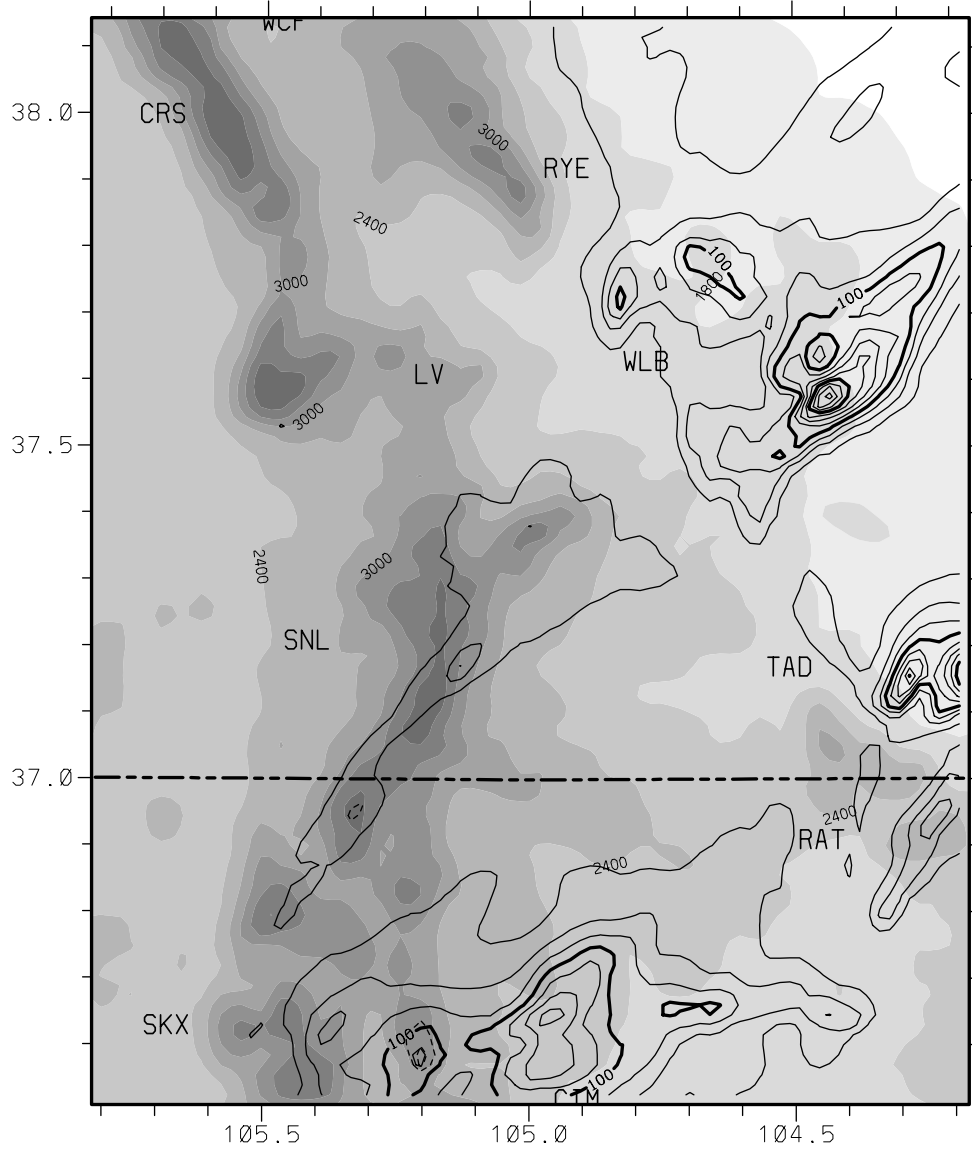


**Figure 29:** Simulated total precipitation and precipitation due to hail on Grid 4 for Simulation 210. Details are as in Fig. 7.

#### *4.4 Saguache Creek flood of 25 July 1999*

The Saguache Creek flood was an LC, Type IV event that occurred on the afternoon of 25 July 1999 in region 3, the Southwest Mountains (Fig. 1). This was a very wet period in Colorado, when an extension of the southwest monsoon brought abundant moisture to the state. The large scale conditions at 500mb that morning are shown by the Eta-based RAMS initialization on Grid 1 in Fig. 30. The east-west ridge from northern Mexico to Tennessee is characteristic of Type IV events. In this case, however, instead of a weak easterly short wave south of the ridge axis as in Fig. 3, there was a very weak short wave near the Four Corners (not evident in Fig. 30) that propagated eastward and amplified over southern Colorado during the day. Surface conditions that morning, shown on Grid 2 in Fig. 31, indicate moist conditions with no strong surface forcing as in Type I events.

To our knowledge, no detailed case study or rainfall analysis has been completed for the Saguache Creek event. In lieu of such an analysis, we constructed a radar-inferred rain distribution over the same domain as the RAMS Grid 4 (Fig. 32), as described below. The Saguache Creek basin empties into the northwestern portion of the San Luis Valley at the town of Saguache (SAG). The estimated rain pattern shows the storm occurred to the northwest of SAG in the middle of the mountain-ringed basin. The maximum rainfall stated in Table 2, 7.5" in 1.5h, was obtained from an on-line search (Lang, 1999). Storm Data<sup>1</sup> states that heavy rainfall flooded Saguache Creek from 2315 UTC 25 July to 0230 UTC 26 July, washing out roads and a few bridges and causing \$75,000 damage to property and crops.

We examined the storm evolution using 15-min, 2x2 km<sup>2</sup> national mosaics of radar reflectivity data<sup>2</sup>. Although reflectivity values are unreliable over the Colorado Rockies due to the distant NEXRAD radars and partial beam blocking by mountains, the data reliably reveal the location of deep convection and provide useful information on relative intensities. The radar data indicate that convection began about mid-day north of the San Luis Valley over the southern Sawatch Range and to the west over the San Juan and La Garita Mountains. In early afternoon, the mountain convection to the west began drifting eastward and organizing into a northeast-southwest oriented band, and new convection developed on the northern and western portions of the San Luis Valley, including the northern portion of the Saguache basin. The storms over the Saguache basin intensified around 2130 UTC as the convective band reached the area from the west. The intensified storm remained strong and slow-moving for only 1.5h before it began weakening and moving eastward. All storm activity moved east of the area by 0000 UTC, apparently in association with the short wave that had amplified during the day. The resulting estimated rain field in Fig. 32 is a time integration of 15-min rainrate

---

<sup>1</sup> Storm Data is published monthly by the National Oceanic and Atmospheric Admin.

<sup>2</sup> This dataset is called NOWrad (TM), produced by and a registered trademark of WSI Corporation. The dataset was provided by the Global Hydrology Resource Climate Center, Huntsville, Alabama.

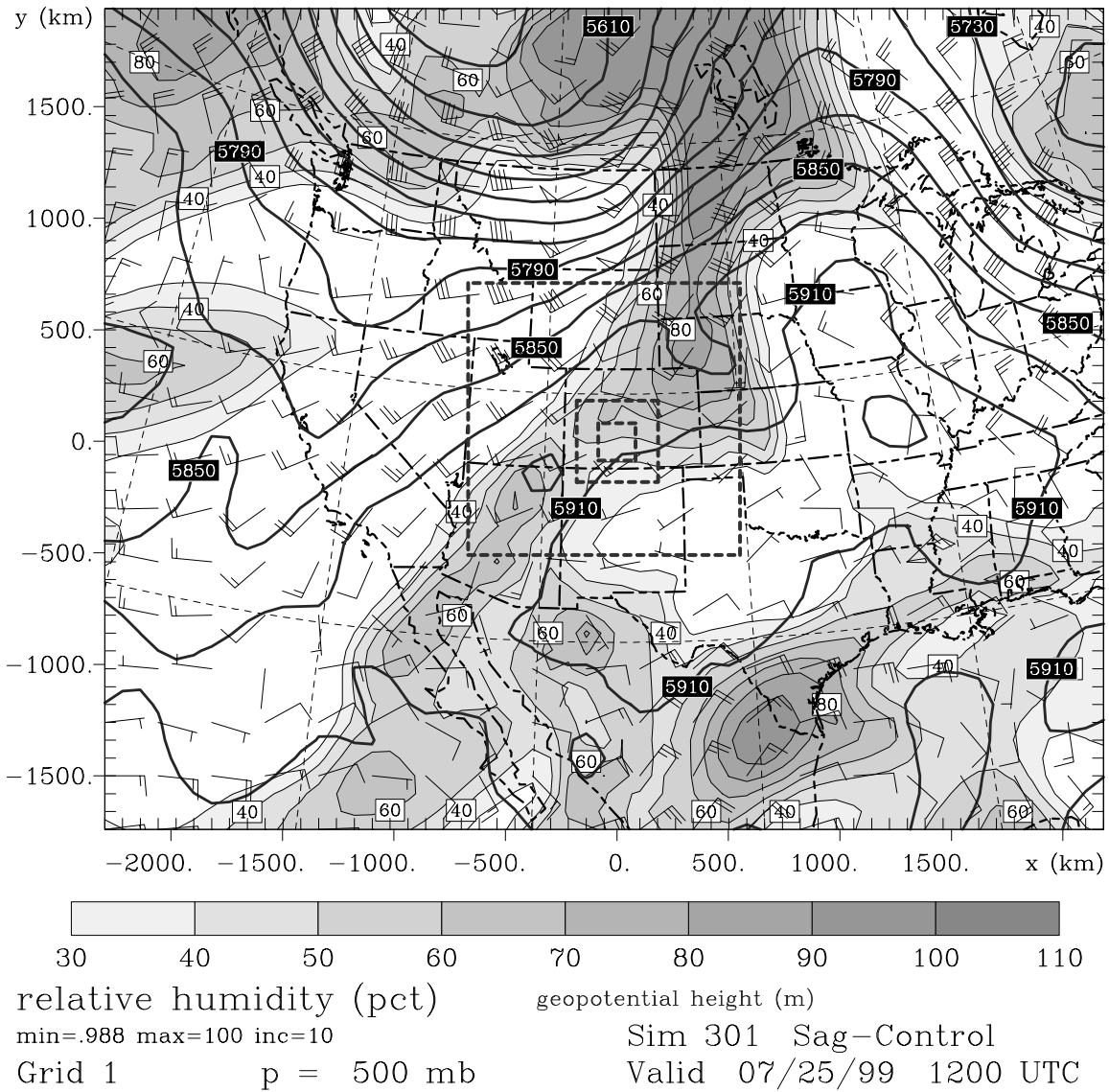


**Figure 30:** RAMS initialization, at 1200 UTC 25 July 1999, at 500mb on Grid 1 for Simulation 301 (Saguache Creek control run). Details are as in Fig. 4.

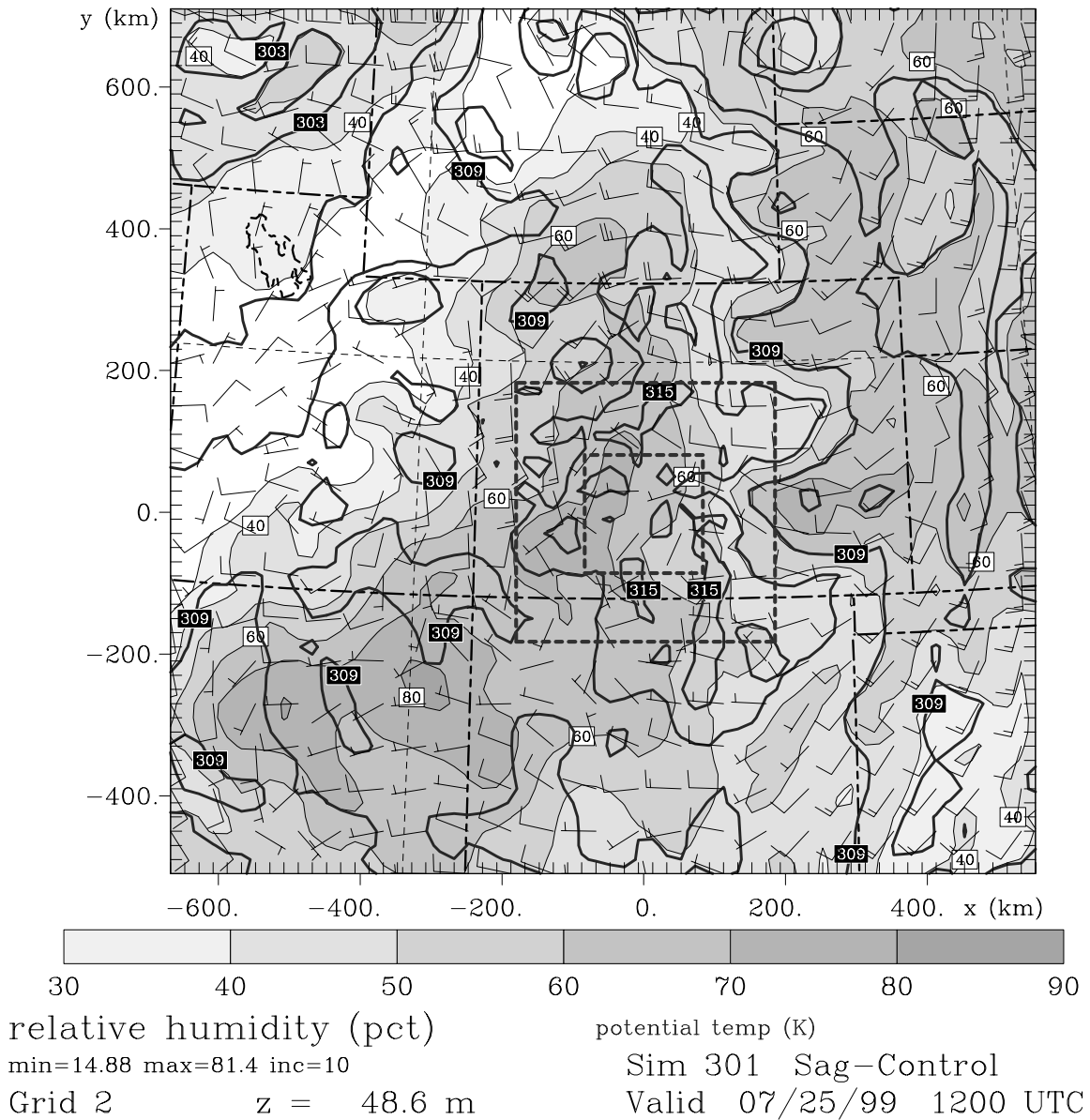


**Figure 31:** RAMS initialization, at 1200 UTC 25 July 1999, at surface on Grid 2 for Simulation 301 (Saguache Creek control run). Details are as in Fig. 5.

Saguache Creek: Z-R rain estimate(mm), 18-04z 7/25-26/99

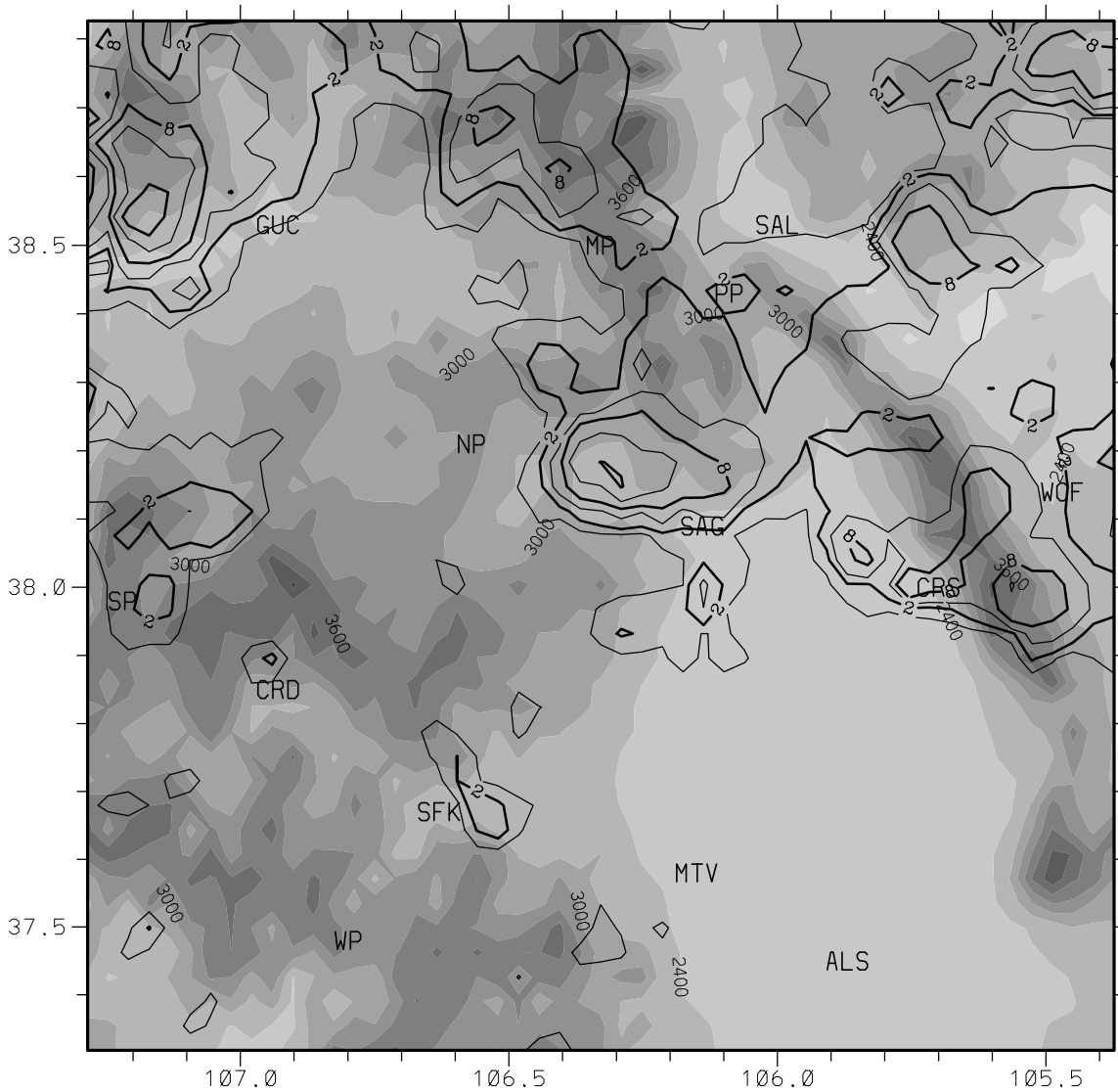


**Figure 32:** Radar-estimated rainfall for the Saguache Creek event from 1800 UTC 25 July to 0400 UTC 26 July 1999. Solid contours are isohyets beginning at 1mm and doubling in value for each isohyet. Topography is progressively shaded at 300m intervals. Area is the same as Simulation 301 Grid 4.

fields estimated from the reflectivity fields using the default NEXRAD algorithm. For reasons stated above, this technique severely under-estimates the actual rain in this region. Runoff time between the heavy rain and the period of flood damage in Storm Data explains the 2h lag.

Only one simulation was performed for the Saguache Creek event. Figure 33 shows the total precipitation in Simulation 301. As was observed, simulated convection developed around mid-day to the west and north of the San Luis Valley. Both areas of convection expanded eastward and then propagated southward. The western activity produced three high-elevation maxima exceeding 100mm relatively early, with the stronger storms exiting the southern boundary of Grid 4 around 0100 UTC. In contrast, the northern activity remained relatively weak until about 0100 UTC, then intensified as new cells developed on the western and southern flanks of a storm north of Monarch Pass (MP). This storm produced a precipitation maximum of 129mm high in the Sawatch range, with up to two-thirds of that due to hail. This storm propagated southward to the northern fringe of the Saguache basin and continued precipitating in that area until about 0530 UTC, when the activity weakened and moved off to the east. No convection was simulated in the northern San Luis Valley or the Saguache basin as was observed.

#### ***4.5 Dallas Creek flood of 31 July 1999***

The Dallas Divide flood occurred on the afternoon of 31 July 1999, and like the Saguache Creek flood that occurred only six days earlier, was an LC, Type IV event. The RAMS Eta-based initialization that morning at 500mb on Grid 1 (Fig. 34) indicates conditions that had persisted for a week, including an east-west ridge across the southern plains and moist southwesterly flow in western Colorado. The eastward propagating short wave in this event, over Utah and entering Colorado, is larger and much more evident than in the Saguache Creek event. Again, the accompanying surface conditions, shown on Grid 2 in Fig. 35, indicate moist conditions with no strong surface forcing.

Overviews and analyses of this event include a case study by National Weather Service forecasters in Grand Junction (Avery et al., 2001), a detailed analysis of radar and lightning data by Henz (2000), a survey of the hydrogeological effects of the flood by Jarrett (personal communication), and documentation in Storm Data. As with the Saguache Creek flood, no analysis of the accumulated rainfall distribution has been published for this recent event. Therefore, we integrated rain-rate fields as estimated from the 15-min, 2x2 km<sup>2</sup> national mosaics of radar reflectivity data, to produce a rainfall analysis over the Grid 4 domain (Fig. 36). The storm system consisted of a series of cells forming near Dallas Divide (DAL) and into the upper reaches of the San Miguel River basin near Telluride (TEL). They translated and propagated northeastward into and down the Dallas Creek watershed east of DD towards Ridgeway (RDG). Avery et al. (2001) reported that during the latter stages, the heaviest rain progressed slightly southward. Storm Data cites a measured maximum of 3.77" in the Dallas Creek drainage (most occurring in 2h) and property damage along Dallas Creek of \$1.3 million. Henz (2000) calculated peak rainfall amounts of 4-5 inches based on radar data. While the radar-inferred rainfall in Fig. 36 is under-estimated, the pattern shows an axis of

Sim 301: Sag-Control

Tot precip, hail (mm)

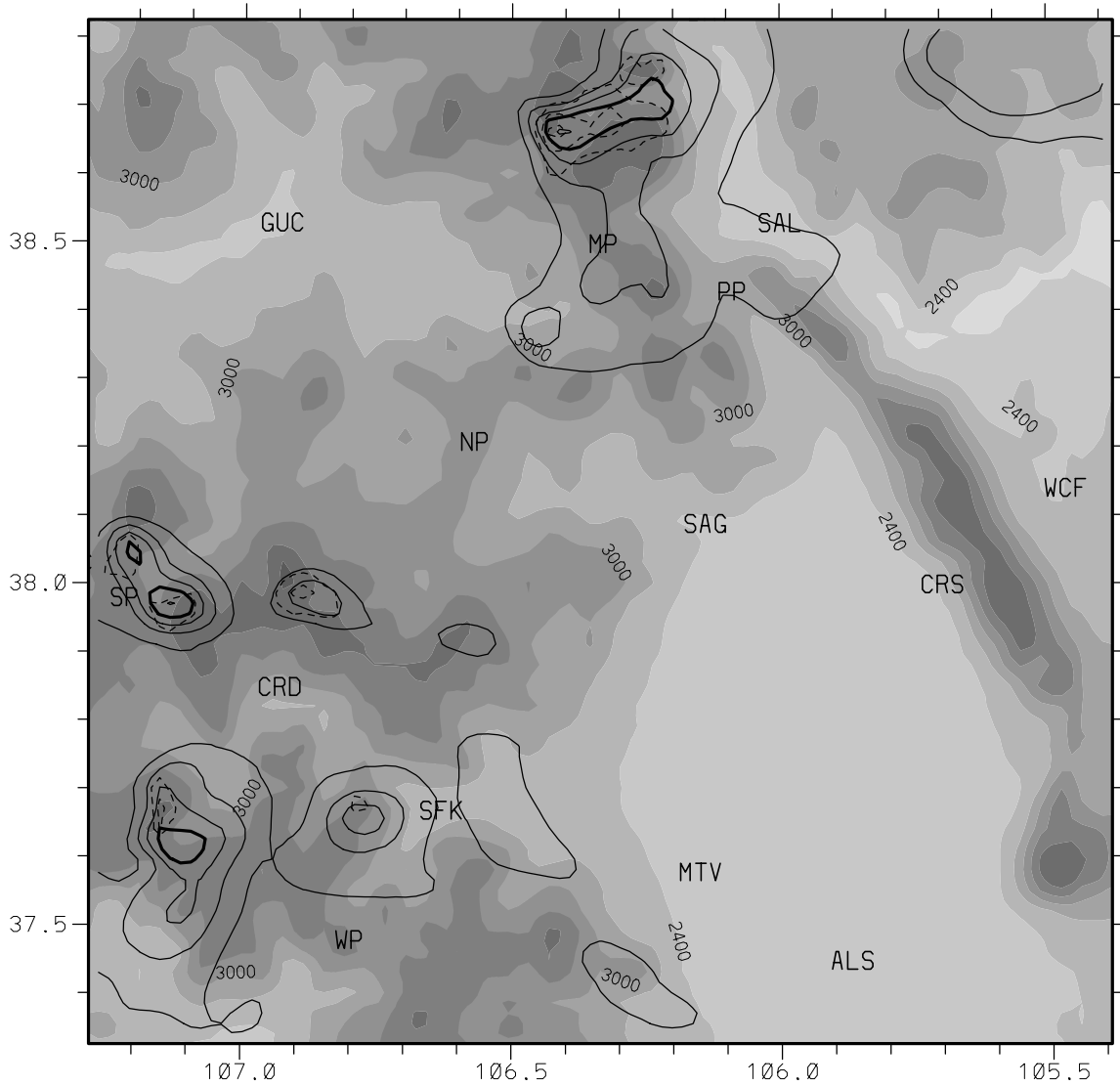


**Figure 33:** Simulated total precipitation and precipitation due to hail on Grid 4 for Simulation 301. Details are as in Fig. 7.

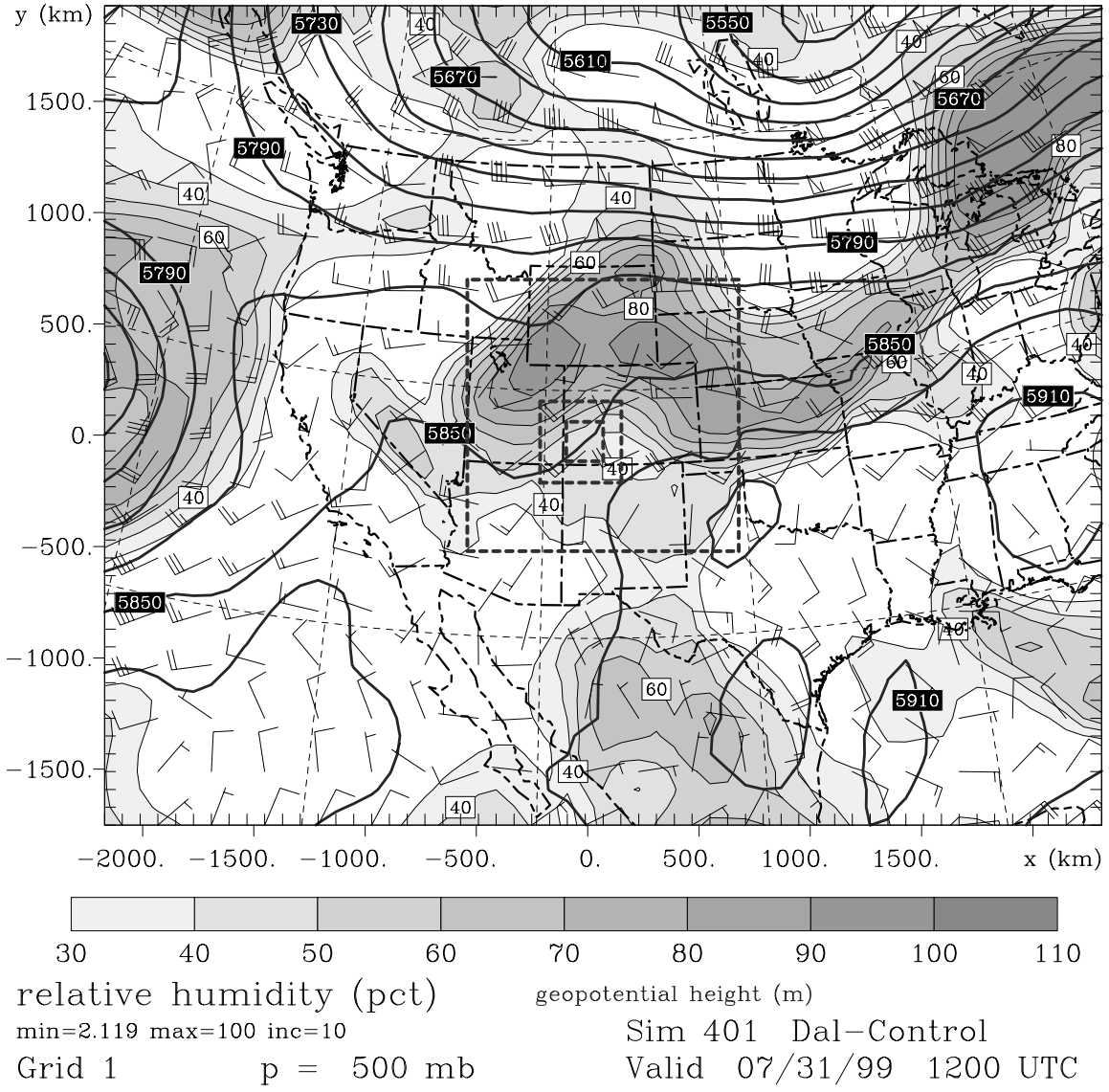


**Figure 34:** RAMS initialization, at 1200 UTC 25 July 1999, at 500mb on Grid 1 for Simulation 401 (Dallas Creek control run). Details are as in Fig. 4.

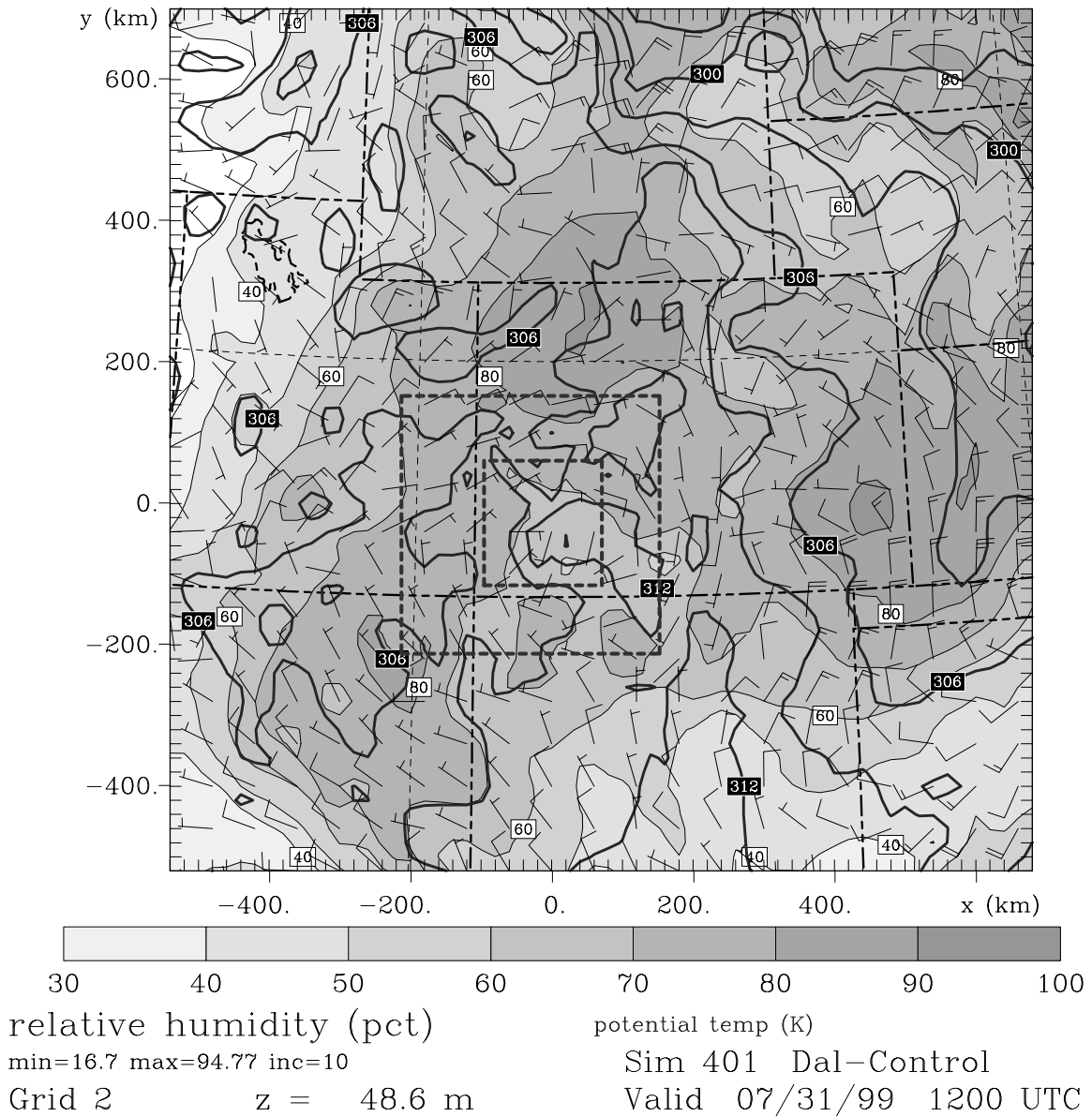


**Figure 35:** RAMS initialization, at 1200 UTC 31 July 1999, at surface on Grid 2 for Simulation 401 (Dallas Creek control run). Details are as in Fig. 5.

Dallas Creek: Z-R rain estimate(mm), 18-04z 7/31-8/1/99

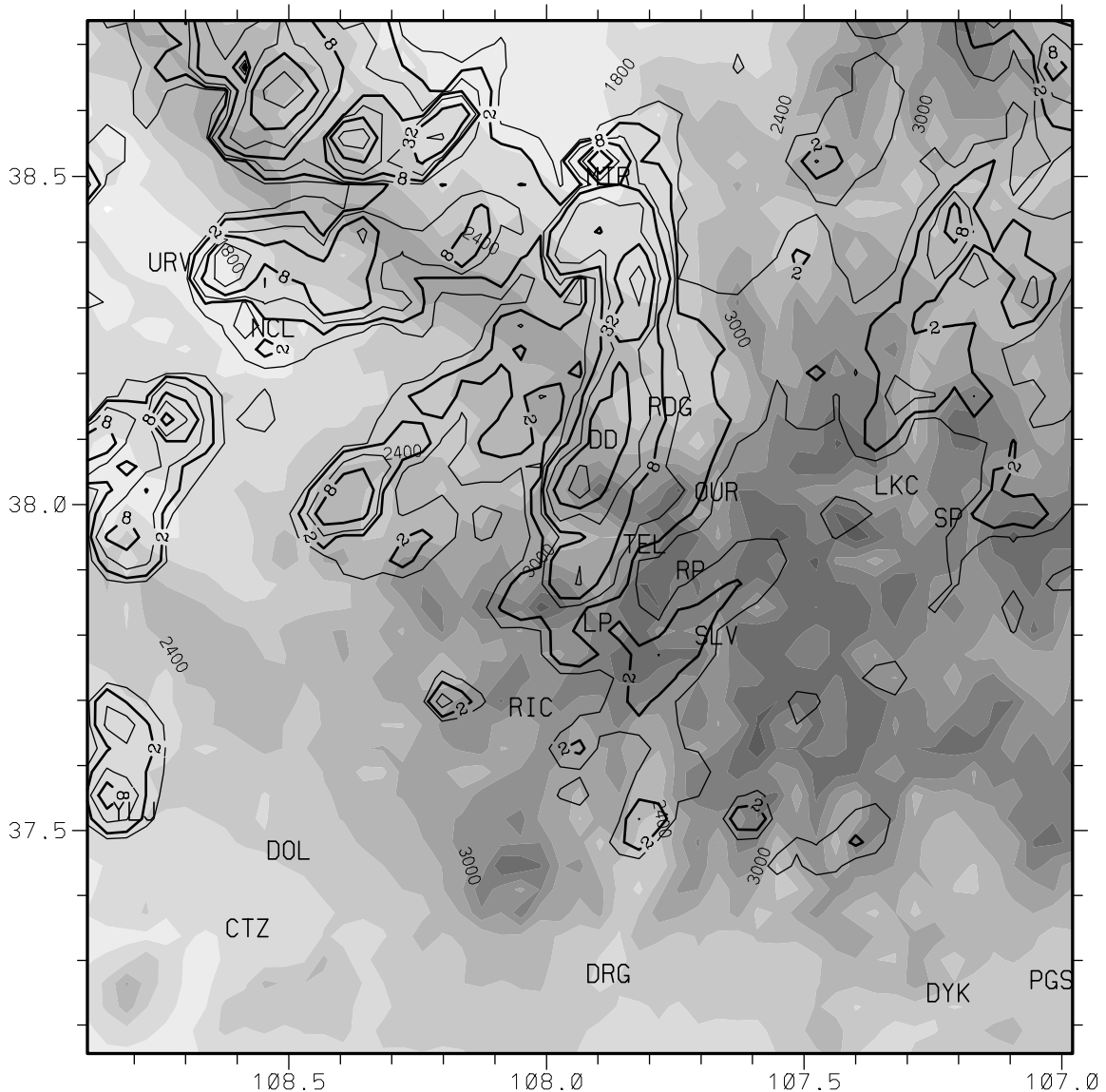


**Figure 36:** Radar-estimated rainfall for the Dallas Creek event from 1800 UTC 31 July to 0400 UTC 1 August 1999. Area is the same as Simulation 401 Grid 4. Other details are as in Fig. 32.

maximum amounts extending northeastward across Dallas Divide, with the estimated local maximum to the west of DD in the Leopard Creek drainage. In fact, in addition to the entry for the Dallas Creek flood, Storm Data cites extensive flooding on Leopard Creek, many mudslides and extensive road damage in that drainage and in the upper San Miguel basin, and property damage of \$50,000. Note the secondary axis of maximum rain, just west of TEL, extending southward from the main axis across DD. Storm Data also cites pea-sized hail accumulation up to 8" deep on Dallas Divide.

Four simulations based on the Dallas Divide event are included in this report, all utilizing the Eta model analyses for initialization and nudging. Simulations 401 and 402 differ only in their soil moisture and initialization: in 401, it is set at 40% (70%) below (above) 6000' elevation, while 402 uses the Eta soil moisture and temperature. Since most of the Grid 4 domain is above 6000' (1829m), initial soil moisture in 401 is 70% over most of Grid 4, consistent with the extensive antecedent rains in southwest Colorado. In 402, the Eta-based moisture is as high as 83% saturation, but averages close to the 70% value used in 401. Thus, it is not surprising that Simulations 401 and 402 were very similar in convective evolution and total precipitation (Figs. 37 and 38). In both runs, a succession of convective cells developed (beginning after 2000 UTC) to the south of Dallas Divide (DD), in the upper San Miguel River basin just west of Telluride (TEL). The cells intensified as they tracked northeastward over Mt. Sneffels, and subsequently weakened as they moved downslope toward the upper Uncompahgre River above Ridgeway (RDG). Most of these had almost identical tracks, with the multi-cell system eventually propagating southeastward away from the previous dominant track and the activity ceasing by 0200 UTC on 1 Aug.

The resultant maximum total precipitation in Simulations 401 and 402 was 193mm and 185mm, respectively, at the same grid point just northeast of Mt. Sneffels, and at an elevation of 3783m. This simulated evolution is similar to that described by Henz (2000) and Avery et al. (2001), except the simulated scenario occurred 15-18 km to the south-southeast of the observed location and at higher elevations. The main cell generation region in the simulations is more consistent with the secondary axis of maximum rain observed west of TEL in Fig. 36 than with the main axis across DD. Maximum simulated hail was 168mm (167mm) atop Mt. Sneffels, with the simulated rain maximum a few kilometers down the northeastern slope of the mountain and a smaller maximum on the upwind southwest slope near TEL. This spatial distribution of maximum rain and hail agrees with the observed patterns as inferred from Storm Data and Fig. 36, except that it occurs over Mt. Sneffels instead of across Dallas Divide. Only minor differences occurred between these two runs, such as a lower elevation storm that produced over 125mm of rain near Uravan (URV) in Simulation 402, probably a result of its more moist soil at lower elevation than in 401.

Simulation 403 was identical to the 401, except a regional moisture perturbation was imposed, raising RH to 85% from the surface to 500mb. This was after an earlier moisture perturbation run was attempted based on RH raised to 95%. In that run, very little convection developed due to too much cloud cover and insufficient solar heating, thus leading to the attempt with 85% RH. In Simulation 403 (Fig. 39), convective evolution was quite similar to 401 and 402, except the similar scenario was another 15km further south from the Dallas Creek basin, with cells developing further upstream (southwest). Also, the main storm activity occurred about 2h later, probably a result of more cloud cover that delayed convective development in 403. This is the only simulation in this report where the rain maximum, at 3656m, occurred at a higher elevation than the hail maximum, although only by 114m.

In the first two runs based on the Dallas Creek event (401 and 402), significant precipitation was produced on Grid 2 (20km spacing) on the eastern slope outside the nested Grids 3 and 4, consistent with heavy rains observed there. We thus ran a series of three-grid simulations with Grid 3 (5km spacing) at various locations on the eastern

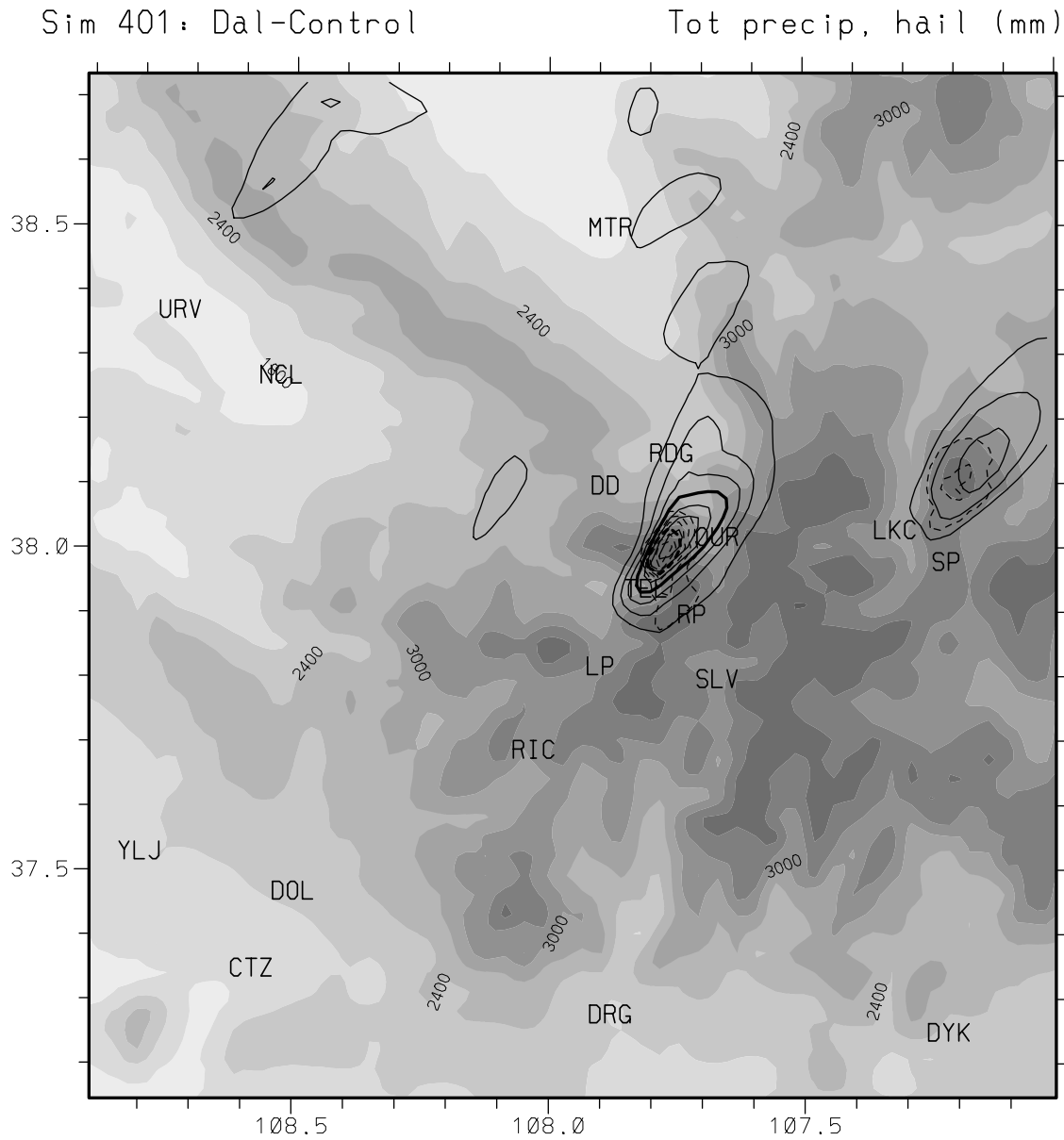


**Figure 37:** Simulated total precipitation and precipitation due to hail on Grid 4 for Simulation 401. Details are as in Fig. 7.

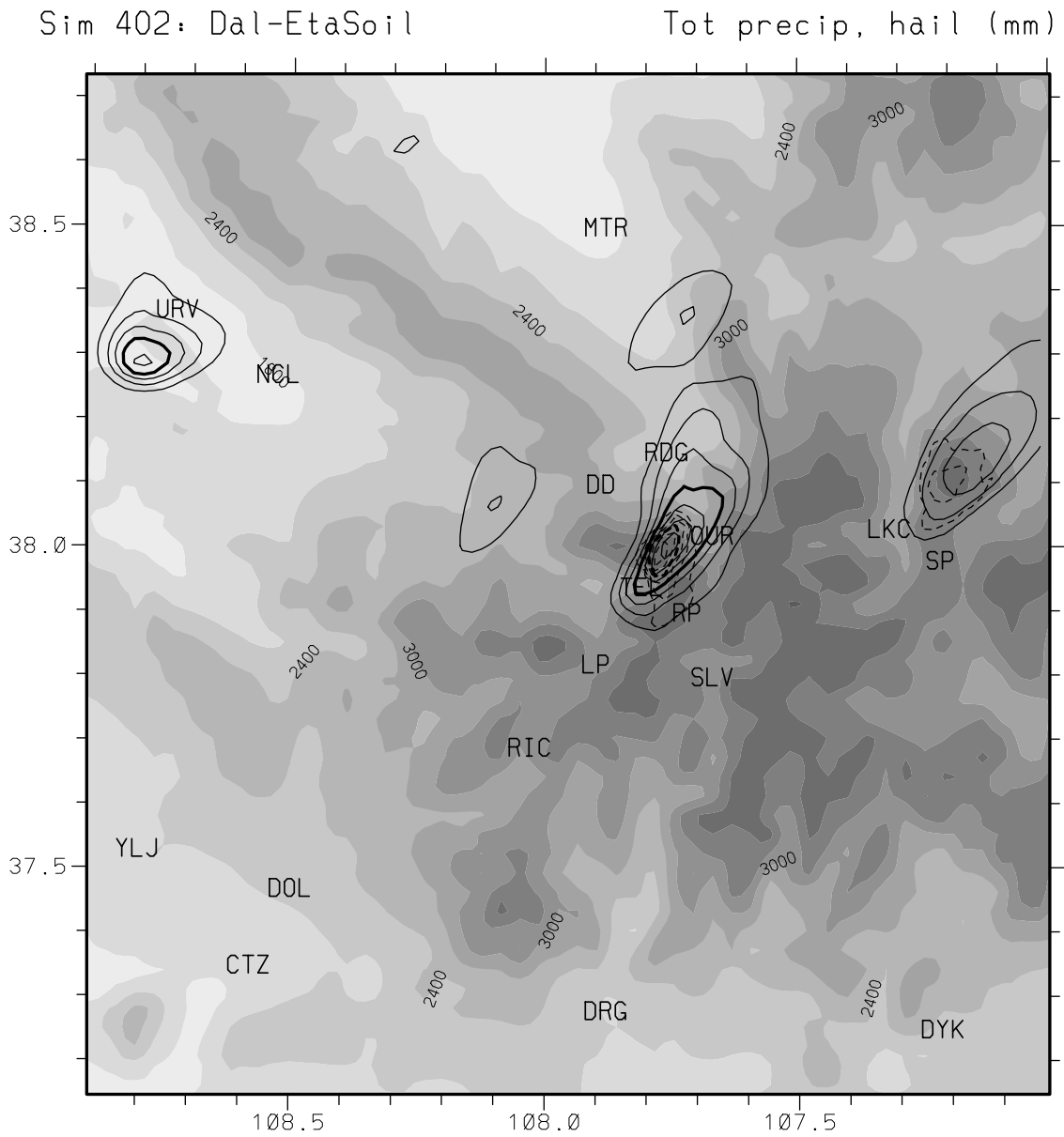


**Figure 38:** Simulated total precipitation and precipitation due to hail on Grid 4 for Simulation 402. Details are as in Fig. 7.

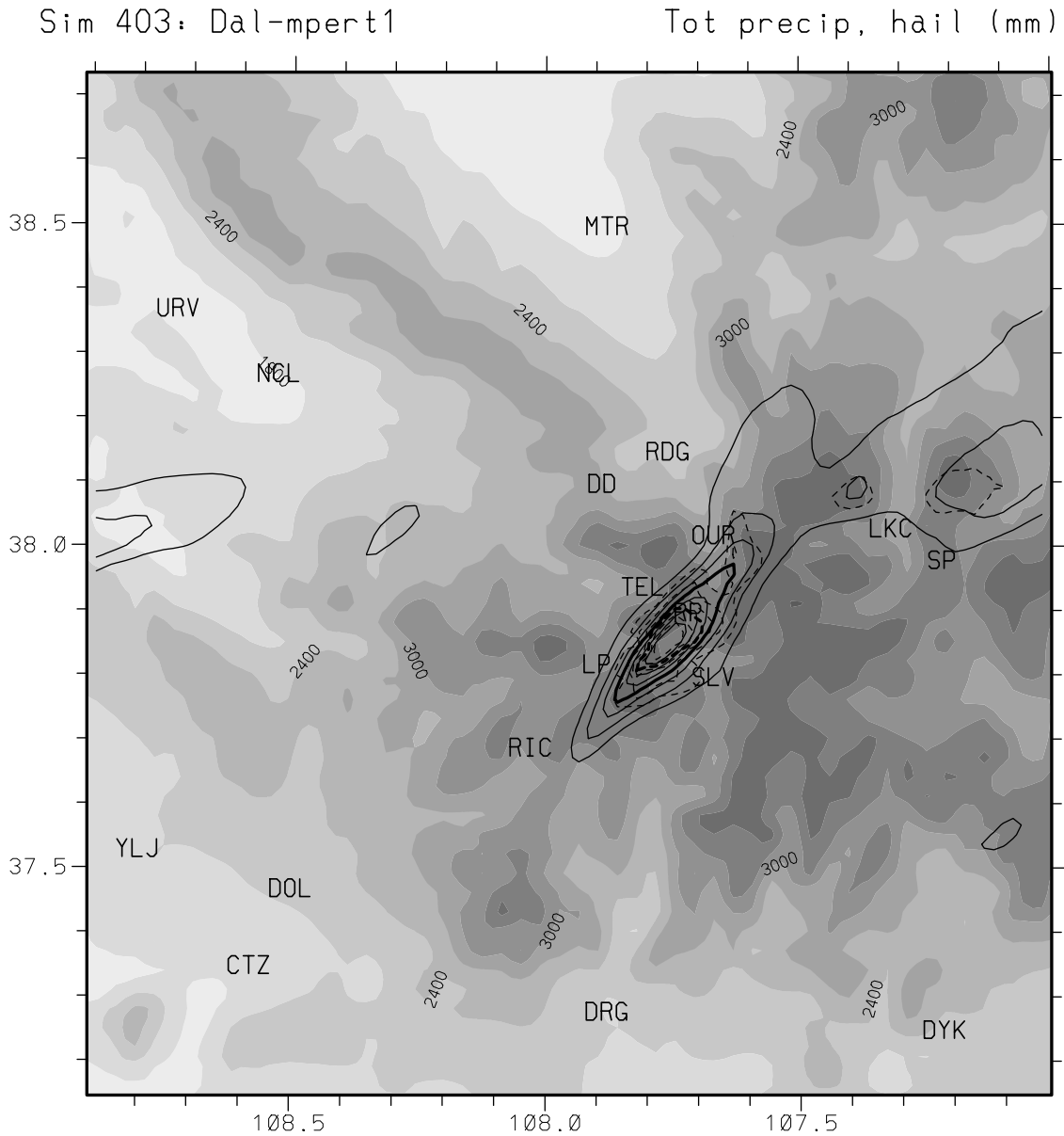


**Figure 39:** Simulated total precipitation and precipitation due to hail on Grid 4 for Simulation 403. Details are as in Fig. 7.

This led to Simulation 404, with Grids 3 and 4 centered north of Colorado Springs. It uses the exact same setup as 402 (including Eta-based soil moisture and temperature) except for the east slope location of the finer grids. In Simulation 404, deep convection first developed at about 2000 UTC on 31 July in the northwestern corner of Grid 4 near Loveland Pass (LP in Fig. 40). This convection propagated eastward, with more convection developing further south at high elevations in the western portion of Grid 4 and also moving eastward. Some of these propagating storms evolved into a characteristic bow-echo shape commonly seen in many severe storms, which is consistent with a funnel cloud reported near the El Paso County Fairgrounds (Storm Data). Meanwhile, a simulated slow-moving cell intensified north of Pueblo (PUB) after 0130

UTC on 1 Aug, and merged into the leading flank of a multi-cell mountain-generated cluster moving in from the west. Simulated precipitation rates exceeded 300mm for over 2h before and after the merger. This storm produced 423mm of precipitation north of PUB. Storm Data cites local flooding from slow moving storms from southwest Colorado Springs (COS) northeastward to Ramah. Comparison with radar data (not shown) shows that the simulated storm evolution and accumulated precipitation distribution are very reasonable, with the axis of heavy rain north and northeast of PUB in Fig. 40 about 40km

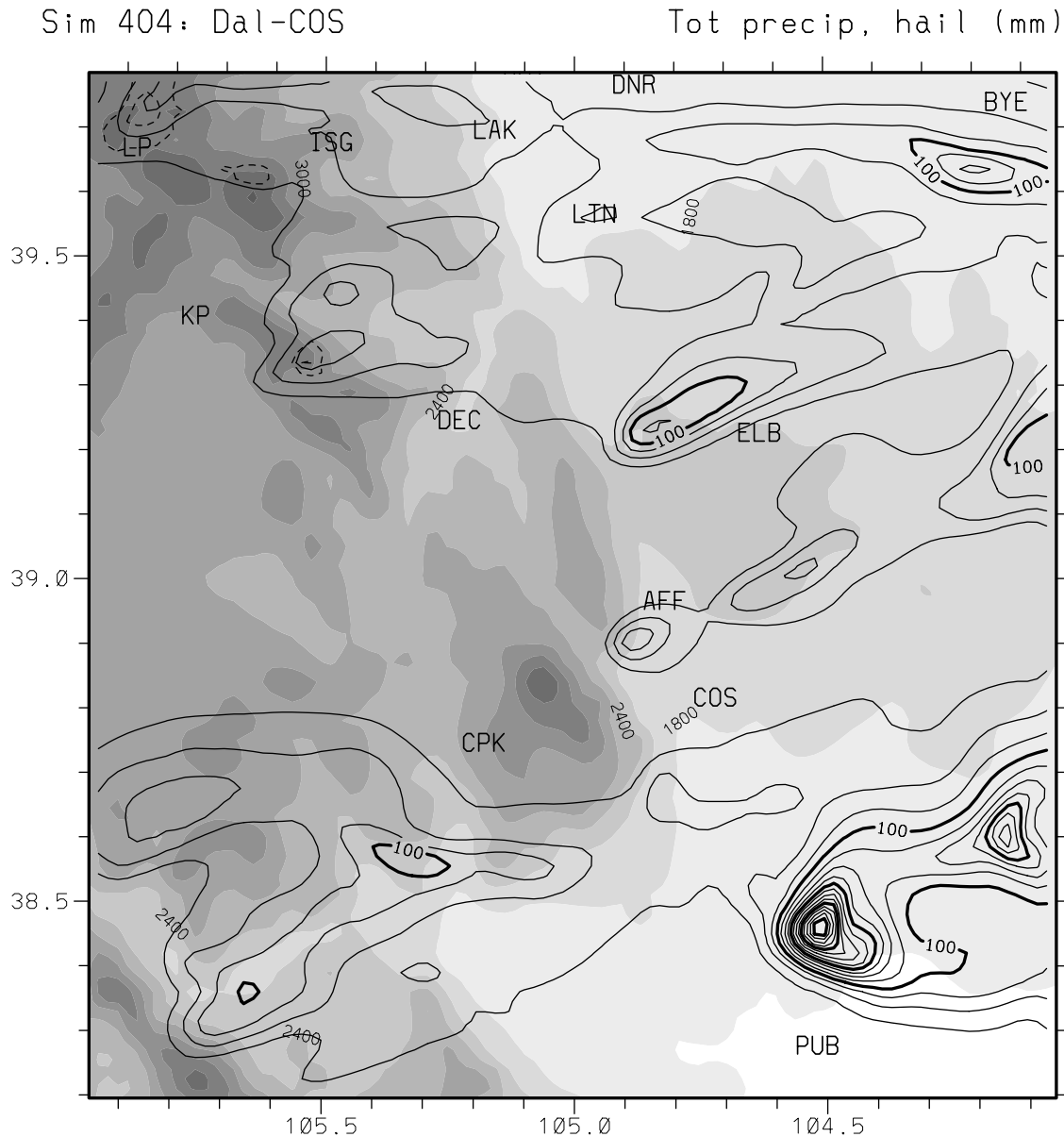


**Figure 40:** Simulated total precipitation and precipitation due to hail on Grid 4 for Simulation 404. Details are as in Fig. 7.

#### ***4.6 Park Range heavy rain event of 18-21 September 1997***

The Park Range storm system of 18-21 September 1997 was classified as a GLC, Type III event. The episode was due to a synoptic scale wave that dug into Nevada, closed off, and gradually moved eastward through Utah and southern Wyoming. The 500mb forecast on Grid 1, 36h into the control run for this case (Simulation 501), shows the large scale conditions as the low was digging into Nevada (Fig. 41). Strong moist southwesterly flow is seen over eastern Utah and western Colorado. Much of the abundant moisture over the southwestern U.S. originated from a weakening tropical system (Linda) in the eastern Pacific, which about a week earlier had been one of the strongest hurricanes ever recorded in that basin. The 500mb low entering Nevada in Fig. 41 is a southwestern extension of a strong wave in Saskatchewan and Montana. That northern wave as well as the cut-off low is associated with a strong surface high centered in southern Alberta and British Columbia. In the 36h surface forecast on Grid 2 (Fig. 42), the potentially cool, moist northeasterly flow in the northern Rockies and plains is associated with that high pressure system. Frontal forcing between the Canadian and southwestern U.S. air masses was an important ingredient to the heavy precipitation episode.

We aren't aware of any detailed precipitation analyses for this fairly recent event. However, Doesken (personal communication) provided recording raingage data from two National Atmospheric Deposition Program (NADP) precipitation sites in the Park Range north of Steamboat Springs: the Tower site on Buffalo Pass and the Dry Lake site about 700m lower in elevation and 8km west of the Tower site. These offer excellent time-resolved data, and are supplemented by on-line daily rain amounts at other NADP sites and by routine daily and hourly NWS and cooperative precipitation data. These data indicate precipitation totals during 18-24 September of over 2" north of the Colorado River to the Wyoming border in the Northern Basin and Northern Mountain hydroclimatic regions (Fig. 1). Over 4" fell from Meeker and Craig east-northeastward to the Park Range, with sites in the Flat Tops and at Steamboat Springs recording over 5". The largest observed amounts were 6.19" (157mm) and 8.08" (205mm) at the Dry Lake and Tower sites, respectively. The time series of accumulated rain for these sites (DLK and TWR in Fig 43a) show that 70-80% of the total occurred in the first 2.5 days after rain began falling on the 18th, with most of the rest falling on the following day (the 21st).

Satellite images and the national mosaics of radar data show numerous bands and clusters of rain propagating from the southwest during the period, with generally more intense convective development during the late afternoon and early evening. However, radar coverage is poor over the Park Range due to distance from the radar and partial beam blocking by terrain, especially for orographically forced rain clouds that are not too deep. In fact, radar-inferred rainfall patterns (not shown) using these data (as was done for the Saguache Creek and Dallas Creek events in Figs. 32 and 36, respectively) show a false minimum over the poorly observed upper Yampa Valley, the Park Range

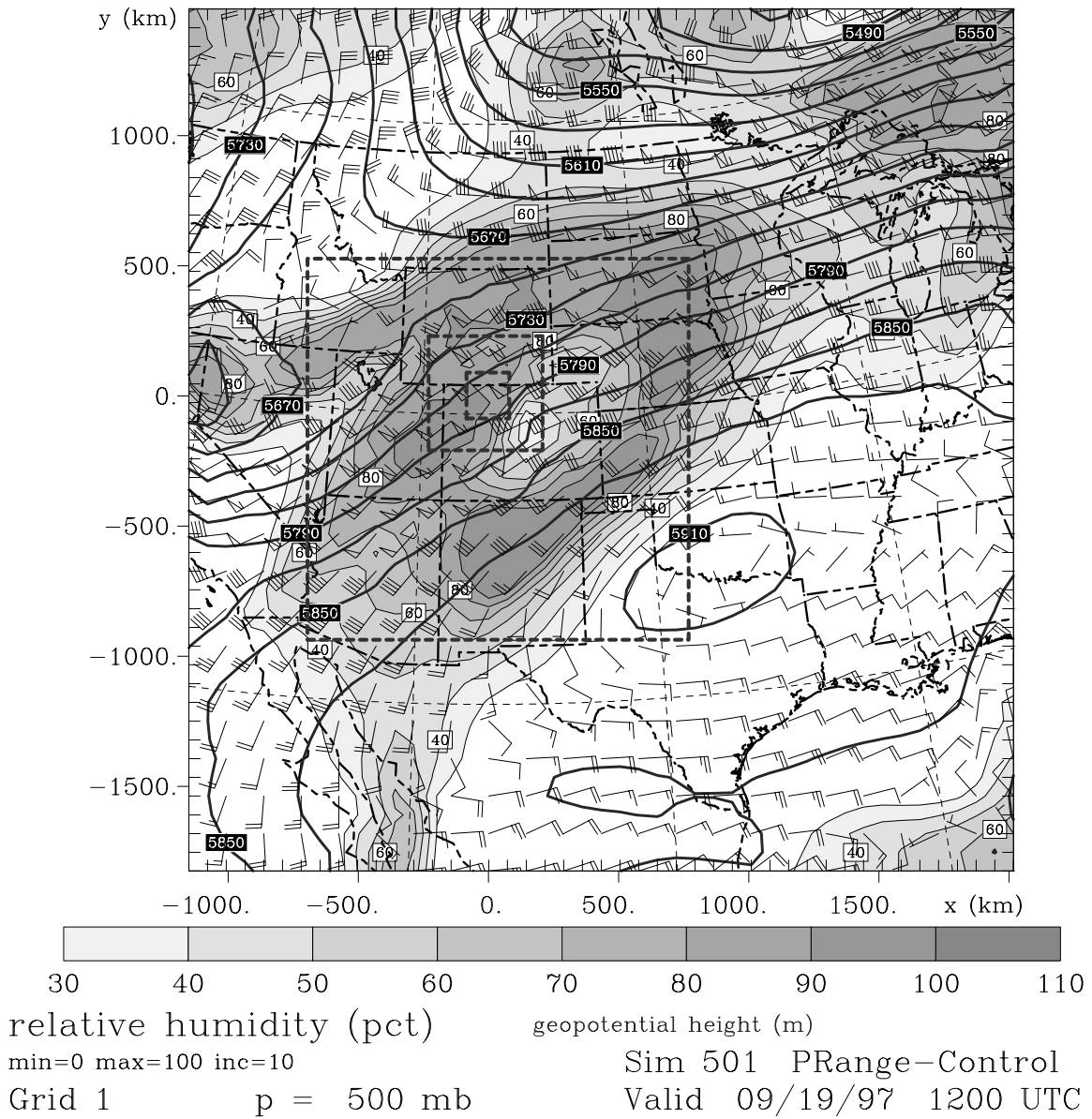


**Figure 41:** Simulated conditions at 500mb on Grid 1 in RAMS Simulation 501 (Park Range control run), valid 36h into the run at 1200 UTC 19 September 1997. Details are as in Fig. 4.

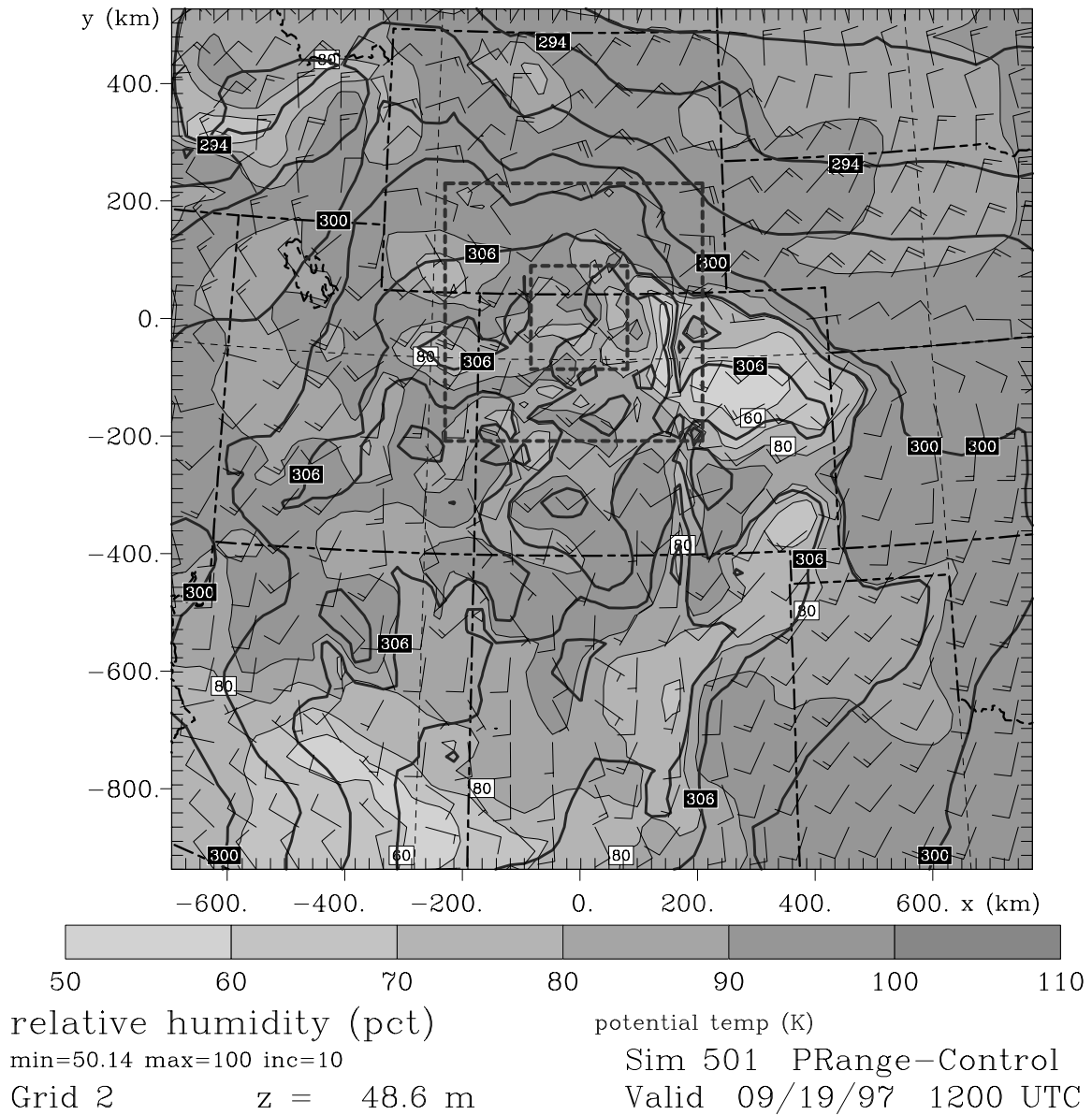


**Figure 42:** Simulated conditions at surface on Grid 2 in Simulation 501 (Park Range control run), valid 36h into the run at 1200 UTC 19 September 1997. Details are as in Fig. 4.

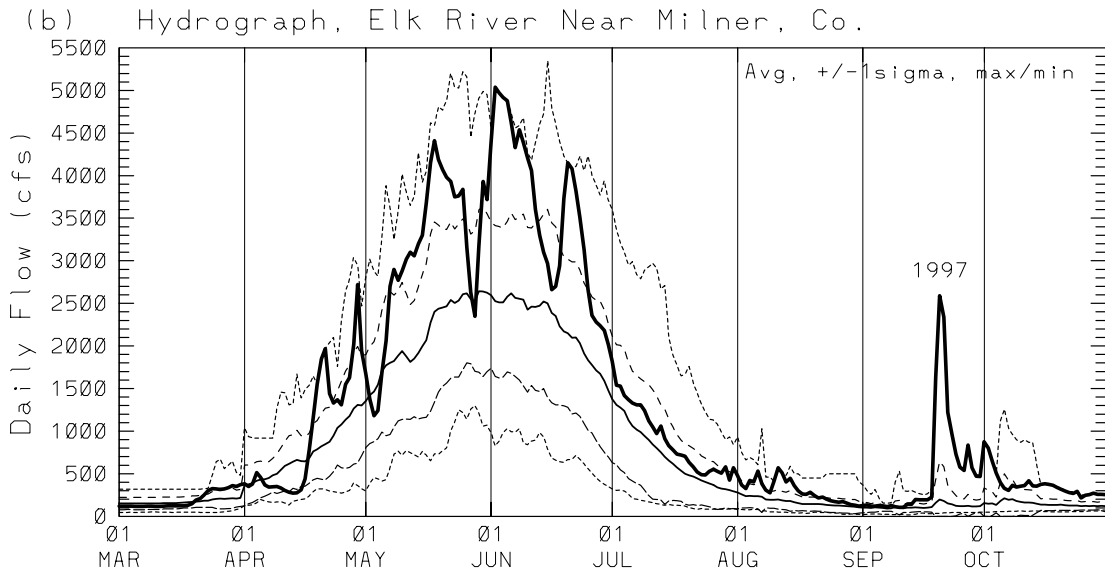
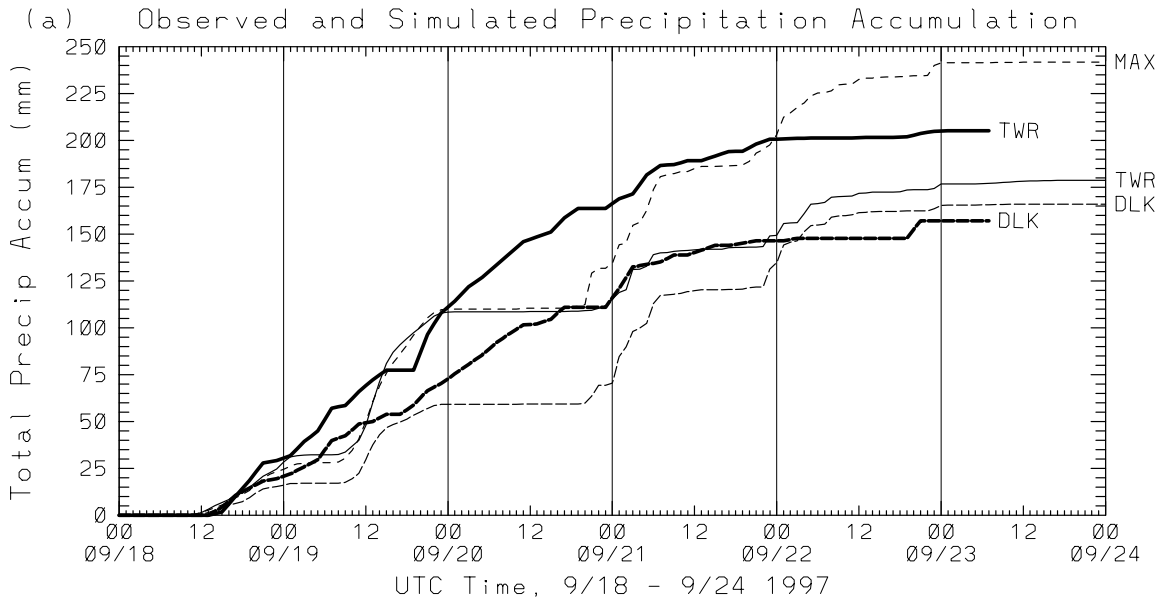


**Figure 43:** (a) Observed time series (heavy curves) of accumulated rainfall during Park Range event at Tower (TWR) and Dry Lake (DLK) NADP sites. Simulated time series of total accumulated precipitation at grid points corresponding to TWR and DLK and at the Grid 4 maximum (MAX) are shown by thin curves. (b) Mean daily discharge of Elk River near Milner, Colorado, during 1997 (heavy curve). Thin curves show the average hydrograph (solid), the average plus and minus one standard deviation, and the minimum and maximum daily discharges, based on 30-31 years of data at this station.

and North Park, suggesting a general absence of deep convection that would have been better detected. This, combined with the relatively steady precipitation rates observed at TWR and DLK in Fig. 43a, suggests that the precipitation over the Park Range was dominated by relatively low-topped, orographically enhanced storms.

The magnitude of this event can be seen by examining on-line streamflow data made available by the U.S. Geological Survey (USGS). In Fig. 43b, the bold solid curve is the 1997 mean daily discharge rate at Elk River near Milner, Colorado (USGS station 09242500). The thin solid curve is the average mean daily discharge rate as derived from 30-31 years of archived data (from the periods 1904-1927 and 1990-2000), and the average curve is bracketed by curves for plus and minus one standard deviation and minimum and maximum flows for the date. The 1997 curve rose sharply on 19 September 1997, peaked on the 20th and remained high on the 21st. This spike in the 1997 curve is clearly an anomalous feature in the fall, and in fact is the same magnitude as the average peak flow during the spring snowmelt runoff. A similar peak flow for this event (equal to its average spring runoff peak) occurred at a station on Fish Creek near Steamboat Springs, while event peak flows at stations on the White River and Yampa River were only slightly below their respective spring runoff peaks. Numerous entries for local flash flooding and severe weather in northwestern Colorado appear in Storm Data for this period.

Simulation 501 for this event was initialized with the Eta analysis at 0000 UTC 18 September 1997. Several preliminary two-grid runs were made with a larger domain extending into the Pacific, in which the digging synoptic wave did not develop sufficiently. We experienced similar difficulties with the Type III event described in the next section, but in that case assumed it was due to the coarse 2.5 x 2.5-deg NCEP reanalysis data used in the initialization and/or nudging. With the 40-km Eta data used for this event, the problem is less likely due to poor resolution and may be due to undetected features that were critical to the large scale evolution, e.g., an offshore jet streak. Thus it was necessary to draw in the western boundary onto the U.S. mainland as shown in Fig. 41 in order to directly nudge the wave into our domain. The finest Grid 4 in this GLC event has 2 km grid spacing, slightly coarser than the 1.67 km spacing used in the LC events. This compromise enables the widespread rains affecting the entire Park Range and Flat Tops to be included on Grid 4, while still reasonably resolving convective processes of the embedded convection.

Simulation 501 was run through 0000 UTC 24 September 1997, or six days. The maximum of the accumulated precipitation field (Fig. 44) is 242 mm, occurring about 17 km to the north-northeast of Steamboat Springs (SBS) in the Mount Zirkel Wilderness at 3252m elevation. About 130-140 mm of this maximum is due to hail. The maximum rain accumulation is 229mm and occurs several hundred meters lower in elevation, about 2-3 km to the north of the Dry Lake site (DL). Other areas with significant local precipitation maxima in Fig. 44 include the northern extension of the Park Range across the Wyoming border (>175mm), a maximum of 225mm along the northern border that was produced by a simulated convective storm system, and a maximum >125mm in the Flat Tops.

The time distribution of simulated precipitation at grid points corresponding to the Tower and Dry Lake sites and at the simulated maximum in the Park Range (thin curves in Fig. 43a) is in reasonable agreement with the observations, although the simulated synoptic wave remained somewhat stronger and produced precipitation in the Park Range

for a day longer than observed. Also, the simulated curves are more episodic than the steadier observed curves and are dominated by four intense periods of more convective precipitation. A non-precipitating period in Simulation 501 through most of the 20th is in

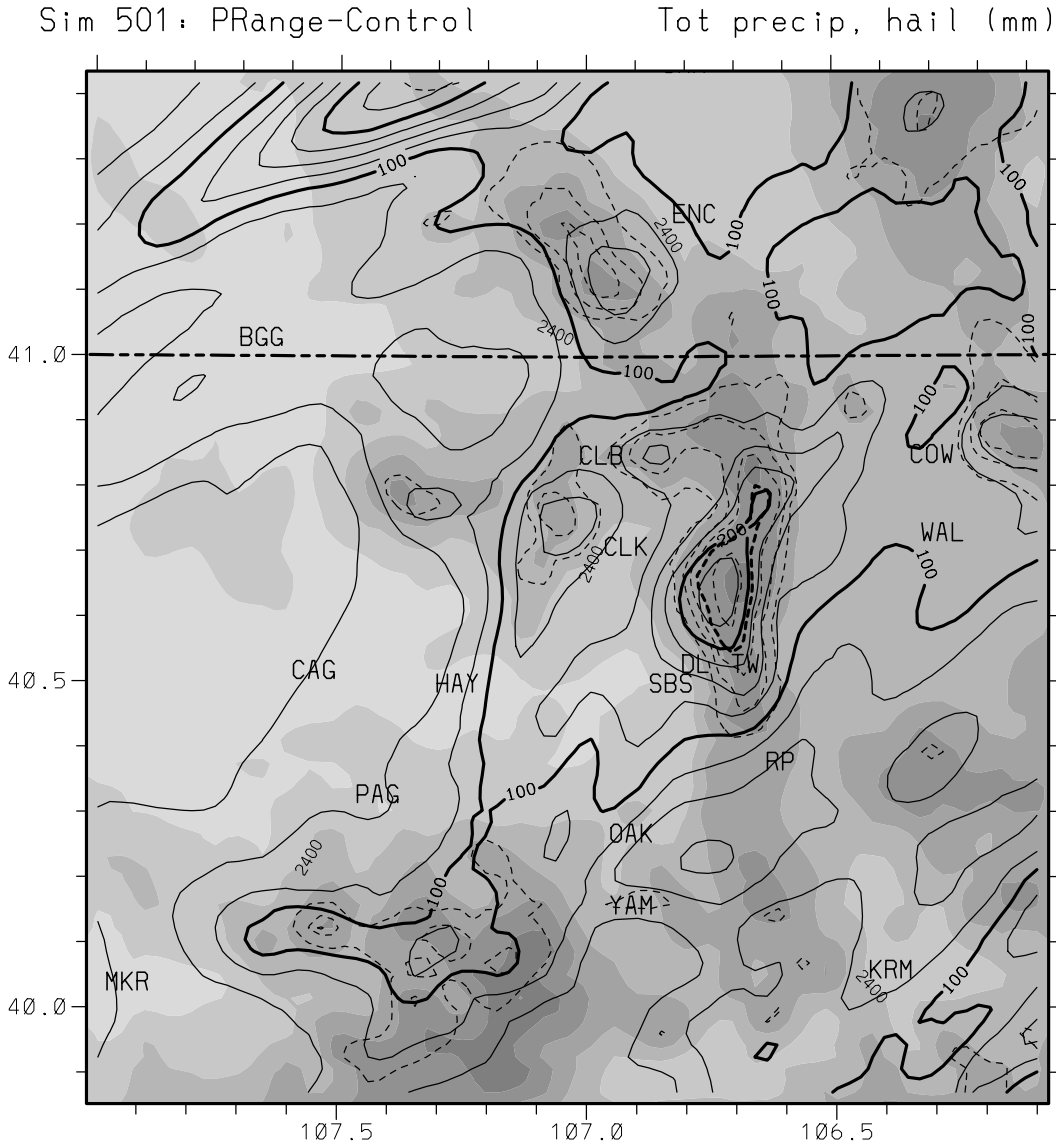


**Figure 44:** Simulated total precipitation and precipitation due to hail on Grid 4 for Simulation 501. Details are as in Fig. 7.

An additional run based on the Park Range event was conducted, identical to the control Simulation 501 except for an imposed moisture perturbation west of  $106^{\circ}$ , wherein RH was increased to 95% up through 500mb. This run, Simulation 502, produced the 6-day precipitation pattern in Fig. 45. The effect of the moisture perturbation was to increase the maximum precipitation to 333mm and to shift it southwestward from the Park Range to the Flat Tops. Maximum precipitation due to hail,

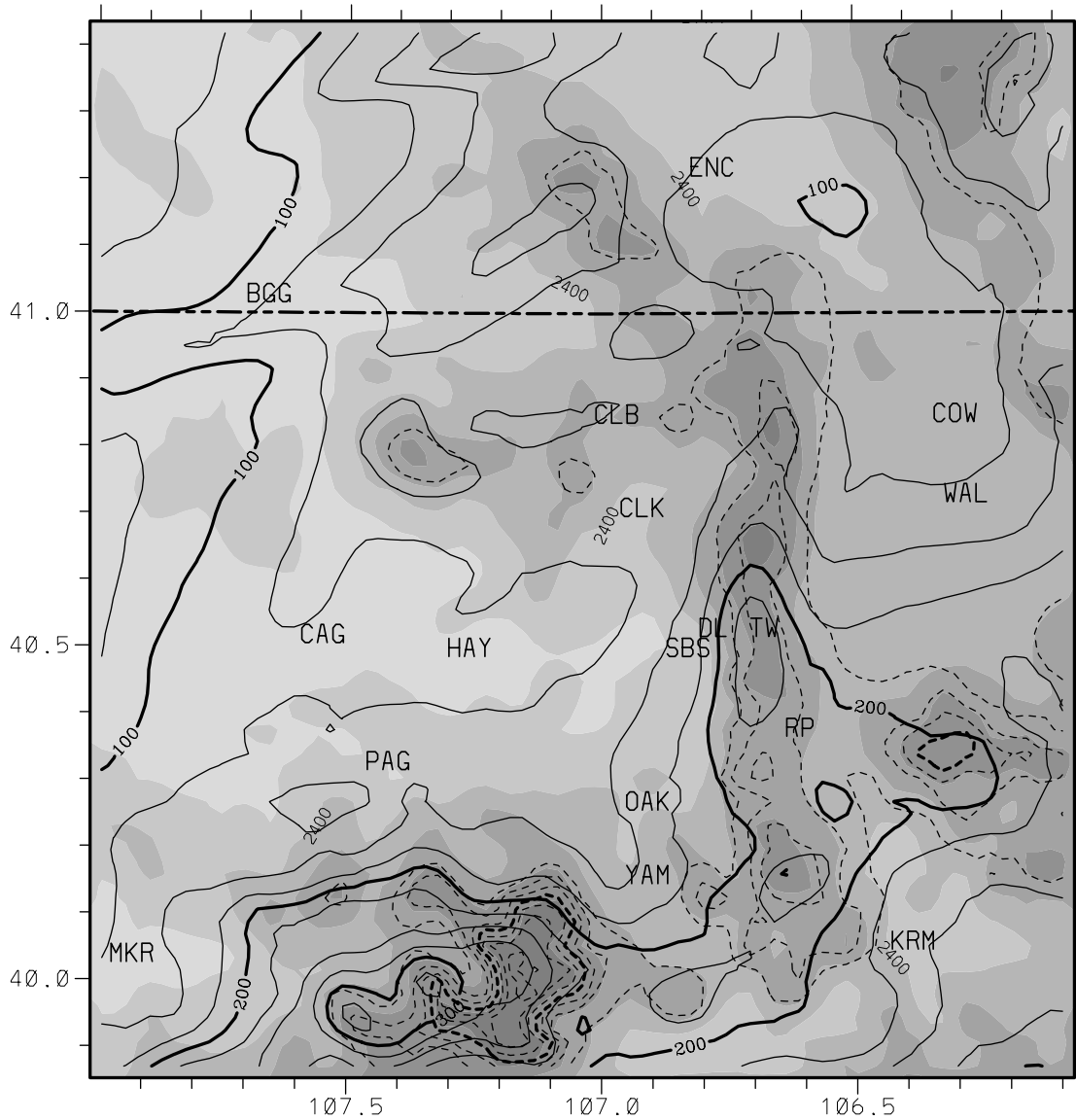


**Figure 45:** Simulated total precipitation and precipitation due to hail on Grid 4 for Simulation 502. Details are as in Fig. 7.

189mm at high elevation in the Flat Tops, was the largest seen in all the runs. A similar shift in maximum precipitation toward the upwind direction of the moisture perturbation, as well as increased production of high-elevation hail, also occurred in the moisture perturbation run for the Dallas Divide case (Figs. 37 and 39).

**4.7 Southwest Colorado/Dove Creek event of 4-6 September 1970**

An extreme precipitation event during 4-6 September 1970 caused extensive flooding over the southwestern U.S. It was a G, Type III event that in Colorado impacted hydroclimatic regions 3 (Colorado Plateau) and 5 (Southwest Mountains). Like most

Type III events, it was a transition-season, multi-day storm associated with a synoptic wave entering the western United States. From 3-5 September 1970, a wave initially in the polar jet flow off the British Columbia coast dug southeastward over the Great Basin, splitting off from the jet that remained further north. The closed system slowly moved eastward for another day, then lifted out rapidly toward the northeast on 7 September. Figure 46 shows the RAMS 36h forecast at 500mb on Grid 1 about midway through this period, at 1200 UTC 5 September 1970. A key aspect of this event was the presence of the westward moving Tropical Storm Norma, which at the beginning of the period was located at about 20N, 115W. A rich southerly flow of moisture emanated from the tropical system and entered the southwestern U.S. just as the baroclinic system dug into the Great Basin, as indicated by the high RH over the southwest in Figs. 46-47. The result was devastating rain from 4-6 September in Arizona, extreme southeastern Utah, and southwestern Colorado [Fig. 48; this and other observational data discussed below are taken from a compilation of reports and data in a case-study file from the Colorado Climate Center (Doesken, personal communication)].

In the control simulation for this event, we used only NCEP reanalysis data at 6h intervals for initialization and nudging files. The simulation was initialized at 0000 UTC 4 September and ran 72h to 0000 UTC on the 7th. In order to simulate the large areal extent and extended duration of this General storm event, the 3km finest grid used here is larger and coarser than the respective 1.67km and 2.0km fine grids used in the LC and GLC events. Although embedded convection was present in the system, precipitation was primarily orographic (at least over the mountains); thus there is less need for as fine a grid in these type of events than for LC and GLC events. In order to see if the overall large-scale evolution was reasonable, our first experiment was with only the coarsest 2 grids, with the parent grid larger and extending much further west and north than in Fig. 46. However, as with the Park Range event, the system did not dig southward sufficiently and cut off over the Great Basin, but propagated eastward too fast as an open wave. Since the wave initially straddled the northern boundary of the parent grid on the British Columbia coast, we thought that the lack of baroclinic development might have been due to inadequate boundary conditions that poorly introduced the wave fully into the domain. Our second attempt was to expand the northern and western boundaries of the parent grid by several degrees, hoping that the initial wave's full inclusion in the domain would result in more accurate development. However, the same under-development problems occurred, suggesting that the problem may lie in inadequate spatial resolution in the 2.5x2.5-degree NCEP reanalysis data.

Therefore we pulled in the Grid 1 western and northern boundaries closer to the Great Basin, in an attempt to introduce the cut-off system directly into that region through the lateral boundary conditions rather than through modeled physical evolution. A 2-grid run showed that this strategy worked well, so the full 4-grid control simulation

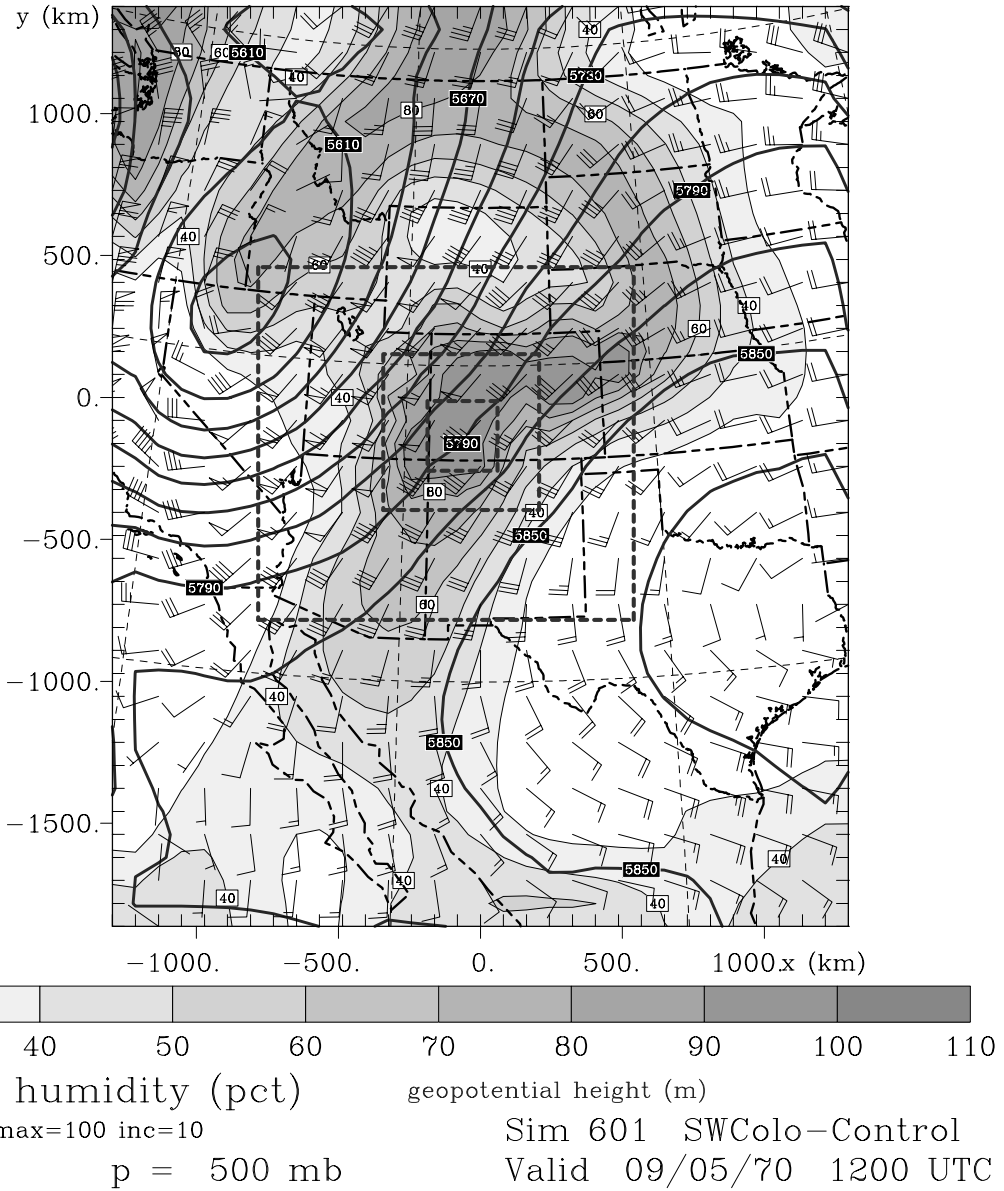


**Figure 46:** Figure 46. Simulated conditions at 500mb on Grid 1 in RAMS Simulation 601 (Southwest Colorado control run), valid 36h into the run at 1200 UTC 5 September 1970. Details are as in Fig. 4.

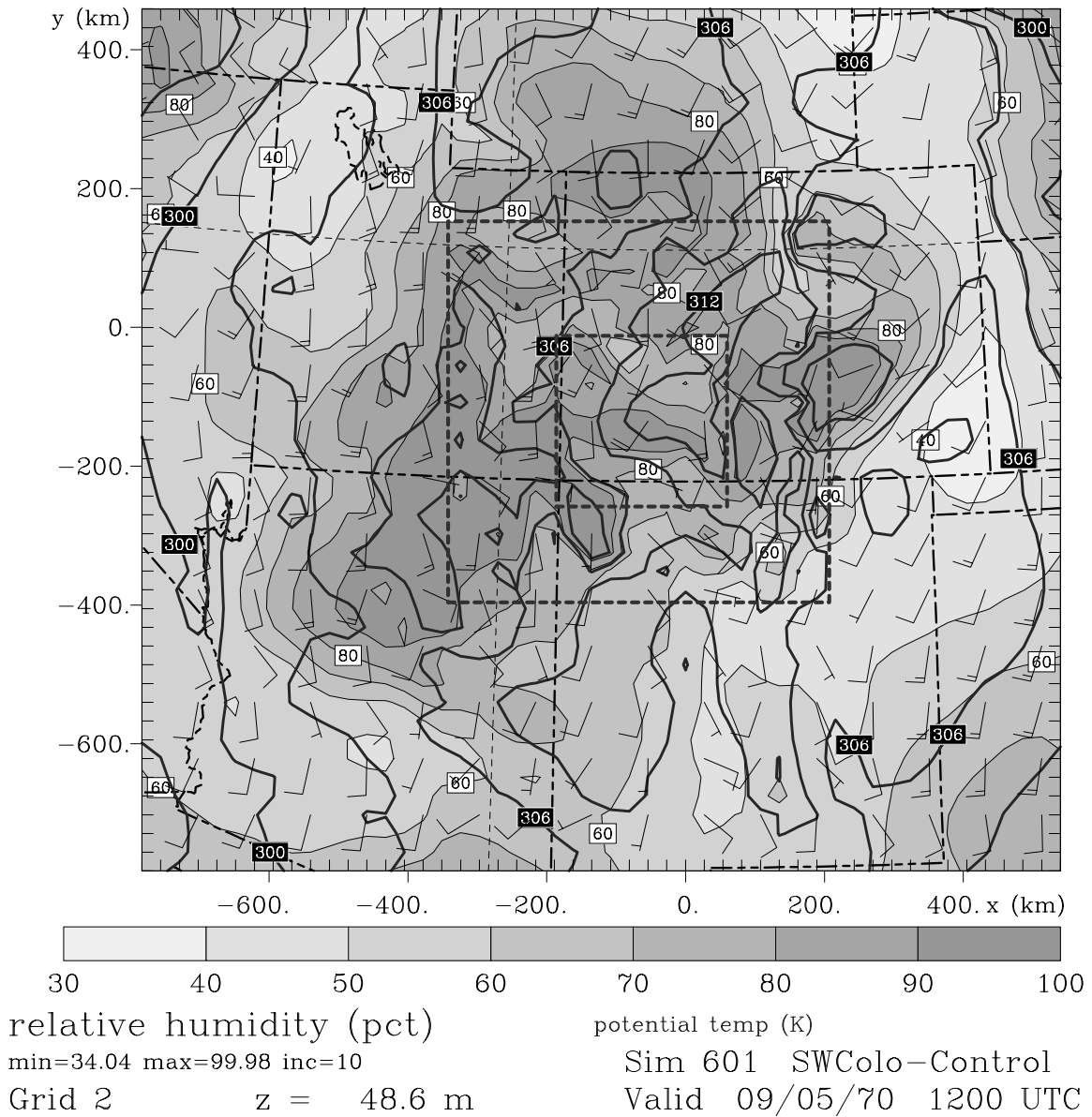


**Figure 47:** Simulated conditions at surface on Grid 2 in Simulation 601 (Southwest Colorado control run), valid 36h into the run at 1200 UTC 5 September 1970. Details are as in Fig. 4.

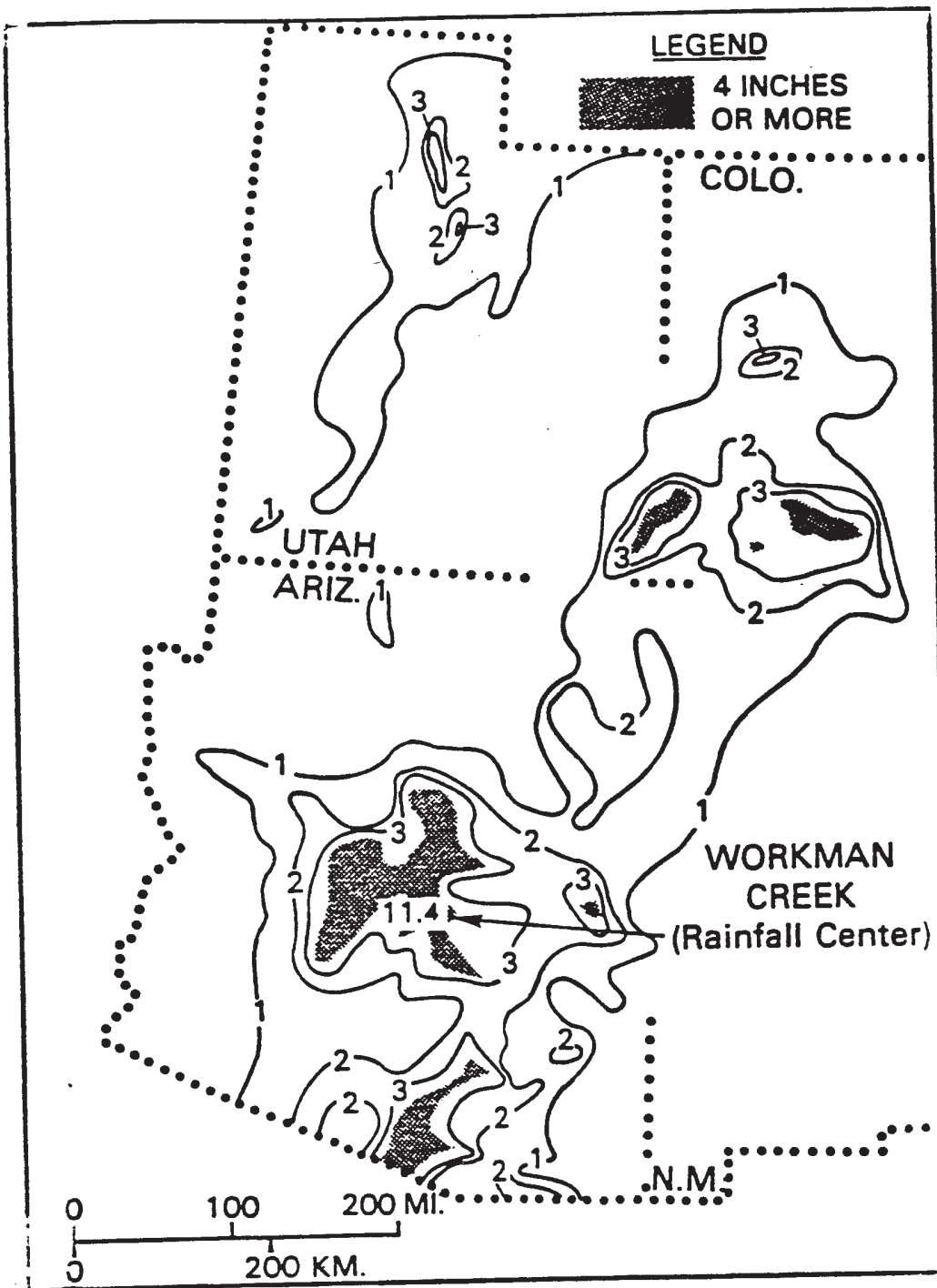


**Figure 48:** Generalized isohyetal pattern over the southwestern U.S. on 4-7 September 1970. Isohyets of 1, 2, 3 and 4" are indicated. Reproduced from case study materials on file at the Colorado Climate Center.

utilized this smaller parent grid. This grid configuration for Simulation 601 is shown in Figs. 46-47.

Simulation 601's total 3-day precipitation on Grid 2 is shown in Fig. 49. In general, the overall pattern in southwestern Colorado, which is covered by the 9km Grid 3, agrees well with the analysis in Fig. 48, although simulated precipitation exceeds the observed by about 50%. The maxima observed in central and southern Arizona and north-central Utah, on the other hand, were outside Grid 3 and were not simulated well on the 27km Grid 2.

A finer-scale observational analysis of the southwestern Colorado total precipitation (5-6 September) pattern is shown in Fig. 50. Two maxima occurred, a broad one exceeding 4" near the top of the southern-facing slopes of the San Juan mountains north of Durango and Pagosa Springs, and a smaller but more intense maximum >6" near Dove Creek on the Colorado/Utah border. A common 2" isohyet with an area of about 20,000 km<sup>2</sup> envelopes both maxima, while the 1" isohyet covers the southwestern 75% of the indicated Grid 4 domain.

Total 3-day precipitation simulated on Grid 4 is shown in Fig. 51. The swath of heavy precipitation exceeding 125mm (5") from northeast of Durango (DRG) to Wolf Creek Pass (WP), with local maxima exceeding 200mm, matches the observed eastern maximum in Fig. 50 quite well. The maximum to the northwest of DRG does not appear in the observational analysis, nor do the heavier patterns further north along the Uncompahgre Plateau and in the West Elk Mountains [to the west and northeast, respectively, of Montrose (MTR)]. However, observations of >3.5" during this period on Grand Mesa, just north of the Grid 4 domain, along with a general lack of observations in elevated terrain, suggest that the 2-day analysis in Fig. 50 may under-represent the episode total (e.g., the 1" and 2" isohyets in Fig. 49 extend further north from the San Juans than in Fig. 50). The primary discrepancy in the simulation is the absence of heavy precipitation in the lower-elevation region around Dove Creek. This region is very close to the western boundary of Grid 4, and the observed maximum was most likely dominated by convection. Thus the 3km grid spacing, combined with a lack of any well-resolved convection on Grid 3 (9km grid) that might have propagated onto Grid 4 in this region, makes an accurate simulation of this maximum very difficult using this grid configuration.

A significant portion of the heavy precipitation simulated over the San Juans occurred as frozen precipitation, primarily hail. The total 3-day precipitation due to hail in Fig. 51 shows a band of high-elevation accumulations of up to 50-75mm liquid equivalent along the southern facing upper reaches of the San Juans. Maximum hail was 95mm at an elevation of 3566m. Maximum 3-day rain accumulation was 150-175mm along a lower-elevation axis at about 2800-3000m. Thus the largest rain accumulation is 25-50mm less, and 200-400m lower in elevation, than in the total precipitation pattern in

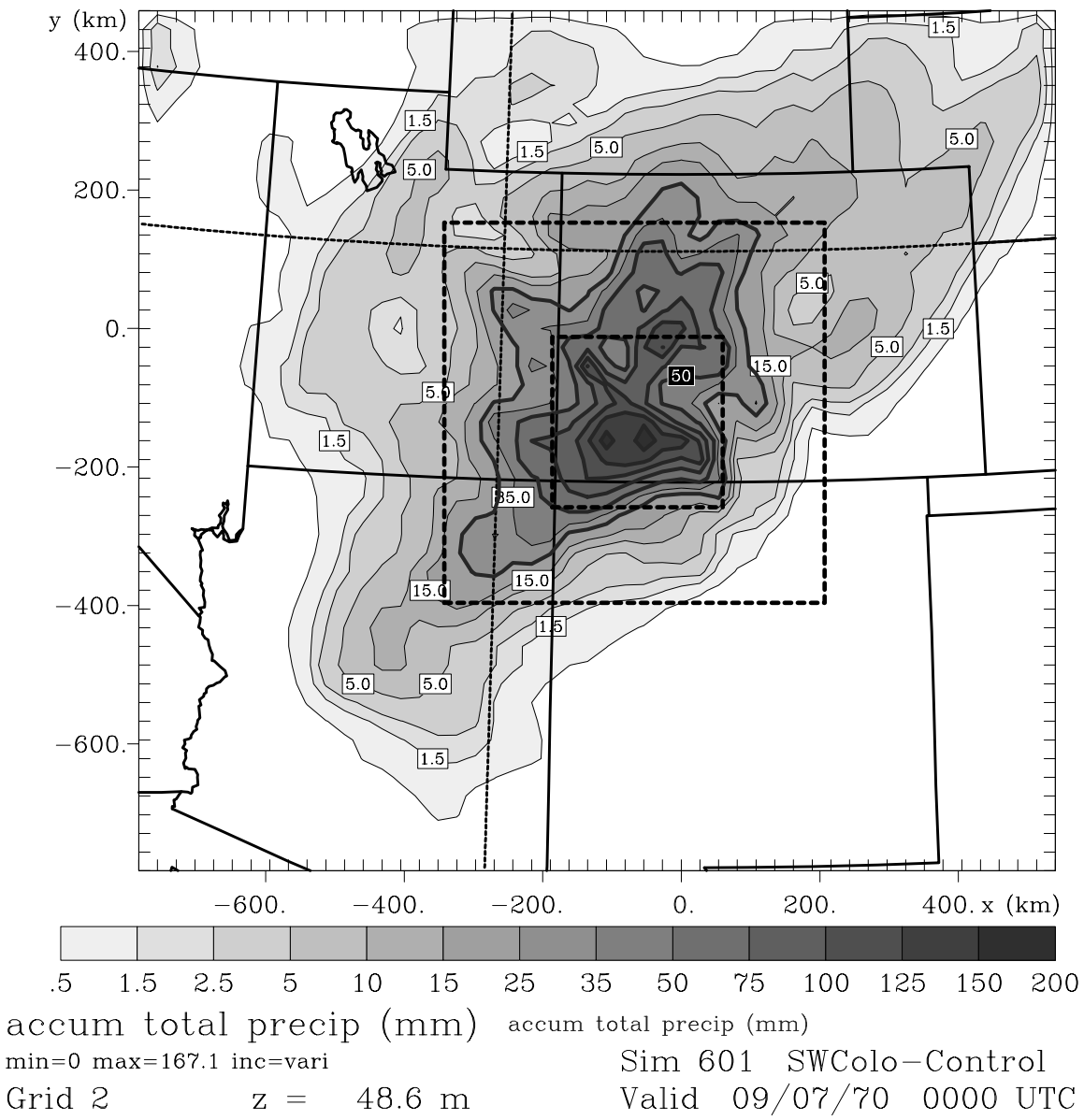


**Figure 49:** Simulated 72h total precipitation accumulation on Grid 2 for Simulation 601. Isohyets are contoured and shaded at variable intervals; those at 25mm (about 1") increments are highlighted with bold contours. Locations of nested Grids 3-4 are shown by dashed boxes.

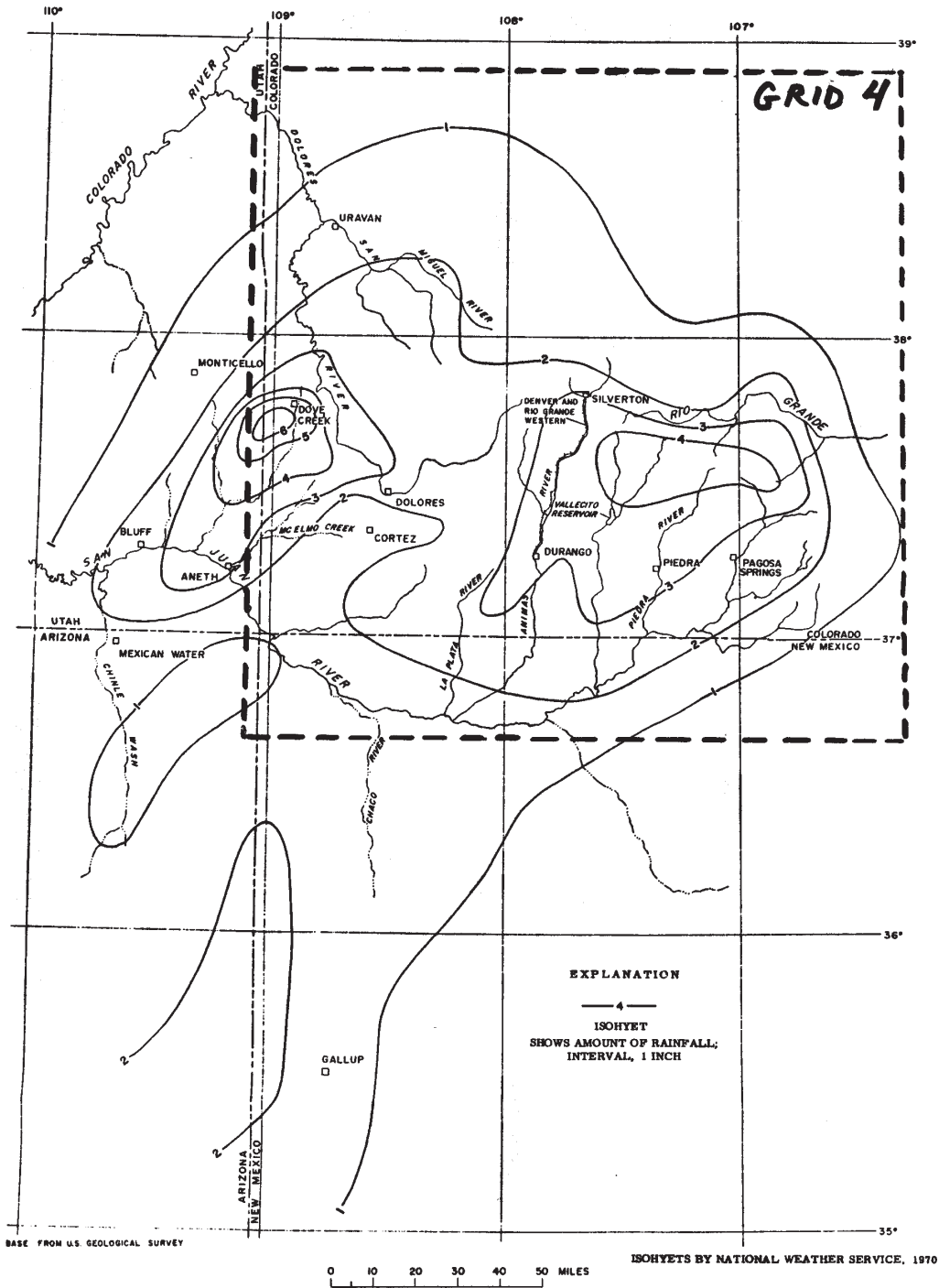


**Figure 50:** Rainfall analysis over Four Corners region for 5-6 September 1970. Isohyets are for integral inches up to 6". Reproduced from case study materials on file at the Colorado Climate Center. Dashed square indicates Grid 4 domain.



The time distribution of the modeled precipitation appears to be in good agreement with observations. In Fig. 52 are observed time series available in the case study file, including those identified as Piedre River (marked as PR to the west of Pagosa Springs (PGS) in Fig. 51), Dyke, Colorado (marked DYK, very close to PR) and Lemon

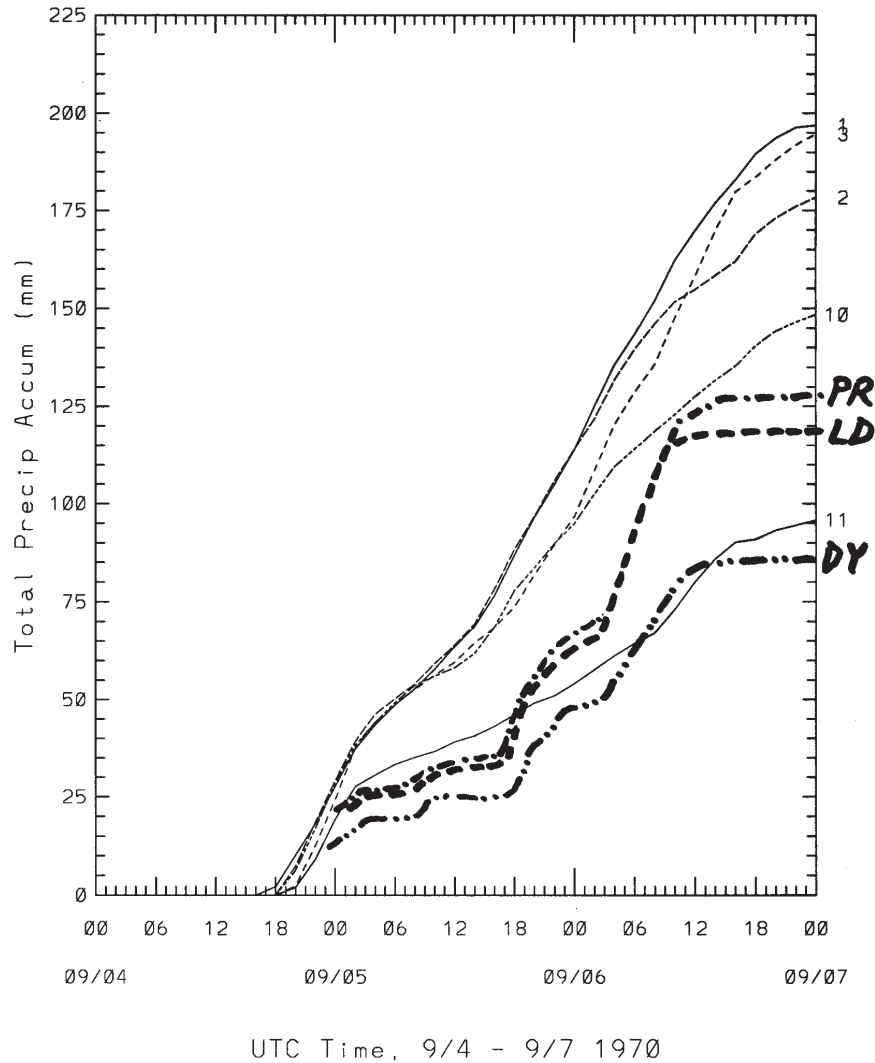


**Figure 52:** Time series of accumulated precipitation over 4-6 September 1970. Heavy curves are observed time series at Piedre River (PR; refer to Fig. 51 for locations), Dyke, Colorado (DY), and Lemon Dam (LD), reproduced from case study materials on file at the Colorado Climate Center. Thin curves are simulated time series of total precipitation at selected gridpoints from Grid 4. Curves 10 and 11 are at Lemon Dam (LD) and Piedre River (PR), respectively. Curves 1-3 are at local maxima in 72h total rainfall, to the northwest of Durango (DRG), to the northeast of DRG, and to the north of Pagosa Springs (PGS), respectively (refer to Fig. 51).

Dam (LD, northeast of Durango (DRG)). Time series of simulated total precipitation accumulation at selected grid points from Grid 4 are also indicated: curves 10 and 11 are at grid points at the Lemon Dam and Piedre River sites in Fig. 51, allowing direct comparison with the observed curves at LD and PR (and DY). Curves 1-3 are taken at the maximum rain totals in Fig. 51 in the elevated terrain to the northwest of Durango (DRG), to the northeast of DRG, and to the north of PGS, respectively.

The observed curves indicate three primary heavy raining periods: an initial period late on 4 September (these are coincident with the model curves and aren't drawn), another beginning about 1800 UTC on the 5th and the final period beginning around 0200 UTC on the 6th. The model curves show the initial phase, but tend to be steadier, and less intense and episodic, through the final two observed phases. Nevertheless, the trends and totals for curves 10 and 11 (100-150") are in reasonable agreement with the observed curves at LD, PR and DY. They are also consistent with 3-day totals of 5.25" (133mm) observed 6 miles SSE of Palisade Lakes (marked PL in Fig. 51) and 5.72" (145mm) at Wolf Creek Pass (WP).

Curves 1-3, for the elevated rain maxima of 175-200mm (7-8"), are all at elevations of about 2800-2950m (9200-9700'). These totals include less than 5mm (0.2") of hail liquid water equivalent. The closely corresponding hail maxima in Fig. 51 are within 2-3 gridpoints (<9km) of the rain maxima, and about 200-600m higher in elevation. Total precipitation at the hail maxima locations consisted of 100-125mm rain and 75-100mm of hail liquid equivalent. The corresponding total precipitation maxima in Fig. 51 are located about midway between the rain and hail maxima, and consist of about 125-175mm rain and 25-75mm hail. A number of observation logs indicate frozen precipitation during this event, although there is insufficient data for determining fractions of rain vs. frozen precipitation. Nevertheless, there is evidence of mixed precipitation, and the RAMS model offers valuable guidance on the relative fractions as a function of elevation.

## **5. Implications to Altitude Dependence on Extreme Precipitation in Colorado**

The results of the simulations that were described individually in Section 4 are discussed collectively in this section in order to highlight general characteristics of the modeled extreme precipitation and how it varies with region and elevation over Colorado. We believe that these modeled characteristics generally apply to actual extreme precipitation in Colorado and shed light on PMP estimation and the assessment of high elevation flood potential.

Much of this discussion concerns the partitioning of simulated total precipitation between rain and frozen precipitation. In particular, the simulated precipitation maxima in extreme events consist almost entirely of rain at lower elevations, while the maxima at higher elevations may include a substantial fraction due to frozen precipitation. The implicit assumption is that frozen precipitation in the high altitude events will melt gradually and thus will not contribute significantly to rapid runoff and flash flooding. It must be emphasized that this partitioning is sensitive to the mean diameter and other

constants (e.g., cloud condensation nuclei concentration and size distribution shape parameter) chosen for each hydrometeor habit in the one-moment bulk microphysical parameterization. These selections also affect simulated processes such as sub-cloud evaporation and storm propagation, and thus the total amount of precipitation reaching the ground and its distribution as well as the rain/ice partitioning (e.g., van den Heever 2001). Because these microphysical settings were unchanged in all simulations described in this report, these sensitivities have not been explored in the context of these extreme precipitation events. Despite some sensitivity to these parameters, we expect that the general transition from all rain at lower elevations to substantial frozen precipitation at higher altitudes is a robust result of this research.

In this discussion, the difference between simulated total precipitation and rain is regarded as being solely due to the hail hydrometeor category, with contributions from other frozen categories (graupel, aggregates, snow and pristine ice) considered negligible. This is a very accurate generalization for all of the LC simulations (series 100-400), where frozen precipitation (consisting of hail and graupel only in these runs) accounts for up to 17.8% of areally-integrated total accumulated precipitation on Grid 4, but with hail accounting for over 99% of the frozen precipitation in each simulation. In the G and GLC simulations (series 500-600), frozen precipitation (all categories) is more extensive in high elevations and accounts for up to 13.8% of areally-integrated total precipitation, but hail still accounts for at least 84.4% of the frozen precipitation in each simulation.

### ***5.1 Simulation maxima of total precipitation, rain and hail***

The gridpoint-maximum precipitation produced on the cloud-resolving Grid 4, along with its elevation, was discussed for each simulation in the previous section. Table 5 lists that information, along with the gridpoint-maximum precipitation due to rain and hail and their elevations. The geographic location of these maxima can generally be found (or inferred for the rain maxima) from the previous total precipitation and hail distribution plots in Section 4. Also in Table 5 are the duration that Grid 4 was active and the mean total precipitation on Grid 4 for each simulation.

The maximum precipitation by type (total, rain, hail) vs. elevation from Table 5 is shown graphically for each simulation in Figs. 53-55. The ensemble members based on the Big Thompson event (simulation series 100) are shown in Fig. 53, while all the Fort Collins-based members (series 200) are in Fig. 54. Ensemble members for series 300-600, all based on events that occurred west of the Front Range and Eastern Foothills hydroclimatic region, are collectively shown in Fig. 55.

For each Big Thompson ensemble member (Fig. 53), the hail maximum occurs at a high elevation above 3300m (along the crest of the Front Range in Figs. 7-14), and a larger rain maximum occurs at a lower elevation. The rain maxima occur anywhere from only a few hundred meters below the hail maxima (highest is 3210m in simulation 106) to as low as 1863m, but can all be considered to be in the foothills or mountains and away from the lower elevation plains. In all but simulation 106, the rain and hail maxima

are produced by distinctly different convective storms. In some simulations, the total precipitation maximum is co-located (or nearly so) with the lower elevation rain

**Table 5.** Selected results for simulations.

Storm Event	Sim #	Grid 4 Duration (h)	Mean Precip (mm)	Max Precip (mm)	Elev. (m)	Max Rain (mm)	Elev. (m)	Max Hail (mm)	Elev. (m)
<b>Big Thompson</b>	101	23.5	33.9	292.8	1863	292.7	1863	68.6	3645
	102	22.0	46.8	176.8	3215	176.4	2102	70.4	3686
	103	24.0	44.6	200.8	2111	200.6	2111	63.1	3453
	104	23.0	23.1	150.7	1998	150.6	1998	43.5	3364
	105	22.0	42.3	187.3	3592	163.3	2336	96.8	3552
	106	24.0	60.9	246.0	3559	209.3	3210	109.4	3552
	107	23.0	52.7	237.0	2791	234.8	2791	67.6	3756
	108	23.0	53.7	281.8	2671	281.2	2671	121.8	3608
<b>Fort Collins</b>	201	22.25	67.6	424.9	1423	424.9	1423	88.1	3527
	202	18.0	57.0	322.0	3210	303.8	3145	90.6	3527
	203	21.0	69.1	402.1	1432	402.1	1432	98.1	3576
	204	21.5	68.4	341.5	1517	341.5	1517	87.8	3527
	205	21.0	66.7	371.1	1806	371.1	1806	84.6	3527
	206	19.5	64.6	290.5	3380	275.6	3380	101.5	3576
	207	24.0	16.6	664.4	1626	664.4	1626	0.7	3644
	208	22.25	37.3	315.4	1495	315.4	1495	26.4	3542
	209	12.0 <sup>1</sup>	16.1	115.3	3133	103.6	1465	93.0	3576
	210	12.0 <sup>1</sup>	25.7	288.1	1835	288.1	1835	61.7	3271
	211	12.0 <sup>1</sup>	39.8	218.0	3101	200.6	1811	114.8	3365
<b>Saguache Creek</b>	301	21.0	12.9	128.6	3585	114.3	3353	84.4	3585
<b>Dallas Creek</b>	401	17.0	5.4	192.5	3783	145.2	2772	168.8	3813
	402	17.0	5.5	184.5	3783	135.2	2772	166.6	3783
	403	18.0	8.8	198.9	3542	99.3	3656	174.6	3542
	404	18.5	38.6	423.2	1571	423.2	1571	62.7	3579
<b>Park Range</b>	501	144.0	81.2	241.9	3252	229.1	2363	140.1	3381
	502	144.0	149.2	333.3	3204	287.7	2838	188.9	3474
<b>SW CO/Dove Cr</b>	601	72.0	77.5	223.5	3405	195.8	2709	94.6	3566

<sup>1</sup>Grid 4 spawned 6h after initialization.

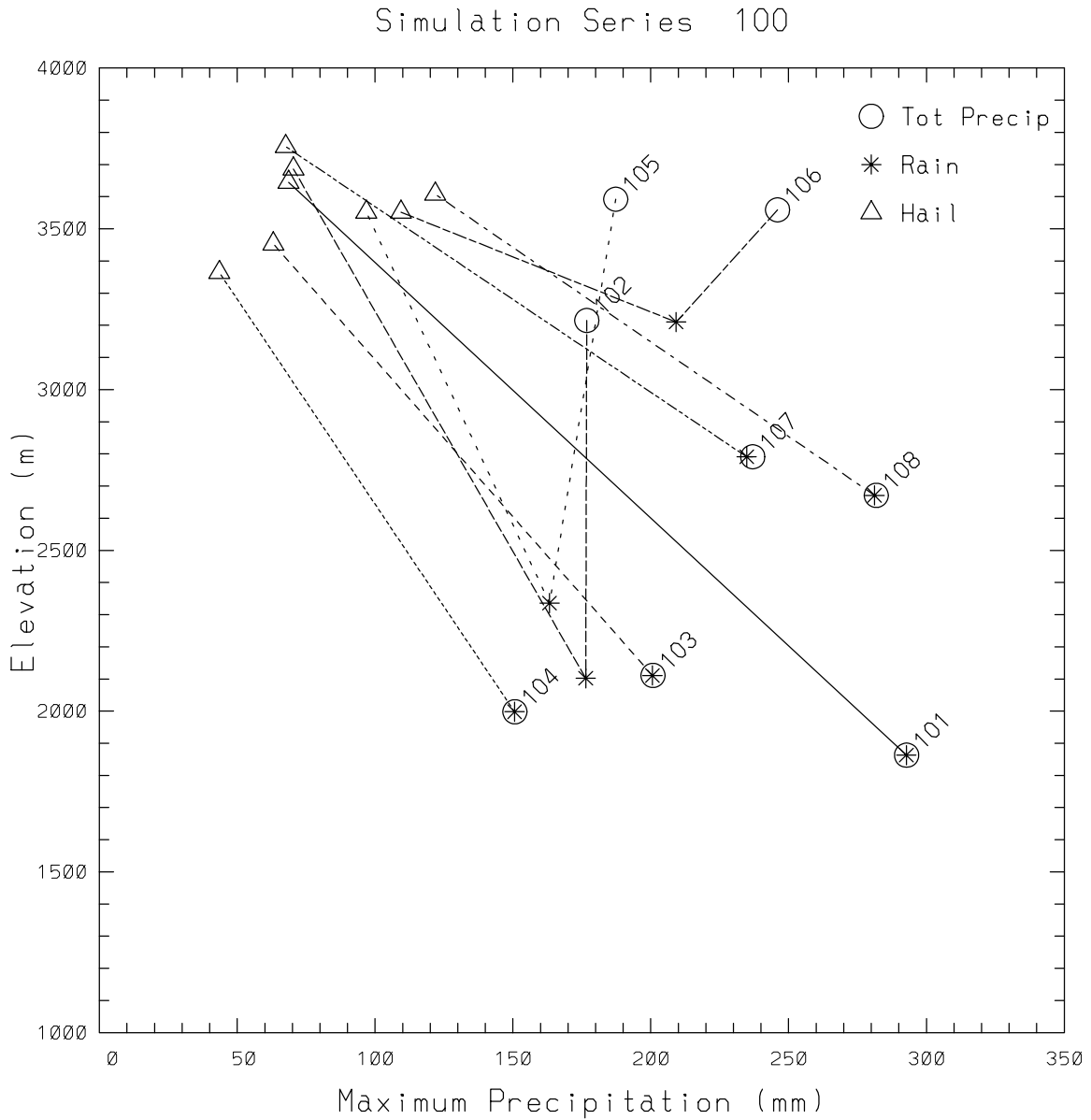


**Figure 53.** Maximum grid-point values of simulated total precipitation (circles), rain (asterisks), and hail (triangles) vs. model elevation in simulation series 100 (based on Big Thompson event). Lines drawn with a given dashed pattern connect maximum precipitation, rain and hail values for a given simulation, labelled by simulation number near its maximum precipitation value.

Simulation Series 200

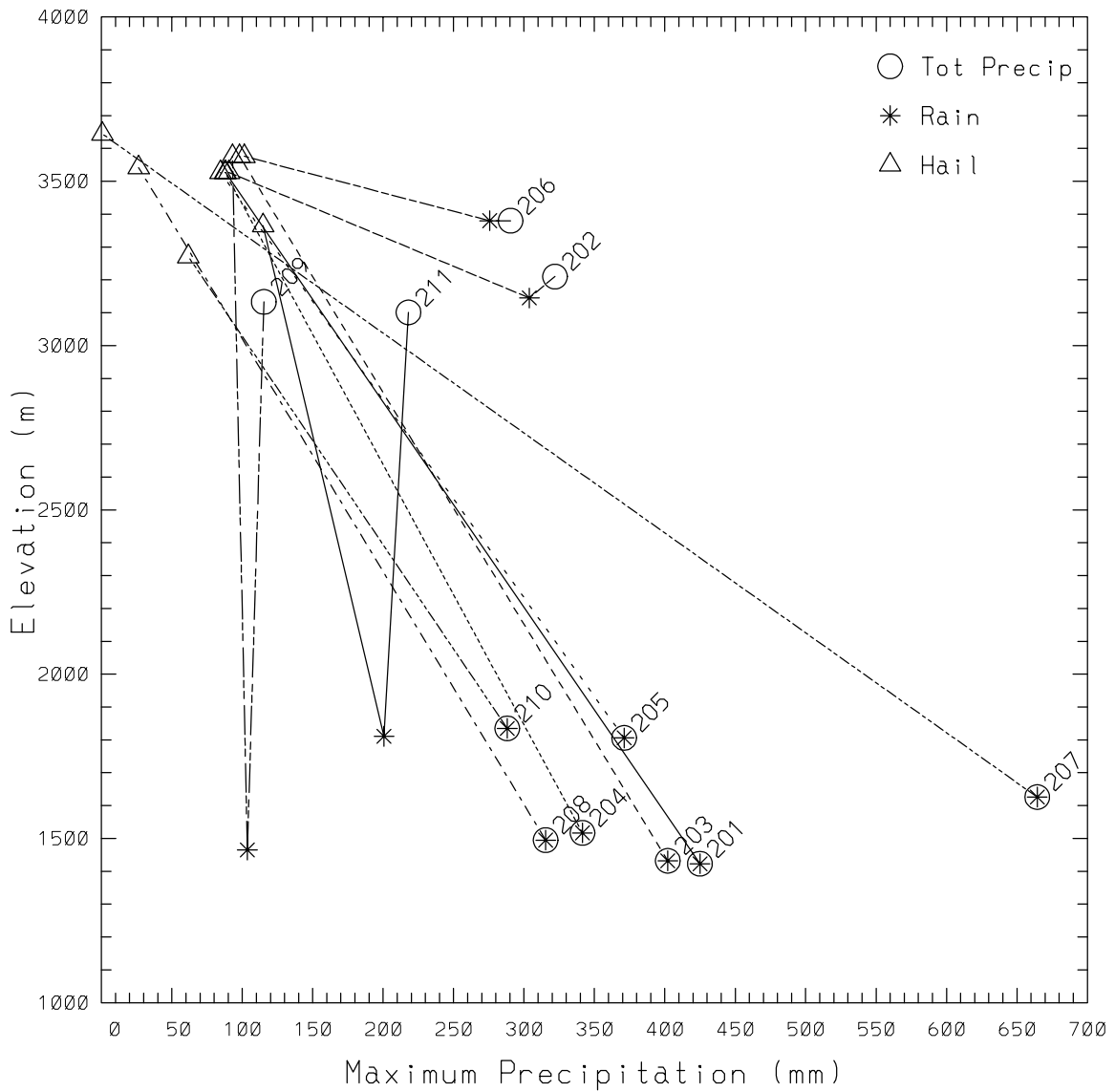


**Figure 54.** Maximum grid-point values of simulated total precipitation, rain, and hail vs. model elevation in simulation series 200 (based on Fort Collins event). Details are as in Fig. 53.

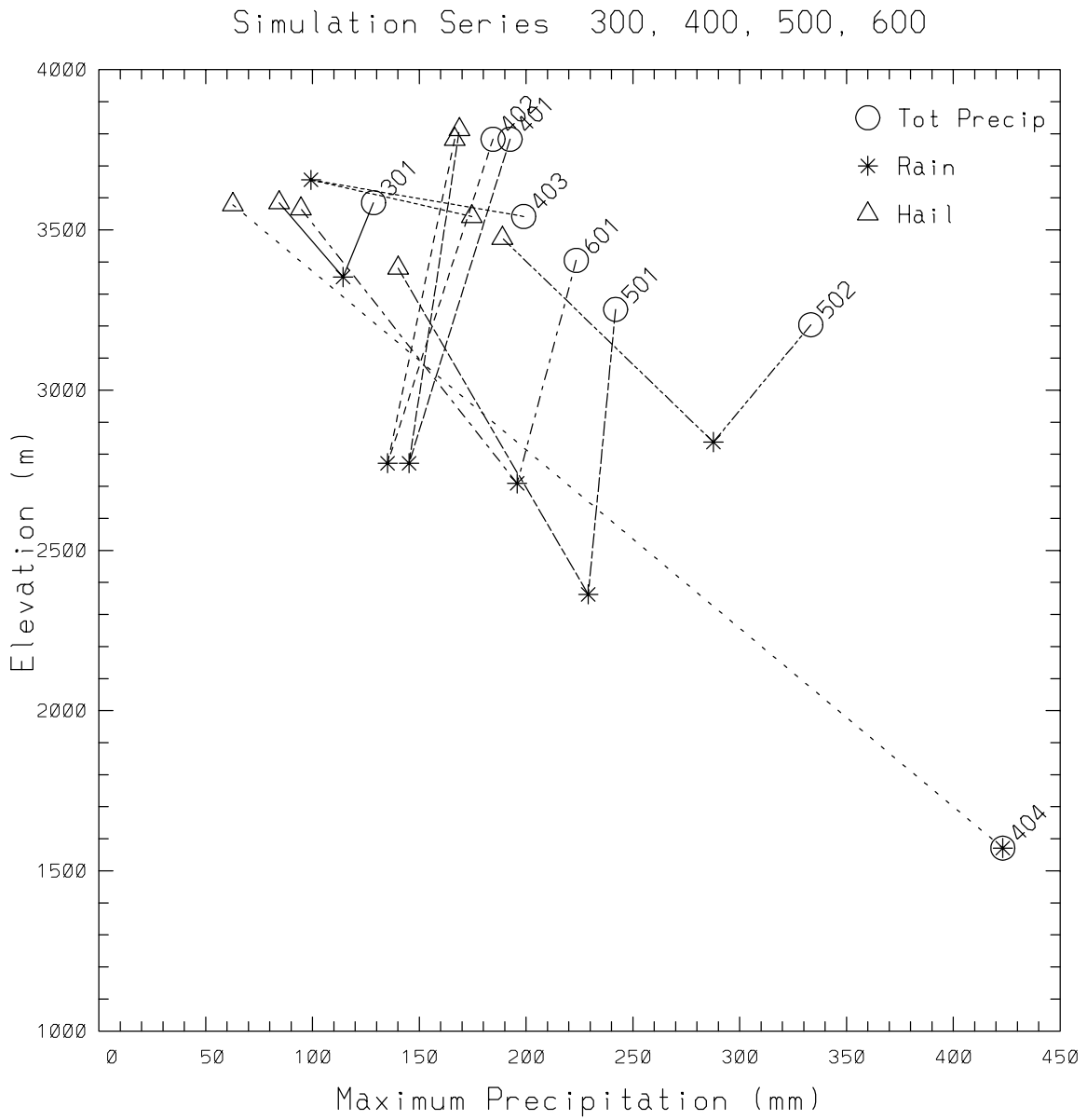


**Figure 55.** Maximum grid-point values of simulated total precipitation, rain, and hail vs. model elevation in simulation series 300, 400, 500 and 600 (based on Saguache Creek, Dallas Creek, Park Range, and southwest Colorado events, respectively). Details are as in Fig. 53.

maximum and consists almost entirely of rain (simulations 101, 103, 104, 107 and 108). In the others, the total precipitation maximum occurs at high elevations (simulations 102, 105 and 106) and includes an appreciable fraction of hail.

The Fort Collins ensemble members (Fig. 54) similarly all have high elevation hail maxima along the crest of the Front Range (Figs. 18-27), or in the Sangre de Cristos for the transposed simulation 210 (Fig. 29). Seven out of the eleven series 200 simulations have co-located rain and total precipitation maxima at elevations lower than in the series 100 runs and as low as 1423m. This is consistent with the lower-elevation Fort Collins storm occurring at the plains/foothills interface, versus the Big Thompson storm that occurred at intermediate elevations well up the canyon. Simulation 207 produced the largest precipitation maximum (664mm) and also the smallest hail maximum (1mm) of all simulations. Simulations 209 and 211 produced the smallest rain maxima (at lower elevations) of the series 200 runs, and also the smallest total precipitation maxima (at higher elevations). These small maxima are due to the cool initial soil temperature used in those simulations. In simulations 202 and 206, the nearly co-located rain and total precipitation maxima were produced by high elevation storms in the southwestern portion of Grid 4, while the hail maxima were associated with separate storms about 70km further north along the Front Range crest.

In most of the series 100 and 200 ensemble runs, the high elevation hail maximum and lower-elevation rain maximum are produced by different convective storms, and the total precipitation maximum is generally associated with either the high or lower elevation storm activity. The maximum precipitation vs. elevation characteristics for the Saguache Creek and Dallas Creek events are somewhat different in that there are overall fewer storms and significantly less mean precipitation (Table 5) on Grid 4, and the rain, hail and total precipitation maxima are more generally produced by the same convective storm system. In the single simulation of the Saguache Creek event (301), for instance, the total precipitation (129mm) and hail maxima (84mm) were co-located at 3585m in the high-elevation storm in the northern portion of Fig. 33 in the Sawatch Range; thus 66% of the total precipitation maximum was due to hail. Although the absolute rain maximum (114mm) occurred in a different high elevation storm in the southwestern portion of Grid 4 in Fig. 33, the local rain maximum in the northern storm was almost as large (100mm) and occurred on the eastern Sawatch slope at an elevation of 3000m.

The first two Dallas Creek simulations (401 and 402), which differed only slightly in their initial soil moisture and temperature fields, produced very similar storms high over Mt. Sneffels (Figs. 37, 38). Their total precipitation and hail maxima were essentially co-located near the top of the Mt. Sneffels topography on Grid 4 at about 3800m (Fig. 55), the highest elevation maxima of all the simulations. The rain maxima in these runs occurred about 1000m lower on the leeside (northeastern) slope toward the Uncompahgre River, with smaller local rain maxima (but still exceeding 112mm) on the upwind slope above Telluride at about 3300m. Simulation 403, with a lower tropospheric moisture enhancement, likewise produced co-located precipitation and hail maxima at high elevation further south in the San Juan's (Fig. 39). As in simulations 401 and 402,

local rain maxima occurred in the same storm both upstream and downstream of the precipitation/hail maximum, with the upstream rain maximum occurring 100m higher at 3656m (Fig. 55). This rain maximum of 99mm was the highest elevation rain maximum of all simulations. Simulations 401-403 were also the only ones in which the hail maximum exceeded the rain maximum, due to the high elevations of the storms. Simulation 404, with Grid 4 placed on the eastern slope near Colorado Springs (Fig. 40), was similar to most of the Fort Collins simulations: it had co-located total precipitation and rain maxima at a lower elevation and a high-elevation hail maximum.

The multi-day simulations for the GLC Park Range event (501 and 502) and the G southwestern Colorado event over the San Juan's (601), like the series 300 and 400 simulations for the LC events west of the Front Range and Eastern Foothills hydroclimatic region, produced relatively high elevation precipitation and rain maxima as well as high elevation hail maxima (Fig. 55). Although the absolute rain maxima occurred at lower elevations away from the primary simulated precipitation events in simulations 501 and 601, slightly smaller local rain maxima occurred in the primary events just a few hundred meters lower than the total precipitation and hail maxima.

## ***5.2 Common grid***

In order to facilitate the collective analysis of the simulations, a common grid was established on which precipitation fields from each simulation could be re-mapped and treated with all other simulations. The grid covers all of Colorado west of 104W at 2km grid spacing, only slightly reduced resolution than provided by the 1.67km spacing used in the LC simulations.

One product generated on the common grid is maximum precipitation for a given duration at each grid point produced by all simulations. Output for each simulation was retained at least as frequently as every 2h and usually every 15min. For a given duration then, say 6h, a given simulation has multiple time windows of 6h duration. The precipitation that falls in a given 6h time window at a given point on the common grid can be compared to all other time windows for that simulation, with the maximum 6h amount retained at that point. Each other simulation with its fine grid over that location can similarly be analyzed for maximum 6h precipitation at that point, and if it exceeds the previously retained maximum it becomes the new maximum.

An example of this technique is illustrated in Fig. 56 for a duration of 48h. Since only the Park Range simulations 501 and 502 and the southwest Colorado simulation 601 ran as long as 48h, only those runs contribute to the 48h map. The box over southwestern Colorado is the Grid 4 domain in simulation 601, and the contoured field is the maximum 48h precipitation at each grid point that fell in the 72h simulation. Since most of the simulated precipitation occurred in the last 54h (Fig. 52), the field is only slightly reduced from the full 72h precipitation in Fig. 51. The box in northern Colorado is the Grid 4 domain for simulations 501 and 502, and the contoured field is the maximum 48h precipitation at each point that fell in either 144h simulation.

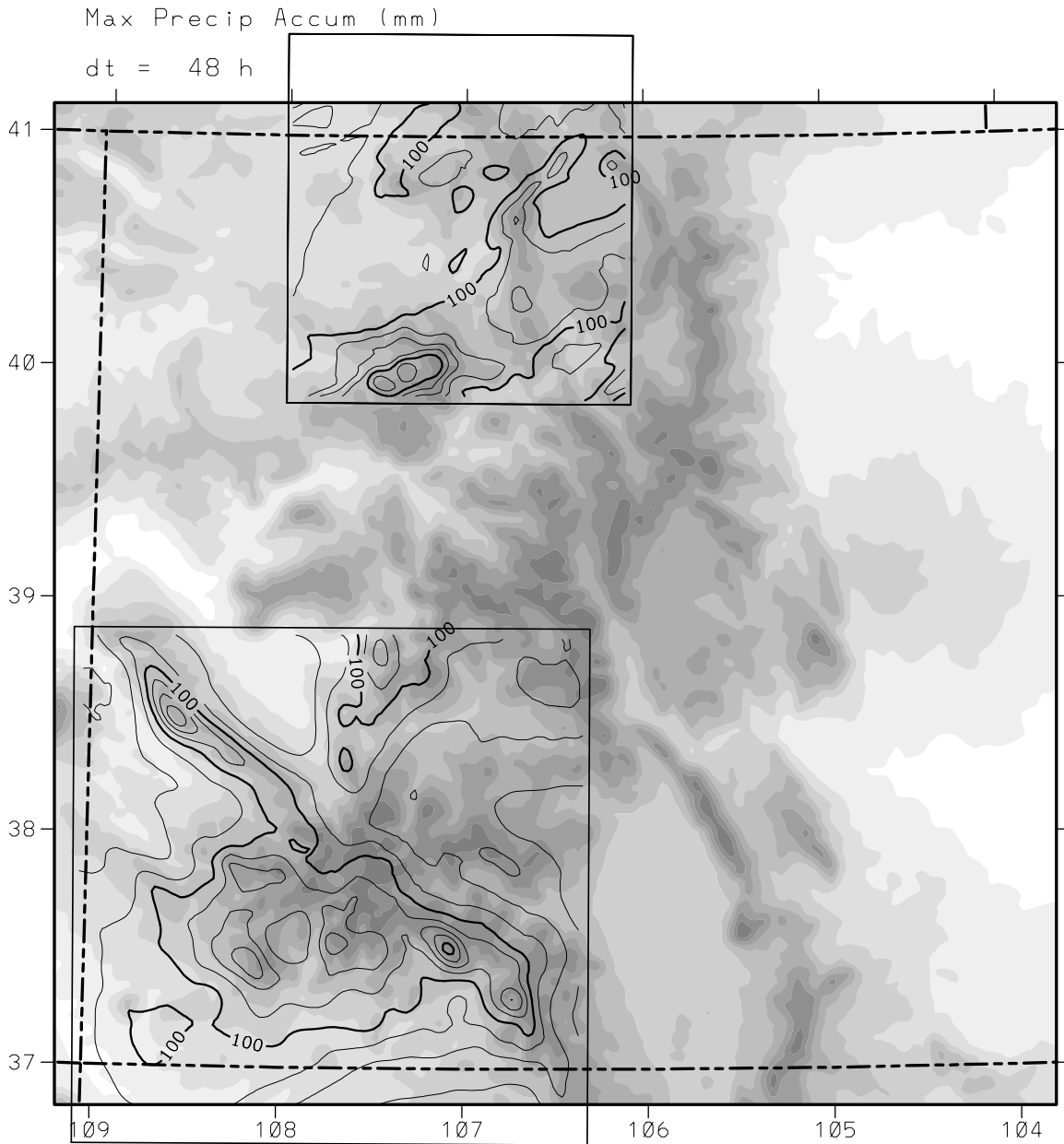


**Figure 56.** Maximum 48h precipitation from Grid 4 for simulations that ran at least 48h (Simulations 501, 502, and 601), mapped onto a common grid covering all of Colorado west of  $104^{\circ}$ . Solid contours are isohyets at 25mm increments beginning at 25mm, with heavy contours for multiples of 100mm. Topography is progressively shaded at 300m intervals.

The maximum 6h precipitation map is shown in Fig. 57. Since Grid 4 was active for at least 12h in all simulations, this product represents maximum coverage over Colorado provided by all 27 simulations. The boxes, beginning in southwestern Colorado and proceeding counter clockwise, represent the Grid 4 domains for simulation 601 (as in Fig. 56); the smaller inset domain for the Dallas Creek simulations 401-403; the south-central domain for the Saguache Creek simulation 301; the southeastern domain for the transposed Fort Collins simulation 210; the east-central domain for the Grid 4 placement in simulation 404; the northeastern domain for the Fort Collins simulations 201-209 and 211; the largely overlapping domain (but extending further north and west) for all Big Thompson simulations 101-108; and the northwestern domain for simulations 501 and 502. Many of the features on the common grid can be readily associated with storms seen in the total precipitation plots for the individual simulations, such as the storms in the San Juan Mountains associated with the Dallas Creek events, and the storms seen in the single-simulation domains in the south-central, southeastern, and east-central portions of the common grid. The overlapping domains for the eight Big Thompson and ten Fort Collins simulations in the northeast provide the maximum 6h realization from all storms in those simulations, including the absolute 6h maximum of 644mm from simulation 207.

One can see that the many series 100 and 200 simulations in the northeast provide a large number of extreme precipitation realizations (for LC events) distributed over that area. On the other hand, the single (or a just a few) simulations in the other portions of the common grid provide a very limited picture of extreme precipitation scenarios in those areas, and a significant portion of the common grid was not covered at all by Grid 4 in any of the simulations. Given a very large number of extreme precipitation simulations over all portions of the common grid, and fully utilizing all cases in Table 1, this technique could provide a direct estimate of simulated extreme precipitation at each grid point over the entire area.

Figure 58 presents the maximum grid-point precipitation for various durations on the common grid vs. elevation, averaged over all grid points in 100m elevation bins (thin curves). The 2h and 12h curves maximize at low elevations, reflecting the widespread coverage of storms on the plains in the northeastern Grid 4 domains seen in Fig. 57 and also in the east-central and southeastern domains. These 2h and 12h curves have a minimum through intermediate elevations, due to relatively few heavy convective storms seen at those elevations in the series 300-600 simulations. A secondary maximum at higher elevations is due to the storms along the Front Range crest in the series 100-200 simulations and at high elevations in some of the other runs. The 36h and 72h curves include only the long-duration series 500-600 simulations and reflect the widespread heavy precipitation at intermediate through high elevations in those events. The fraction of the indicated precipitation in each elevation bin due to hail is indicated by the bold curves of the corresponding dash patterns. Beginning at intermediate elevations, the average hail fraction associated with maximum gridpoint precipitation increases sharply to 50-65% at highest elevations.

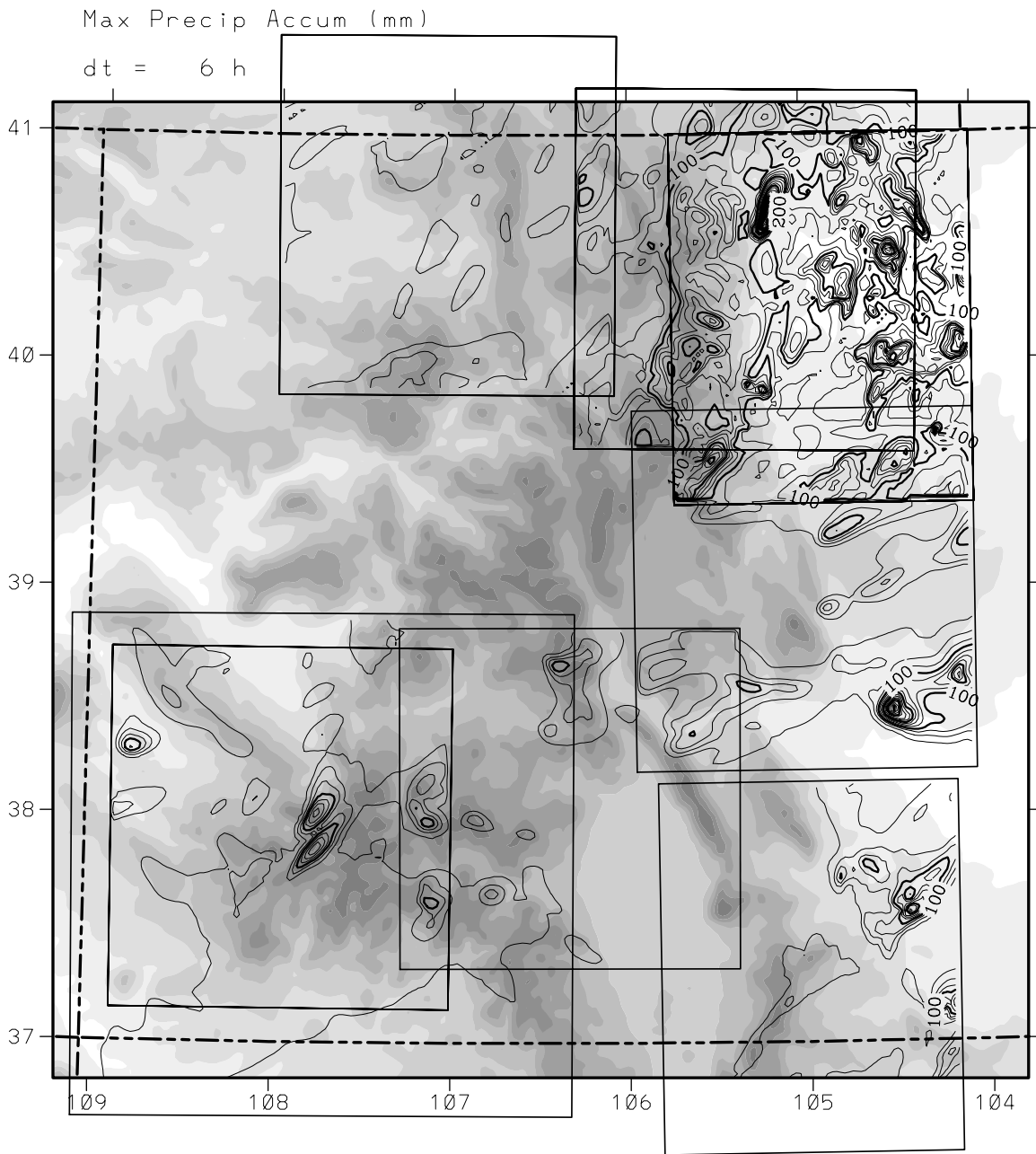


**Figure 57.** Maximum 6h precipitation from Grid 4 for all simulations, mapped onto the common grid. Details are as in Fig. 57.

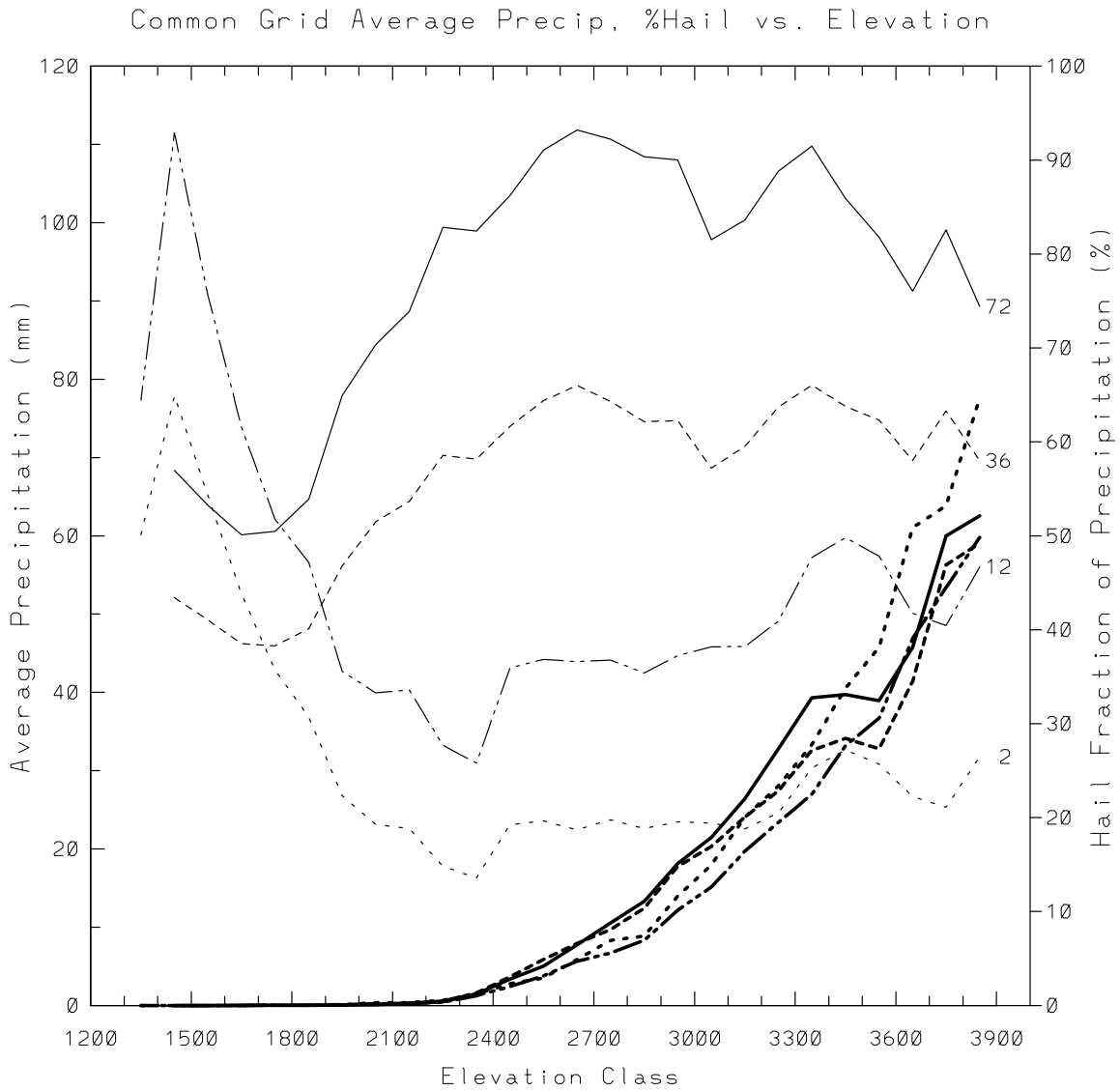


**Figure 58.** Average grid-point values vs. elevation class, of maximum precipitation of various durations from all simulations on the common grid. Thin curves with a given dashed pattern are for durations (h) labeled at the end of the curve. Heavy curves with the same dash patterns are the percent of the plotted average precipitation values that is due to hail for the respective duration. Elevation classes are at 100m increments.

A similar plot appears in Fig. 59, showing the absolute maximum precipitation for a given duration in each elevation class. The 2h and 12h curves are dominated by local maxima produced by storms at various elevations in the series 100-200 simulations, including the most extreme storm in simulation 207 that spanned several lower elevation bins. The 36h and 72h curves show maximum precipitation vs. elevation in simulations 501, 502 and 601, peaking at 3200-3300m. The fraction of these precipitation maxima due to hail is indicated by the bold curves. Below about 2500m, virtually all of the maximum precipitation is rain. From intermediate to high elevations, the fraction of maximum precipitation due to hail increases to 30-40% for the 2h and 12h curves. The hail fraction is larger at intermediate to high elevations for the 36h and 72h curves, peaking at 65-70% at 3400-3500m.

### ***5.3 Identification of depth-area-duration events***

In the next section, an analysis of simulated extreme precipitation events and their application to PMP estimation is based on a set of depth-area-duration (DAD) events with the highest mean depths for various durations and areas from each simulation. The identification and selection of these DAD events is a complicated problem in which several approaches were considered. The precipitation that fell on a given simulation's Grid 4 in each time window of a given duration was the basic starting information. One method of identifying DAD events is to find the mean depth for a given time window within a fixed geometric shape (e.g., circle or square) of a given area of interest, centered on a specific grid point. By examining the mean depths for such areas centered on every grid point for the time window (or centered on a number of local maxima in the field), candidate DAD events could be identified for that time window. However, using an arbitrary shape generally would not maximize the mean depth for that area surrounding a local maximum, whereas the isohyet with the same area that encloses the maximum would more generally have the maximum mean depth possible of any shaped area of that size. Thus we chose an isohyetal approach for identifying DAD events.

In the first step of this process, we used software that was originally developed by Augustine (1985) to measure cold cloud top areas within specified temperature thresholds in infrared satellite imagery. We modified this code to identify and measure areas within specified isohyets in the simulated precipitation field for a given time window. For a given precipitation threshold, the program finds all contiguous areas where all grid points have values equal to or exceeding that threshold. Such an area may be a single grid point, a closed isohyetal area of contiguous grid points, or an unclosed isohyetal area along a border of the grid. For a given threshold, multiple occurrences of such isohyetal areas in a given time window are identified and documented. The documentation included the sum of the grid points (and total area) within the threshold; the grid point maximum in each area along with its latitude, longitude and elevation; average precipitation (mean depth) within the area; and the precipitation-weighted mean latitude, longitude and elevation of the grid points within the area.

For each time window, the maximum grid point value was identified and became the starting isohyet for that field, with an area and depth defined by that single point.

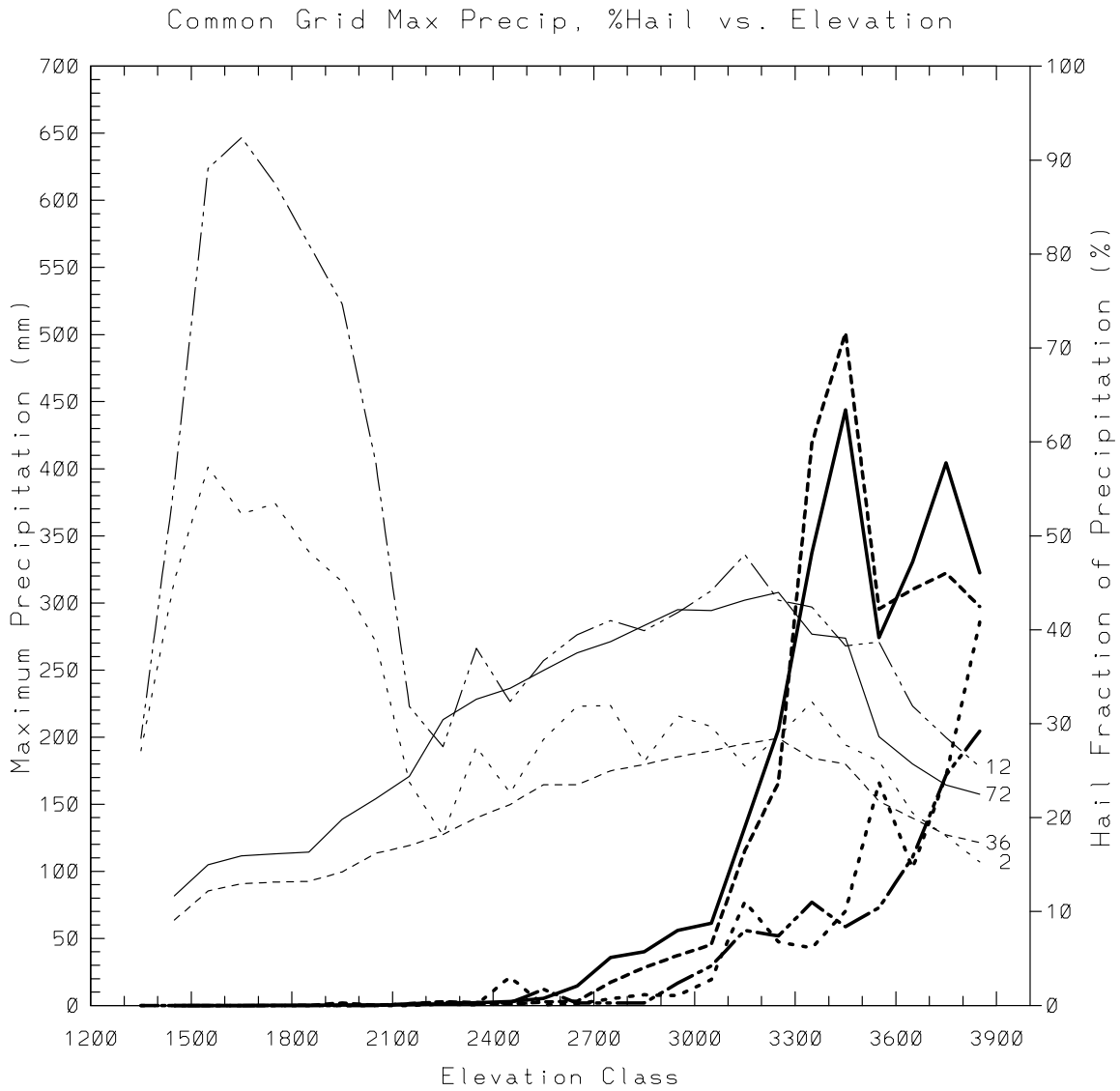


**Figure 59.** Maximum grid-point values vs. elevation class, of maximum precipitation of various durations from all simulations on the common grid (thin curves). Heavy curves are the percent of the plotted maximum precipitation value that is due to hail for the respective duration. Details are as in Fig. 58.

Then the threshold was lowered to the next multiple of 5mm less than the maximum, and subsequently in 5mm increments to a threshold of 0mm. For each lowered threshold, the program documents every isoheytal area in the time window defined by the threshold. These areas are documented in the search order that they are found. The final 0mm threshold documents the mean precipitation for that time window on the entire Grid 4.

The next step was to re-group the documentation for each thresholded area according to common maxima. All isoheytal areas having the same maximum (identified by its location) were re-grouped by descending threshold from the smallest to largest isohyets surrounding that maximum. Thus the absolute maximum has the full range of thresholds for the time window from the maximum value down to 0mm. Other local maxima have their own isoheytal areas from the largest threshold surrounding that maximum to the largest 5mm threshold that has the same maximum. The threshold below that, while defining an isoheytal area still surrounding this same local maximum, would have a greater maximum elsewhere in the field and would be re-grouped with those isohyets. The re-grouped isoheytal information associated with a common maximum is termed an isoheytal event.

The isoheytal events are examined from all available time windows of a given duration, with up to 50 events with the largest maxima retained for each simulation. Criteria were developed to examine whether events from overlapping time windows were actually different time samplings of the same event. For instance, if two 2h isoheytal events were found for 0000-0200 UTC and for 0015-0215 UTC, and they had maxima at about the same location, then it was assumed that they are due to the same precipitation event (or storm), and only the isoheytal event with the largest maximum was retained. In this way, the largest realizations of storm events (based on their maxima) were retained, and over-samplings of slightly lesser realizations of the same events were discarded. We believe that this methodology adequately identifies all significant precipitation "events" of a given duration for each simulation, while also maximizing each event and minimizing their over-sampling.

Finally, from the retained isoheytal records for a given duration, fixed isoheytal areas of 10, 100, 1000, and 10,000 km<sup>2</sup> were identified, if possible, for each event. For each of these given areas, the pair of isohyets (at 5mm increments) larger and smaller than the area of interest was found, and the interpolated isohyet having that area was calculated. In addition, the mean depth and precipitation-weighted mean location and elevation of the interpolated area were also interpolated from the 5mm-increment isoheytal record. These interpolated isohyets and their mean depths define the set of DAD events for given areas and durations.

These DAD events are illustrated in Fig. 60 for a 2h time window from simulation 105. The thin contours are 2h precipitation at 10mm increments, with a field maximum of 119mm west of Longmont (LGM). The heavy contours indicate the 2h DAD events found for this time window. The eleven smallest closed heavy contours are 2h/10km<sup>2</sup> events, including one for the maximum west of LGM and one along the southern border. Surrounding seven of those 10 km<sup>2</sup> events are larger 2h/100 km<sup>2</sup> events. Only a single

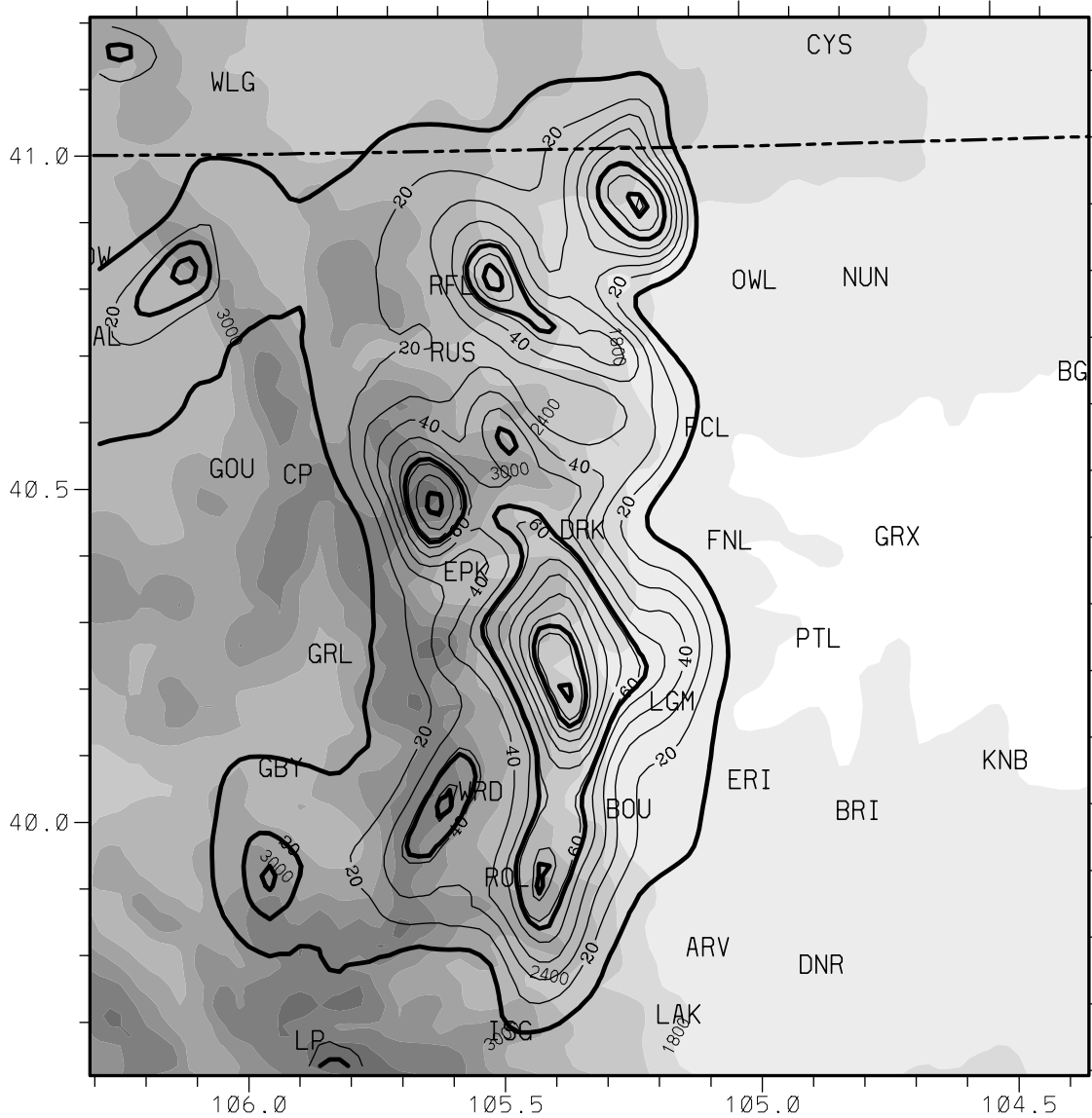


**Figure 60.** Example of depth-area-duration (DAD) events of 2h duration, objectively identified from the simulated total precipitation occurring in a given time window from Simulation 105. Thin contours are isohyets beginning at 10mm and at 10mm increments. Heavy contours are interpolated isohyets of various areas that qualify as among the most significant DAD events for this simulation. The qualifying 2h events include eleven events of 10km<sup>2</sup> (smallest heavily contoured areas), seven events of 100km<sup>2</sup>, a single event of 1000km<sup>2</sup>, and a single event of 10,000km<sup>2</sup>. Other details are as in Fig. 7.

2h/1000 km<sup>2</sup> event, enclosing the field maximum, was retained from this time window, and the largest heavy contour is the only 2h/10,000 km<sup>2</sup> DAD event for this window. The DAD events retained from all simulations form the database for the analysis in Section 6.

To compare how the major DAD characteristics vary with elevation, the five largest DAD events (based on their mean depths) from each simulation were selected for several DAD classes. They were grouped into 300m elevation bins based on their interpolated precipitation-weighted average elevations. The average mean depth in each DAD class is plotted vs. elevation bin in Fig. 61. All three DAD classes have maximum mean depths at lower thresholds, lower mean depths at intermediate elevations, and secondary maxima at a higher elevation. The average fraction of precipitation due to hail in these events (bold curves) varies from negligible below the 1800-2100m elevation bin for all DAD classes, to about 35% at the highest elevation bin that 6h/100km<sup>2</sup> and 12h/1000km<sup>2</sup> events were found, and to 80% at 3600-3900m for the 2h/10km<sup>2</sup> class. Thus, the fraction of precipitation due to hail in the dominant DAD events and its variation with elevation is quite similar to that seen for grid-point maximum precipitation of various durations on the common grid (Figs. 58-59).

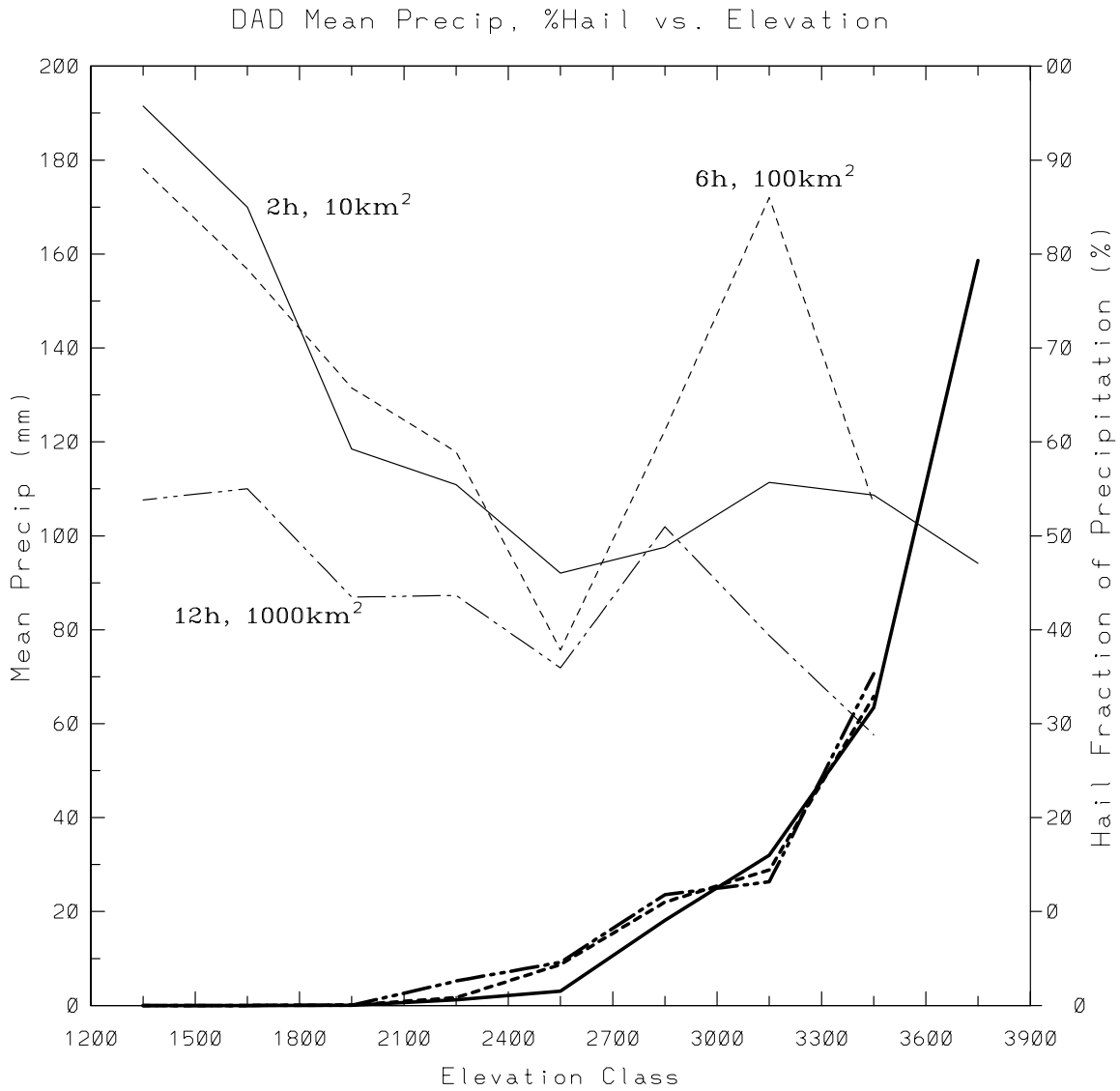


**Figure 61.** Mean precipitation depth vs. elevation class of the five largest qualifying DAD events from all simulations for the various area-duration classes. Thin curves with a given dashed pattern are for the labelled area-duration classes. Heavy curves with the same dash patterns are the percent of the plotted mean precipitation depth that is due to hail for the respective area-duration class. Elevation classes are at 300m increments. Each DAD event is assigned to an elevation class based on the precipitation-weighted mean elevation of the event.

## 6. Mapping Technique

For the purpose of generating continuous maps of point variables derived from those discussed in the previous section, we utilize the geostatistical procedure known as kriging (Wackernagel 1998; Isaaks and Srivastava, 1989). This technique has been used in varying capacities including the estimation of ore-reserve grades from prospective samples (David, 1977), ground-water contamination studies (Cooper and Istok, 1988) and extreme precipitation estimation based on raingauge data (Chang and Sun, 1997). All of the theory presented in this section can be found in most textbooks dealing with multivariate geostatistics. The first two references of this section are excellent resources.

The underlying problem is the estimation of a quantity (e.g. accumulated precipitation, probable maximum precipitation, surface temperature, etc.) at locations where the quantity has not been sampled. In the context of this study, the term "estimate" in the previous sentence is referring to the estimation associated with spatial interpolation or mapping, not the procedure used in converting modeled precipitation to extreme precipitation estimates. The latter estimation problem must be solved at selected points prior to tackling the problem of spatial estimation or mapping. Spatial mapping is the same goal that objective analysis procedures, such as the Barnes or Cressman analysis schemes (Barnes, 1973; Cressman, 1959), attempt to achieve. Unlike these inverse-distance weighted schemes, kriging utilizes a statistical model for estimation and gives some measure of the uncertainty associated with spatial interpolation/extrapolation. This uncertainty is the kriging variance.

In order to simplify the theoretical background discussion, we will first discuss the problem of *ordinary kriging*. We assume that a variable,  $z$ , has been sampled at  $N$  different locations with each sample labeled  $z(\bar{\mathbf{x}}_\alpha)$ , where  $\alpha=1, \dots, N$ , and  $\bar{\mathbf{x}}_\alpha$  is the position vector of sample  $\alpha$ . Each of these samples may be considered to be a realization of a regionalized random variable  $Z(\bar{\mathbf{x}})$ . Here,  $Z$  refers to a spatially varying random function, while  $z$  refers to a realization of this random function (e.g. a mapped precipitation field) and  $z(\bar{\mathbf{x}}_\lambda)$  is the value of this realization at  $\bar{\mathbf{x}}_\lambda$ . We wish to estimate this realized quantity at location  $\bar{\mathbf{x}}_0$ , the estimation point, which in general does not correspond to the locations of any of the samples. This estimate will be denoted  $z^*(\bar{\mathbf{x}}_0)$ , while the true and unknown value will be  $z(\bar{\mathbf{x}}_0)$ . The corresponding random functions are  $Z^*(\bar{\mathbf{x}}_0)$  and  $Z(\bar{\mathbf{x}}_0)$ . The kriging estimator is a linear function of the sample values:

$$z^*(\bar{\mathbf{x}}_0) = \sum_{\alpha=1}^N \omega_\alpha z(\bar{\mathbf{x}}_\alpha), \quad (1)$$

where we also assume that,

$$\sum_{\alpha=1}^N \omega_\alpha = 1. \quad (2)$$

Equation (2) guarantees that the estimate is unbiased, given additional simplifying assumptions to be discussed shortly. The mean square error associated with this estimator is,

$$\begin{aligned}\sigma^2 &= E\left[\left(Z^*(\bar{\mathbf{x}}_0) - Z(\bar{\mathbf{x}}_0)\right)^2\right] = E\left[\left(\sum_{\alpha=1}^N \omega_\alpha Z(\bar{\mathbf{x}}_\alpha) - Z(\bar{\mathbf{x}}_0)\right)^2\right] \\ &= E\left[\left(\sum_{\alpha=1}^N \omega_\alpha Z(\bar{\mathbf{x}}_\alpha) - Z(\bar{\mathbf{x}}_0) \underbrace{\sum_{\alpha=1}^N \omega_\alpha}_{=1 \text{ (Eq.2)}}\right)^2\right]\end{aligned}$$

, where  $E$  is the expectation operator. Hence,

$$\begin{aligned}\sigma^2 &= E\left\{\left[\sum_{\alpha=1}^N \omega_\alpha (Z(\bar{\mathbf{x}}_\alpha) - Z(\bar{\mathbf{x}}_0))\right]^2\right\} = \\ &E\left\{\sum_{\alpha=1}^N \sum_{\beta=1}^N \omega_\alpha \omega_\beta [Z(\bar{\mathbf{x}}_\alpha) - Z(\bar{\mathbf{x}}_0)][Z(\bar{\mathbf{x}}_\beta) - Z(\bar{\mathbf{x}}_0)]\right\} = \\ &\sum_{\alpha=1}^N \sum_{\beta=1}^N \omega_\alpha \omega_\beta E\left\{[Z(\bar{\mathbf{x}}_\alpha) - Z(\bar{\mathbf{x}}_0)][Z(\bar{\mathbf{x}}_\beta) - Z(\bar{\mathbf{x}}_0)]\right\}.\end{aligned}\quad (3)$$

At this point, we define the *increment* associated with two points  $\bar{\mathbf{x}}_1$  and  $\bar{\mathbf{x}}_2$  as,  $I_Z(\bar{\mathbf{x}}_1, \bar{\mathbf{x}}_2) = z(\bar{\mathbf{x}}_1) - z(\bar{\mathbf{x}}_2)$ . A second-order intrinsically stationary regionalized variable is then defined as one which satisfies,

$$\text{A.) } E\left[I_Z(\bar{\mathbf{x}}, \bar{\mathbf{x}} + \bar{\mathbf{h}})\right] = 0 \quad (4)$$

$$\text{B.) } \frac{1}{2} E\left[\left(I_Z(\bar{\mathbf{x}}, \bar{\mathbf{x}} + \bar{\mathbf{h}})\right)^2\right] \equiv \gamma(\bar{\mathbf{h}}), \quad (5)$$

where  $\gamma(\bar{\mathbf{h}})$  is independent of  $\bar{\mathbf{x}}$ .

This is the intrinsic second-order stationarity hypothesis, which allows one to estimate  $\gamma(\bar{\mathbf{h}})$ , called the *variogram*, from the sample data which is scattered in space. The variogram quantifies the expected dissimilarity between data values at varying displacements  $\bar{\mathbf{h}}$ . We now turn to the problem of expressing  $\sigma^2$  in terms of  $\gamma$ . The term in curly braces in the last equation of (3), is simply the covariance of increments and can be rewritten by adding and subtracting  $\frac{1}{2}[Z(\bar{\mathbf{x}}_\alpha)]^2, \frac{1}{2}[Z(\bar{\mathbf{x}}_\beta)]^2$ :

$$[Z(\bar{\mathbf{x}}_\alpha) - Z(\bar{\mathbf{x}}_0)] \cdot [Z(\bar{\mathbf{x}}_\beta) - Z(\bar{\mathbf{x}}_0)] = \frac{1}{2} \left\{ \begin{array}{l} -[Z(\bar{\mathbf{x}}_\alpha)]^2 + 2Z(\bar{\mathbf{x}}_\alpha)Z(\bar{\mathbf{x}}_\beta) - [Z(\bar{\mathbf{x}}_\beta)]^2 \\ + [Z(\bar{\mathbf{x}}_\alpha)]^2 - 2Z(\bar{\mathbf{x}}_\alpha)Z(\bar{\mathbf{x}}_0) + [Z(\bar{\mathbf{x}}_0)]^2 \\ + [Z(\bar{\mathbf{x}}_\beta)]^2 - 2Z(\bar{\mathbf{x}}_\beta)Z(\bar{\mathbf{x}}_0) + [Z(\bar{\mathbf{x}}_0)]^2 \end{array} \right\}$$

Applying the expectation operator and substituting this into (3) gives,

$$\sigma^2(\bar{\mathbf{x}}_0) = - \sum_{\alpha=1}^N \sum_{\beta=1}^N \omega_\alpha \omega_\beta \gamma(\bar{\mathbf{x}}_\alpha - \bar{\mathbf{x}}_\beta) + 2 \sum_{\alpha=1}^N \omega_\alpha \gamma(\bar{\mathbf{x}}_\alpha - \bar{\mathbf{x}}_0) - \gamma(\bar{\mathbf{0}}). \quad (6)$$

Now, we wish to determine the weights,  $\omega_\alpha$ , that minimize  $\sigma^2$ , subject to the constraint,  $\sum_{\alpha=1}^N \omega_\alpha = 1$ .

Using a Lagrange undetermined multiplier  $\mu$ , we thus have the following system:

$$\begin{aligned} \frac{\partial \sigma^2}{\partial \omega_\alpha} - \mu &= 0, \quad \forall \alpha = 1, \dots, N, \text{ and} \\ \sum_{\beta=1}^N \omega_\beta &= 1. \end{aligned}$$

Upon evaluating the partial derivative, this becomes,

$$\begin{aligned} \sum_{\beta=1}^N \omega_\beta \gamma(\bar{\mathbf{x}}_\beta - \bar{\mathbf{x}}_\alpha) + \mu &= \gamma(\bar{\mathbf{x}}_\alpha - \bar{\mathbf{x}}_0), \quad \forall \alpha = 1, \dots, N, \text{ and} \\ \sum_{\beta=1}^N \omega_\beta &= 1. \end{aligned} \quad (7a)$$

In matrix form, this is,

$$\begin{bmatrix} \gamma(\bar{\mathbf{0}}) & \gamma(\bar{\mathbf{x}}_1 - \bar{\mathbf{x}}_2) & \cdots & \gamma(\bar{\mathbf{x}}_1 - \bar{\mathbf{x}}_N) & 1 \\ \gamma(\bar{\mathbf{x}}_2 - \bar{\mathbf{x}}_1) & \gamma(\bar{\mathbf{0}}) & & & 1 \\ \vdots & & \ddots & & \vdots \\ \gamma(\bar{\mathbf{x}}_N - \bar{\mathbf{x}}_1) & & & \gamma(\bar{\mathbf{0}}) & 1 \\ 1 & 1 & \cdots & 1 & 0 \end{bmatrix} \bullet \begin{bmatrix} \omega_1 \\ \omega_2 \\ \vdots \\ \omega_N \\ \mu \end{bmatrix} = \begin{bmatrix} \gamma(\bar{\mathbf{x}}_1 - \bar{\mathbf{x}}_0) \\ \gamma(\bar{\mathbf{x}}_2 - \bar{\mathbf{x}}_0) \\ \vdots \\ \gamma(\bar{\mathbf{x}}_N - \bar{\mathbf{x}}_0) \\ 1 \end{bmatrix}. \quad (7b)$$

This system is solved for the weights  $\omega_\beta$  and  $\mu$ , individually for each estimate point  $\bar{\mathbf{x}}_0$  on a regular grid, producing a mapped estimate field. Additionally, once the weights and Lagrange multiplier are determined at an estimation point, the Kriging variance or  $\sigma^2$  is computed from:

$$\sigma^2(\bar{\mathbf{x}}_0) = \mu - \gamma(\bar{\mathbf{0}}) + \sum_{\alpha=1}^N \omega_{\alpha} \gamma(\bar{\mathbf{x}}_{\alpha} - \bar{\mathbf{x}}_0). \quad (8)$$

Equation 8 is obtained formally by substituting (7a) into (6). In most applications,  $\gamma(\bar{\mathbf{0}})$  vanishes. However, sample measurement uncertainty can be included in the Kriging system through the variogram. Otherwise, the Kriging variance is only the uncertainty associated with estimating the unmeasured value given measured values at a finite number of spatially distributed locations. This method of interpolation, or estimation has some interesting properties, which are relevant to the problem of extreme precipitation estimation.

1.) The procedure used to create mapped values should be an estimation algorithm for interpolation, not simply a discretized smoothing algorithm. When  $\gamma(\bar{\mathbf{0}})=0$ , the best estimate at an already sampled location is clearly the sampled value (or a previously estimated extreme precipitation statistic), in which case  $\sigma^2=0$  (Remember that  $\sigma^2$  is the uncertainty associated only with interpolation). It can be seen, from (7b) that when the estimation location is that of a sample location ( $\bar{\mathbf{x}}_0 = \bar{\mathbf{x}}_{\alpha}$ , for some  $\alpha$ ), the right-hand side vector is identical to  $\alpha$ -th column of the left-hand matrix. Thus one solution is that all  $\omega$ 's and  $\mu$  are equal to 0, except for  $\omega_{\alpha}=1$ . Since the left-hand matrix is not singular, this is the only solution. This corresponds to the estimate at that location being equal to the sample value and the variance vanishing. Hence, Kriging is an *exact* interpolator; all sample values are preserved in the estimate and surrounding estimates vary continuously into these samples. Schemes such as the Barnes and Cressman schemes are not exact and will create estimates at sample locations that differ from the sample values themselves.

2.) Kriging takes into account not only the distance between the estimation point and the sample locations (right hand side of 7b), but it also considers the distances between the sample points themselves (left hand matrix in 7b). One resulting behavior is that if two samples are separated by a distance for which the variogram is very small, that is the two sample values are already expected to be very similar, the Kriging weights will be reduced for these two individual samples, effectively treating them as one sample. This of course makes sense, and is one reason why the Barnes and other inverse distance weighted schemes are less appropriate for unevenly spaced, or clustered data. These schemes generally do not take into consideration, variations in sample spacing. Due to the fact that extreme precipitation modeling is constrained to the finest resolution grid in our simulations, one can expect the resulting sample points to be unevenly distributed over the state of Colorado with significant clustering over areas subjected to the largest number of simulations.

3) Closely related to issue 2, is that inverse distance weighting schemes require the user to specify one to several parameters related to the range of influence of sample data points. This effectively controls the amount of smoothing that will be present in the resulting field. Generally, one will want to choose these parameters such that the length scale of the variations in the estimated field is larger than the mean sample separation

distance. This results in a loss of detail where sample density is high. With kriging, the smoothness and detail in the field varies uniformly over the domain depending on the inter-sample spacing near the estimation point and the variogram model. Once the variogram is determined from the sample data, the transition from a highly structured field where samples are dense to a smooth field where samples are lacking occurs seamlessly and automatically.

4.) This interpolation scheme can be extended to include measurements of an auxiliary variable such as elevation. This can be useful if the primary variable  $Z$ , is only sparsely sampled and a correlation exists with the auxiliary variable  $Y$  which is densely sampled. This is known as *cokriging* and is summarized in the next section.

### **Cokriging**

Suppose that in addition to the available  $N$  samples of the primary variable  $Z(\bar{\mathbf{x}}_\alpha)$ , we have  $N$  collocated samples of an auxiliary variable, say topography,  $S(\bar{\mathbf{x}}_\alpha)$ . Also, suppose that at every point  $\bar{\mathbf{x}}_0$  where we desire an estimate of  $Z$ , we have a measurement of  $s = s(\bar{\mathbf{x}}_0)$ . We then augment our ordinary kriging estimator which becomes:

$$z^*(\bar{\mathbf{x}}_0) = \omega_0 s(\bar{\mathbf{x}}_0) + \sum_{\alpha=1}^N \left[ \omega_\alpha^1 z(\bar{\mathbf{x}}_\alpha) + \omega_\alpha^2 s(\bar{\mathbf{x}}_\alpha) \right], \quad (9)$$

where the subscripts denote the sample location and the superscripts denote the variable with "1" being the primary variable and "2" being the auxiliary variable (e.g. elevation). The special weight for the auxiliary variable at the estimation point is  $\omega_0$ .

This is the *collocated cokriging estimator*. The only  $s$ -samples are those that are collocated with the  $z$ -sample points and the estimation point in question.

We also need to generalize the variogram concept to the bivariate case. Three variograms are defined:

The direct- or auto-variograms:

$$\gamma_{11}(\bar{\mathbf{h}}) \equiv \frac{1}{2} E \left\{ \left[ Z(\bar{\mathbf{x}} + \bar{\mathbf{h}}) - Z(\bar{\mathbf{x}}) \right]^2 \right\} = \gamma_{11}(-\bar{\mathbf{h}}) \geq 0,$$

$$\gamma_{22}(\bar{\mathbf{h}}) \equiv \frac{1}{2} E \left\{ \left[ S(\bar{\mathbf{x}} + \bar{\mathbf{h}}) - S(\bar{\mathbf{x}}) \right]^2 \right\} = \gamma_{22}(-\bar{\mathbf{h}}) \geq 0$$

and the cross variogram,

$$\gamma_{12}(\bar{\mathbf{h}}) \equiv \frac{1}{2} E \left\{ \left[ Z(\bar{\mathbf{x}} + \bar{\mathbf{h}}) - Z(\bar{\mathbf{x}}) \right] \left[ S(\bar{\mathbf{x}} + \bar{\mathbf{h}}) - S(\bar{\mathbf{x}}) \right] \right\} = \gamma_{21}(\bar{\mathbf{h}}) = \gamma_{12}(-\bar{\mathbf{h}}).$$

Note that  $\gamma_{12}(\bar{\mathbf{h}})$  can be either positive or negative. As before we have assumed second-order intrinsic stationarity with regard to the increments, direct- and cross-variograms. Again, this allows for the variograms to be determined from the sample

data. In addition, while the direct variograms are related in a one-to-one fashion to the direct spatial covariances (assuming they exist; a regionalized variable may be intrinsically stationary but have a non-existent mean and spatial covariance), the cross-variogram only describes the even part of the spatial cross-covariance of the increments. The cross-covariance of increments is defined as,

$$C_{12}(\bar{\mathbf{x}}_1, \bar{\mathbf{x}}_2) \equiv E \left\{ \left[ Z(\bar{\mathbf{x}}_1) - Z(\bar{\mathbf{0}}) \right] \left[ S(\bar{\mathbf{x}}_2) - S(\bar{\mathbf{0}}) \right] \right\}.$$

This function can be decomposed into even and odd components. The cross-variogram is proportional to the even component. Nonetheless the spatial correlation is often modeled with a variogram as an approximation — that is, as an approximation to the cross-covariance of the increments — due to what is often a dearth of sample data. Insufficient data will often force the analyst to adopt an isotropic variogram model based only on the magnitudes or distances involved in the increments. In this case the covariance of increments is even by definition and the variogram becomes a sufficient representation of the even increment covariance.

Using the variograms thus defined, the variance, or expected error for this estimator is

$$\begin{aligned} \sigma^2 = & 2 \sum_{i=1}^2 \sum_{\alpha=1}^N \omega_{\alpha}^i \gamma_{i1}(\bar{\mathbf{x}}_{\alpha} - \bar{\mathbf{x}}_0) - \sum_{i=1}^2 \sum_{j=1}^2 \sum_{\alpha=1}^N \sum_{\beta=1}^N \omega_{\alpha}^i \omega_{\beta}^j \gamma_{ij}(\bar{\mathbf{x}}_{\alpha} - \bar{\mathbf{x}}_{\beta}) \\ & - 2\omega_0 \sum_{i=1}^2 \sum_{\alpha=1}^N \omega_{\alpha}^i \gamma_{i2}(\bar{\mathbf{x}}_{\alpha} - \bar{\mathbf{x}}_0) - \gamma_{11}(\bar{\mathbf{0}}) + 2\omega_0 \gamma_{12}(\bar{\mathbf{0}}) - (\omega_0)^2 \gamma_{22}(\bar{\mathbf{0}}). \end{aligned} \quad (10)$$

The cokriging variance is minimized in a manner similar to that for ordinary kriging, producing

$$\begin{aligned} \sum_{j=1}^2 \sum_{\beta=1}^N \omega_{\beta}^j \gamma_{ij}(\bar{\mathbf{x}}_{\alpha} - \bar{\mathbf{x}}_{\beta}) + \omega_0 \gamma_{i2}(\bar{\mathbf{x}}_{\alpha} - \bar{\mathbf{x}}_0) + \mu_i = \gamma_{i1}(\bar{\mathbf{x}}_{\alpha} - \bar{\mathbf{x}}_0), \forall \alpha = 1, \dots, N \\ \text{and } i = 1, 2 \end{aligned} \quad (11a)$$

$$\sum_{j=1}^2 \sum_{\beta=1}^N \omega_{\beta}^j \gamma_{2j}(\bar{\mathbf{x}}_{\beta} - \bar{\mathbf{x}}_0) + \omega_0 \gamma_{22}(\bar{\mathbf{0}}) + \mu_2 = \gamma_{12}(\bar{\mathbf{0}}), \quad (11b)$$

$$\sum_{\beta=1}^N \omega_{\beta}^1 = 1 \quad (11c)$$

$$\sum_{\beta=1}^N \omega_{\beta}^2 + \omega_0 = 0. \quad (11d).$$

System 11 is the collocated cokriging system. Constraints 11c&d guarantee an unbiased estimate. This system has two undetermined Lagrange multipliers  $\mu_1$  and  $\mu_2$  because of these two constraints. This can be solved as a block matrix system consisting of the NxN direct and cross-variogram matrices, the direct- and cross-variogram vectors about the estimation point and the two unbiasedness constraints. This creates a  $(2N+3)^2$

size matrix. Unlike in ordinary kriging, where the left hand matrix contains variogram matrices based only on the samples, the collocated cokriging matrix also contains variogram values that depend on the location of the estimate point  $\bar{\mathbf{x}}_0$ . The ordinary kriging system can be solved by LU-decomposing the left hand matrix only once and obtaining estimates by back-substitution at each estimate point. In the collocated cokriging system, the left-hand matrix must be LU-decomposed, at every estimation point making this technique considerably more expensive (runtime increases from 30 seconds to 9 hours for a system with 300 sample points and 5000 estimation points on a modern PC).

Once the weights and Lagrange multipliers have been determined at an estimation point, the kriging variance is given by,

$$\sigma^2 = \sum_{i=1}^2 \sum_{\alpha=1}^N \omega_{\alpha}^i \gamma_{i1}(\bar{\mathbf{x}}_{\alpha} - \bar{\mathbf{x}}_0) + \omega_0 \gamma_{12}(\bar{\mathbf{0}}) - \gamma_{11}(\bar{\mathbf{0}}) + \mu_1, \quad (12)$$

which is obtained by substituting system (11) into equation (10).

Like ordinary kriging, collocated cokriging more or less preserves sample values. The "more-or-less" condition is required because technically, when  $\bar{\mathbf{x}}_0 = \bar{\mathbf{x}}_{\alpha}$ , Eq. 11a with  $i=2$ , and 11b become identical, resulting in a singular matrix. However, as  $\bar{\mathbf{x}}_0 \rightarrow \bar{\mathbf{x}}_{\alpha}$ ,  $z^*(\bar{\mathbf{x}}_0) \rightarrow z(\bar{\mathbf{x}}_{\alpha})$  and  $\sigma^2 \rightarrow 0$  if  $\gamma_{ij}(\bar{\mathbf{0}}) = 0$  for all  $i,j$ . Therefore the problem can be resolved by either removing the redundancy or simply skipping the estimate, replacing it with the sample value and setting the variance to zero at the estimation point.

It is also important to note that the cokriging estimator becomes the ordinary kriging estimator when the auxiliary variable weights are all zero and  $\mu_2=0$ . This much of the solution certainly obeys the unbiasedness constraint. Hence, the ordinary kriging solution is a *possible* solution to the collocated cokriging system. The cokriging solution will only differ from the ordinary kriging solution if it produces a smaller variance. When the primary and auxiliary variable are spatially correlated, cokriging can provide significantly better estimates with smaller variances. If no significant correlation exists, the two solutions will be nearly identical.

### **Variogram Models**

The expressions for the kriging and cokriging variances (Eqs. 8 and 12) can also be written as,

$$\sigma^2 = \tilde{\bar{\omega}} \cdot \Gamma \cdot \bar{\omega}, \quad (13)$$

where,  $\bar{\omega}$  is the weight vector, which includes not only the variable weights but also the Lagrange multipliers, and  $\Gamma$  is the variogram matrix that appears in Eqs. 7b and 11. Clearly, the variance must be greater than or equal to zero, which in turn implies that the variogram matrix must be positive definite. If this condition is not met, then the entire problem becomes meaningless and the resulting solutions will often be unrealistic. Hence, the first priority in variogram modeling is to ensure the positive definite

characteristic of the variogram matrix. There exist several, commonly used variogram models which are known to produce positive definite variogram matrices in the ordinary kriging problem. A few of these are listed below.

### Spherical Model

$$\gamma(h) = \begin{cases} b \cdot \left[ \frac{3h}{2a} - \frac{1}{2} \left( \frac{h}{a} \right)^3 \right], & \text{for } h \leq a, \\ b & \text{for } h > a \end{cases}, \quad (14a)$$

where  $a$ , called the *range*,  $b$ , called the *sill*, are constants. As  $h$  becomes large, this variogram becomes equal to the sill value. The range controls how quickly the variogram approaches the sill value as a function of distance,  $h$ . This model is depicted in the upper left panel of Figure 62, using a sill of 1.0 and range of 100 km.

### Exponential Model

The exponential model is given by,

$$\gamma(h) = b \cdot \left( 1 - e^{-\frac{3h}{a}} \right), \quad (14b)$$

where again,  $a$  and  $b$  are the range and sill respectively. This model is distinguished from the spherical model by its slope variation, or curvature. The exponential model has its greatest curvature at the origin while the spherical model maximizes the curvature at the range. In addition, the slope of the exponential model is greater at the origin, for the same sill and range value. The exponential model with sill=1.0 and range=100 km is shown in the upper right panel of Figure 62.

### Gaussian Model

The Gaussian model is given by,

$$\gamma(h) = b \cdot \left( 1 - e^{-\frac{3h^2}{a^2}} \right) \quad (14c)$$

This model is shown for the same sill and range parameters as the previous models. Unlike the exponential and spherical models, the slope of this variogram approaches zero at both the origin and for distances large compared to the range. Between these values lies the steepest point of the variogram which also contains the inflection point. The other models discussed do not contain an inflection point. Because of the continuous, quadratic behavior at the origin, this variogram is susceptible to extrapolation (negative kriging weights assigned to some of the sample points). This can result in estimation outside the physical range of the variable being estimated at distances removed from closely spaced samples. Combining this model with a small nugget model, discussed next, will alleviate this problem (Wackernagel, 1998, Ch. 17).

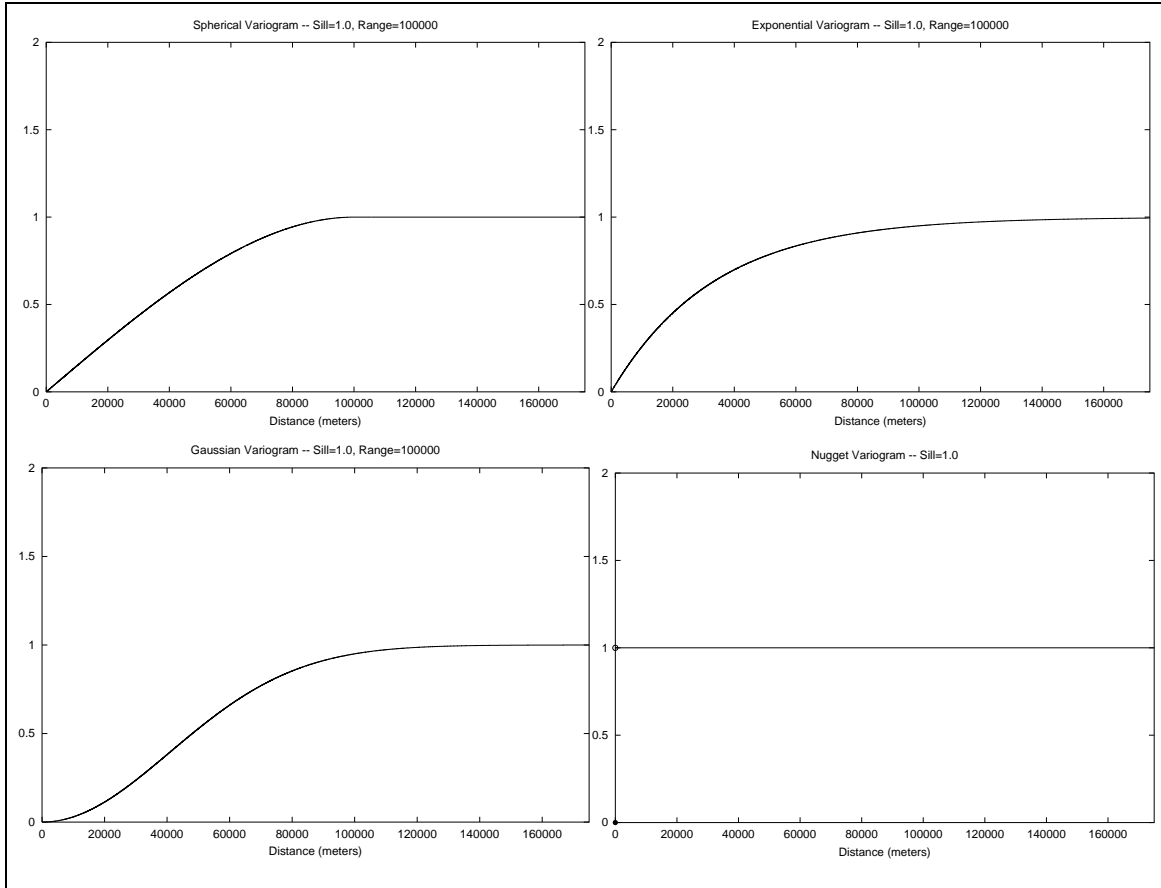


**Figure 62:** Selected model variograms. Spherical (upper left), exponential (upper right), Gaussian (lower left) with sill=1.0 and range=100.0 km. Nugget model (lower right) with sill=1.0.

### Nugget Model

The nugget model is given by,

$$\gamma(h) = \begin{cases} b & \text{for } h > 0, \\ 0 & \text{for } h = 0 \end{cases} \quad (14d)$$

This model is constant for all non-zero  $h$  and is zero at the origin. The magnitude  $b$  is called the nugget effect, sill or value. Hence, this variogram is discontinuous at the origin. A pure nugget model used in ordinary kriging will result in all estimates not coincident with a sample point being set to the domain average, while estimation points coinciding with the sample points will be set to the corresponding sample value. Hence, the discontinuity in this variogram also results in a discontinuous estimate. These discontinuities are usually removed. When combined with one of the previous variogram models the effect is typically a smoothing effect, and when combined with a Gaussian variogram, the extrapolative power of the Gaussian variogram is destroyed. Mathematically, this model is similar to the concept of "white noise" in that it implies a

constant, *non-vanishing* expected dissimilarity at all distances even as the separation distance approaches zero (the name comes from the effect of isolated high grade gold nuggets on the grade of a prospective sample).

If, in addition to being second-order intrinsically stationary, the random variable under consideration is second-order stationary, then the sill of the direct variogram is simply the variance of the random variable. For cokriging, if the covariance of the primary and auxiliary variable is modeled as an even function and second order stationarity is assumed, then the cross-variogram sill is the covariance of the two variables. Hence, the choice of a sill value is often aided by computation of the sample variance and covariance (or correlation coefficient) for the variables in question. The range parameter is chosen by fitting the model variogram to the sample variogram. Generally, this is done by eye due to the fact that the behavior of the variogram near the origin (continuity, differentiability, etc.) has the largest effect on the estimates, and as noted previously, the fitted model must be positive definite. Hence, procedures such as least squares fitting, are not terribly helpful.

In order to demonstrate the construction of a model variogram, we consider the direct variogram for topography. As noted earlier, the common grid consists of 57600 grid-points at 2-km spacing. This results in  $57600 \cdot 57599/2 = 1.6588512 \cdot 10^9$  non-trivial pairs. The trivial pairs are the 57600 self-pairing of the grid points, for which the separation distance is zero and the squared difference in elevation is zero identically. We pseudo-randomly select 1/80 of these 1.6 billion pairs to create the *variogram cloud*. Each point in this cloud corresponds to a distinct pair of grid points on the common grid with the horizontal axis corresponding to the distance between the grid point pair. The vertical axis corresponds to the quantity,  $(\Delta z)^2/2$ , where  $\Delta z$  is the difference in elevation between the points. The sample variogram is simply the expectation of this latter quantity for a given distance. This is computed by binning the abscissa axis into 100 bins and taking the arithmetic average of the ordinate values within the bin. This results in the sample variogram shown in Figure 63. Also shown in this figure is the spherical model that was fit by eye to the sample variogram. This model uses a range of 235.0 km and a sill value of  $425.0 \cdot 10^3 \text{ m}^2$ . All cokriging done with respect to elevation utilizes this model for the elevation direct variogram.

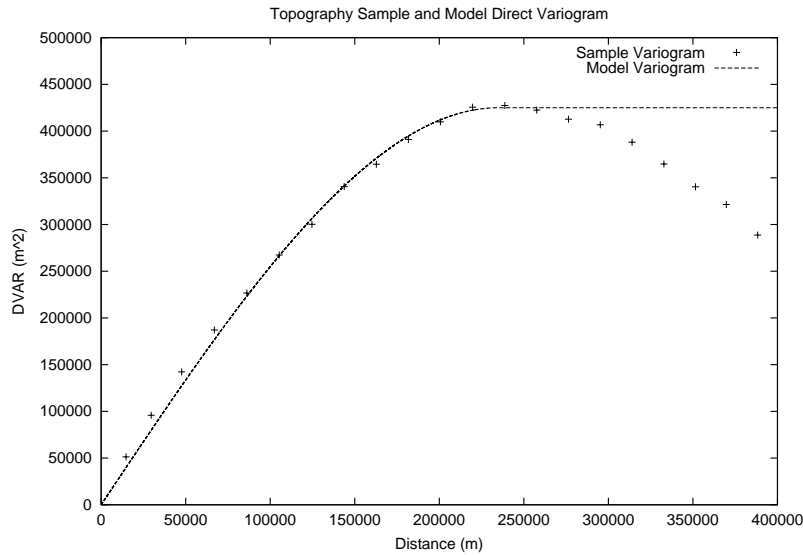


**Figure 63:** Sample and model direct variogram for elevation on common grid.

The decrease in the variogram past ~235 km is partly due to the fact that for many of the larger distance pairs, the pairs straddle the Continental Divide, resulting in a lower variogram value than for shorter distances. This decrease cannot be modeled with positive definite variograms discussed above. Additionally, this decrease is of little consequence in practice since this variogram is only used in cokriging. The proximity of the samples to the estimation points, as well as the knowledge of the elevation at the estimation point makes the longer distance topography samples less relevant to the final estimate of the cokriged quantity.

## 7. A New Method of PMP Estimation

Up to this point the discussion of simulation results has been focused on simulated precipitation and event identification. Attempts to increase low-level moisture, transpose synoptic conditions and relocate the cloud-resolving grid were met with very limited success, in terms of precipitation maximization. Despite the severity of some of the simulated precipitation magnitudes, we cannot assume that any of these simulated events represent the PMP at the simulated location for any given area or duration. To the extent that the numerical model used is physically realistic, we can only deduce that the unknown PMP values are bounded below by the simulated events. We now examine the problem of PMP estimation using the simulated events.

Here, we face many of the same problems that confront previous efforts based entirely on observed storms (Hansen et. al., 1988; World Meteorological Organization, 1973; United States Department of Commerce, 1960). Namely, the simulated events occur at very definite locations in the model domain leaving the vast majority of the state with no significant simulated precipitation event. Secondly, and as already noted, the simulated events only place a lower bound on a model based PMP estimate at the location of occurrence, and do not constitute a PMP estimate, regardless of the accuracy of the model. Hence, two procedures are required before PMP estimation can even be

attempted. Firstly, there must be some allowance for storm transposition. More specifically, the accumulated precipitation for a given area and duration must be transposed to an estimation location. This is distinct from a physical rainstorm transposition technique in which the precipitation amounts are transposed while adjusting moisture availability for elevation and maximum sustained low-level dewpoint. These limiting factors are included indirectly through limits on the horizontal transposition distance and vertical displacement between the simulated event and an estimation location. Secondly, some extrapolation technique must be used to estimate PMP from the simulated storms that have been transposed to an estimation location. This extrapolation is accomplished using the Hershfield method for PMP estimation (Hershfield, 1961, 1965). The transposition and extrapolation procedures are discussed below.

Firstly, a grid of points is established which includes all of the cloud-resolving grids across all simulations. This grid has 2-km grid spacing, contains 57,600 grid points, and is depicted below in Figure 64, which also shows information to be discussed later. We will call this grid the "common-grid" (CG). The goal is to obtain a PMP estimate at each one of these grid points, and the procedure is outlined below. A detailed discussion of each step will be presented following this summary.

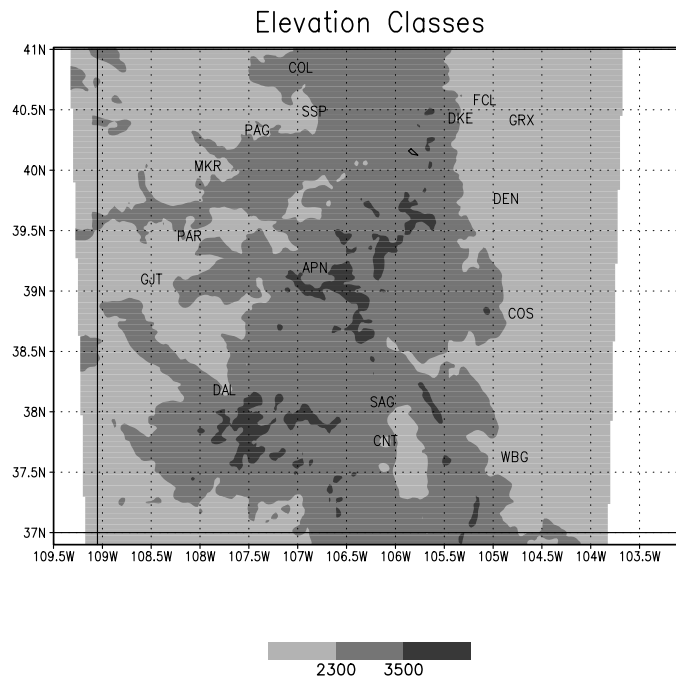


**Figure 64:** Elevation classes used in transposition.

A few definitions are required first. The location of a modeled event is defined as the precipitation-weighted mean latitude and longitude within the enclosing isohyet. The elevation associated with a modeled event is the precipitation-weighted mean elevation within the defining isohyet. The areas examined in this research are 10, and 100 km<sup>2</sup>. These are obtained by linearly interpolating the average total precipitation depth, location and elevation of the previously identified events whose isohyet areas bound the specific area size of interest. In the case that the largest magnitude isohyet, modulo 5 mm,

surrounding a point maximum, already exceeds the area of interest, the linear interpolation occurs from the grid point maximum assuming an area equal to the area of the fine grid cells (e.g., 2.78 km<sup>2</sup> for the simulations using 1.67 km grid spacing). Because of the small size of the convection resolving grids used in these simulations, no correction was made for the polar-stereographic projection. With these definitions, the procedure is as follows:

For events of a given area and duration:

- 1.) At each CG grid point we transpose events of the area and duration of interest to the estimation CG point. Limits are imposed on the transposition in terms of a maximum horizontal transposition distance and maximum vertical (topographical) displacement. Hence, each grid-point receives simulated events that are sufficiently close and lie within a restricted elevation range of the estimation point.
- 2.) Once this database of events is established for a single estimation point, these events are used as input to the Hershfield estimation equation for PMP, provided that *at least* 10 events were transposed to the given CG estimation point. If this last criterion is not met, then the point is considered undefined. This technique is discussed in more detail in the next section.
- 3.) Steps 1 and 2 are carried out for each gridpoint on the common grid leaving each *defined* point on the common grid with two primary parameters (Hershfield mean and product of the frequency factor and coefficient of variation). Plots of these two fields are constructed.
- 4.) Both of the Hershfield equation parameters are sampled at more or less subjectively determined locations. This step is necessary because the fields produced in step 3 are noisy and contain discontinuities due to the transposition cutoff radius and elevation tolerance. Avoiding sampling near these discontinuities is the primary guiding factor in the sampling procedure, in addition to avoiding the sampling of grid points that are spatially isolated in terms of being defined. The two parameters are sampled separately because the discontinuities in each parameter are not necessarily collocated.
- 5.) The samples are kriged or cokriged for each of the two Hershfield parameters. Once these fields are kriged or cokriged back onto the common grid, the entire common grid contains defined values of both Hershfield equation parameters. These fields are spatially variable and possibly correlated with elevation, depending on the modeled variogram.
- 6.) The kriged fields are substituted back into the Hershfield equation to provide a final mapped PMP-estimate field over the entire CG for the given area size and duration.

The Hershfield extrapolation procedure and kriging details are discussed in the next section.

## **Hershfield Extrapolation**

Here we describe the relatively simple technique of Hershfield extrapolation. As already noted, a collection of transposed events, for a given area and duration, is assigned to each estimation point on the common grid according to the rules for limiting horizontal and vertical transposition. Once this database is constructed for a grid point these events serve as input to the Hershfield extrapolation procedure. This procedure consists of the following steps. Assuming one has  $N$  events transposed to the estimation grid point, the largest event, that is the event with the largest average depth, is temporarily removed producing a collection of  $N-1$  events. The mean,  $m_{N-1}$  and the standard deviation,  $\sigma_{N-1}$ , are calculated for the truncated sample set. One then calculates the value of the constant  $K$ , required to reproduce the omitted event by the formula,

$$p_{\max} = m_{N-1} + K\sigma_{N-1}, \text{ where } p_{\max} \text{ is the magnitude of the largest, omitted event.}$$

Once this value of  $K$  is determined, the mean,  $m_N$ , and standard deviation,  $\sigma_N$ , are recalculated using all  $N$  events and the PMP estimate is computed from,

$$PMP = m_N + K\sigma_N.$$

The preceding two equations can also be written as,

$$p = m(1 + K \cdot CV), \tag{15}$$

where  $CV = \sigma / m$  is the coefficient of variation.

The  $K \cdot CV$  term will also be referred to as simply  $KCV$  later. This technique is described in more detail in Hershfield (1961) and Hershfield (1965). As described in these two references, the Hershfield equation was originally designed to be used with annual maximum precipitation data for a specified duration at a single measurement site. As such, it only provides an estimate of the point PMP. This does not imply that the Hershfield technique is inherently limited to point PMP estimates. Rather this was the only practical application since rain gauges were the primary source of precipitation data at that time with a sufficiently long record. Here we apply this technique to durations and areas ranging from 2 to 12 hours and 10 to 1000 km<sup>2</sup> by using transposition to create the database at each CG grid point. The underlying assumption is that nearby simulated storms within a certain elevation range could have conceivably occurred at the estimation location.

Due to the fact that each region of the CG grid was subjected to simulations corresponding to differing types of extreme precipitation events — General, General Local Convective, and Local Convective — and given that physiographical influences may have an effect on the Hershfield parameters, it is necessary to allow for the spatial variation of these parameters. In this study, values of the Hershfield mean and the product,  $K \cdot CV$  were kriged or cokriged separately and final PMP maps were produced via

Equation 15 operating on the separately kriged fields. This is similar to the WMO (1973, Ch. 4) suggestion that generalized PMP estimation using the Hershfield method, should consist of a subjective contouring of the mean and coefficient of variation separately.

### **Example of Procedure for total-precipitation, 10-km<sup>2</sup>, 2-hour events**

We now consider a step-by-step example for the 10-km<sup>2</sup>, 2-hour duration events, considering only total-precipitation. Results will also be shown for liquid-only (rain-only) and the resulting estimate will be called Probable Maximum Liquid Precipitation (PMLP). The allowable horizontal transposition was chosen to be 50 times the radius of a circle with area 10-km<sup>2</sup>, or equivalently, 89.2 km. Step 1, was actually carried out for transposition scale factors of 2, 5, 10, 20 and 50 times the equivalent radius of a 10-km<sup>2</sup> circle. It should be clear that as the transposition scale factor is decreased, the number of defined CG points (possessing at least 10 transposed events) decreases. Thus, factors in choosing this threshold are that enough CG grid points must be defined such that a.) it makes sense to continue with the procedure with the end goal of a mapped field in mind and b.) one can examine the spatial structure of the plotted Hershfield parameters so that sampling can be done prudently. One will generally choose the multiplicative factor (2, 5, 10, 20 or 50) such that it decreases with increasing area due to the increase in equivalent radius.

The vertical limit on transposition was the same for all areas and durations. This limit was defined in terms of the following elevation classes:

Class 1:  $z < 2300$  m (2300 m  $\cong$  7500 ft)

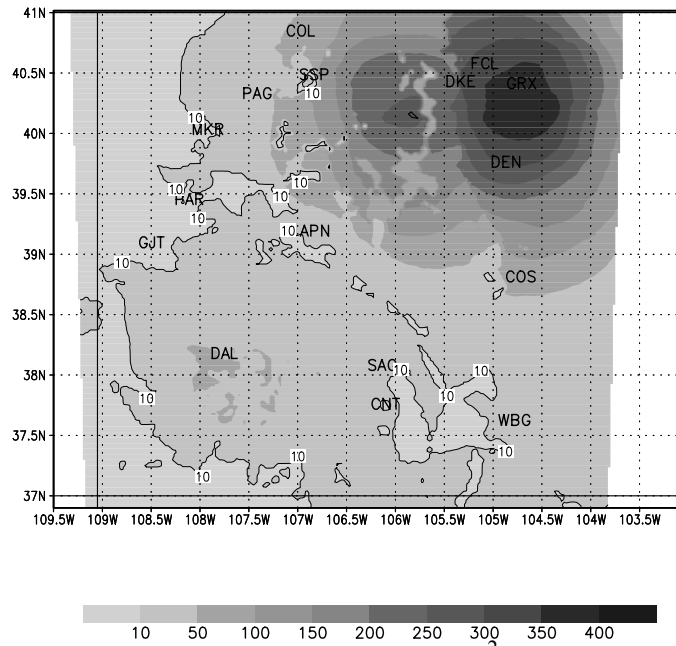
Class 2:  $2300$  m  $\leq z < 3350$  m

Class 3:  $z \geq 3350$  m (3350 m  $\cong$  10990 ft), where  $z$  is elevation (MSL).

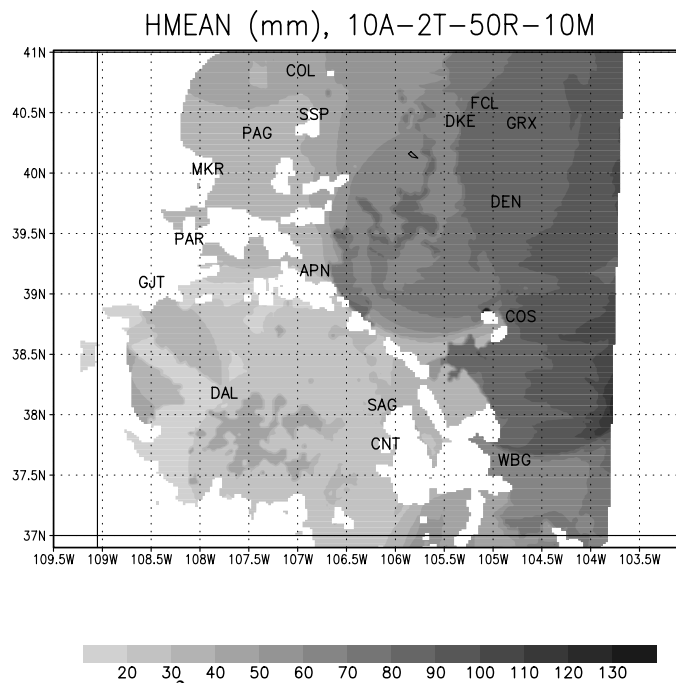
These classes are shown in Figure 64. In order for an event to be transposed from the simulated location to an estimation location, both locations must belong to the same elevation class, or be separated by no more than 100 m in the vertical. The elevation classes were introduced to allow an elevation influence to be apparent, if it exists, by not allowing low-elevation storms to be transposed to the high elevation classes (Classes 2 and 3) and vice-versa. Yet, these classes needed to be broadly defined to allow for a sufficient number of storm transpositions. The 100-m overlap was originally included to moderate the discontinuous inclusion or exclusion of events based on what are somewhat arbitrary boundaries for the elevation classes.

Figure 65 shows the number of transposed events for the 10-km<sup>2</sup>, 2-hour events, as a function of position. This figure illustrates that nearly three-quarters of the state had fewer than 30 events. For this reason, the remainder of this analysis should be interpreted as a demonstration of a proposed technique for generalized PMP estimation using model output, and that this demonstration is one which is based on a relatively small amount of data over much of the domain.

The computed Hershfield mean for this area-duration combination is shown in Figure 66. Note that these are the raw values output from the Hershfield method and no N, 10A-2T-50R-10M



**Figure 65:** Number of transposed events for the 10-km<sup>2</sup>, 2-hour duration simulations using a 50-scale factor for horizontal transposition. The 10-event boundary is also contoured.



**Figure 66:** HMEAN for 10-km<sup>2</sup>, 2-hour duration events using 50-scale factor for horizontal transposition. Shading interval is 10-mm. Undefined points are unshaded.

kriging has yet been performed. These plots are useful for examining the behavior of the Hershfield procedure. What is evident in this figure is that the effect of the transposition radius, visible as circular boundaries of ~90-km radius, is most pronounced in the areas with less than ~120 transposed events (Figure 65). The noise and discontinuities in this plot makes its direct use in a PMP estimate impossible. However, this field can be sampled for the purpose of this demonstration, if an effort is made to avoid sampling near transposition induced discontinuities. This was done at 23 separate locations, primarily in the northeastern portion of the grid over high- and low-elevation areas to the east and west of the Continental Divide, and also included 4 samples from southwestern and southern Colorado, one sample from northwestern Colorado between Parachute and Steamboat Springs, and two samples from the area around Colorado Springs.

These samples had a variance of  $404.76 \text{ mm}^2$  and a linear correlation coefficient with elevation of  $-0.65$ . The sample variogram was fit, crudely given the lack of data, with a Gaussian variogram with a sill value of  $750.0 \text{ mm}^2$ , a range of  $433.01 \text{ km}$ , and a small nugget value of  $50 \text{ mm}^2$  (Figure 67). This variogram provided a relatively good fit to the sample variogram below distances of  $150 \text{ km}$  but underestimated the sample variogram for larger distances. At distances larger than  $250 \text{ km}$ , the sample variogram indicates values in excess of  $1200 \text{ mm}^2$ , which is nearly three times the sample variance. At the same time,  $250 \text{ km}$  is over one half the total domain width and thus one should not be using the sample data at these lengths to fit the variogram restrictively. This is because the variogram is supposed to represent a second-order intrinsically stationary function and it is stationarity that justifies the use of the sample data for fitting the variogram. However, for lengths approaching one-half the domain size, the number of realizations of variations on this scale is much smaller than for shorter distances. Hence, the first priority is to ensure the variogram fits reasonably well at distances shorter than one-half the domain width. Secondly, the sample variogram shows that the samples have a variogram value less than the sample variance at distances less than ~ $175 \text{ km}$ , and is less than the sill by construction. Given that there are only 23 samples, and that many of the samples are located in the northeastern quarter of the grid, the sample variance should underestimate the variance of the underlying random function since they are samples from a spatially correlated field. Therefore, the choice of the model sill was essentially a compromise between the sample variance and the apparent sample sill value.

The Gaussian variogram was chosen due to the presence of positive curvature in the sample variogram for distances below  $200 \text{ km}$ . It should be noted however, that the diameter of the transposition circle at any grid point is approximately  $180 \text{ km}$ . Therefore, the positive curvature in the sample variogram may have been the result of transposition induced homogenization of the Hershfield mean (HMEAN) within the transposition diameter. With the limited data available, the transposition radius could not be reduced without significantly decreasing the number of transposed events. Table 7 shows the statistics and variogram model parameters used for each of the three area and duration combinations.

Additional sample data would allow for a more informed choice for the sill and the choice of variogram model. Increasing the number of samples is of course possible,

but the quality and continuity of the underlying field needs to be judged and it was felt that no more samples were justified given the density of discontinuities and noise in Figure 66.

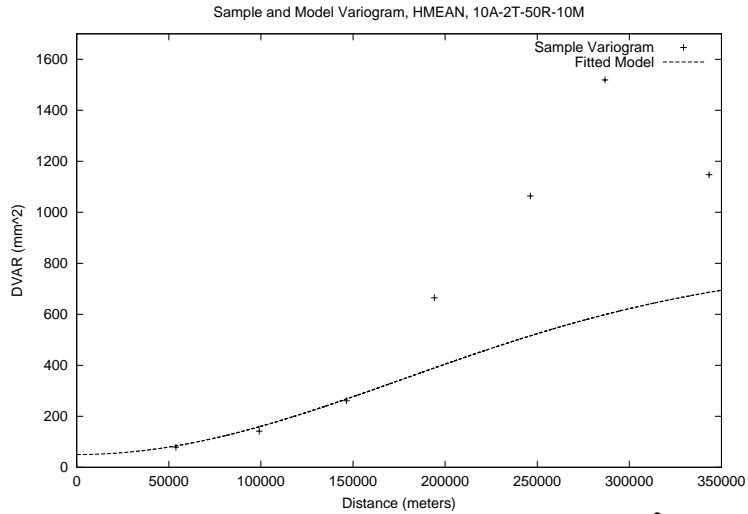


**Figure 67:** Sample and model variogram for HMEAN and 10-km<sup>2</sup> area, 2-hour duration events with 50-scale-factor horizontal transposition.

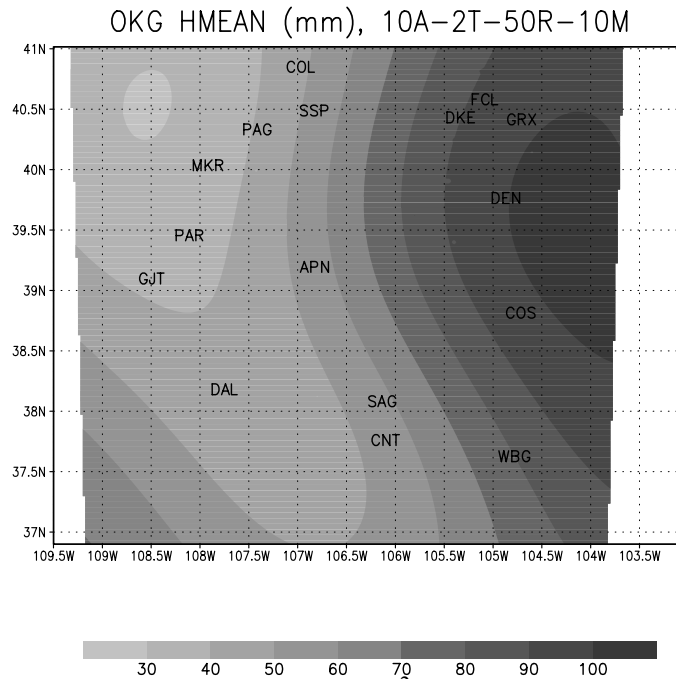


**Figure 68:** Ordinary-kriged HMEAN for 10-km<sup>2</sup> area, 2-hour duration events with 50-scale-factor for transposition. Shading interval is 10 mm.

### Coregionalization

Because of the -0.65 correlation with elevation, HMEAN was also cokriged. The method of constructing the cross variogram, or *coregionalization*, is based on that

investigated by Hevesi et. al. (1992, hereafter called HIF). A necessary requirement for the cokriging variogram matrix to be positive definite, is that the Cauchy-Schwarz inequality must be satisfied for all distances, h:

$$\gamma_{ij}(h) \leq [\gamma_{ii}(h)\gamma_{jj}(h)]^{1/2}.$$

HIF define the right side of this equation as the "positive definite condition" or PDC. Assuming second order stationarity, and an even covariance between the primary and auxiliary variable, the sill of the left-hand side cross variogram is simply the covariance, and the sills of the right hand side direct variograms are simply the variances.

Hence, one can use, as a starting point for modeling the cross-variogram,

$\gamma_{ij} = r \cdot PDC$ , where r is the correlation coefficient between the primary and auxiliary variable. This does not guarantee that the resulting cross-variogram will be positive definite. However, HIF found that in their study, cross-variogram models which did not lie close to this expression were either close to failure for being positive definite or gave unfavorable cross-validation results with respect to the estimate and/or kriging variance. For the current study, the multiplicative constant was initially set to the sample correlation coefficient and adjusted until an adequate fit was found by eye. This was done for all of the cokriged results.

With more data, one would want to guarantee the positive definite condition by using a linear combination of variogram models for the direct and cross-variograms and ensuring that the weights or sills of the cross-variogram models obey the Cauchy-Schwarz condition with respect to the same models used in the direct variograms (Isaaks and Srivastava, 1989, Ch. 16). However, in the current case, the small amount of data really cannot justify the level of spatial complexity modeled by nested or linear coregionalization models. This coupled with the fact that the direct elevation variogram utilizes a single spherical structure, while that of the Hershfield mean utilizes a single Gaussian structure already guarantees that the Cauchy-Schwarz inequality will not hold when applied to the sills if a linear model of coregionalization is adopted. Therefore a linear model of coregionalization is not used and instead the PDC approach is used as a first guess for the variogram model itself. The positive definite condition is partially checked in the end by ensuring that no estimates result in a negative cokriging variance.

While not true for other variables (such as  $K \cdot CV$ ), the 10-km<sup>2</sup>, 2-hour duration, kriged and cokriged HMEAN fields were virtually identical when a -0.75-PDC function was used. This is likely because the direct variograms for the Hershfield mean and topography exhibit different modeled spatial structures, as evidenced by the fact that the mean uses a Gaussian model with nugget, while the topography uses a spherical model. The kriged HMEAN is shown in Figure 68. This plot has little spatial structure except for a dominant east-west gradient with smaller values occurring west of the Continental Divide, a strong gradient through the center portion of the state, and a minimum in northwest Colorado.

KCV for this same area and duration was sampled at 16 locations throughout Colorado and exhibited a -0.62 correlation coefficient with elevation. The KCV sample variogram did not exhibit the same distinct area of positive curvature that was present in the HMEAN sample variogram. For this reason, a spherical model was used with a sill value of 1.00, a range of 180 km and a small nugget of 0.04. The cross-variogram with elevation utilized a -0.75-PDC function. The cokriged KCV field is shown in Figure 69. Here, the influence of topography is evident despite the fact that KCV has a slightly smaller value of correlation with elevation than did HMEAN. Again, this is likely because in the case of KCV, the spatial structure is, as evidenced by the use of a spherical model for KCV, more compatible with the spherical elevation direct variogram. It is also important to understand the linear correlation coefficient uses all of the samples and does not take into account separation distance. Hence, two variables may be highly correlated over short distances, throughout the entire domain, but may have a small total correlation coefficient due to the failure of the correlation at large separation distances (in which case, qualitatively, the samples will control the large-scale distribution and elevation is used to fill in the gaps). Anyhow, as can be seen in Figure 70, which shows the sample and model direct variogram for KCV, the spherical model fit is based on few sample variogram bins which are coarsely spaced. Aside from one outlier, the fit is approximate at best. This figure is shown to emphasize that the spherical model used should be considered *very* approximate.

The PMP estimate resulting from HMEAN and KCV for this area and duration is shown in Figure 71. One will note the maximum located near COS (Colorado Springs). This is primarily a result of the KCV field and it should be noted that a plot of the raw Hershfield output (not shown), clearly indicated an anomalous high value of 4-6 in a circle which was clearly defined by the transposition radius and centered near COS. In addition, the discontinuity at the boundary of this circle was one in which the surrounding values ranged from 1-2. As noted previously, an effort was made to not sample near the graphically obvious transposition boundaries. However, the magnitude of discontinuity between the center of this circle (4-6) and the surroundings (1-2) makes the inclusion of samples from anywhere within the circle questionable. Therefore, the PMP maximum here should be viewed with caution. It is also important to remember that exactly one simulation was performed over COS.

In addition to the 10-km<sup>2</sup>, 2-hour duration, similar products were created for the 10-km<sup>2</sup>, 6-hour duration and the 100-km<sup>2</sup>, 6-hour duration. These are shown in Figures 72 and 73 respectively. The variogram parameters along with the transposition parameters are summarized in Table 7. Some important points concerning these products and other attempted products are the following:

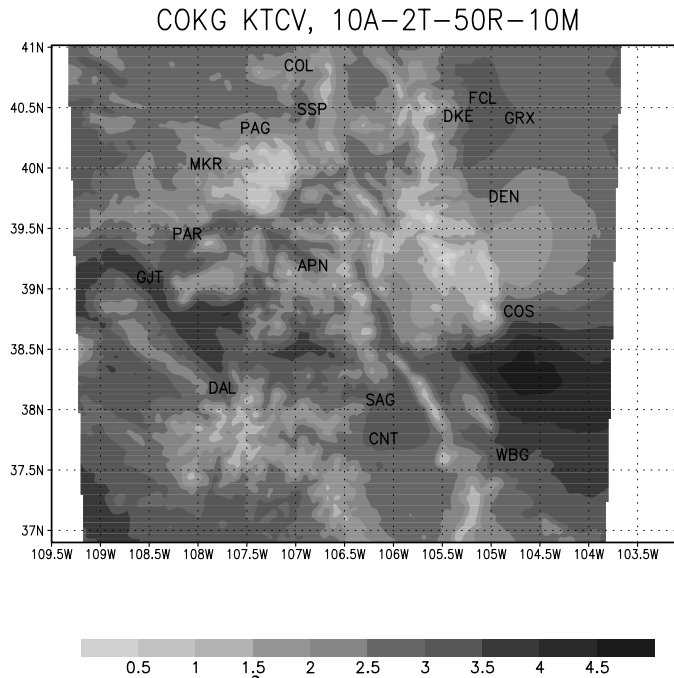


**Figure 69:** Cokriged KCV for 10-km<sup>2</sup>, 2-hour duration events using 50-scale factor transposition. Shading interval is 0.5 (dimensionless).

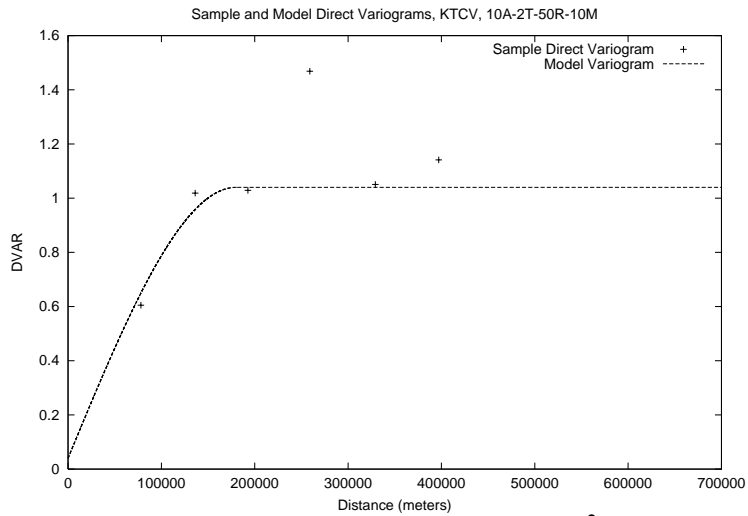


**Figure 70:** Model and sample variograms for KTCV, 10-km<sup>2</sup> area, 2-hour duration events with 50-scale factor transposition.

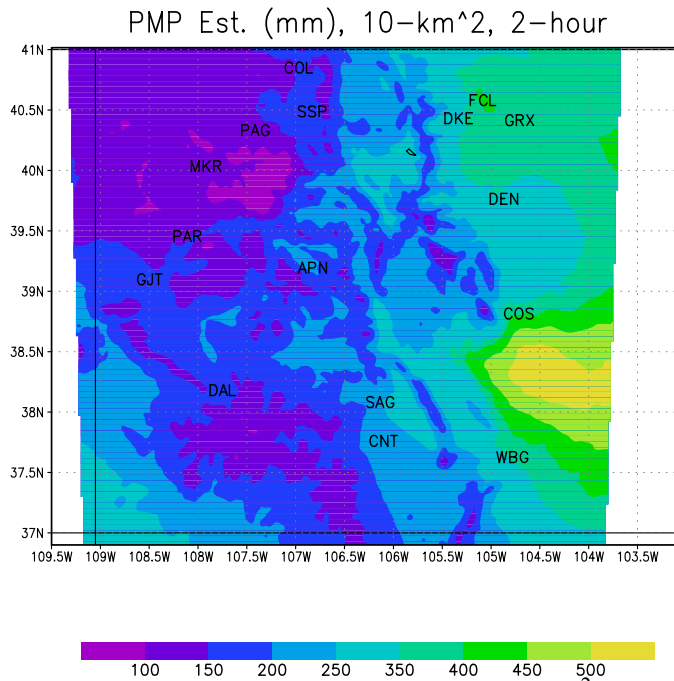


**Figure 71:** PMP (total-precipitation) estimate (mm) for 10-km<sup>2</sup>, 2-hour duration

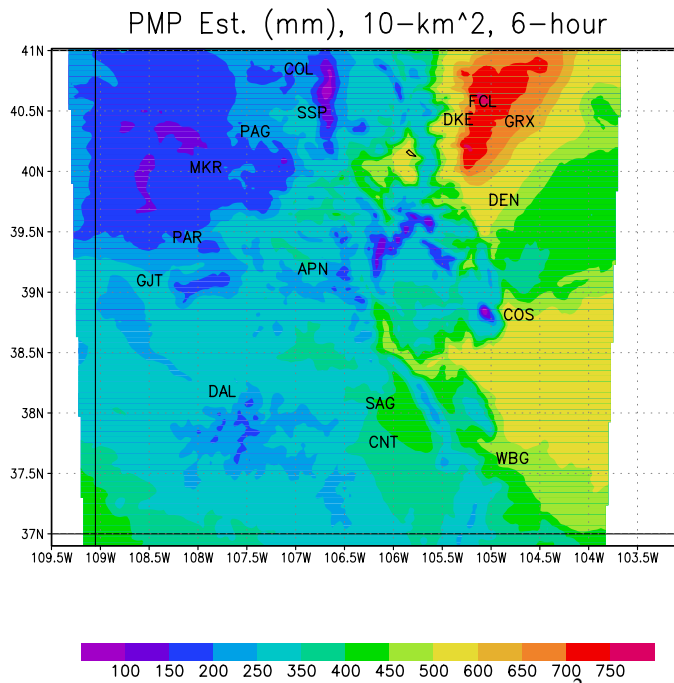


**Figure 72:** PMP (total-precipitation) estimate (mm) for 10-km<sup>2</sup>, 6-hour duration

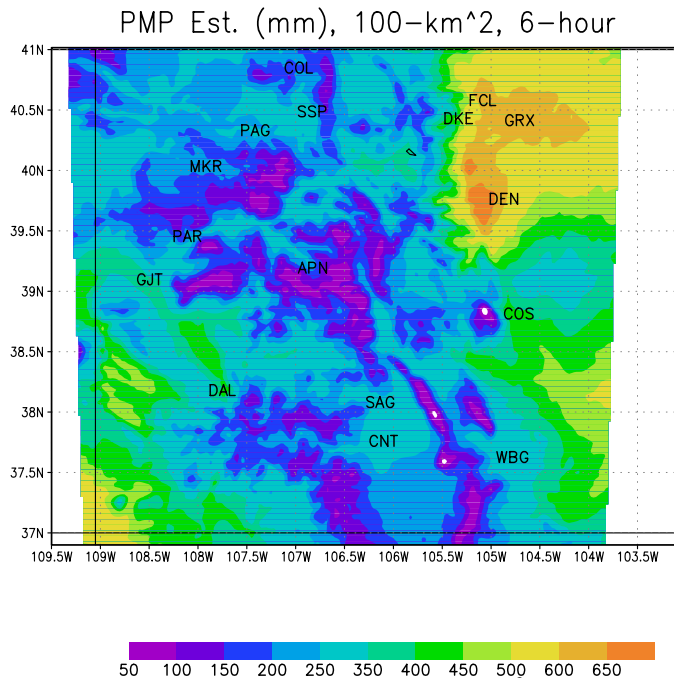


**Figure 73:** PMP (total precipitation) estimate for 100-km<sup>2</sup>, 6-hour duration

- The 10-km<sup>2</sup>, 12-hour duration was attempted. However, the Hershfield parameters were very similar to those for the 6-hour duration, which seemed to violate common sense. A probable explanation for this behavior is that the largest 10-km<sup>2</sup> events are generated in the simulations of LC events (McKee and Doesken, 1997), which, in reality and in our simulations, did not persist much longer than 6-hours.
- 10-km<sup>2</sup> has an equivalent radius of 1.78 km, which is comparable to the finest grid spacing in our simulations. Generally speaking, one should avoid focusing on grid point values. However, accumulated precipitation, even on a grid-point basis, is an aggregation of storm behavior and precipitation characteristics within and across storms for the duration of interest. Therefore, the small equivalent radius is not seen as a problem or unrepresentative of a realistic grid-cell area accumulation.
- As the area and duration increase, the number of events available for transposition decreases. Hence, for the mapped products, durations were not extended above 6-hours nor were areas extended above 100-km<sup>2</sup> due to lack of data.
- The simulations that were performed over various regions of the state were of different types (LC, GLC, and G), each of which can be expected to produce, in some cases by definition, extreme events at differing length and time-scales. No General cases were simulated east of the Continental Divide and only one LC case was simulated west of the Continental Divide. At the same time, the events simulated were selected from the most "extreme" events that are known to have occurred over the State of Colorado in a way that was intended to be

representative of each region (McKee and Doesken, 1997). This should be kept in mind when interpreting the PMP estimates.

- The products that were produced should be considered experimental and an example of a possibly useful, though involved procedure, for utilizing model output for PMP estimation.

We can compare some of these estimates with those from HMR 55A (Hansen et. al., 1988). The 10-km<sup>2</sup> products cannot be directly compared to the General storm type PMP estimates in 55A because no DAD relations were given for areas below 10-mi<sup>2</sup> in that report. Therefore the Local Storm indices from that report are used for comparison to 10-km<sup>2</sup> products following the stepwise instructions for Local Storm PMP provided in HMR 55A. This involves transforming the 1-mi<sup>2</sup> PMP index to the local elevation using the maximum persisting 12-hour 1000-mb dewpoints for July given in HMR 55A, converting the 1-hr durations to 2- and 6-hour durations using the depth-duration chart for Local Storms, and finally converting the 1-mi<sup>2</sup> area to 10-km<sup>2</sup> (~3.86 mi<sup>2</sup>) for each duration separately using the depth-area chart for Local Storms. For comparison to our 100-km<sup>2</sup> products, the General storm PMP estimates from HMR 55A are converted to 100-km<sup>2</sup> (38.6 mi<sup>2</sup>) estimates using the DAD relations for the appropriate terrain classification and subregion. These results are summarized below with 55A values rounded to the nearest inch.

**Table 6.** Comparison of PMP/PMLP estimates at selected locations from this report and HMR 55A (Hansen et. al., 1988).

	2-hr, 10-km <sup>2</sup>	6-hr, 10-km <sup>2</sup>	6-hr, 100-km <sup>2</sup>
<b>FORT COLLINS, CO</b> <i>(orographic subregion C from 55A)</i>			
This study: (PMP):	15.8"	29.6"	24.3"
This study: (PMLP)	15.5"	29.0"	24.4"
HMR 55A:	12"	14"	24"
<b>ESTES PARK, CO</b> <i>(assumed elev. 7890 ft, orographic subregion C from 55A)</i>			
This study: (PMP)	12"	21.8"	16.3"
This study: (PMLP)	11.6"	19.5"	15.2"
HMR 55A:	10"	12"	13"
<b>FRANKTOWN, CO</b> <i>(assumed elev 6300 ft, minimum non-orographic subregion C from 55A)</i>			
This study: (PMP)	11.1"	17"	18.1"
This study: (PMLP)	12.3"	18.3"	15.1"
HMR 55A:	12"	14"	24"
<b>SQUAW PASS</b> <i>(assumed elev. 9807', orographic subregion C from 55A)</i>			
This study: (PMP)	8.7"	13.4"	13.2"
This study: (PMLP)	9.3"	11.3"	9.2"
HMR 55A:	8"	9"	13"

\* Franktown, Colorado is used as an illustration of PMP estimation only. The number of simulated storms at this location is too few for reliable estimates.

Note that for Franktown, CO (located along Cherry Creek), the 6-hr, 10- and 100-km<sup>2</sup> results, using our method, are inconsistent as the latter has a larger average depth than the former. This is one of the major drawbacks to the proposed method in that it does not guarantee consistency among the various areas because DAD relations are not explicitly used. Presumably, if more data (model output), were to become available, the inconsistencies would become less frequent in the final mapped field. It should also be remembered that only one simulation was actually performed with a convection resolving grid that included Franktown.

The HMR 55A results seem to have similar inconsistencies for all four locations, but this is ambiguous. As noted earlier, the HMR 55A, 6-hr, 10- and 100-km<sup>2</sup> PMP estimates are for different types of storms in that study -- Local for the former and General for the latter. Our estimates are significantly larger at all three locations for the 6-hr, 10-km<sup>2</sup> duration, when compared to the 55A Local Storm PMP, and larger for the other three duration-area combinations except at Franktown. Note, however, these estimates include contributions by hail. We next examine PMP estimates for rain-only under the assumption that hail will melt so slowly that major flooding will not occur.

Figures 74, 75 and 76 show PMLP (rain-only) estimates using the same procedure used in estimating PMP. Table 8 shows the model variogram parameters used in the kriging and cokriging of HMEAN and KTCV for the rain-only isohyetal events. As with the total-precipitation PMP estimates, the lack of sample data results in modeled variograms that are approximate at best. It should also be noted that the estimation procedure previously outlined does not guarantee consistency between the PMP and PMLP estimates. That is, it is possible for the procedure to produce PMLP estimates which are larger than the collocated PMP estimates, which is clearly incorrect. The main areas in which this inconsistency occurs are the lower elevations of northwestern and southeastern Colorado as well as the Palmer Divide. In these areas, the PMLP estimate often exceeds the PMP estimate by over 10%.

The greatest reductions of PMLP relative to PMP are in western Colorado, excepting the 100-km<sup>2</sup>, 6-hour which also shows significant reductions over the high elevations of the Front Range. PMLP estimates for Squaw Pass, Fort Collins, Estes Park and Franktown are shown along with the previously discussed PMP estimates at these points in Table 6. The PMP/PMLP inconsistency is most apparent at Franktown. At Fort Collins the PMLP and PMP estimates are similar due to the high rain fraction simulated in the Fort Collins flood simulations at 5100 ft. elevation. Reductions at Estes Park are less than 10% for each area and duration. At Squaw Pass, the reduction percentages are 16% and 30% for the 6-hour, 10- and 100-km<sup>2</sup> estimates respectively. At 2-hour, 10-km<sup>2</sup>, there again exists a PMP versus PMLP inconsistency at Squaw Pass.

**Table 7.** Total-precipitation, transposition, sample statistics and variogram specifications for 10-km<sup>2</sup> 2-hour, 10-km<sup>2</sup> 6-hour, and 100-km<sup>2</sup> 6-hour area duration combinations. "r" is the correlation coefficient, and a and b are the variogram model range and sill values, respectively.

	10 km <sup>2</sup> , 2-hour	10 km <sup>2</sup> , 6-hour	100-km <sup>2</sup> , 6-hour
Equivalent radius (km)	1.78	1.78	5.64
Transposition scale factor	50	50	20
Transposition radius (km)	89.2	89.2	112
HMEAN sample std. dev.(mm)	20.1	21.5	22.9
HMEAN-ELEV sample r	-0.65	-0.60	-0.70
KCV sample std. dev.	0.98	1.49	1.47
KCV-ELEV sample r	-0.62	-0.46	-0.67
HMEAN direct vario. (mm <sup>2</sup> )	Nug.=50.0 Gauss: b = 750.0 a = 433 km	Nug. = 50.0 Gauss: b = 750.0 a = 346 km	Nug. = 30.0 Gauss: b = 700.0 a = 381 km
HMEAN-ELEV cross vario.	—	—	-0.70·PDC
KCV direct vario.	Nug. = 0.04 Sphere: b = 1.0 a = 180 km	Nug = 0.6 Sphere: b = 1.9 a = 125 km	Nug = 0.1 Sphere: b = 2.4 a = 180 km
KCV cross vario.	-0.75·PDC	-0.52·PDC	-0.66·PDC

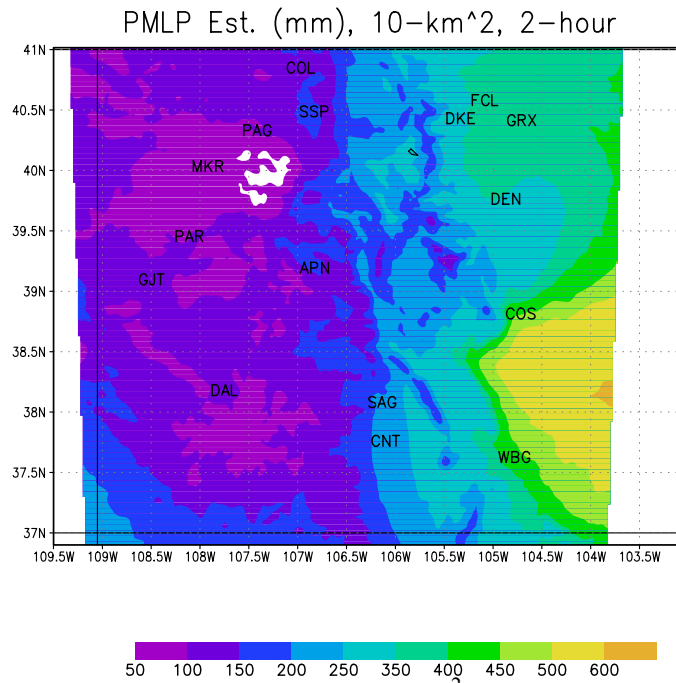


Figure 74: PMLP estimate (rain-only) for the 10-km<sup>2</sup>, 2-hour duration.

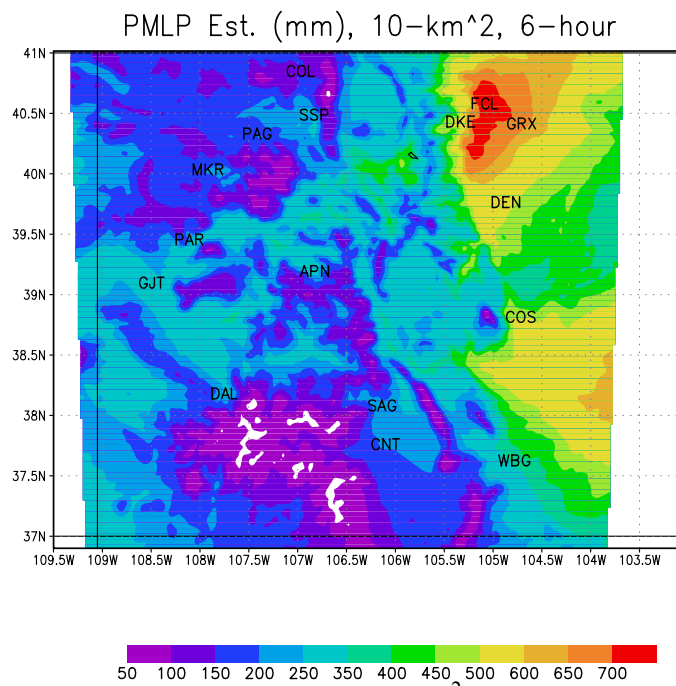


Figure 75: PMLP estimate (rain-only) for the 10-km<sup>2</sup>, 6-hour duration.

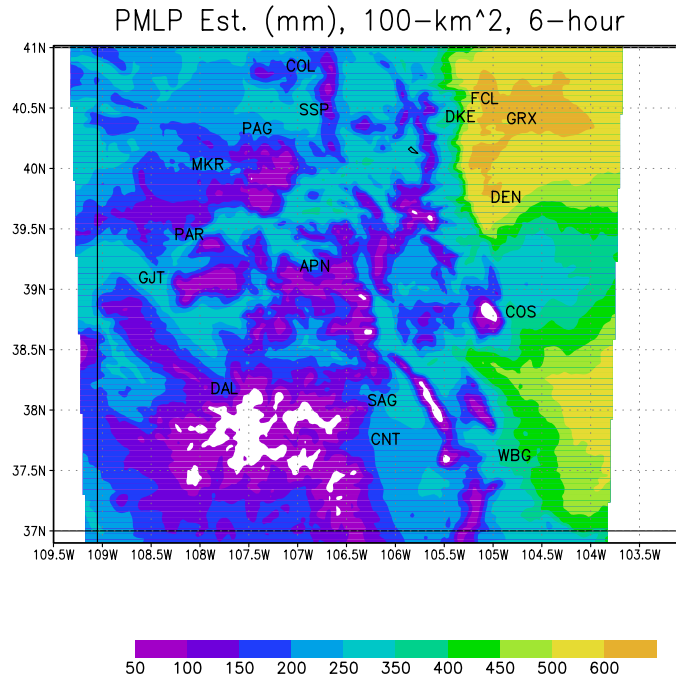


Figure 76: PMLP estimate (rain-only) for the 100-km<sup>2</sup>, 6-hour duration.

**Table 8.** Same as Table 7 except for liquid-precipitation. Transposition statistics identical to that for total precipitation (Table 7). "r" is the correlation coefficient, and a and b are the variogram model range and sill values, respectively.

	10 km <sup>2</sup> , 2-hour	10 km <sup>2</sup> , 6-hour	100-km <sup>2</sup> , 6-hour
HMEAN sample std. dev.(mm)	19.4	24.3	23.8
HMEAN-ELEV sample r	-0.68	-0.73	-0.62
KCV sample std. dev.	1.23	1.57	1.57
KCV-ELEV sample r	-0.57	-0.57	-0.84
HMEAN direct vario. (mm <sup>2</sup> )	Nug.=30.0 Gauss: b = 720.0 a = 450 km	Nug. = 50.0 Gauss: b = 900.0 a = 400 km	Nug. = 30.0 Gauss: b = 700.0 a = 381 km
HMEAN-ELEV cross vario.	—	-0.50PDC	-0.70-PDC
KCV direct vario.	Nug. = 0.1 Sphere: b = 2.1 a = 320 km	Nug = 0.7 Sphere: b = 2.1 a = 200 km	Nug = 0.3 Sphere: b = 2.7 a = 180 km
KCV cross vario.	-0.67-PDC	-0.57-PDC	-0.67-PDC

## 8. Summary and Conclusions

We have developed a new approach to extreme precipitation estimation using a convective-storm-resolving mesoscale model (RAMS). RAMS was run for six historical heavy precipitating cases over Colorado. A total of 27 simulations have been performed for these case studies in which land surface parameters such as soil moisture are varied, various model parameters (e.g., for diffusion) are varied, different large-scale analyses are used, atmospheric moisture perturbations are imposed, and the synoptic pattern is transposed relative to the underlying terrain. The following conclusions have been drawn from the analyses of these cases.

- In each of the observed extreme precipitation cases, RAMS is able to produce one or more heavy rain events. However, the position and timing of those events does not always coincide with the observations. Typical spatial and timing errors are 10 to 50km and one to several hours, respectively.
- The most accurate control simulations occur with the least convective, large-scale forced storms like the San Juan and Park Range storms. The least successful simulations occur with the older convective events like the Big Thompson storm. This is likely due to the coarse resolution of the initial NCEP reanalysis data used for the older events and unavailability of good, high-resolution soil moisture data. More recent cases in which ETA upper air and surface analysis data plus ETA soil moisture data generally provide the best agreement with observations.
- Even in cases where the maximum simulated precipitation amounts are in close agreement with observations, the actual scenario of convective evolution is often different from that observed. We believe that this is primarily due to inadequate detail in the initialization datasets for the atmosphere and land-surface parameters (especially soil moisture). Thus, the simulated scenarios of extreme precipitation in a given favorable synoptic setting may differ appreciably from the observed event. This problem is generally worse for older cases.
- Sensitivity tests reveal that simulations of heavy convective events are highly sensitive to the specification of initial soil moisture fields.
- Attempts to simulate more extreme events by increasing precipitable water in low- to mid-levels often produce the opposite effect, due to increased widespread cloudiness that reduces surface insolation. An exception was the case of increasing precipitable water on the western slope for the Fort Collins Flood. In that run the increased moist air and cloudiness to the west did not reduce the eastern slope surface heating or strength of the mountains-plains solenoid, and the advection of mid-level moisture from the west resulted in the most extreme rainfall event of all the simulations performed.
- Precipitation maxima occurring at higher elevations have significant contributions from hail, which may reduce surface runoff rates due to prolonged melting.

- A PMP method designed for use with model output has been proposed and demonstrated. However a larger dataset is required in order to evaluate the effects of variogram models on the PMP estimates.

## 9. Suggestions for Future Research

There are several opportunities for improving the quality of historical simulations in the near future. Fedor Mesinger (personal communication) of NCEP is finalizing an ETA reanalysis data set. In contrast to the current NCEP MRF reanalysis data, this should provide higher vertical and horizontal resolution, and we expect that using these data should lead to improved simulation of extreme precipitation events back to the mid-1950's. In addition, our group as well as other groups is developing new methods for estimating soil moisture contents with higher horizontal spatial resolution. Thus some of the variability in model simulations of extreme precipitation events associated with soil moisture uncertainties can be minimized.

Our simulations of extreme precipitation events conclude with rainfall on the ground. But the destructive power of those events is dependent upon the local topography, land-use, soil wetness, and vegetation. Thus it would be desirable to interface RAMS with a runoff/routing model such as CASC2D to explicitly represent runoff and streamflow associated with extreme precipitation events.

This research has also shown that at high elevations, a significant fraction of the total precipitation occurs in the form of hail. We speculate that since it takes time for hail to melt, this decreases the chance that flashfloods will result from such extreme precipitation events at higher elevations. It is desirable to test this hypothesis more fully by developing a surface hail melting model that can be interfaced with RAMS and a surface runoff/routing model. While this is being done one could also implement or develop a surface snow melting model so that one could examine situations in which heavy rainfall occurs over a snow surface and then the coupled effects of rainfall runoff and snowmelt runoff can be examined.

Transferability or adaptability of the storm-resolving model based extreme precipitation methodology is also something that needs consideration. While this may not be important to the State of Colorado, other Federal, State, local or foreign government agencies may wish to adapt this approach to their regions of interest. Because of the strong terrain forcing in Colorado, storm-resolving simulations in Colorado may be easier than in regions without such intense physiographic forcing. Our own research has shown (see Bernardet et al., 2000) that storms over flatter terrain in the central U.S. require better definition of soil moisture mapping and preexisting mesoscale disturbances (i.e., thunderstorm cold pools) than over Colorado. Thus this approach may be less successful in those regions than in Colorado. Still this should be examined as this simulation approach offers the opportunity to extend the data base needed for PMP estimation procedures beyond what can be currently provided by historical storms.

Future studies should examine the Hershfield procedure in more detail. Specifically, the relationship between the Hershfield equation and extreme value distributions should be quantified and related to the collection of DAD events under consideration [c.f. Chow (1951) and Gumbel (1958)]. This may aid in planning future sets of simulations with the goal of obtaining a more statistically homogeneous collection of input DAD events at each estimation point and quantifying the uncertainty in the Hershfield parameters.

Should enough sample data become available in the future, one may be able to utilize anisotropic variogram models. This could significantly improve estimates in a region such as Colorado where the major orographic features tend to be oriented in a north-south direction.

### **Acknowledgements**

This research was supported by the State of Colorado Department of Natural Resources under Contract ENC #C154213. We thank the program director, Alan Pearson, for his patience in dealing with our slowness in completing this research and dealing with university researchers who are rarely timely in producing progress reports. We also must emphasize that we appreciate that he and the Colorado Department of Natural Resources, were willing to stick their necks out and provide support for a very different approach to extreme precipitation estimation than has been done in the past. We doubt that any U.S. federal laboratory would have been so bold or have the foresight to support the development of this approach to extreme precipitation estimation.

### **References**

- Ashby, T., 2001: Impact of Soil Moisture Initialization on a Simulated Flash Flood. M.S. Thesis, Colorado State University, Dept of Atmospheric Science, Fort Collins, CO 80523, in preparation.
- Augustine, J.A., 1985: An automated method for the documentation of cloud-top characteristics of mesoscale convective systems. NOAA Tech. Memo. ERL ESG-10, NOAA, Environmental Research Laboratories, Environmental Sciences Group, Boulder, CO, 121 pp.
- Avery, B.A., C.N. Jones, J.D. Colton, and M.P. Meyers, 2001: A southwest Colorado mountain flash flood in an enhanced monsoonal environment. Online paper at <http://www.crh.noaa.gov/gjt/science.htm>, National Weather Service, Grand Junction, Colorado.
- Barnes, S.L., 1973: Mesoscale objective map analysis using weighted time series observations. NOAA Tech. Memo. ERL NSSL-62, 60 pp. [NTIS COM-73-10781].

- Bernardet, L.R., L.D. Grasso, J.E. Nachamkin, C.A. Finley, and W.R. Cotton, 2000: Simulating convective events using a high-resolution mesoscale model. *J. Geophys. Res.*, **105**, D11, 14,963-14,982.
- Caracena, F., R.A. Maddox, L.R. Hoxit and C.F. Chappell, 1979: Mesoanalysis of the Big Thompson storm. *Mon Wea. Rev.*, **107**, 1-17.
- Chang, T.J., and H.Y. Sun, 1997: Study of potential flash floods by Kriging method., *J. Hydrol. Eng.*, **2**(3), 104-108.
- Chow, V.T., 1951: A general formula for hydrologic frequency analysis. *Trans. Amer. Geophys. Union*, **32**, 231-237.
- Cooper, R. M., and J. D. Istok, 1988: Geostatistics applied to groundwater contamination. I: Methodology, *J. Environ. Eng.*, **114**, 270-286.
- Cotton, W.R., R.A. Peilke, Sr., R.L. Walko, G.E. Liston, C.T. Tremback, H. Jiang, R.L. McAnelly, J.Y. Harrington, M.E. Nicholls, 2002: RAMS 2001: Current status and future directions. *Meteor. And Atmos Physics*, in press
- Cressman, G., 1959: An operational analysis system. *Mon. Wea. Rev.*, **87**, 367-374.
- David, M., 1977: *Geostatistical Ore Reserve Estimation*. Elsevier Scientific Publishing Company, 364 pp.
- Doesken, N.J. and T.B. McKee, 1998: An analysis of rainfall for the July 28, 1997 flood in Fort Collins, Colorado. Climatology Rep. 98-1, Department of Atmospheric Science, Colorado State University, 55 pp. [Available from Colorado Climate Center, Department of Atmospheric Science, Colorado State University, Fort Collins, CO, 80523]
- Gumbel, E.J., 1958: *Statistics of extremes*. Columbia University Press, 371 pp.
- Hansen, E.M., 1987: Probable maximum precipitation for design floods in the United States. *J. Hydrol.*, **96**, 267-278.
- Hansen, E. M., D. D. Fenn, L. C. Schreiner, R. W. Stodt, and J. F. Miller, 1988: *Probable Maximum Precipitation Estimates-United States between the Continental Divide and the 103rd Meridian.*, Hydrometeorological Report No. 55A, U.S. Dept of Commerce, NOAA, U.S. Dept. of Army, COE, U.S. Dept. of Interior, BOR, 242 pp.
- Harrington, Jerry Y., 1997: The effects of radiative and microphysical processes on simulated warm and transition season Arctic stratus. Ph.D. dissertation, Atmospheric Science Paper No. 637, Colorado State University, Dept. of Atmospheric Science, Fort Collins, CO 80523, 289 pp.

- Harrington, J.Y., T. Reisin, W.R. Cotton, and S.M. Kreidenweis, 1999: Cloud resolving simulations of Arctic stratus. Part II: Transition-season clouds. *Atmos. Res.*, **55**, 45-75.
- Henz, J.F., 2000: Cloud-to-ground lightning relationships to flash flooding in western Colorado monsoon thunderstorms. Poster presentation, Southwest Weather Symposium (Tucson, AZ), National Weather Service, University of Arizona, and COMET.
- Hershfield, D. M., 1961: Estimating the probable maximum precipitation., *J. Hydraulics Div. Proc. Amer. Soc. Civil Eng.*, **HY5**, 99-116.
- Hershfield, D. M., 1965: Method for estimating probable maximum rainfall, *J. Amer. Water Works Assoc.*, **57**, 965-972.
- Hevesi, J. A., J. D. Istok, and A. L. Flint, 1992: Precipitation estimation in mountainous terrain using multivariate geostatistics. Part I: Structural analysis., *J. Appl. Meteor.*, **31**, 661-676.
- Isaaks, E. H., and R. M. Srivistava, 1989: *An Introduction to Applied Geostatistics*. Oxford University Press, 561pp.
- Jarrett, R.D., 1983: Flood elevation limits in the Rocky Mountains. In Kuo, C.Y., ed., Engineering hydrology -- Proceedings of the symposium sponsored by the Hydraulics Division of the American Society of Civil Engineers, San Francisco, CA, July 25-30, 1983, New York, American Society of Civil engineers, p. 180-185.
- Jarrett, R.D., and J.E. Costa, 1983: Multidisciplinary approach to the flood hydrology of foothill streams in Colorado. *International Symposium on Hydrometeorology* (A.I. Johnson and R.A. Clark, eds.), American Water Resources Association, June 13-17, 1982, Denver, pp. 565-569.
- Kalnay, E., and co-authors, 1996: The NCEP/NCAR 40-year reanalysis project. *Bull. Amer. Meteor. Soc.*, **77**, 437-471.
- Lang, L.F., 1999: 1999 flood response update. Memorandum, Agenda item 10, September 27-28, 1999 Board Meeting, Colorado Water Conservation Board. 4 pp. (downloaded from <http://cwcb.state.co.us/agendas/Sep%2099/item10.pdf>)
- Maddox, R.A., F. Caracena, L.R. Hoxit and C.F. Chappell, 1977: Meteorological aspects of the Big Thompson Flash Flood of 31 July 1976. NOAA Tech. Report ERL 388-APCL 41, U.S. Dept. of Commerce, National Oceanic and Atmos. Admin., Environmental research Lab., 83 pp.
- Maddox, R.A., F. Canova, and L.R. Hoxit, 1980: Meteorological characteristics of flash flood events over the western United States. *Mon. Wea. Rev.*, **108**, 1866-1877.

- McKee, Thomas B., and Nolan J. Doesken, 1997: Colorado extreme storm precipitation data study. Final Report. Summary of accomplishment and work performed February 15, 1995 through October 31, 1996. Climatology Report 97-1, CSU, Fort Collins, CO, May, 107 pp.
- Meyers, M.P., R.L. Walko, J.Y. Harrington, and W.R. Cotton, 1997: New RAMS cloud microphysics parameterization. Part II: The two-moment scheme. *Atmos. Res.*, **45**, 3-39.
- Nachamkin, J., W.R. Cotton, 2000: Interaction between a developing mesoscale convective system and its environment. Part II. Numerical simulation. *Mon. Wea. Rev.*, **128**, 1225-1244.
- Olsson, P.Q., J.Y. Harrington, G. Feingold, W.R. Cotton, and S. Kreidenweis, 1998: Exploratory cloud-resolving simulations of boundary layer Arctic stratus clouds. Part I: Warm season clouds. *Atmos. Res.*, **47-48**, 573-597.
- Petersen, W.A. and Coauthors, 1999: Mesoscale and radar observations of the Fort Collins flash flood of 28 July, 1997. *BAMS*, **80**, 191-216.
- Pielke R.A. and Coauthors, 1992: A comprehensive meteorological modeling system -- RAMS. *Meteorol. Atmos Phys.*, **49**, 69-91.
- United States Department of Commerce, 1960: *Generalized Estimates of Probable Maximum Precipitation for the United States West of the 105th Meridian*, Tech. Paper No. 38, United States Department of Commerce, Weather Bureau., 66 pp.
- van den Heever, S.C. 2001: The impact of several hail parameters on simulated supercell storms. Ph.D. dissertation, Colorado State University, Dept. of Atmospheric Science, Fort Collins, CO 80523, 265 pp. (Available as Atmospheric Science Paper No. 711.)
- Wackernagel, Hans, 1998: *Multivariate Geostatistics*. Springer, 291 pp.
- Walko, R.L., L.E. Band, J. Baron, T.G.F. Kittel, R. Lammers, T.J. Lee, D. Ojima, R.A. Pielke, C. Taylor, C. Tague, C.J. Tremback, and P.L. Vidale, 2000: Coupled Atmosphere-Biophysics-Hydrology Models for Environmental Modeling. *J. Appl. Meteor.*, **39**, 931-944.
- Walko, R.L., W.R. Cotton, J.L. Harrington, M.P. Meyers, 1995: New RAMS cloud microphysics parameterization. Part I: The single-moment scheme. *Atmos. Res.*, **38**, 29-62.
- Walko, R.L., and C.J. Tremback, 2000: RAMS, Regional Atmospheric Modeling System, Version 4.2 Model input namelist parameters. Formerly distributed by Mission Research Corp. ASTeR Division. (Available from the authors of this report.)

Warner, T.T., and H-M. Hsu, 2000: Nested-model simulation of moist convection: The impact of coarse-grid parameterized convection on fine-grid resolved convection. *Mon. Wea. Rev.*, **128**, 2211-2230.

World Meteorological Organization, 1973: *Manual for Estimation of Probable Maximum Precipitation*, Operation Hydrology Rep. No. 1, World Meteorological Organization, 190 pp.

## Appendix 1

The following listing is the “RAMSIN” namelist that specifies the default model settings used for the simulations described in this report.

```

$MODEL_GRIDS
EXPNAME = 'DALLAS-CONTROL1',
VTABCUST='standard',

RUNTYPE = 'INITIAL',      ! type of run: MAKESFC, INITIAL, HISTORY,
                          ! MAKEVFILE, or MEMORY

TIMEUNIT = 's',          ! 'h','m','s' - Time units of
                          ! TIMMAX, TIMSTR, VTIME

TIMMAX= 86400.,          ! Final time of simulation

! Start of simulation or ISAN processing

IMONTH1 = 07,           ! Month
IDATE1 = 31,            ! Day
IYEAR1 = 1999,          ! Year
ITIME1 = 1200,          ! GMT of model TIME = 0.

NGRIDS = 4,              ! Number of grids to run

NNXP = 57,62,74,101,    ! Number of x gridpoints
NNYP = 47,62,74,107,    ! Number of y gridpoints
NNZP = 44,44,44,44,     ! Number of z gridpoints

NZG = 7,                 ! Number of soil layers
NZS = 1,                 ! Maximum number of snow layers

NXTNEST = 0, 1, 2, 3,   ! Grid number which is the next
                          ! coarser grid

! Coarse grid specifications

IHTRAN = 1,              ! 0-Cartesian, 1-Polar stereo
DELTAX = 80000.,        ! X and Y grid spacing
DELTAY = 80000.,

DELTAZ = 100.,          ! Z grid spacing (set to 0. to use ZZ)
DZRAT = 1.12,           ! vertical grid stretch ratio
DZMAX = 800.,           ! maximum delta Z for vertical stretch

ZZ= 0.0,
  30.0, 60.0, 90.0, 120.0, 150.0,
  180.0, 210.0, 240.0, 270.0, 300.0,

                          ! Vertical levels if DELTAZ = 0

DTLONG = 60.,           ! Coarse grid long timestep
NRATIO = 3,              ! Small timestep ratio

                          ! Nest ratios between this grid
                          ! and the next coarser grid.
NSTRATX = 1, 4, 4, 3,   ! x-direction
NSTRATY = 1, 4, 4, 3,   ! y-direction
NNDTRAT = 1, 3, 3, 2,   ! time

NESTZ1 = 0,              ! contort coarser grids if negative
NSTRATZ1=1,1,3,3,3,3,2,2,2,2,1,1,1,1, !
NESTZ2 = 0,              ! contort coarser grids if negative
NSTRATZ2=1,1,3,3,3,3,2,2,2,2,1,1,1,1, !

```

```

POLELAT = 38.2,           ! Latitude of pole point
POLELON = -107.8,        ! Longitude of pole point

CENTLAT= 38.999, 39.0, 37.929, 37.929,      ! Center lat of grid
CENTLON= -107.001, -107.0, -108.07, -107.94, ! Center lon of grid

! Grid point on the next coarser
! nest where the lower southwest
! corner of this nest will start.
! IF NINEST or NJNEST = 0,
! use CENTLAT/LON
NINEST = 1, 0, 0, 0,      ! i-point
NJNEST = 1, 0, 0, 0,      ! j-point
NKNEST = 1, 1, 1, 1,      ! k-point

NNSTTOP = 1, 1, 1, 1,     ! Flag (0-no or 1-yes) if this
NNSTBOT = 1, 1, 1, 1,     ! nest goes the top or bottom of the
! coarsest nest.

GRIDU = 0., 0., 0., 0.,   ! u-component for moving grids
GRIDV = 0., 0., 0., 0.,   ! v-component for moving grids

$END

$MODEL_FILE_INFO

! Variable initialization input

INITIAL = 2,               ! Initial fields -
! 1=horiz.homogeneous, 2=variable
VARFPFX = '../var/var',   ! varfile prefix

NUDLAT = 5,               ! number of points in the lateral bnd region
TNUDLAT = 200.0,          ! nudging time scale (s) at lateral boundary
TNUDCENT = 0.,           ! nudging time scale (s) in center of domain
TNUDTOP = 300.0,         ! nudging time scale (s) at top of domain
ZNUDTOP = 20000.,        ! nudging at top of domain above
! this height (m)

! History file input

TIMSTR= 25200.,           ! time of history start (see TIMEUNIT)
HFILIN = '../history/s.h1976-07-31-190000', ! input history file name

! History/analysis file output

IOUTPUT= 2,              ! 0-no files, 1-save in ASCII,
! 2-save in binary
HFILOUT= '../history/s.h', ! history file prefix
AFILOUT= '../analysis/s.a', ! analysis file prefix
FRQHIS = 3600.,          ! history file frequency
FRQANL = 900.,           ! analysis file frequency
KWRITE = 0,              ! 1-write, 0-don't write scalar K's
! to analysis

! Input topography variables

SFCFILES = '../surface/sfc', ! File path and prefix for surface
! characteristic files.
SSTFPFX = '../surface/sst', ! Path and prefix for sst files

ITOPTFLG = 1,1,1,1,      ! 2 - Fill data in "rsurf"
ISSTFLG = 1,1,1,1,      ! 0 - Interpolate from coarser grid
IVEGTFLG = 1,1,1,1,      ! 1 - Read from standard Lat/Lon data file
ISOILFLG = 2,2,2,2,      ! soil files not yet available:
! avoid isoilflg=1

NOFILFLG = 2,2,2,2,      ! 2 - Fill data in "rsurf"
! 0 - Interpolate from coarser grid

```

```

IUPDSST = 0,                ! 0 - No update of SST values during run
                             ! 1 - Update SST values during run

                             ! The following only apply for IxxxxFLG=1
                             ! And they are all grid dependent

ITOPTFN = '/ul/rams/data/DEM30s/EL',
           '/ul/rams/data/DEM30s/EL',
           '/ul/rams/data/DEM30s/EL',
           '/ul/rams/data/DEM30s/EL',

ISSTFN = '/ul/rams/data/sst42/S',
          '/ul/rams/data/sst42/S',
          '/ul/rams/data/sst42/S',
          '/ul/rams/data/sst42/S',

IVEGTFN = '/ul/rams/data/ogedata/GE',
           '/ul/rams/data/ogedata/GE',
           '/ul/rams/data/ogedata/GE',
           '/ul/rams/data/ogedata/GE',

ISOILFN = ' ',              ! ****soil files not yet available
           ',
           ',
           ',
           ',

SILAVWT = 0., 0., 0., 0.,   ! Weighting of topo silhouette averaging
TOPTWVL = 4., 4., 4., 4.,   ! Topo wavelength cutoff in filter

MKCOLTAB = 0,                ! make microphysics collection table:
                             ! 0 = no, 1 = yes

COLTABFN = '/users/ashby/429/data/ct2.0',
           ! collection table filename to read
           ! or write

$END

$MODEL_OPTIONS

NADDSC = 0,                  ! Number of additional scalar species
      ! Numerical schemes

ICORFLG = 1,                 ! Coriolis flag/2D v-component -
                             ! 0=off, 1=on

IBND = 1,                    ! Lateral boundary condition flags
JBND = 1,                    ! 1-Klemp/Wilhelmson, 2-Klemp/Lilly,
                             ! 3-Orlanski, 4-cyclic

CPHAS = 20.,                 ! Phase speed if IBND or JBND = 1
LSFLG = 1,                   ! Large-scale gradient flag for
                             ! variables other than normal velocity:
                             ! 0 = zero gradient inflow and outflow
                             ! 1 = zero gradient inflow, radiative b.c.
                             ! outflow
                             ! 2 = constant inflow, radiative b.c. outflow
                             ! 3 = constant inflow and outflow

NFPT = 0,                    ! Rayleigh friction - number of points from
                             ! the top

DISTIM = 400.,              ! dissipation time scale

      ! Radiation parameters

ISWRTYP = 3,                 ! Shortwave radiation type 0-none, 2-Mahrer/Pielke, 1-Chen

```

```

ILWRTYP = 3, ! Longwave radiation type 0-none, 2-Mahrer/Pielke, 1-Chen
RADFRQ = 900., ! Frequency of radiation tendency update in seconds
LONRAD = 1, ! Longitudinal variation of shortwave (0-no, 1-yes)

! Cumulus parameterization parameters

NNQPARM = 1, 0, 0, 0, ! convective parameterization flag
! 0-off, 1-on

CONFRQ = 1200., ! Frequency of conv param. updates in seconds
WCLDBS = .001, ! vertical motion needed at cloud base for convection

! Surface layer and soil parameterization

NPATCH = 2, ! number of "patches" per grid cell (min of 2)

NVEGPAT = 1, ! number of "patches" per grid cell to be filled from
! vegetation files (min of 1, max of NPATCH-1)

ISFCL = 1, ! surface layer/soil/veg model
! 0-specified surface layer gradients
! 1-soil/vegetation model

NVGCON = 1, ! Vegetation type
! 1 -- Crop/mixed farming 2 -- Short grass
! 3 -- Evergreen needleleaf tree 4 -- Deciduous needleleaf tree
! 5 -- Deciduous broadleaf tree 6 -- Evergreen broadleaf tree
! 7 -- Tall grass 8 -- Desert
! 9 -- Tundra 10 -- Irrigated crop
!11 -- Semi-desert 12 -- Ice cap/glacier
!13 -- Bog or marsh 14 -- Inland water
!15 -- Ocean 16 -- Evergreen shrub
!17 -- Deciduous shrub 18 -- Mixed woodland

TVGOFF = 0., ! Initial veg temp offset

PCTLCON = 1.0, ! constant land percentage if for all domain
NSLCON = 6, ! constant soil type if for all domain
! 1=sand 2=loamy sand 3=sandy loam
! 4=silt loam 5=loam 6=sandy clay loam
! 7=silty clay loam 8=clay loam 9=sandy clay
! 10=silty clay 11=clay 12=peat

ZROUGH = 0.05, ! constant roughness if for all domain
ALBEDO = 0.2, ! constant albedo when not running soil model
SEATMP = 280.0, ! constant water surface temperature

DTHCON = 0., ! constant surface layer temp gradient for no soil
DRTCEN = 0., ! constant surface layer moist gradient for no soil

SOILDZ = 0., ! soil model grid spacing

SLZ = -2.0, -1.3, -.82, -.5, ! soil grid levels (m)
-.29, -.15, -.06,

SLMSTR = 0.4, 0.4, 0.4, 0.4, ! initial soil moisture
0.4, 0.4, 0.4

STGOFF= 0.0, 0.0, 0.0, 0.0, ! Initial soil temperature offset
0.0, 0.0, 0.0, ! lowest atmospheric level

! Eddy diffusion coefficient parameters

IDIFFK = 1,1,1,2, ! K flag:
! 1 - Horizontal deformation/ Vertical Mellor-Yamada
! 2 - Anisotropic deformation (horiz and vert differ)
! 3 - Isotropic deformation (horiz and vert same)
! 4 - Deardorff TKE (horiz and vert same)

CSX = .2, .2, .2, .2, ! Adjustable param., deform. horiz. K's coefficient
CSZ = .2, .2, .2, .2, ! Adjustable param., deformation vert. K's coefficient

```

```

XKHKM = 3.,3.,3.,3., ! Ratio of horizontal K_h to K_m for deformation
ZKHKM = 3.,3.,3.,3., ! Ratio of vertical K_h to K_m for deformation

AKMIN= 0.6, 0.75, 1.0, 1.8, ! Ratio of minimum horizontal eddy viscosity
! coefficient to typical value from deformation K

! Microphysics

LEVEL = 3, ! moisture complexity level
INUCPRG = 0, ! Prognose ice nuclei (0-no, 1-yes)

ICLOUD = 4, ! Microphysics flags
IRAIN = 2, !-----
IPRIS = 5,
ISNOW = 2, ! 1 - diagnostic concen.
IAGGR = 2, ! 2 - specified mean diameter
IGRAUP = 2, ! 3 - specified y-intercept
IHAIL = 2, ! 4 - specified concentration
! 5 - prognostic concentration

CPARM = .3e9,
RPARM = .1e-2, ! Microphysics parameters
PPARM = 0., ! -----
SPARM = .1e-2, ! Characteristic diameter,
APARM = .1e-2, ! number concentration, or
GPARM = .1e-2, ! y-intercept
HPARM = .3e-2,

! gnus for: cloud rain pris snow aggr graup hail
GNU = 2., 2., 2., 2., 2., 2., 2., ! gamma shape parms

$END

$MODEL_SOUND
! Sounding specification

! Flags for how sounding is specified

IPSFLG=1, ! specifies what is in PS array
! 0 - pressure (mb), 1 - heights (m), PS(1)=sfc press(mb)

ITSFLG=0, ! specifies what is in TS array
! 0 - temp(C), 1 - temp(K), 2 - pot. temp(K)

IRTSFLG=3, ! specifies what is in RTS array
! 0 - dew pnt.(C), 1 - dew pnt.(K), 2 - mix rat(g/kg)
! 3 - relative humidity in %, 4 - dew pnt depression(K)

IUSFLG=0, ! specifies what is in US and VS arrays
! 0 - u,v component(m/s), 1 - umoms-direction, vmoms-speed

HS = 0.,
PS = 1010.,1000.,2000.,3000.,4000.,6000.,8000.,11000.,15000.,20000.,25000.,
TS = 25., 18.5, 12., 4.5, -11., -24., -37., -56.5, -56.5, -56.5, -56.5,
RTS = 70.,70.,70.,70.,20.,20.,20.,20.,10.,10.,10.,
US = 10.,10.,10.,10.,10.,10.,10.,10.,10.,10.,
VS = 0.,0.,0.,0.,0.,0.,0.,0.,0.,0.,

$END

$ISAN_CONTROL
MSTAGE = 1, 1, 1, ! Main switches for
! pressure, isentropic, "varfile" processing

ISAN_INC=0300, ! ISAN processing increment (hhmm)
! range controlled by TIMMAX, IYEAR1,...,ITIME1

```

```

GUESS1ST='PRESS',      ! Type of first guess input- 'PRESS', 'RAMS'

I1ST_FLG=2,            ! What to do if first guess file should be used, but
                        ! does not exist.
                        ! 1=I know it may not be there, skip this data time
                        ! 2=I screwed up, stop the run
                        ! 3=interpolate first guess file from
                        ! nearest surrounding times, stop if unable
                        ! (not yet available)

IUPA_FLG=3,            ! UPA-upper air, SFC-surface
ISFC_FLG=3,            ! What to do if other data files should be used, but
                        ! does not exist.
                        ! 1=I know it may not be there, skip this data time
                        ! 2=I screwed up, stop the run
                        ! 3=Try to continue processing anyway.

!   Input data file prefixes

IAPR   = '../plevel/data/ip', ! Input pressure level dataset
IARAWI = '../obs/ir',         ! Archived rawinsonde file name
IASRICE = '../obs/is',        ! Archived surface obs file name

!   File names and dispose flags

IFNPRS = 'ip', ! Pressure file name prefix
IOFLGP= 0,      ! Dispose flag: 0 = no write, 1 = write

IFNISN = 'ii', ! Isentropic file name prefix
IOFLGI= 0,      ! Dispose flag: 0 = no write, 1 = write

IFNSIG = 'is', ! Sigma-z file name prefix
IOFLGS= 0,      ! Dispose flag: 0 = no write, 1 = write

IFNVAR = '../var/var', ! "Variable initialization" file name prefix
IOFLGV= 1,      ! Dispose flag: 0 = no write, 1 = write

$END

-----
! Isentropic and sigma-z processing
-----

$ISAN_ISENTROPIC

!-----
! Specify isentropic levels
!-----

NISN   = 59,      ! number of isentropic levels
LEVTH  = 280,282,284,285,286,288,290,292,294,296,298,
        300,303,306,309,312,314,316,318,320,322,324,
        326,328,330,332,334,336,340,345,350,355,360,
        365,370,375,380,390,400,420,440,
        460,480,500,520,540,560,580,600,620,640,660,
        680,700,720,740,760,780,800,

!-----
! Analyzed grid information:
!-----

NIGRIDS = 2,      ! number of RAMS grids to analyze

TOPSIGZ = 25000., ! sigma-z coordinates to about this height

HYBBOT  = 2000., ! Bottom (m) of blended sigma-z/isentropic layer
           ! in varfiles

```

```

HYBTOP = 5000.,      ! Top (m) of blended sigma-z/isentropic layer
SFCINF  = 1000.,      ! Vertical influence of surface observation analysis
SIGZWT  =   1.,      ! Weight for sigma-z data in varfile:
                  !   0.= no sigz data,
                  !   1.=full weight from surface to HYBBOT
NFEEEDVAR =   1,      ! 1 = feed back nested grid varfile info, 0 = don't

                  !-----
                  !   Observation number limits:
                  !-----

MAXSTA=300,          ! maximum number of rawinsondes (archived + special)
MAXSFC=1000,        ! maximum number of surface observations

NONLYS  =   0,      ! Number of stations only to be used
IDONLYS = '76458',  ! Station ID's used

NOTSTA  =   0,      ! Number of stations to be excluded
NOTID   = 'r76458', ! Station ID's to be excluded
                  !   Prefix with 'r' for rawinsonde, 's' for surface

STASEP  =   .1,     ! Minimum surface station separation in degrees.
                  !   Any surface obs within this distance
                  !   of another obs will be thrown out unless it has
                  !   less missing data, in which case the other obs
                  !   will be thrown out.

ISTAPLT =   0,      ! If ISTAPLT = 1, soundings are plotted;
ISTAREP =   0,      ! If ISTAREP = 1, soundings are listed;
                  !   no objective analysis is done.
                  ! If ISTAREP/ISTAPLT = 0, normal processing is done

IGRIDFL =   3,      ! Grid flag = 0, if no grid point data, only obs
                  !           1, if all grid point data and obs
                  !           2, if partial grid point and obs
                  !           3, if only grid data

GRIDWT  =   .01, 6.25e-4,
                  ! Relative weight for the gridded pressure data compared
                  ! to the observational data in the objective analysis

GOBSEP  =   5.0,     ! Grid-observation separation (degrees)
GOBRAD  =   5.0,     ! Grid-obs proximity radius (degrees)

WVLNTH  = 1200., 1200.,
                  ! Used in S. Barnes objective analysis.
                  !   Wavelength in km to be retained to the RESPON
                  !   percent from the data to the upper air grids.

SWVLNTH = 500., 500.,
                  ! Wavelength for surface objective analysis

RESPON  =   .9, .9,
                  ! Percentage of amplitude to be retained.

$END

```